Investigation of offshore wind turbine wakes by numerical modeling and full-scale measurements

Maria Krutova

Thesis for the degree of Philosophiae Doctor (PhD)
University of Bergen, Norway
2024

UNIVERSITY OF BERGEN

Investigation of offshore wind turbine wakes by numerical modeling and full-scale measurements

Maria Krutova

Thesis for the degree of Philosophiae Doctor (PhD)
at the University of Bergen

Date of defense: 30.04.2024

Year: 2024

Title: Investigation of offshore wind turbine wakes by numerical modeling and full-scale measurements

Name: Maria Krutova

Print: Skipnes Kommunikasjon / University of Bergen

Scientific environment

This study was carried out at the Geophysical Institute, University of Bergen. The work was funded by the University of Bergen.

The author has been a part of the Bergen Offshore Wind Center (BOW). BOW is an interdisciplinary research center established at UiB to coordinate offshore wind activities. The author was implicitly involved in the 'HIghly advanced Probabilistic design and Enhanced Reliability methods for the high-value, cost-efficient offshore WIND' (HIPERWIND) project, which has received funding from the European Union's Horizon 2020 Research and Innovation Programme under Grant Agreement No. 101006689. The participation involved taking part in the setting up the multi-scale modeling network. The author was also involved in the 'Research on smart operation control technologies for offshore wind farms (CONWIND)' project supported by the Research Council of Norway, ENERGIX, with grant number 304229.

The lidar data used for this thesis work was collected during OBLEX-F1 measurement campaign carried out in 2015−2016 by the Offshore Boundary-Layer Observatory (OBLO) project. The OBLEX-F1 field campaign was performed under the Norwegian Centre for Offshore Wind Energy (NORCOWE), funded by the Research Council of Norway (RCN) under project number 193821. The scanning Doppler wind lidar system (Leosphere WindCube 100S) has been made available via the National Norwegian infrastructure project OBLO (Offshore Boundary Layer Observatory) also funded by RCN under project number 227777.

Wind speed and direction data at FINO1 were made available by the RAVE (Research at Alpha Ventus) initiative, which was funded by the German Federal Ministry of Economic Affairs and Energy on the basis of a decision by the German Bundestag and coordinated by Fraunhofer IWES.

Resources for simulations were provided by UNINETT Sigma2 – the National Infrastructure for High Performance Computing and Data Storage in Norway (project numbers NS9506K, NS9696K, NS9871K).

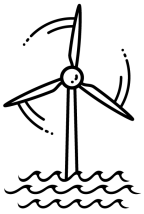

Acknowledgments

I was happy to work with my supervisors at UiB Mostafa Bakhoday-Paskyabi, Joachim Reuder, and Finn Gunnar Nielsen and would like to thank them for the help provided over these four years and fruitful discussions we had.

I would like to thank Astrid Nybøfor providing processed time series from FINO1 for different stability conditions that were essential to one of the papers.

The LES simulations for the study have been performed by using the high performance computer facilities of the Norwegian e-infrastructure Uninett Sigma2. Siggi Raasch and PALM Group were very helpful in solving technical problems aroused with PALM and its compatibility to the computational cluster.

I would like to thank Kjersti Birkeland Daae and Stephan Kral for making this template available on Overleaf and Tore Birkeland and Raymond Nepstad for creating the original version of the template.

I would like to thank Leilane Gonçalves dos Passos and her cats for keeping me company during dark and rainy days in Bergen.

Maria Krutova
Bergen, 2023

Abstract

A wind turbine wake is the flow structure formed behind a wind turbine rotor due to the extraction of kinetic energy from the flow. The resulting flow structure is characterized by reduced wind speed and increased turbulence intensity. Due to the turbulent mixing, the wake flow eventually recovers to the free-flow characteristics. Nevertheless, a wake may reach downstream turbines and affect their inflow. Wakes from several turbines in a wind farm will combine and form a wind farm wake, which may span longer distances than a single turbine wake. The arrangement of wind turbines within a wind farm, including the choice of turbines' size and type, plays a crucial role in how wind farm wakes potentially affect the wind resources availability. Estimating wake effects thus becomes an essential part of wind energy research.

Knowledge of wake behavior is important in several applications, to name a few: estimation of the yearly energy production of a wind farm, short-term forecasts for the wind turbine control, development of the control strategies for wake deflection, or evaluation of the wake effect of the nearby farms on a potential construction site. The precision needed and methods used also vary accordingly. For example, industrial applications prefer fast and simple-to-run methods for power production estimation and wind turbine control, provided the accuracy remains adequate for decision-making. Many simplified methods can be derived from complex equation-solving approaches and assumptions. However, any new method should be validated prior to application. The validation is hindered if little observational data are available or the experiment cannot be reproduced on a smaller scale in a wind tunnel. Thus, building a research framework to select models and approaches relevant to the task is equally important as performing the study itself.

This thesis approaches wake research from both the modeling and observational perspectives. The modeling part considers analytical wake models and numerical simulations, particularly large-eddy simulations (LES). Throughout the thesis papers, a modeling chain is demonstrated. The preparatory stage involves selecting the analytical wake model and verifying the grid refinement in the PALM LES code. Knowing how the grid refinement improves the model's flow resolution, a transient event over the North Sea is simulated over the Alpha Ventus wind farm using mesoscale and microscale simulations. The dynamic wake field obtained as the simulation output is then analyzed with the previously selected analytical models to evaluate how well they adapt to rapidly changing conditions. It was found that the super-Gaussian model estimates the wake shape well and does not require corrections. Therefore, it should be worth focusing on this model and implementing it wider in wake research.

Another part of the thesis focuses on observational data. This part tackles an important aspect of studying turbine wakes from wind fields measured with a scanning lidar. While scanning lidars are versatile instruments capable of measuring a two-dimensional wind field, scan resolution hinders using them for wake analysis. Thus, wake identification and characterization methods should consider the case of insufficient resolution or noise in the data. The thesis suggests a dynamic thresholding method for wake identification. The thresholding approach for wake identification selects a value that explicitly separates a wake from the free flow and allows studying either of them. Although the thresholding approach is not new in wake research, the existing applications use a fixed

threshold value. The fixed threshold value shows good results for wind fields from a wind tunnel or numerical simulation. However, it may not work as well with lidar data which may have noise or low spatial resolution. The presented novel method dynamically selects the threshold, allowing it to adapt to the coarse and noisier lidar data. A subsequent procedure to detect the wake centerline, regardless of whether the wind direction is known, is also suggested, making the method less dependent on the data quality and supporting time series availability.

The drawback of scanning lidars is that they do not measure the actual wind speed but only the line-of-sight velocity along the lidar beam. The scanned wind field is the closest to the original when the lidar's line of sight is aligned with the wind direction. A special procedure, so called lidar retrieval, is required to reconstruct the original wind field. This procedure also allows mapping of the wind speed components and local wind direction. One of the available methods for the wake field retrieval was validated on a larger lidar data set and additional time series. The method used was further tested for the sensitivity to the initial guess and weights used during the optimization process. During the new validation, it was found that wakes in the regarded lidar scans were wider and stronger than in the validation of the original algorithm. The more prominent wakes disrupted the retrieval algorithm so that it returned unnaturally increased wind speed along the wakes. This effect could be mitigated by masking wakes with the previously described dynamic thresholding method. Thus, it is shown how different approaches may be combined to improve the processing of observational data. The validation left several options for further improvement of the method; the next stage should involve comparison with the numerical simulation data.

The papers constituting the thesis describe the setting up of the multi-scale modeling framework and lidar scan processing for the wake analysis. Although they may use seemingly independent methods, it is shown how the synthesis of the methods benefits the understanding and analysis of the wake field. While the additional processing codes produced during the work on this thesis have room for improvement, they have proved their capability of performing designated tasks for wake identification, lidar retrieval, and analytical model fitting. The multi-scale modeling framework established during the studies can then be used for simulating new cases and performing flow analysis in a similar way.

Sammendrag

Bak en vindturbin rotor som trekker kinetisk energi ut fra luftstrømmen, blir strømningsforholdene endret. Dette området kalles vindturbinens vake. Vaken er karakterisert av redusert vindhastighet og økt turbulensintensitet. På grunn av den turbulente blandingen med strømningen utenfor vaken, vil vaken etter hvert gjenvinne egenskapene i den frie vindstrømmen. Likevel kan vaken fra en turbin nå en nedstrøms turbin og påvirke dennes innstrømningsforhold. Den samlede virkning av flere vaker fra turbiner i en vindpark vil summeres og danne en vindpark vake. Denne vaken vil kunne ha større utstrekning enn vaken fra en enkel turbin. Plasseringen av turbiner i en vindpark, inklusive valg av turbinstørrelse og type, spiller en vesentlig rolle for tilgjengeligheten av vindressursene. Estimering av vake-effekter er derfor en vesentlig del av vindeenergiforskningen.

Kunnskap om tubin-vaker er viktig i mange sammenhenger, for å nevne noen få: beregning av årlig energi produksjon, korttids prognoser for vindturbinkontroll, utvikling av kontrollstrategier for å avbøye vaker, eller evaluering av vake-effekten av nærliggende vindparker på en potensiell ny vindparks byggeplass. Den nødvendige presisjonen og metodene som benyttes varierer også. For eksempel vil en i industrielle applikasjoner foretrekke raske og enkle metoder for kraftproduksjonsestimering og vindturbinkontroll, forutsatt at nøyaktigheten forblir tilstrekkelig for beslutninger. Mange forenklede metoder kan utledes fra komplekse ligningsløsninger og antakelser. Hver ny metode bør imidlertid valideres før den tas i bruk. Valideringen vanskeliggjøres dersom lite observasjonsdata er tilgjengelig eller eksperimentet ikke kan reproduseres i mindre skala i en vindtunnel. Derfor er det viktig å bygge et forskningsrammeverk for å velge modeller og metode er like viktig som å utføre vakestudiene i seg selv.

Denne avhandlingen tilnærmer seg vake-forskning både fra et modellerings- og et observasjonsperspektiv. Modelleringsdelen betrakter analytiske vake-modeller og numeriske strømnings-simuleringer, spesielt *large-eddy simulation*, LES (stor virvelsimulering). Forskningsartiklene tar for seg ulike aspekter i en modelleringskjede og analyse av resultater. De forberedende trinnene innebærer å velge egnede analytiske vake-modeller og verifisere den romlige oppløsning i LES løseren implementert i PALM simuleringskoden. Når det er kjent hvordan romlig oppløsning forbedrer modellens oppløsning av vindstrømningen, simuleres en transient hendelse over Nordsjøen over Alpha Ventus vindparken ved bruk av simuleringskoder i mesoskala og mikroskala. Det komplekse vind/vake-feltet som oppnås som simuleringsresultatet blir deretter analysert med de valgte analytiske vake-modellene for å evaluere hvor godt de tilpasser seg raskt skiftende vindforhold. Det ble funnet at den supergaussiske modellen estimerer vakens formen godt og ikke krever korreksjoner. Derfor er det verdt å fokusere på denne modellen og implementere den bredere i vake-forskningen.

En annen del av avhandlingen fokuserer på observasjonsdata. Denne delen tar for seg et viktig aspekt ved å studere vake fra vindfelt målt med en skanning lidar. Mens skanning lidarer er allsidige instrumenter som er i stand til å måle todimensjonalt vindfeltet, begresnser skanneoppløsning bruken i analyse av vaker. Derfor bør en vurdere metoder for vake-identifikasjon og -karakterisering når en har utilstrekkelig oppløsning eller støy i dataene. Avhandlingen foreslår en dynamiskterskel metode for vake-identifikasjon. Terskel-metoder for vake-identifikasjon velger en verdi som eksplisitt skiller en vake fra

den frie strømmen og muliggjør å studere hver av dem separat. Selv om terskel-metoder ikke er nye i vake-forskningen, bruker de eksisterende applikasjoner en fast terskelverdi. Den faste terskelverdien gir gode resultater på vindfelt fra en vindtunnel eller numerisk simulering. Men den fungerer ikke så godt på vindfelt fra lidar-skanning som kan ha støy eller lav romlig oppløsning. Den nye metoden som presenteres velger dynamisk terskelverdien, slik at den kan tilpasse seg de grove og mer støyfylte lidardataene. Videre er det foreslått en prosedyre for å detektere vakens senterlinje, uavhengig av om vindretningen er kjent, noe som gjør metoden mindre avhengig av datakvaliteten og tilgjengelighet av ekstra tidsserier.

Ulempen med skanning lidarer er at de ikke måler den faktiske vindhastigheten, men bare siktlinjehastigheten langs lidarstrålen. Det målte lidar-vindfeltet blir mest likt det virkelige vindfeltet når lidarens siktlinje er på linje med vindretningen. Likevel krever lidar-skanninger behandling med så kalte *lidar retrieval* (lidar-innhenting) prosedyre for å rekonstruere det originale vindfeltet. Denne prosedyren trenges for å kartlegge detaljene i hver av komponentene til vindhastigheten og for å finne lokal vindretning. En av de lidar-innhenting metodene ble validert på et større lidar-datasett og ekstra tidsserier i denne avhandlingen. Metoden ble testet for følsomhet for den initielle gjetningen og vektene som ble brukt under optimaliseringsprosessen. I den nye valideringen ble det funnet at de betraktede lidar-skanningene hadde bredere og sterkere vaker enn det i den originale valideringen av den samme metoden. De sterkere vakene forstyrret algoritmen slik at den returnerte unaturlig økt vindhastighet langs vaker. Denne effekten kan dempes ved å maskere vaker med den foreslåtte dynamiske terskel-metoden. Det ble dermed vist hvordan ulike tilnærminger kan kombineres for å forbedre behandlingen av observasjonsdata. Valideringsprosessen identifiserte noen muligheter for ytterligere forbedring av metoden; neste trinn bør innebære sammenligning med de numeriske simuleringsdataene.

Artiklene som utgjør avhandlingen beskriver oppsettet av et rammeverk for flerskalamodellering og lidar-skannings prosessering for vake-analyser. Selv om artiklene bruker tilsynelatende uavhengige metoder, vises det hvordan kombinasjonen av metodene bedrer forståelsen og analysen av vake-feltet. Mens de ekstra prosesseringskodene utviklet i denne avhandlingen har rom for forbedring, er det demonstrert hvordan de kan brukes til vake-identifikasjon, bruk av lidar data og analytisk modelltilpasning. Rammeverket for flerskalamodellering etablert under studiene kan deretter brukes til å simulere nye tilfeller og utføre vakeanalyser på tilsvarende måte.

Outline

This thesis consists of an introductory part and six scientific papers. Chapter 1 introduces key challenges in wind energy research, the role of wind observations, numerical simulations, and their mutual influence. Chapter 2 gives a detailed overview of the wake modeling and processing methods, focusing on those used in the papers. The specific data sets and models' parameters are listed in Chapter 3, along with the repositories of Python codes produced for the papers. A summary of each paper's findings is given in Chapter 4, with the conclusions and outlook presented in Chapter 5. The following papers are included in this thesis in Chapter 6:

1. **Krutova, M.**, Bakhoday-Paskyabi, M., Nielsen, F. G., and Reuder, J.: Evaluation of Gaussian wake models under different atmospheric stability conditions: Comparison with large eddy simulation results. *Journal of Physics: Conference Series*, **1669(1)**, 012016 (2020), doi:10.1088/1742-6596/1669/1/012016

2. **Krutova, M.**, Bakhoday-Paskyabi, M., Reuder, J., and Nielsen, F. G.: Self-nested large-eddy simulations in PALM model system v21.10 for offshore wind prediction under different atmospheric stability conditions. *Geoscientific Model Development*, **16(12)**, 3553–3564 (2023), doi:10.5194/GMD-16-3553-2023

3. Bakhoday-Paskyabi, M., **Krutova, M.**, Bui, H., and Ning, X.: Multiscale simulation of offshore wind variability during frontal passage: Brief implication on turbines' wakes and load. *Journal of Physics: Conference Series*, **2362**, 012003 (2022), doi:10.1088/1742-6596/2362/1/012003

4. **Krutova, M.** and Bakhoday-Paskyabi, M.: Gaussian wake model fitting in a transient event over Alpha Ventus wind farm. *Wind Energy Science Discussions* **[preprint]**, (2023), doi:10.5194/wes-2023-79

5. **Krutova, M.**, Bakhoday-Paskyabi, M., Reuder, J., and Nielsen, F. G.: Development of an automatic thresholding method for wake meandering studies and its application to the data set from scanning wind lidar. *Wind Energy Science*, **7(2)**, 849–873 (2022), doi:10.5194/wes-7-849-2022

6. **Krutova, M.**, Bakhoday-Paskyabi, M., and Reuder, J.: Validation of the 2D-VAR lidar retrieval algorithm for non-homogeneous wind fields using FINO1 and SCADA data. *Authorea*, **[preprint]** (2023), doi:10.22541/au.168809547.78501650/v1

In addition, the author of this thesis provided numerical simulations for the following paper. This standalone paper is not included in the thesis.

7. Bakhoday-Paskyabi, M., **Krutova, M.**, Nielsen, F. G., Reuder, J., and Guernaoui, O.: On stochastic reduced-order and LES-based models of offshore wind turbine wakes. *Journal of Physics: Conference Series*, **1669(1)**, 012018 (2020), doi:10.1088/1742-6596/1669/1/012018

Contents

List of Figures

List of Tables

1 Introduction

1.1 Overview

Wind energy is an intermittent renewable energy source that is gradually increasing its share in electricity production (Fig. 1.1). The number and size of wind farms are growing worldwide, with offshore wind energy steadily increasing the installed capacity. According to *Global WInd Energy Council* (2023), the capacity of new offshore wind installations in 2021−2022 accounts for 34% of the total offshore wind capacity since 2006. The International Energy Agency (IEA) predicts growth of offshore capacity by 240% within 2021−2026, reaching the share of 1.5% in electricity produced from renewable sources (including hydropower) (*International Energy Agency*, 2021).

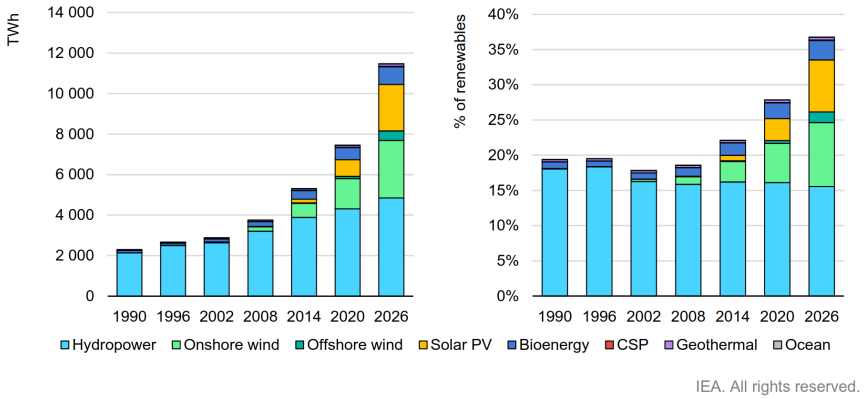

Figure 1.1: Renewable electricity generation by technology, 1990-2026 (left) and share by technology, 1990-2026 (right). Reproduced from the International Energy Agency (2021) report.

General wind energy concepts, e.g., wind power production or flow physics, apply to both onshore and offshore wind farms. Nevertheless, the offshore conditions bring new specifics into the research, to name a few:

- The sea surface roughness is generally lower than over the land. Therefore, the wind flow offshore is less affected by the surface friction. However, the sea surface roughness changes dynamically with the wave conditions (*Johnson et al.*, 1998), causing dependencies between wind speed, turbulence, and surface roughness, which are not as pronounced onshore.

- The wind speed profile is affected by whether the wind blows from the land or sea (*Kettle*, 2014). Wind profiles over the sea may strongly diverge from logarithmic and cause differences in wind flows at the top and bottom of a turbine rotor.

- Offshore wind farms alter the flow enough to affect nearby farms. The sea surface allows a unique usage of satellite data for visualizing the wind farm flow, confirming the effect (*Christiansen and Hasager*, 2006; *Hasager et al.*, 2015).

- Meteorological measurements are more scarce offshore than onshore due to the complications of installing measurement masts and deploying instruments (*Hasager et al.*, 2008).

Although new concepts for wind energy extraction emerge regularly (*Cherubini et al.*, 2015; *Jamieson*, 2018), horizontal-axis wind turbines (HAWT) remain the primary choice for large-scale wind farms and electricity production. HAWT extracts kinetic energy from the wind flow that passes through the rotor. The power production is capped at the rated power specific to each turbine design. The rated power corresponds to the rated wind speed above which the power production is kept constant. Below the rated wind speed, the power production depends on the cube of the inflow wind speed U_0 as

$$P = \frac{1}{2}\rho C_P A U_0^3, \tag{1.1}$$

where ρ is the air density. C_P is the power coefficient showing what fraction of the wind power can be extracted. The power coefficient depends on the wind turbine design but cannot exceed the Betz limit of 0.59. $A = \pi(D/2)^2$ is the area of a rotor with the diameter D. With the modern HAWTs reaching $C_P = 0.4 - 0.5$ during operation (*Dai et al.*, 2016) and the power coefficient giving only a linear increase ($P \sim C_P$), the improvement in this direction focuses on better control strategies rather than turbine design. The contribution of the other two terms is the factor to consider before planning a wind farm. Consequently, HAWTs tend to grow in size ($P \sim D^2$), and areas with high mean wind speed are being developed for wind farm construction ($P \sim U_0^3$).

It should be noted that the inflow wind speed U_0 is not necessarily the free-flow wind speed U_∞. The inflow may be affected by nearby turbines or local fluctuations caused by a transient flow. The cubic relationship for the power output in Eq. (1.1) amplifies any fluctuation or estimation error in the wind speed below rated. Above the rated wind speed, the power output is kept stable through wind turbine control; hence, the changes in the inflow wind speed affect energy output less. Still, the loads and turbulence effects caused by the wind flow should be considered.

The most important influence on the inflow in a wind farm is caused by the wind turbines themselves. The extraction of kinetic energy from the flow results in an area downstream of the turbine characterized by decreased wind speed and increased turbulence intensity – namely, the wake effect.

The wind turbine wake is a three-dimensional, horizontally elongated, and highly dynamic structure in the flow field. The shape of an instantaneous wake is typically irregular and constantly changes depending on the flow characteristics, which, in turn, are strongly influenced by atmospheric stability (*Larsen et al.*, 2008; *España et al.*, 2011; *Abkar and Porté-Agel*, 2015; *Foti et al.*, 2016). Eventually, the wake flow recovers to the free flow through mixing caused by turbulent eddies. However, if the wake flow reaches another wind turbine downstream before full recovery, the inflow speed to this turbine decreases compared to the free-flow speed. Consequently, a new wake is formed with the wind speed decreasing again; the wake recovery is delayed. The more wind turbines are placed along the wind direction, the more persistent are the wake effects.

Due to the low surface friction, offshore conditions usually favor slow wake recovery. Wakes from individual turbines merge and amplify downstream wakes, forming the wind farm wake. As shown by *Christiansen and Hasager* (2005, 2006), wind farm wakes could

reach a length of at least 10−20 km, which exceeded ten rotor diameters of the regarded turbines. *Ahsbahs et al.* (2020) observed wind farm wakes of a similar length. *Platis et al.* (2018) estimated up to 40% wake deficit and five times higher turbulence levels at 5−10 km downstream of the wind farm. The same paper showed that a wake deficit of 1 m/s (10−20% of the free-flow wind speed) and a slight increase in the turbulence levels could still be seen at 45 km further downstream. With the new wind farms built near existing ones and producing cluster wakes (*Cañadillas et al.*, 2022), the long-distance wake effects should be quantified and considered during the planning and operation (*Akhtar et al.*, 2021; *Finserås et al.*, 2024).

The wake problem could be solved by placing wind turbines far apart to avoid wake effects completely. However, the wind farm size is limited by the area available for construction and associated costs, e.g., the price of power cable per meter. Usually, wind turbines are placed within 6−8 rotor diameters from each other, where wake effects are weakened but still noticeable. Hence, the wake effects must be adequately quantified to estimate structural loads and power output deficit. In addition, control strategies can be utilized to change the rotor angle and deflect the wake in the desired direction – thus, the wake effect on the downstream turbine is decreased (*Adaramola and Å. Krogstad*, 2011; *Fleming et al.*, 2014). Modern wind farms often adopt a staggered layout for the same purpose of mitigating wake effects: each row is shifted from the previous one so that the turbines are not aligned in the dominant wind direction (*Chamorro et al.*, 2011; *Stevens et al.*, 2016). Alternatively, the algorithms to optimize an irregular wind farm layout are gaining popularity (*Tao et al.*, 2020). The optimization of power production through turbine control and wind farm layout means that the downstream turbines in such farms are often exposed to a non-uniform inflow instead of being directly hit by a wake. The non-uniform flow, in turn, causes asymmetric rotor loads, which affect the turbine's lifetime. Therefore, optimizing power production must go in hand with quantifying wake effects and dynamic loads. With more historical datasets available on wind farm operation and atmospheric conditions, offshore wind research gains more data for analysis, development of new methods and improvement of the old ones.

The interest in measuring offshore wind started to rise as the first offshore farms were deployed in the 1990s (*Hasager et al.*, 2008). Considering this and the difficulties of installing meteorological equipment offshore, the meteorological measurements over the sea appear to be much scarcer than over the land. Hence, numerical modeling plays a prominent role in offshore wind energy research. However, the computational time required by high-fidelity models renders numerical simulation inapplicable for industrial applications such as short-term forecasting or wind farm layout optimization. Although the latter is not performed in real-time, utilizing a fast model allows the comparison of numerous layout variations within a short period. Thus, the simplifications of wind flow physics are introduced to obtain fast but reliable models for predicting the wake effect on loads and power production. Most of these approaches are based on analytical or engineering models that rely solely on mathematical expressions and root-finding procedures. Regardless of the simplification level, the models should still be validated on the observational data or other verified high-fidelity models. Neither models nor observations may be sufficient as a standalone. Regarding them together helps to increase the estimation accuracy and improve processing methods (Fig. 1.2).

On a fundamental level, each new method must be first verified and validated with the observational data. The validation becomes complicated if insufficient observations

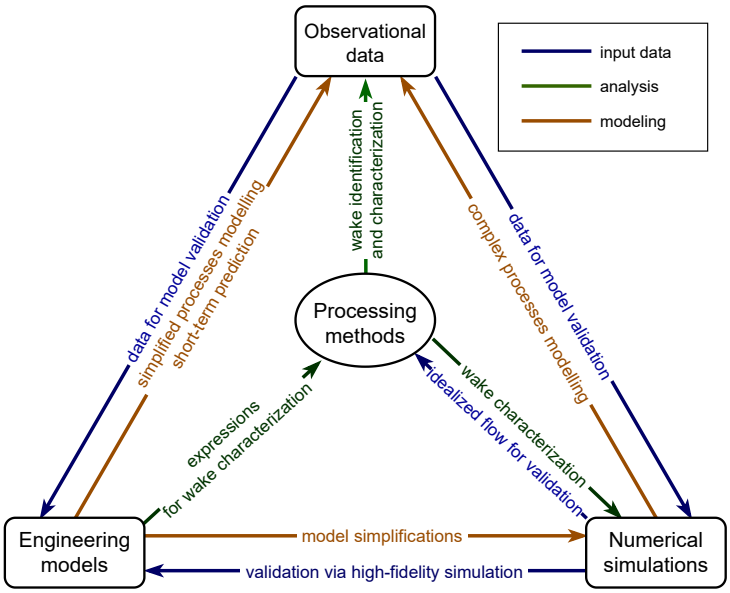

Figure 1.2: Mutual influence of the observational data, modeling approaches, data processing and analysis.

are available, especially when a complex transient case is regarded. For example, the low-level jet (LLJ) – a low-altitude maxima of the wind speed. While onshore LLJs are primarily nocturnal, offshore LLJs behave differently and form at lower heights of 200−300 m (*Nunalee and Basu*, 2014; *Wagner et al.*, 2019; *Møller et al.*, 2020). Considering the similar order of the modern turbines' size, the behavior of LLJ raises concerns for new offshore wind farms. Other challenging events that hinder short-term forecasts are characterized by rapid changes in wind speed and direction and can be caused by open cellular convection (OCC) or frontal passages. OCC events belong to transient flow cases not characteristic of onshore sites (*Atkinson and Zhang*, 1996).

The scarcity of offshore measurements, particularly those related to LLJ and OCC events, makes offshore wind research rely on numerical modeling and model coupling to study complex atmospheric conditions. In this case, a numerical model is first verified and validated so that the model's drawbacks in simulating turbulent flows are known and quantified. Then, a numerical simulation of a more complex flow, e.g., LLJ or OCC, can be accepted with a certain degree of reliability and used for analysis or as a foundation to develop simplified models. Generally, a modeling framework is a chain of validating a model with observational data to use the established model as a high-fidelity reference for analytical models or complex flows (Fig. 1.3) (*Bakhoday-Paskyabi et al.*, 2022).

Similarly, lidar retrieval methods – algorithms to reconstruct the original wind field from lidar measurements – should also be validated prior to the application. Verification using only observations is limited because instruments measuring actual wind characteristics, e.g., cup and sonic anemometers, provide only point measurements and cannot be deployed in quantities enough to cover a large area. On the contrary, a numerical wind flow obtained with a high-fidelity model is commonly used to perform cross-comparison with lidar data (*Chatterjee et al.*, 2018; *Rahlves et al.*, 2022).

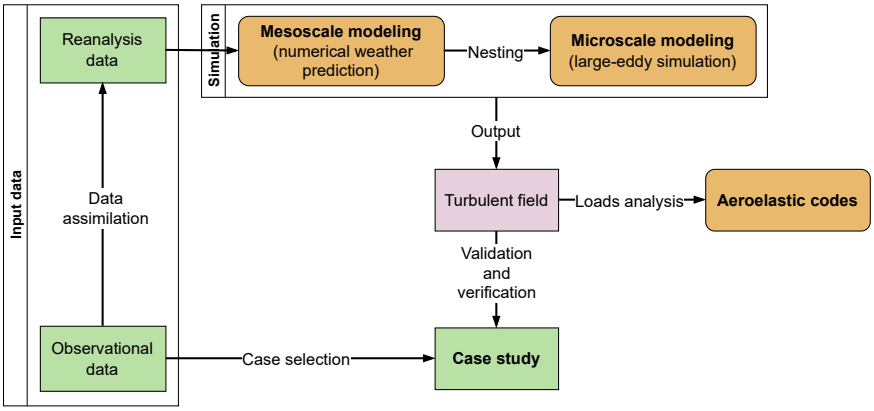

Figure 1.3: Example of a multi-scale modeling chain that starts with atmospheric processes simulated at the mesoscale level. The simulation is then down-scaled to micro-levels, allowing more precise simulation of the turbulence and calculation of rotor loads.

Sometimes, a processing method involves a concept relevant both for observed and simulated fields, e.g., wake detection – identification of a turbine wake in a wind field for further characterization. Hence, wake-processing methods should be applicable in either case. When developed with universality in mind, the processing method can be first tested on numerical fields, which are generally less noisy than actual measurements.

1.2 Objectives and research questions

The thesis approaches the wake flow problem from several perspectives, each paper focusing on a different aspect of wake measuring and modeling (Fig. 1.4). The addressed research questions can be summarized as follows:

1. **What are the most relevant measurement techniques and methods to investigate the wake flow? Are all parameters – wake width and length, velocity deficit, turbulence intensity, and wake meandering – equally important, or does their relevance change depending on the study goals?**

   Due to the wake complexity, wake research utilizes a wide range of measurement tools and modeling methods. Hence, it is important to know which existing methods are the most efficient when studying wakes. The general purpose methods should also be considered, as some may be improved or tuned to the specific tasks related to wake analysis. Regarding short-term forecasts, the developed routines must be fast to perform and rely on real-time data. Industrial applications would prefer techniques that can be seamlessly implemented into established approaches.

   Most of the papers in the thesis tackle this question to a certain extent. Paper I gives a short overview of the Gaussian wake models. Paper II explores an existing numerical modeling code for the flows at wind speeds characteristic of wind energy research. Paper V describes and verifies a new algorithm for wake identification and characterization. The algorithm is subsequently implemented as a sub-routine in the observational data processing performed in Paper VI.

2. **What are the drawbacks of the existing approaches for wake modeling and analysis? Can those drawbacks be mitigated to become negligible, or should they be accounted for?**

   This question is addressed in Paper II and explored in Papers V and VI. The latter two papers suggest solutions for challenges encountered in lidar data processing.

3. **What can we learn about a wake from the limited data available?**

   While numerical simulations can generate a three-dimensional wake field, both as averaged and instantaneous snapshots, real-world observations have more constraints and limitations. Still, observational data are essential for model validation and verification. Getting as much information about the wake as possible expands the list of quantities available for comparison between models and measurements.

   This question primarily concerns observational data. However, Paper V shows how a wake-processing method developed for the measured wind flow is also applicable to the simulated data.

4. **How do the established approaches for stationary and non-stationary wake situations perform in complex flow cases, e.g., transient flow? Is it possible to predict and quantify the turbine response in these events, for example, by introducing completely new routines or building up a special routine upon the existing model?**

   Rapid changes in the inflow conditions due to a gust, transient, or extreme events raise the question of whether a model interprets the flow correctly. The transient flow situation, particularly the OCC event, is explored in Paper III by establishing a multi-scale modeling chain to simulate wind turbine response in this kind of event. Paper IV explores the resulting wake field to analyze how simple wake models react to rapidly changing flow characteristics.

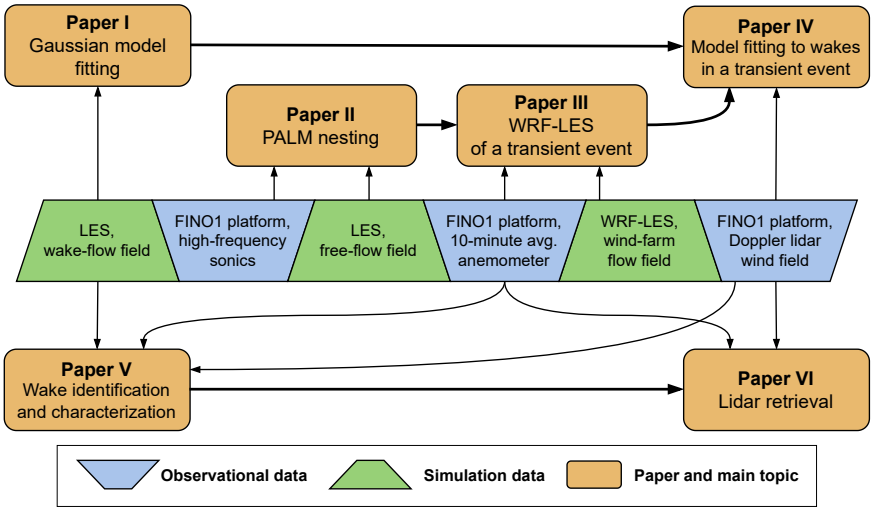

Figure 1.4: Connection between main topics of the thesis papers and data used.

2 Scientific background

2.1 Wind turbine wakes and observations

2.1.1 Wake structure

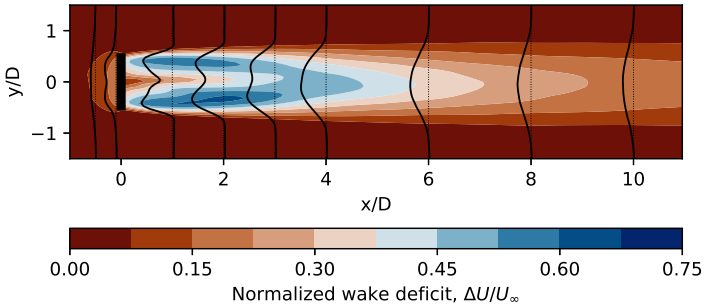

Figure 2.1: Cross-sectional profiles of the velocity deficit at various distances in a simulated flow upstream and downstream of the wind turbine.

A wind turbine extracts kinetic energy from the wind flow. Consequently, a structure with decreased wind speed forms behind the turbine rotor – a wind turbine wake (Fig. 2.1). Upstream of the turbine, a small induction region also shows a decrease in the wind speed, although not as substantial as in the wake at the same distance from the rotor (*Medici et al.*, 2011; *Simley et al.*, 2016). Several dynamic streak-like structures form because of the pressure difference caused by blade rotation: tip vortices at the blade's tip (*Ivanell et al.*, 2010) and a hub vortex forming from the nacelle and blade's root vortices (*Zhang et al.*, 2012, 2013). The tip vortices persist for several rotor distances before full dissipation (*Sherry et al.*, 2013) and obstruct mixing with the free flow, thus slowing down the wake recovery (*Lignarolo et al.*, 2014). Their dissipation accelerates in a highly turbulent flow (*Khan et al.*, 2017). On the contrary, the hub vortex is rather unstable; its strongest effect on the flow speed occurs in the near-rotor region. Still, the fluctuations caused by the hub vortex partially contribute to the wake speed at further downstream distances (*Ashton et al.*, 2016). The chance for hub vortex instability increases in the low turbulent flow.

Wakes are the most prominent structures in a wind farm flow field. Hence, their effect on turbines poses one of the main challenges for predicting structural loads and wind power output. The wake velocity deficit ΔU describes the difference between the magnitudes of the free-flow wind speed U_∞ and wind speed U behind the rotor:

$$\Delta U = U_\infty - U. \tag{2.1}$$

The normalized velocity deficit $\Delta\overline{U}$ characterizes the strength of a wake. $\Delta\overline{U} = 1$ corresponds to the absence of the flow movement, and $\Delta\overline{U} = 0$ means the full recovery

to the free-flow wind speed:

$$\Delta\overline{U} = \frac{U_\infty - U}{U_\infty} = 1 - \frac{U}{U_\infty}. \tag{2.2}$$

For wake studies, a local Cartesian coordinate system is typically centered at the rotor center or wind tower foundation. The x-axis may be fixed or rotate dynamically with the horizontal wind direction. The y-axis is perpendicular to the x-axis and lies in a horizontal plane. Depending on the characteristics, a wake can be split into the near and far wake (*Crespo et al.*, 1999; *Vermeer et al.*, 2003). The near wake is characterized by strong tip vortices and a possibility of a double peak in the velocity deficit distribution. The normalized velocity deficit $\Delta\overline{U}$ is the strongest in the near wake and may reach $0.6-0.8$ (Fig. 2.1). The criteria for separating near and far wakes vary depending on the study's purposes. For example, *Vermeer et al.* (2003) defined the near wake for $x/D \leq 1$, where the influence from hub vortices is still strong. On the contrary, *Crespo et al.* (1999) excluded the near-rotor region at $x/D < 2$ for the same reasons and regarded the near wake at $2 \leq x/D \leq 5$, which is now a more typical range to define the near wake. A short transitional region may also be defined, where the velocity deficit approaches self-similar Gaussian distributions of the far wake. The far wake is then defined at $x/D > 6-8$ and spans until the full recovery to the free flow.

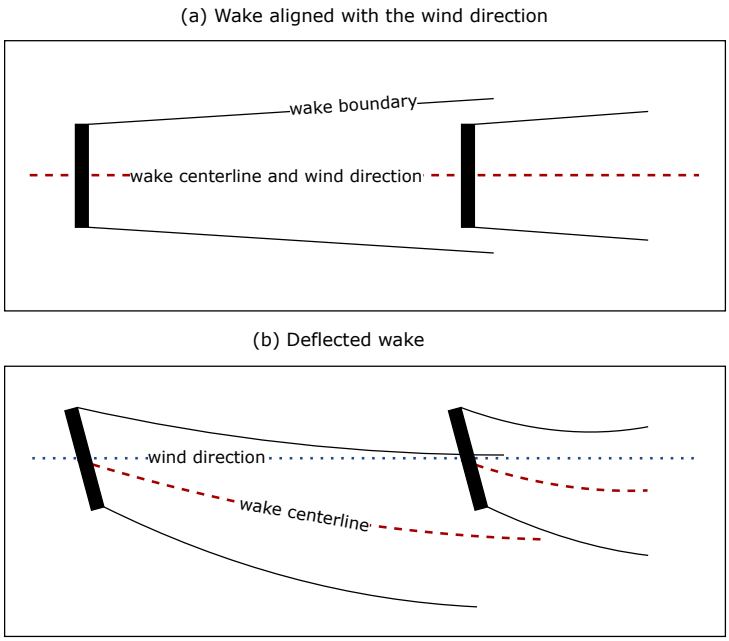

Figure 2.2: A schematic of (a) a wake aligned with the wind direction and (b) a wake deflected by the turbines with the rotor's yaw angle of 10°.

The longer the wake, the more noticeable its deflection from the rotor axis and distortion of the circular shape in the cross-section. Weak deflection and divergence from a regular circular shape always occur due to the effect of the Coriolis force, regardless of the wind turbine orientation (*Abkar and Porté-Agel*, 2016; *van der Laan and Sørensen*,

2017). The deflection can be also affected by altering the rotor's position. Changing the rotor's yaw angle (Fig. 2.2b) causes strong horizontal deflection and helps to decrease the wake effect on downstream turbines and increase the power production (*Adaramola and Å. Krogstad*, 2011; *Fleming et al.*, 2014). Changing the tilt angle increases the vertical deflection of a wake and leads to the wake's mirroring from the sea surface; the mirroring creates a small section downstream where the velocity deficit is slightly lower compared to a non-deflected wake (*Johlas et al.*, 2022).

The instantaneous wake center oscillates around the averaged wake's centerline – a so-called wake meandering (*Larsen et al.*, 2007; *España et al.*, 2011; *Foti et al.*, 2018). Together with the wake deflection, the wake meandering subjects downwind turbines to non-uniform loads, complicating the estimation of fatigue and lifetime. The oscillation amplitude increases with the downstream distance, especially in the horizontal plane (*Foti et al.*, 2018). The oscillations are weaker but still prominent in the vertical plane (*España et al.*, 2011). Although the physics behind the wake meandering is not fully understood, the dominant hypothesis attributes meandering to vortex shedding and large-scale turbulence influence (*Larsen et al.*, 2007, 2008; *Mao and Sørensen*, 2018). Other factors like wind turbine vibrations may also contribute to the meandering. While the wake meandering is not important for the long-term estimations of wind energy production, it is a crucial factor to consider when studying dynamic loads, as those are evidently correlated with the behavior of an instantaneous wake (*Moens et al.*, 2019).

2.1.2 Wakes and atmospheric stability

Assuming Cartesian coordinates, the wind speed U can be split into directional components u, v, and w:

$$U^2 = u^2 + v^2 + w^2. \tag{2.3}$$

Each directional wind speed component in a turbulent flow, e.g., u, can be split into the mean term denoted with an overline, $\overline{u}$, and the fluctuating term denoted with prime symbol, u'. Then for each component:

$$u = \overline{u} + u',\ v = \overline{v} + v',\ w = \overline{w} + w'. \tag{2.4}$$

The same is valid for the total wind speed U

$$U = \overline{U} + U'. \tag{2.5}$$

The sum of squared mean speed components corresponds to the flow's mean kinetic energy per unit mass E:

$$E = \frac{1}{2}\overline{U}^2 = \frac{1}{2}\left(\overline{u}^2 + \overline{v}^2 + \overline{w}^2\right). \tag{2.6}$$

Similarly, the fluctuating components represent the turbulent kinetic energy e (TKE):

$$e = \frac{1}{2}\left(u'^2 + v'^2 + w'^2\right). \tag{2.7}$$

The turbulence intensity I of the flow describes the strength of turbulent fluctuations in comparison to the mean wind. For example, the turbulence intensity of the u-component of the wind speed is given by

$$I_u = \frac{\sigma_u}{\overline{u}}, \tag{2.8}$$

where σ_u is the standard deviation of u.

The temperature T may be insufficient for use in meteorological studies due to the effects of atmospheric pressure and humidity. Hence, the potential temperature θ is introduced to account for the pressure p

$$\theta = T \left(\frac{p_0}{p} \right)^k, \tag{2.9}$$

where p_0 is the standard pressure of 100 kPa or the surface pressure. The exponent k is typically taken as $k = 2/7$, assuming the ideal diatomic gas. Additionally, the virtual potential temperature θ_v shows the potential temperature θ of dry air with the same density as moist air. Although the difference between θ and θ_v may reach only a few degrees, it must be considered to resolve correctly the turbulence intensity and movement due to buoyancy.

The turbulence intensity is linked with the atmospheric stability conditions, which are affected by the wind shear $\partial\overline{U}/\partial z$ and the potential temperature gradient $\partial\theta/\partial z$ (*Stull*, 1988; *Churchfield et al.*, 2012). To classify atmospheric stabilities, the Obukhov length L is introduced to describe the relation between wind shear and buoyancy:

$$L = -\frac{u_*^3 \, \theta_v}{\kappa g \, \overline{w'\theta_v'}}, \tag{2.10}$$

where $\kappa = 0.4$ is the von Karman constant, $g = 9.81\,\mathrm{m/s}$ – the acceleration due to the Earth's gravity; u_* – the friction velocity. $\overline{w'\theta_v'}$ – the surface heat flux.

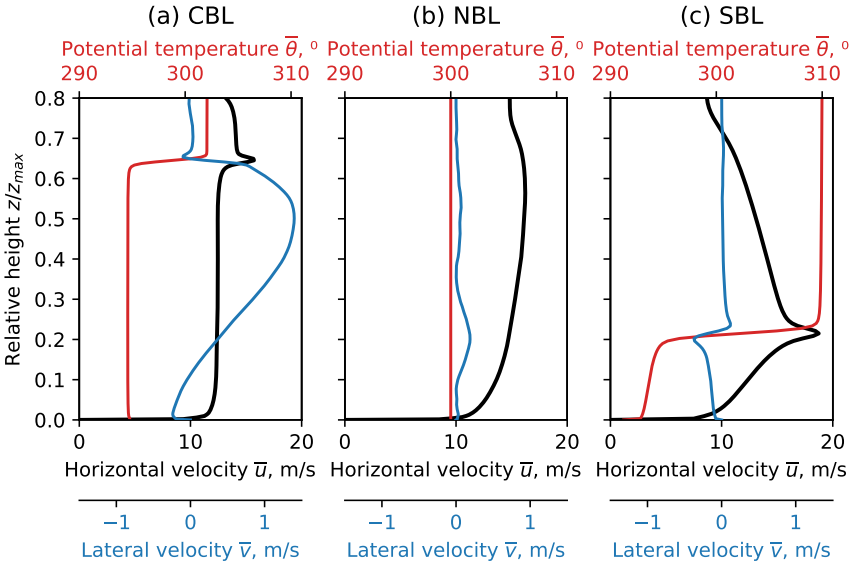

Figure 2.3: Schematic profiles of mean velocity components and potential temperature for (a) convective, (b) neutral, and (c) stable boundary layers in a numerical simulation. The vertical axis is normalized by the respective domain height.

Atmospheric stability of the boundary layer is defined depending on whether the Obukhov length L is positive or negative:

- Unstable or convective boundary layer (CBL), $L \leq 0$ (Fig. 2.3a): the adiabatic lapse rate of a rising air parcel decreases slower than that of the surrounding air. Hence, the air parcel remains warmer and less dense than its surroundings and continues to rise because of the buoyancy. The mean wind shear is low. The variance of velocity components is relatively high and causes strong turbulence fluctuations (*Deardorff*, 1972; *Schmidt and Schumann*, 1989).

- Neutral boundary layer (NBL), $|L| \to \infty$ (Fig. 2.3b): weak to zero potential temperature gradient, the air parcel mainly moves horizontally because of the wind; the vertical profile of the mean wind speed is close to logarithmic (*Stull*, 1988).

- Stable boundary layer (SBL), $L > 0$ (Fig. 2.3c): the air motion is suppressed, the rising air parcel is colder and denser than its surroundings and tends to return to its level of origin. Stable atmosphere is characterized by high wind shear and low turbulence. The mean wind speed vertical profile diverges from logarithmic and may be distorted with one or more local maxima due to low-level jets (*Kettle*, 2014).

Table 2.1: Detailed classification of the atmospheric stabilities based on the Obukhov length. Reproduced from Peña et al. (2010)

Stability class		Obukhov length
Unstable	Very unstable	$-100 < L \leq -50$
	Unstable	$-200 < L \leq -100$
	Near neutral/unstable	$-500 < L \leq -200$
Neutral		$\lvert L \rvert \geq 500$
Stable	Near neutral/stable	$200 \leq L < 500$
	Stable	$50 \leq L < 200$
	Very stable	$10 \leq L < 50$

Several intermediate stratifications may be introduced to separate very stable/unstable conditions from near neutral (Table 2.1) (*Wijk et al.*, 1990; *Peña et al.*, 2010; *Rodrigo et al.*, 2015). A true neutral atmosphere is a rare case; close to neutral conditions are usually observed on a cloudy day or during the transition from stable to unstable conditions and vice versa. Diurnal variations in stability are especially pronounced onshore due to the surface heating and cooling. Unstable conditions onshore can be expected during the clear sky day when the surface is heated faster than the air. Stable conditions are often observed at night when the land surface is cooler than the air.

Offshore, diurnal variations in stability are not as prominent compared to seasonal variations (*Sathe et al.*, 2011; *Barthelmie et al.*, 2015). If any diurnal pattern emerges, it differs from onshore sites and shows a slight increase of stable conditions occurrence in the evening (*Motta et al.*, 2005). The hourly and monthly distributions of stabilities are noticeably affected by the offshore site proximity to the land: winds from the coast or the open sea bring patterns characteristic to their respective origins (*Motta et al.*, 2005).

Turbulence intensity offshore strongly depends on the wind speed since it affects the surface roughness through the wave formation (*Türk and Emeis*, 2010). However, turbulence levels are generally lower than over the land due to a lower surface roughness. Combined, these factors lead to an increased occurrence of very stable conditions for wind speeds of $8 - 15\,\mathrm{m/s}$ – common rated wind speed for wind turbines; the total SBL occurrences gradually decrease for winds above $15\,\mathrm{m/s}$ (*Motta et al.*, 2005; *Sathe et al.*, 2013; *Cheynet et al.*, 2018; *Nybø et al.*, 2020).

The increased chance of SBL occurrence over the sea is important for wind research because SBL is usually thin and reaches the order of 300 m or even lower in the extremely stable atmosphere (*Smedman et al.*, 1995). Since modern offshore wind turbines tend to grow in size, the upper part of a wind turbine rotor may reach the boundary of SBL and become subjected to a more complex flow even outside extremely stable conditions (*Wagner et al.*, 2019).

Wakes also recover differently under different stability conditions. The longer and stronger the wake is, the higher its possibility to affect downstream turbine inflow and loads. The influence of atmospheric stability on power production was studied for several European offshore wind farms (*Barthelmie and Jensen*, 2010; *Hansen et al.*, 2011; *Alblas et al.*, 2014; *Barthelmie et al.*, 2015) and USA onshore wind farm data (*Wharton and Lundquist*, 2012). The results agree upon that a higher velocity deficit and slower wake recovery are observed during stable conditions leading to decreased power production. Neutral and convective conditions show less wake losses due to higher turbulence intensity and better mixing. If compared between very stable and very unstable conditions, the difference in power production of the wake-affected turbines may reach $10 - 20\%$ of the free-flow power output. However, when sampled for the same mean wind speed, the normalized power production in stable, neutral and unstable cases may show less difference (*Barthelmie et al.*, 2015).

Numerical simulation of stability effects in a large wind farm supports the observations. It confirms a faster wake recovery in the CBL (*Churchfield et al.*, 2012), although the wake growth and meandering also became stronger in this case (*Abkar and Porté-Agel*, 2015). The effect of stability on the wake decay is also confirmed in wind tunnel experiments (*Zhang et al.*, 2013; *Hancock and Pascheke*, 2014). Therefore, slower wake recovery in the SBL becomes important to consider in offshore wind farms. Single turbine wakes merge and form a wind farm wake, which may span several kilometers and affect nearby farms. A notable observation of wake effects registered at several tens of kilometers from a large offshore wind farm was described by *Platis et al.* (2018).

2.1.3 Measurement instruments and techniques

Field measurements

Measurements of wind speed in a wake provide data for the model validation and case studies. Since the turbine wake is a three-dimensional structure, not all measurement instruments can provide enough information about the wake flow. The most widespread meteorological instruments – cup and sonic anemometers – measure the wind speed and direction at the point where they are mounted. Usually, the anemometers are used to take measurements of the free flow or at certain points downstream of the turbine. The time resolution of a cup anemometer is generally enough to calculate the turbulence intensity

with Eq (2.8) using a standard deviation of 1 Hz time series and 10-minute wind speed average. While a single cup anemometer registers only the magnitude of wind speed, a sonic anemometer can measure all three directional wind speed components. The time resolution of sonic anemometers reaches up to 100 Hz, allowing to perform high-frequency measurements and get more precise estimation of the standard deviation of velocity components and the turbulence intensity.

While it is theoretically possible to mount several anemometers and get a scope of a two- or three-dimensional wind field through interpolation, the number of instruments required and unavoidable flow distortions from meteorological masts render this method infeasible. For the remote wind measurements, a scanning Doppler wind lidar becomes the primary choice.

A scanning Doppler lidar emits a laser beam and analyzes light energy back-scattered by small particles moving with the air (*Werner*, 2005; *Bingöl et al.*, 2010; *Trujillo et al.*, 2011). The velocities along the lidar's beam, or line-of-sight velocities, are determined based on the Doppler shift in the back-scattered signal frequency.

Scanning lidars are versatile and may operate in several modes. Wind profiling takes advantage of Doppler Beam Swinging (DBS) and Velocity Azimuth Display (VAD) scan patterns (*Lundquist et al.*, 2008; *Drew et al.*, 2013; *Mirocha et al.*, 2015; *Newman et al.*, 2016). Two-dimensional wind fields are obtained as continuous radial scans with varying elevation or azimuth angles. The scanning mode depends on which angle of the lidar beam is fixed.

- *Range Height Indicator (RHI)* – the elevation angle is varied, and the azimuth angle remains constant; the measurements are taken in a vertical plane.
- *Plan-Position Indicator (PPI)* – the elevation angle is constant, and the azimuth angle is varied; the measurements are taken in a horizontal or inclined plane.

The RHI scanning mode is suitable for studying the boundary layer (*Debnath et al.*, 2017; *Späth et al.*, 2022; *Duscha et al.*, 2023) and vertical wake profiles (*Barthelmie et al.*, 2018). The PPI mode allows capturing wakes at different horizontal levels, preferably at the hub height, for further characterization (*Iungo and Porté-Agel*, 2013; *Kumer et al.*, 2015; *Wang and Barthelmie*, 2015; *Bodini et al.*, 2017; *Krishnamurthy et al.*, 2017). However, scanning lidars measure only a radial velocity V_r – a line-of-sight projection of the actual wind vector. The measured velocity corresponds to the original velocity's components as

$$V_r = u \sin\theta \cos\varphi + v \cos\theta \cos\varphi + w \sin\varphi, \tag{2.11}$$

where θ is the azimuth angle, and φ is the elevation angle of the lidar beam.

Often, the radial velocity does not coincide with the actual velocity and may diverge from it greatly. In wind energy research, a lidar is usually mounted at a fixed location and scans a specific sector with the possibility to change elevation or azimuth angles (*Bingöl et al.*, 2010; *Trujillo et al.*, 2011). Therefore, the wakes perpendicular to the line-of-sight will be seen as weak disturbances in the free flow because their radial velocities approach zero. The problem can be overcome by aligning the lidar with the dominant wind direction so that the radial velocity would approach the actual velocity in most scans. Overall, the radial velocity must be processed with a retrieval algorithm to reconstruct the original wind speed and direction. Although various retrieval algorithms were developed as soon as scanning lidars were put into use, the most common

algorithms assume a homogeneous wind field. When applied to non-homogeneous fields, e.g., wakes in a wind farm, such retrieval algorithm may produce erroneous results. Several algorithms varying in complexity and application were developed for the retrieval of non-homogeneous fields (*Gao et al.*, 2006; *Nijhuis et al.*, 2014; *Cherukuru et al.*, 2017; *Fielding and Janisková*, 2020; *Janisková and Fielding*, 2020).

Wake processing

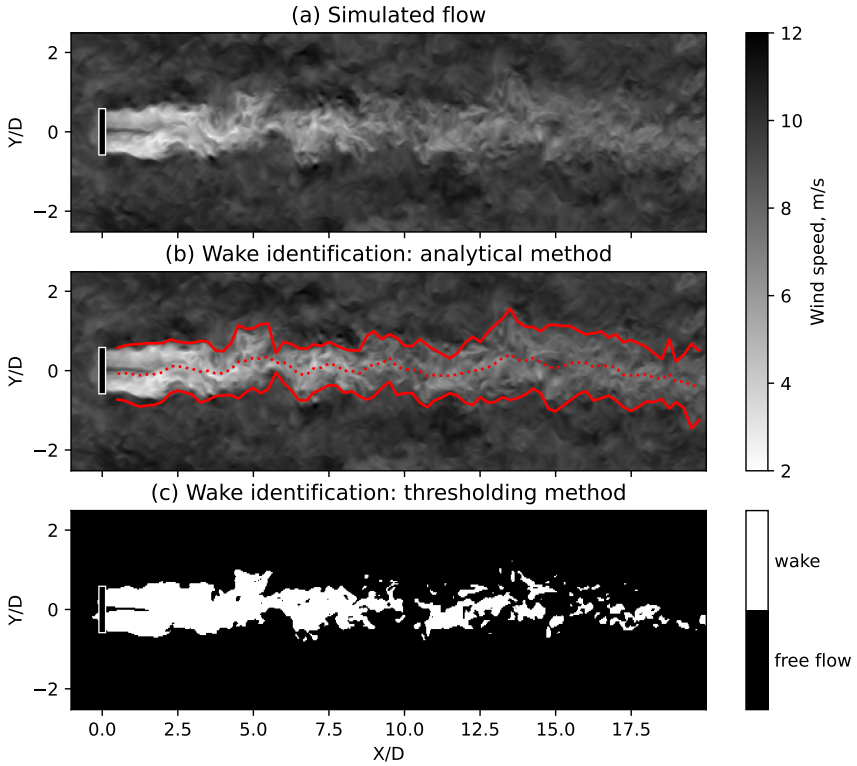

Figure 2.4: (a) A simulated wake from a single turbine and wake identification performed with (b) an analytical and (c) thresholding method.

The information about a wake (Fig. 2.4a) can be obtained by performing wake identification and characterization (*Quon et al.*, 2020). Wake identification is a procedure to determine which points in the two- or three-dimensional flow data belong to a wake. After the wake points are identified, it is possible to characterize the wake: define its boundaries, width, strength, and centerline. The wake characterization has numerous applications and, depending on the goal, does not always have to be carried out thoroughly. For example, the wake centerline poses the most interest in yaw deflection studies. When it comes to the rotor loads, knowing the velocity deficit distribution and turbulence intensity becomes the priority.

Wake identification methods can be generally split into analytical and thresholding methods. Analytical methods set a condition to estimate the wake center and boundaries.

Typically, a Gaussian function is used for fitting the velocity deficit data (Fig. 2.4b) (*Kumer et al.*, 2015; *Krishnamurthy et al.*, 2017), although a more complex expression, e.g., minimum power production within the area, is also viable (*Vollmer et al.*, 2016). The drawback of the analytical methods is that they require knowing the wind speed on a spatial grid. Sufficient data resolution is preferable so that fitting a function can produce meaningful results.

Thresholding methods set a condition to split data into the free-flow and wake points (Fig. 2.4c). The condition may be as simple as assigning a wake point if the normalized velocity deficit exceeds a certain value, e.g., 5% (*España et al.*, 2011; *Bastine et al.*, 2015). Borrowing from more complex techniques used in image processing (*Bakhoday-Paskyabi et al.*, 2016) allows setting a dynamic criterion for thresholding. The algorithm may then adapt to the data resolution and quality. Thresholding methods do not necessarily require exact wind speed values and, therefore, can be also applied to images or photos. However, the thresholded data identifies only the wake shape; additional processing is required to characterize the wake centerline.

2.2 Modeling of the atmospheric flow and wakes

Wake modeling splits into the problems of modeling wind flow and a wind turbine rotor or wind farm. Modern codes utilize a wide range of models and approaches, allowing to select the one that satisfies the requirements for accuracy, speed and computational resources (Fig. 2.5). Simple analytical wake models (Sect. 2.2.2) focus on the velocity deficit and are relatively easy to implement with the possibility of adjustment to the particular study's goals. Analytical models also serve as underlying models in fast codes, e.g., WAsP and PyWake, to estimate annual energy production of a wind farm. Complex numerical models (Sect. 2.2.3) resolve the wind flow in detail and require a built-in rotor model to generate wake and analyze its effect on other wind turbines. Depending on the simulation purposes and code capabilities, the implementation of a wind turbine rotor varies from an actuator model to a fully resolved surface mesh (Sect. 2.2.5).

Newly developed models or methods often utilize data from wind tunnel experiments or measurement campaigns for validation. Although a field measurement dataset may capture various atmospheric conditions at the site, it may not cover different turbines or terrain type. Additionally, the increasing number of offshore wind farms means that nearby farms and measurement instruments may be affected by other farms wakes. While this situation also poses a research interest in its own, it is not suitable for the model validation focused on an unaffected wind farm performance. Several experimental datasets containing controlled and processed data are made available for model validation. As of 2017, *Breton et al.* (2017) lists 36 datasets ranging in terms of access, terrain, scale and number of the turbines observed. Alternatively, a model may be validated with a high-fidelity simulation from a numerical code whose drawbacks and advantages are already documented in detail.

2.2.1 Governing equations of the turbulent flow

Turbulent flows are described by the equation system accounting for the evolution of wind speed components, temperature, moisture, and scalar quantities within space (x, y, z) and time t. The wind speeds typical for wind energy research are low. Therefore, the

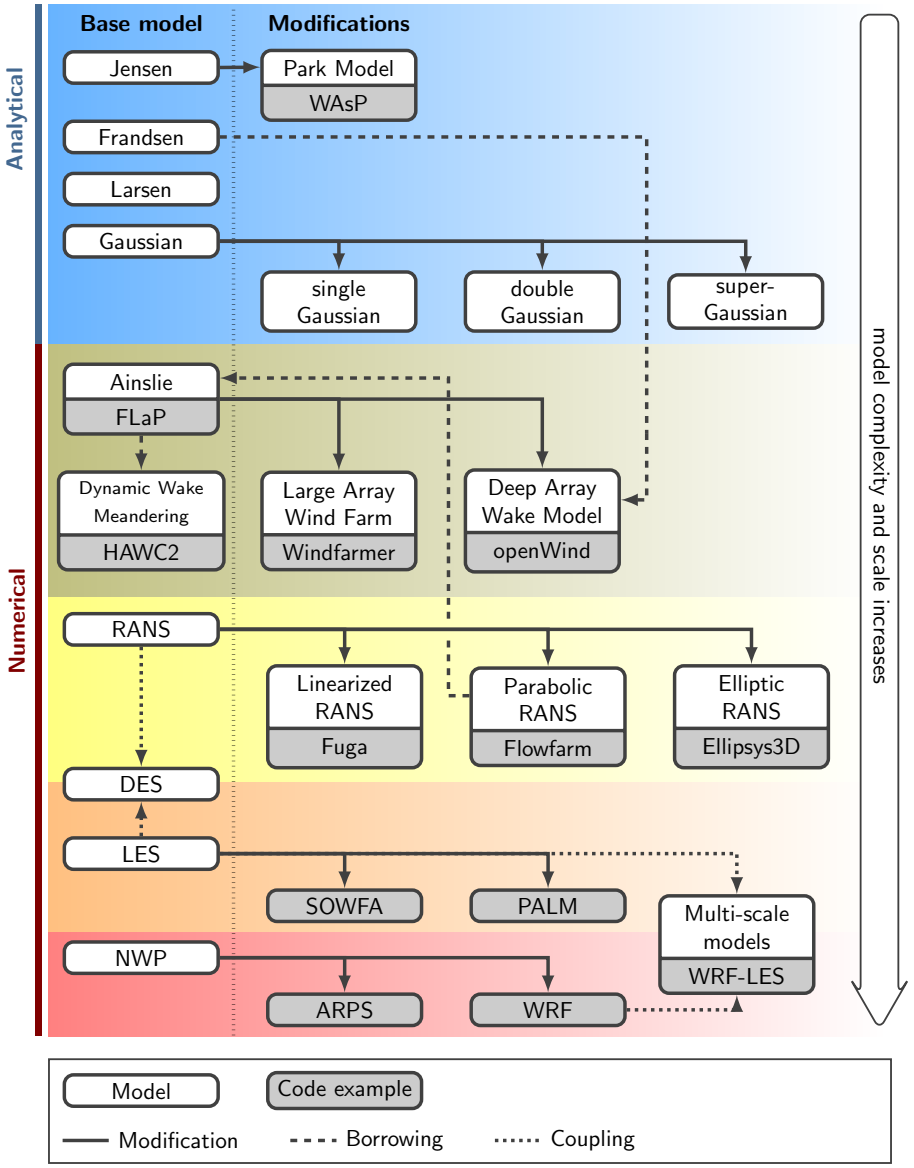

Figure 2.5: Overview of the analytical and numerical models suitable for the wake research and examples of the codes where they are used.

compressibility effects can be disregarded unless a fully-resolved wind rotor and blade's tip speed are specifically considered (*Yan and Archer*, 2018). Hence, the governing equations for turbulent flow can be written in the Boussinesq-approximated form, which considers air density ρ only in the connection with the buoyancy term. The air density is then affected solely by the temperature change with height.

1. Conservation of mass or continuity equation

$$\frac{\partial u_j}{\partial x_j} = 0 \tag{2.12}$$

   Here and in the subsequent equations, indices i, j, and k may take values of 1, 2, or 3 corresponding to one of the three-dimensional axes: $x_1 = x$, $x_2 = y$, $x_3 = z$. u_i are directional wind speed components with $u_1 = u$, $u_2 = v$, and $u_3 = w$.

2. Conservation of momentum equation

$$\frac{\partial u_i}{\partial t} + \frac{\partial u_i u_j}{\partial x_j} = -\frac{1}{\rho}\frac{\partial p^*}{\partial x_i} - \varepsilon_{ijk} f_j u_k + \varepsilon_{ij3} f_3 u_{g,j} - g\frac{\theta_\mathrm{v} - \theta_0}{\theta_0}\delta_{i3} + \nu\frac{\partial^2 u_i}{\partial x_j^2}, \tag{2.13}$$

   where p^* is the perturbation pressure. f is the Coriolis parameter vector accounting for the Earth's rotation $(0,\ 2\omega\cos\varphi,\ 2\omega\sin\varphi)$; the vector's directional components depend on the angular velocity of the Earth $\omega = 0.729 \times 10^{-4}\,\mathrm{rad/s}$ and latitude φ. $u_{g,j}$ are the geostrophic wind components. δ is the Kronecker delta. ν is the kinematic viscosity.

3. Conservation of heat equation

$$\frac{\partial \theta}{\partial t} + u_j\frac{\partial \theta}{\partial x_j} = \nu_\theta\frac{\partial^2 \theta}{\partial x_j^2} + Q, \tag{2.14}$$

   where ν_θ is the thermal diffusivity, and Q is the source term for the heat.

4. Conservation of moisture equation

$$\frac{\partial q_T}{\partial t} + u_j\frac{\partial q_T}{\partial x_j} = \nu_q\frac{\partial^2 q}{\partial x_j^2} + \frac{S_{q_T}}{\rho}, \tag{2.15}$$

   where the total humidity q_T contains vapor q and non-vapor q_L components, so that $q_T = q + q_L$. The diffusivity ν_q is the diffusivity of the water vapor, and S_{q_T} is the source term for processes not already included in the equation.

5. Conservation of a scalar quantity, e.g., concentration C

$$\frac{\partial C}{\partial t} + u_j\frac{\partial C}{\partial x_j} = \nu_C\frac{\partial^2 C}{\partial x_j^2} + S_C, \tag{2.16}$$

   where ν_C is the molecular diffusivity, and S_C is the source term for processes not described by the aforementioned equations, e.g., chemical reactions.

The equation system Eq. (2.12)-(2.16) does not have an analytical solution. Therefore, it is either solved numerically or used as a constraint for analytical models.

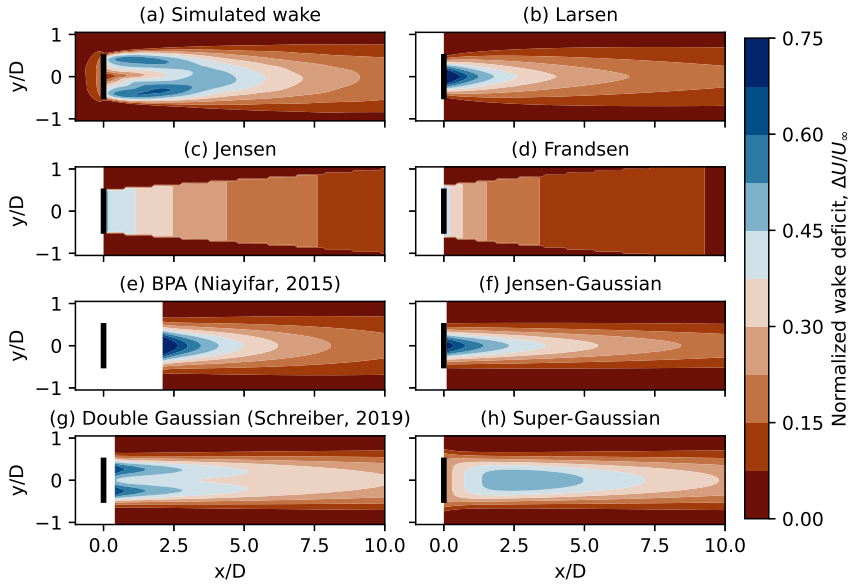

Figure 2.6: Example of a simulated wake and its interpretation by different analytical models for the same free-flow wind speed, thrust coefficient, and turbulence intensity.

2.2.2 Analytical wake models

Analytical wake models, also called engineering models, calculate the velocity deficit with simple mathematical expressions (Fig. 2.6). Since those calculations can be performed fast, the analytical models or their modifications are widely used for estimation of the wind energy production (*Nygaard et al.*, 2022) or layout optimization (*Tao et al.*, 2020). For simplicity, the models assume axisymmetrical self-similar velocity distribution in the wake unaffected by the wind shear. The incoming flow characteristics are accounted for by including dependencies on the thrust coefficient C_T and turbulence intensity I_a. The analytical models are primarily far-wake models and focus on accurately estimating the velocity deficit at a downstream distance of $x \geq 6D$ relevant for wind farm applications. Recently, there have been additions of full-wake models exploring double Gaussian and super-Gaussian distributions to improve the velocity deficit prediction in the near wake.

For uniformity purposes, all models listed in this section are formulated to describe the normalized velocity deficit $\Delta\overline{U}(x,r)$ (Eq. (2.2)), where x is the downstream distance along the rotor axis, and $r = \sqrt{y^2 + (z - z_h)^2}$ is the radial distance from the rotor center located at the hub height z_h. The radial distance collapses to a y-coordinate in the cross-sectional profile or a $(z - z_h)$-coordinate in the vertical profile.

Top-hat models

Top-hat models do not aim to reproduce the velocity distribution in the wake and instead focus on estimating the energy content. The wake velocity and deficit are then considered constant within a circle of the wake diameter in each cross-section.

The Jensen model (Fig. 2.6c) assumes that a fully turbulent wake expands linearly

from the rotor diameter D to the wake diameter $D_w(x)$. The normalized velocity deficit is derived from the conservation principles as

$$\Delta\overline{U} = \left(1 - \sqrt{1 - C_T}\right) \cdot \left(\frac{D}{D_w(x)}\right)^2, \tag{2.17}$$

where D_w is the wake diameter in a cross-section at the downstream distance x:

$$D_w(x) = D + 2kx. \tag{2.18}$$

Although *Jensen* (1983) ties the derivation to the conservation of momentum, it was later shown that the resulting expression is derived from the conservation of mass alone (*Bastankhah and Porté-Agel*, 2014).

The Jensen model does not include the turbulence intensity, only the thrust coefficient. However, the wake expansion coefficient k should be varied depending on the site conditions (*Barthelmie and Jensen*, 2010) or modified to account for the turbulence intensity (*Peña et al.*, 2016). The Park model, a modification of the Jensen model, is the underlying wake model in the WAsP code for wind resource assessment and provides a good estimation of the energy production in a wind farm (*Barthelmie et al.*, 2006; *Göçmen et al.*, 2016).

Another top-hat model, the Frandsen model (Fig. 2.6d), utilizes mass and momentum conservation principles (*Frandsen et al.*, 2006). Unlike the Jensen model, which takes the initial wake diameter $D_w(0) = D$, the Frandsen model assumes an initial wake expansion from D to D_0

$$D_w(0) = D_0 = \sqrt{\beta}D, \tag{2.19}$$

where the coefficient β is

$$\beta = \frac{1 + \sqrt{1 - C_T}}{2\sqrt{1 - C_T}}. \tag{2.20}$$

The wake diameter D_w at the downstream distance x is then calculated as

$$D_w(x) = D\left(\beta^{k/2} + \alpha x/D\right)^{1/k}. \tag{2.21}$$

The induction factor α is either determined experimentally or obtained from the Jensen model. Considering the wake diameters, the area of the initial wake is A_0 and the area of the wake at the downstream distance x is A_w. Then the velocity deficit depends on the wake area change as

$$\Delta\overline{U} = \frac{1}{2} - \frac{1}{2}\sqrt{1 - 2\frac{A_0}{A_w}C_T}. \tag{2.22}$$

Since the Frandsen model takes the initial wake size larger than the rotor, it predicts a wider wake compared to the Jensen model. However, being re-fitted to the data, both models agree better on the wake expansion (*Andersen et al.*, 2014). Currently, the slightly modified Frandsen model is used by the IEC standard 61400-1 edition 3 to assess turbulence intensity levels (*Nielsen et al.*, 2009; *International Electrotechnical Commission*, 2005).

Single Gaussian models

Although it was noticed early, that the velocity deficit in a far wake resembles a Gaussian distribution (*Högström et al.*, 1988), it was not much incorporated into wake models. *Ainslie* (1988) implemented a Gaussian distribution into a numerical model. The primary analytical model with a non-uniform distribution, the Larsen model (*Larsen*, 1988, 2009), however, used a polynomial expression for the velocity deficit. Numerous analytical Gaussian wake models emerged only recently when more experimental and numerical data could be obtained for validation and improved prediction of wind farm performance.

A Gaussian wake model can be shortened to a general form of

$$\Delta\overline{U}(x,r) = F(x, C_T, I_a) \cdot G(r, \sigma(x)), \tag{2.23}$$

where

- $F(x, C_T, I_a)$ is the amplitude function defining the stream-wise changes of the maximum velocity deficit.
- $G(r, \sigma(x))$ is the Gaussian function. A single Gaussian distribution is defined as

$$G(r, \sigma(x)) = \exp\left(-\frac{r^2}{2\sigma(x)^2}\right). \tag{2.24}$$

- $\sigma(x)$ is the standard deviation from which the wake half-width is derived as $r_{1/2}(x) = \sigma(x)\sqrt{2\ln 2}$ (*Bastankhah and Porté-Agel*, 2014). The wake half-width assumes the velocity deficit is half of the maximum velocity deficit of the respective cross-section.

Bastankhah and Porté-Agel (2014) proposed a basic Gaussian wake model (Fig. 2.6e). Its underlying equations were derived from mass and momentum conservation principles assuming Gaussian distribution of the velocity deficit. For brevity, this model is further referred to as the BPA model.

$$\Delta\overline{U} = \left(1 - \sqrt{1 - \frac{C_T}{8\sigma^2}}\right) \cdot \exp\left(-\frac{r^2}{2\sigma^2}\right) \tag{2.25}$$

The BPA model retains the linear expansion of a wake similar to the Jensen model but applies it to the standard deviation σ instead of the wake diameter. The standard deviation depends on the downstream distance x as

$$\sigma(x) = k^* \frac{x}{D_0} + \varepsilon. \tag{2.26}$$

Unlike the wake expansion coefficient $k = \delta r_w/\delta x$ used in the Jensen model (Eq. (2.18)), the coefficient $k^* = \delta\sigma/\delta x$ defines the wake growth rate through the standard deviation $\sigma(x)$ of the velocity deficit. In the subsequent modifications, k^* was split into two coefficients to provide a dependency on the turbulence intensity (*Niayifar and Porté-Agel*, 2016; *Abkar et al.*, 2018)

$$\begin{aligned} k^* &= k_1 + k_2 I_a, \\ k_1 &= 0.003678,\ k_2 = 0.3837. \end{aligned} \tag{2.27}$$

The parameter ε is derived by equating the total mass flow deficit $\int_0^\infty \Delta\overline{U} dA$ calculated at $x = 0$ with the BPA and Frandsen models. As a result, $\varepsilon = 0.25\sqrt{\beta}$ with β defined as in the Frandsen model (Eq. (2.20)). Performing the comparison with numerical simulations, *Bastankhah and Porté-Agel* (2014) suggested using $\varepsilon = 0.2\sqrt{\beta}$ for a better agreement.

Gao et al. (2016) replaced the top-hat distribution in the Jensen model with the Gaussian distribution (Fig. 2.6f). The new Jensen-Gaussian model sets the standard deviation σ so that 99% of the Gaussian distribution lies within the wake radius $r_w = D_w/2$ as calculated with the Jensen model in Eq. (2.18), i.e., $\sigma = r_w/2.58$. Optimizing the model to have the same mass flow as in the Jensen model, leads to the following velocity deficit:

$$\Delta\overline{U} = \left[1 - \frac{5.16}{\sqrt{2\pi}} \cdot \overline{U}^*(x, k_w)\right] \cdot \exp\left(-\frac{r^2}{2\sigma^2}\right), \tag{2.28}$$

where $\overline{U}^*(x, k_w)$ is the normalized wake deficit corrected from the Jensen model Eq. (2.17).

Ishihara and Qian (2018) were the first to propose a single Gaussian model describing the velocity deficit in the near and far wake – the full-wake model. The model expands ideas of the old Ishihara model proposed in 2004 (*Ishihara et al.*, 2004) and takes the BPA original model (Eq. (2.25)) as the starting point. The Ishihara model describes a two-dimensional wake with the maximum velocity deficit located at a certain distance downstream of the rotor, unlike the BPA model, where the maximum deficit occurs directly behind the rotor.

$$\Delta\overline{U} = \left(a + b \cdot x/D + \frac{c}{(1 + x/D)^2}\right)^{-2} \cdot \exp\left(-\frac{r^2}{2\sigma^2}\right) \tag{2.29}$$

The model parameters a, b, and c are calculated as functions of C_T, I_a, and a set of coefficients obtained from the data fitting to a numerical simulation by *Ishihara and Qian* (2018).

$$a = 0.93C_T^{-0.75}I_a^{0.2},\ b = 0.42C_T^{0.6}I_a^{0.2},\ c = 0.15C_T^{-0.25}I_a^{0.7} \tag{2.30}$$

Double Gaussian models

The distribution of the near-wake velocity deficit in the near wake usually has two distinctive peaks, which are lost in single Gaussian models. Double Gaussian models (*Keane et al.*, 2016; *Schreiber et al.*, 2019) are an attempt on developing a full-wake model that accurately captures the velocity deficit distribution in the near and far wake at once.

A double Gaussian function $G_2(r, \sigma(x))$ describes an axisymmetric velocity distribution with two peaks

$$G_2(r, \sigma(x)) = \frac{1}{2}\left(e^{W_+} + e^{W_-}\right),\ W_\pm = -\frac{(r \pm r_0)^2}{2\sigma^2(x)}, \tag{2.31}$$

where r_0 is the radial position of the Gaussian minimum. The function reduces to a single Gaussian function $G(r, \sigma(x))$ in the axisymmetrical model Eq. (2.24) when $r_0 = 0$. The model proposed by *Keane et al.* (2016) followed the steps of *Bastankhah and Porté-Agel* (2014) to solve the momentum flux equation for a double Gaussian distribution

and provided further improvement in *Keane* (2021). *Schreiber et al.* (2019) proposed a correction to the original *Keane et al.* (2016) model to achieve better agreement in the near-wake area (Fig. 2.6g).

Super-Gaussian model

A different approach alters the Gaussian distribution by varying the power coefficient $n = 2$ in $G(r, \sigma, n) = \exp(-r^n/2\sigma^2)$. The super-Gaussian model (*Blondel and Cathelain*, 2020) calculates this coefficient dynamically, depending on the downstream distance (Fig. 2.6h). Being in active development, the model proposes several ways and corrections for n, all complying with the mass and momentum conservation principles. The model shows a promising agreement with numerical simulations by approaching a top-hat distribution in the near wake ($n = 4 - 4.5$) and a single Gaussian distribution in the far wake ($n \to 2.5$).

2.2.3 Numerical models

Direct numerical simulation (DNS) is the only way to appropriately resolve all turbulence scales in the wind flow. However, DNS requirements for computational resources increase gradually with the amount of grid points used, rendering the approach impractical. Hence, various simplifications and assumptions are applied to the equation system Eq. (2.12)–(2.16) to reduce the requirements for computational resources while retaining accuracy. A numerical simulation gradually speeds up if not every turbulence scale is resolved directly. Reynolds-Averaged Navier-Stokes (RANS) equations attempt to solve numerically all kinds of turbulent scales and run in a quasi-steady state ($\partial \overline{u}_i/\partial t = 0$). Although RANS models fall back in resolving large-scale turbulence, they perform well for the boundary layer of a solid body, e.g., blades (*Sørensen et al.*, 2002). A different approach is required for turbulent flow studies.

Large-eddy simulation models

Large-eddy simulation (LES) models resolve turbulence scales larger than the grid spacing and approximate the rest. LES allows using fewer grid points than DNS and, therefore, requires less computational resources. The requirements gradually decrease further if the surface layer of a solid body is not resolved (*Yang and Griffin*, 2020). When compared to RANS models, LES resolves turbulence anisotropy and large-scale mixing better, but requires more computational time. Despite the advancement in computational power, LES is still primarily used in research rather than industrial applications.

In LES, each prognostic variable, e.g., u, is split into resolved (filtered) $\tilde{u}$ and unresolved (subgrid) u'' scales so that $u = \tilde{u} + u''$. Then, a filtering function is introduced to separate resolved and unresolved quantities.

$$\tilde{u}(\boldsymbol{x}, t) = \int u(\boldsymbol{\xi}, t) G(\boldsymbol{x} - \boldsymbol{\xi}, \Delta) d\boldsymbol{\xi}, \tag{2.32}$$

where $G(\boldsymbol{x} - \boldsymbol{\xi}, \Delta)$ is the filter kernel that should satisfy $\int G(\boldsymbol{x}) d\boldsymbol{x} = 1$ for $u_i = \text{const}$. Δ is the filter width, which may be defined in several ways to consider varying grid spacing:

$$\Delta = \begin{cases} (\Delta_x \Delta_y \Delta_z)^{1/3} \text{ – representative grid spacing} \\ \Delta_{\max} = \max(\Delta_x, \Delta_y, \Delta_z) \text{ – maximum grid spacing} \end{cases} \tag{2.33}$$

Various filter kernels were developed. The box filter is an implicit filter defined through a top-hat function; this filter is usually the one applied in finite-difference or finite-volume codes:

$$G(\boldsymbol{x}-\boldsymbol{\xi},\Delta)=\begin{cases}\frac{1}{\Delta}, & \text{if } |\boldsymbol{x}-\boldsymbol{\xi}|\leq\frac{\Delta}{2},\\ 0, & \text{if } |\boldsymbol{x}-\boldsymbol{\xi}|>\frac{\Delta}{2},\end{cases} \tag{2.34}$$

Applying the filtering function to the conservation of momentum equation Eq. (2.13) modifies it into

$$\frac{\partial\tilde{u}_i}{\partial t}+\tilde{u_j}\frac{\partial\tilde{u}_i}{\partial x_j}=-\frac{1}{\rho}\frac{\partial\tilde{p}}{\partial x_i}+\nu\frac{\partial^2\tilde{u}_i}{\partial x_j^2}-\frac{\partial\tau_{ij}}{\partial x_j}, \tag{2.35}$$

where τ_{ij} is the subgrid-scale stress (SGS) defined via the SGS eddy diffusivity K_m as

$$\tau_{ij}=(\widetilde{u_iu_j}-\tilde{u}_i\tilde{u}_j)=-K_m\left(\frac{\partial\tilde{u}_i}{\partial x_j}+\frac{\partial\tilde{u}_j}{\partial x_i}\right)\tilde{S}_{ij}. \tag{2.36}$$

The rate of strain tensor $\tilde{S}_{ij}$ is introduced for brevity and is defined as

$$\tilde{S}_{ij}=\frac{1}{2}\left(\frac{\partial\tilde{u}_i}{\partial x_j}+\frac{\partial\tilde{u}_j}{\partial x_i}\right). \tag{2.37}$$

Filtering turbulent flow equations leads to the new unknown terms that prevent solving the system analytically. To close the equation system, turbulence closures are implemented. Various LES codes provide a selection of closure models to use. Most closures originate from Smagorinsky closure, which was originally suggested with the LES concept (*Smagorinsky*, 1963). *Lilly* (1962) suggested to define K_m through a constant C_S and the rate of strain tensor S_{ij} as:

$$K_m(\boldsymbol{x},t)=(C_S\Delta)^2\sqrt{2\tilde{S}_{ij}\,\tilde{S}_{ij}}, \tag{2.38}$$

Although C_S was supposed to be a universal constant, its value may be varied depending on the simulation conditions and estimation methods. Thus, *Lilly* (1966) demonstrates how different approaches yield values in a range of $C_S\sim0.17-0.23$. *Canuto and Cheng* (1997) argues that the coefficient should be lowered to $C_S\sim0.11$ in the new SGS model and leans to a conclusion that C_S should be calculated dynamically to improve accuracy. *Martínez-Tossas et al.* (2015) confirm that LES using $C_S=0.16$, which is recommended for homogeneous isotropic turbulence, captures the wake transition worse than LES with a smaller value of $C_S=0.08$.

Numerical Weather Prediction (NWP) – mesoscale models

Mesoscale models simulate large-scale atmospheric processes in the domains spanning hundreds or thousands of kilometers. Their drawback is a specific pressure-based coordinate system that limits terrain modeling (*Lundquist et al.*, 2008). This limitation is less crucial for the offshore simulations. Moreover, the wind energy research gains from the mesoscale models' capability to use reanalysis data as an input. Reanalysis datasets are obtained by assimilating available meteorological observations to reconstruct atmospheric processes over large periods and areas. E.g., the publicly available part of the ERA5 dataset (*Hersbach et al.*, 2020) covers the whole Earth and contains hourly atmospheric and wave data from 1979 onwards with a constant spatial resolution of 31 km.

Passing temperature, wind speed and direction data to a mesoscale model allows obtaining complex wind fields to study atmospheric processes at large distances above and around the wind farm. The ability of NWP models to simulate large domains allows capturing wind farm wakes thus making the mesoscale models helpful in studying wake interactions between wind farms (*Jiménez et al.*, 2015). The common choice of mesoscale model in offshore wind farm research is the Weather Research and Forecasting model (WRF) (*Michalakes et al.*, 2005). WRF uses the 3D Smagorinsky or 1.5-order TKE closure. A typical spatial resolution for mesoscale models is of an order of 1 km or more, which is not suitable for modeling individual wakes. Hence, a wind farm is approximated as a whole structure. WRF may approximate a wind farm as a momentum sink (*Fitch et al.*, 2012), apply explicit wake parameterization (*Volker et al.*, 2015) or, as a recent development, estimate wake effects with the Jensen model (*Ma et al.*, 2022). If a rotor model is to be used, then WRF is coupled with an internal LES code and a generalized actuator disk model (*Mirocha et al.*, 2015).

Model coupling

Another way to reduce computational time and improve accuracy is by coupling models of different complexity. Coupling LES with RANS to perform a Detached eddy simulation (DES) combines the advantages of both models. A RANS model resolves the near-surface boundary layer of a solid body, e.g., a rotor blade. LES is then run for the rest of the computational domain to resolve the separated turbulent flow (*Spalart*, 2009).

Coupling LES with WRF (WRF-LES) within the WRF framework or an external LES model allows the simulation of complex large-scale atmospheric conditions with WRF. The resulting dynamic field is then passed to LES to refine the solution in the area of interest. Consequently, LES resolves the complex flow in a wind farm more precisely than the WRF approximations would allow.

2.2.4 LES code: PALM Model System

The PALM Model System is the Fortran LES code developed at the University of Hanover (*Maronga et al.*, 2015, 2020). Besides the base code, PALM utilizes a modular structure that allows switching on and off specific processes or adding new equations via user code. PALM solves an equation system for up to six prognostic quantities: directional wind speed components u_i, potential temperature θ, water vapor mixing ratio q_v, and passive scalar s. Since q_v and s quantities were not relevant for the wake LESs performed in this thesis, the humidity and passive scalar modules were switched off, their respective equations were not solved during simulations. Since the air density changes little at near-surface levels, the prognostic equations solved in PALM assumed that the density of dry air ρ remained constant regardless of the height.

After the simplifications and filtering, the system of Boussinesq-approximated equations Eq. (2.12)–(2.16) reduces to the following three equations for mass, momentum,

and heat conservation:

$$\begin{aligned}
\frac{\partial \tilde{u}_j}{\partial \tilde{x}_j} =& 0, \\
\frac{\partial \tilde{u}_i}{\partial t} =& -\frac{\partial \tilde{u}_i \tilde{u}_j}{\partial x_j} - \frac{1}{\rho}\frac{\partial \tilde{\pi}^*}{\partial x_i} - \varepsilon_{ijk} f_j \tilde{u}_k + \varepsilon_{i3j} f_3 \tilde{u}_{g,j} + g\frac{\tilde{\theta}_\mathrm{v} - \theta_{\mathrm{v,ref}}}{\theta_{\mathrm{v,ref}}}\delta_{i3} - \\
& - \frac{\partial}{\partial x_j}\left(\widetilde{u_i'' u_j''} - \frac{2}{3} e \delta_{ij}\right), \\
\frac{\partial \tilde{\theta}}{\partial t} =& -\frac{\partial \tilde{u}_j \tilde{\theta}}{\partial x_j} - \frac{\partial}{\partial x_j}\left(\widetilde{u_j'' \theta''}\right),
\end{aligned} \tag{2.39}$$

The filtered momentum equation Eq. (2.35) is rearranged in PALM to introduce the modified perturbation pressure $\tilde{\pi}^*$:

$$\tilde{\pi}^* = \tilde{p}^* + \frac{2}{3}\rho e = \tilde{p}^* + \frac{1}{3}\rho \cdot \widetilde{u_i'' u_i''} \tag{2.40}$$

and include SGS turbulence kinetic energy (SGS-TKE) e:

$$e = \frac{1}{2}\widetilde{u_i'' u_i''}. \tag{2.41}$$

The Coriolis parameter f is defined by the input parameters: angular velocity ω and latitude φ. The default value of the latter is set to $\varphi = 55°$ – slightly to the north of the FINO1 platform in the North Sea. The angular velocity can be set to any value if needed and assumes Earth rotation of $\omega = 0.729 \times 10^{-4}\,\mathrm{rad/s}$ by default. If the Coriolis effect is switched off ($\omega = 0$), the horizontal forcing may be added by setting the pressure gradient components $\partial p/\partial x$ and $\partial p/\partial y$ to compensate for the friction losses because of the surface roughness. $\theta_{\mathrm{v,ref}}$ is the temperature of the reference state that can be either an initial state $\theta_0(\boldsymbol{x}, 0)$, horizontal average $\overline{\theta}_\mathrm{v}$, or a fixed value.

When solved for a true neutral case, the temperature gradient is explicitly set to zero, $\partial\theta/\partial z = 0$, and no heat flux is present. The system Eq. (2.39) reduces to two equations:

$$\begin{aligned}
\frac{\partial \tilde{u}_j}{\partial \tilde{x}_j} &= 0, \\
\frac{\partial \tilde{u}_i}{\partial t} &= -\frac{\partial \tilde{u}_i \tilde{u}_j}{\partial x_j} - \frac{1}{\rho}\frac{\partial \tilde{\pi}^*}{\partial x_i} - \varepsilon_{ijk} f_j \tilde{u}_k + \varepsilon_{i3j} f_3 \tilde{u}_{g,j} - \frac{\partial}{\partial x_j}\left(\widetilde{u_i'' u_j''} - \frac{2}{3} e \delta_{ij}\right).
\end{aligned} \tag{2.42}$$

Since the heat conservation equation for $\partial\tilde{\theta}/\partial t$ is not solved in the true neutral mode, less computational time is spent compared to the same simulation with the temperature gradient present.

PALM utilizes a 1.5-order TKE closure developed by *Deardorff* (1980) and modified later by *Moeng and Wyngaard* (1988) and *Saiki et al.* (2000). This closure assumes that SGS eddies transport energy proportional to the local gradients of the mean quantities.

$$\widetilde{u_i'' u_j''} = \frac{2}{3} e \delta_{ij} - K_m \left(\frac{\partial u_i}{\partial x_j} + \frac{\partial u_j}{\partial x_i}\right) \tag{2.43}$$

$$\widetilde{u_i'' \theta''} = -K_h \frac{\partial \theta}{\partial x_i} \tag{2.44}$$

The respective closures for humidity and scalar quantity are omitted since they are not relevant for this thesis. K_h is the SGS diffusivity of heat which depends on the SGS diffusivity of momentum K_m as

$$K_h = \left(1 + \frac{2l}{\Delta} K_m\right). \tag{2.45}$$

K_m is defined similarly to the Smagorinsky SGS closure in Eq. (2.38):

$$K_m = C_S \cdot l\sqrt{e}, \tag{2.46}$$

where $C_S = 0.1$ and l in both equations is the SGS mixing length, which is defined depending on the temperature gradient and grid spacing

$$l = \begin{cases} \min\left(\Delta, 0.76\sqrt{e}\left(\frac{g}{\theta_{\mathrm{v},0}}\frac{\partial\theta_\mathrm{v}}{\partial z}\right)^{-1/2}\right) & \text{for } \frac{\partial\theta_\mathrm{v}}{\partial z} > 0, \\ \Delta & \text{for } \frac{\partial\theta_\mathrm{v}}{\partial z} \leq 0. \end{cases} \tag{2.47}$$

Here, $\theta_{\mathrm{v},0}$ is either a reference value $\theta_{\mathrm{v,ref}}$ or the local value of $\tilde{\theta}$.

The Deardorff closure scheme is completed with the prognostic equation for TKE

$$\frac{\partial e}{\partial t} = -u_j\frac{\partial e}{\partial x_j} - \left(\widetilde{u_i''u_j''}\right)\frac{\partial u_i}{\partial x_j} + \frac{g}{\theta_{\mathrm{v},0}}\widetilde{u_3''\theta_\mathrm{v}''} - \frac{\partial}{\partial x_j}\left[\widetilde{u_j''\left(e + \frac{p''}{\rho}\right)}\right] - \varepsilon, \tag{2.48}$$

where ε is the SGS dissipation rate calculated as

$$\varepsilon = \left(0.19 + 0.74\frac{l}{\Delta}\right)\frac{e^{3/2}}{l}. \tag{2.49}$$

PALM provides several options for the boundary conditions depending on the variable and boundary (Table 2.2). The choice of the top-bottom boundary condition may be restricted by other parameters of the simulation. For example, a CBL is defined in PALM with a constant heat flux. Hence, the bottom boundary should use the Neumann condition for CBL simulations. Otherwise, the prescribed heat flux may not remain constant as the contributions from the resolved scales will be accounted for in the solution. Applying the heat flux is not recommended for defining an SBL in LES, as the model may simulate near-neutral conditions instead of stable (*Basu et al.*, 2008). Therefore, an SBL simulation should use surface cooling. In this case, the bottom boundary condition for the potential temperature θ should be set to the Dirichlet condition to consider the surface temperature change $\Delta\theta$ due to the cooling. For the top boundary, the potential temperature has a special option of constraining via the constant initial temperature gradient: the equations are solved numerically up to $\theta_{k=N}$ so that the top point value is $\theta_{k=N+1} = \theta_{k=N} + d\theta/dz \cdot \Delta z_{k=N}$. The top boundary condition for temperature does not have stability-specific restrictions.

The simultaneous use of Neumann conditions for pressure at top-bottom boundaries is allowed. However, it becomes mutually exclusive in the case of non-cyclic lateral boundary conditions due to the mandatory use of certain solvers. For non-cyclic boundaries, the Neumann condition is preferable at the bottom boundary; consequently, the top boundary has to use the Dirichlet condition.

Table 2.2: Boundary conditions for different quantities in PALM with k being the index of a cell starting from the surface and N – the total number of cells in the vertical direction

Quantity	Dirichlet	Neumann	Default
Bottom boundary			
Velocity, u, v	$u_{k=0} = 0$	$(du/dz)_{k=0} = 0$	Dirichlet
	$v_{k=0} = 0$	$(dv/dz)_{k=0} = 0$	Dirichlet
Pressure, p	$p_{k=0} = 0$	$(dp/dz)_{k=0} = 0$	Neumann
Temperature, θ	$\theta_{k=0} = \theta_s + \Delta\theta(t)$	$(d\theta/dz)_{k=0} = 0$	Dirichlet
Top boundary			
Velocity, u, v	$u_{k=N+1} = u_{g,k=n+1}$	$(du/dz)_{k=N} = 0$	Dirichlet
	$v_{k=N+1} = v_{g,k=n+1}$	$(dv/dz)_{k=N} = 0$	Dirichlet
Pressure, p	$p_{k=N+1} = 0$	$(dp/dz)_{k=N} = 0$	Dirichlet
Temperature, θ	$\theta_{k=N+1} = const$	$(d\theta/dz)_{k=N} = 0$	Initial gradient

The flow type dictates the choice of velocity boundary conditions. An atmospheric boundary layer would have the Dirichlet no-slip condition $u = v = 0$ at the bottom boundary and constrain the flow to the geostrophic wind at the top boundary $u = u_g$, $v = v_g$. Closed-channel flow requires a no-slip condition for both top and bottom boundaries.

Lateral boundary conditions are prescribed based on the type of a flow and simulation goals. A cyclic boundary is a common choice for a homogeneous flow simulation. Non-homogeneous flows should run with a non-cyclic boundary. Otherwise, the affected flow, e.g., the flow disturbed by wakes, would constantly return to the domain as an inflow and alter the prescribed free flow. Non-cyclic conditions are defined by assigning a radiation condition to the inflow plane

$$u_{tr} = -\left(\frac{\partial u_i}{\partial t}\right)\left(\frac{\partial u_i}{\partial n}\right)^{-1} \leq \frac{\Delta_x}{\Delta t}, \tag{2.50}$$

where u_{tr} is the transport velocity, and n denotes the normal to the flow, e.g., $n = x_1 = x$ for the inflow coming from the left boundary. The opposing boundary is then assigned with the Dirichlet condition, making it the outflow boundary; the other two lateral boundaries use cyclic conditions.

While a turbulent flow in a cyclic domain develops quickly in terms of computational time, the flow in a non-cyclic domain may stay laminar and produce a weakly turbulent wake that does not represent the behavior of real wakes (*Witha et al.*, 2014). The laminar inflow may develop turbulence in a non-cyclic domain, provided that the domain is long enough in the flow direction. However, the required length would make wind turbine and farm simulations unfeasible. Hence, a turbulent inflow is usually generated for non-cyclic domains with the precursor-main run approach. A simulation in a precursor cyclic domain is run until a fully turbulent flow develops and reaches a steady state. The resulting flow is passed as an inflow to the main simulation with a larger domain and

non-cyclic boundaries (*Witha et al.*, 2014). Alternatively, a turbulent inflow may be provided using a synthetic turbulence generator (*Gronemeier et al.*, 2015) or a dynamic driver obtained from mesoscale models (*Lin et al.*, 2021). The dynamic driver input allows the simulation of complex atmospheric conditions, including transient events, via WRF-LES coupling (*Vollmer et al.*, 2017; *Wagner et al.*, 2019).

As shown in Eq. (2.32)−(2.34), the turbulent scales resolved by LES strongly depend on the grid spacing. The global refinement of the simulation domain often results in a gradually increased simulation time. Hence, a local refinement is performed via the nesting interface. In this case, the inner domains' lateral boundaries are considered nested. The flow quantities passing through the nested boundaries are interpolated to the new grid, and prognostic equations are solved for the refined nested domain. PALM implements one- and two-way nesting modes. For the one-way nesting mode, the solution for the current time step ends here and moves to the next one. In the case of two-way nesting, the solution from the nested domain is interpolated back to the coarse domain, thus allowing to correct its solution. However, the interpolation procedures also introduce a new source of uncertainties which may alter the final solution. A study of CBL simulation under low wind speed reported a secondary circulation developing in the case of a two-way nested domain (*Hellsten et al.*, 2021). Overall, the two-way nesting mode should be used cautiously despite the advantages it provides over the one-way nesting.

2.2.5 Wind turbine models

Modeling a wind turbine rotor as a moving solid body gradually increases computational time, especially in wind farm simulations. Unless the wind turbine is the focus of a detailed simulation, the rotor can be approximated with one of the available models. Usually, neither a wind tower nor a nacelle are modeled, and their effect is included via an approximation. Attempts to model the nacelle and improve LES predictions were nevertheless performed showing the improvement of TKE and near wake predictions (*Martinez et al.*, 2016; *Yang and Sotiropoulos*, 2018).

Blade Element Momentum method (BEM)

The Blade Element Momentum (BEM) method is a long-established approach in rotor design (*Burton et al.*, 2011). Originally suggested by *Glauert* (1935), it undergone extensive development to improve accuracy for applications in rotorcraft and wind turbine design. BEM allows a simple estimation of the rotor loads by splitting each blade into smaller elements that are assumed to be independent. The approach also assumes that the pressure loss behind the rotor is caused by the wind flow acting upon the blade elements. From these assumptions, the induced velocities and resulting forces acting upon each element are calculated. The total force acting on the rotor is the sum of the forces acting upon each element.

Implementing this approach requires knowledge of the blade geometry and, particularly, airfoils used along the blade. The BEM method assumes a static axisymmetric flow and thus does not account for dynamic effects observed in experiments, such as the response lag of the airfoil (*Snel and Schepers*, 1995). Various corrections are introduced to compensate for the limitations. The set of corrections may vary from code to code

where BEM is implemented. For example, the AeroDyn library (*Moriarty and Hansen*, 2005) used in the NREL FAST code for aero-elastic analysis applies the Glauert correction for induction factors higher than 0.4 to avoid instability (*Shen et al.*, 2005a) and the skewed wake correction to account for the effect from non-axisymmetrical wake (*Pitt and Peters*, 1981).

Actuator models

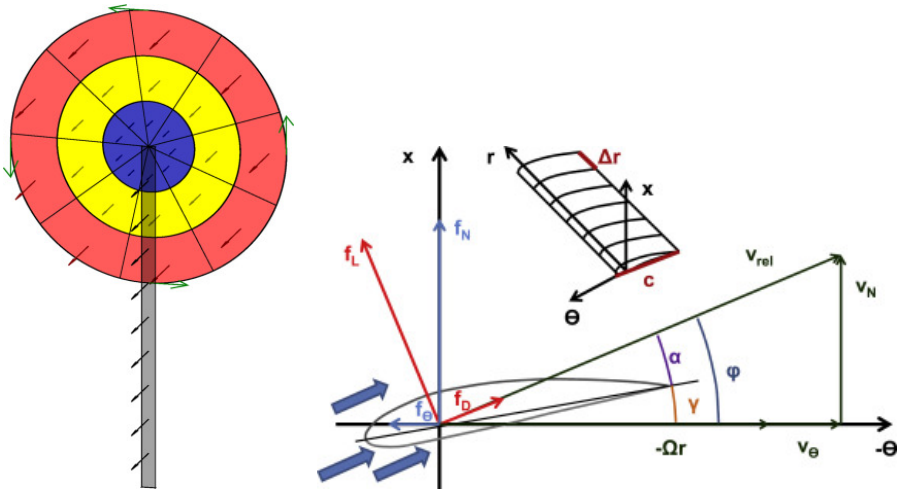

Figure 2.7: Actuator disk sectioning for ADM-R and forces acting upon an airfoil. Reproduced from Dörenkämper et al. (2015) by CC BY-NC-ND 4.0.

The actuator disk model (ADM) also takes originates from long-established principles of the momentum theory. Theorized by *Rankine* (1865) as a link between thrust and momentum, the theory was later expanded by *Froude* (1889) to consider the flow difference in front and behind the rotor disk. In the modern approach, the forces acting upon a rotor are averaged over the rotor disk and explicitly added to the momentum equation. Considering the simplifications, ADM is accurate enough and is cost-effective to use in turbulent-flow simulations instead of a fully-resolved rotor (*Réthoré et al.*, 2014; *Troldborg et al.*, 2015). However, the uniform distribution of forces across the disk does not generate tip vortices and requires a tip-loss correction to improve accuracy (*Shen et al.*, 2005b).

The actuator line model (ALM) imagines forces acting upon the lines that replace rotor's blades (*Shen et al.*, 2005b). Consequently, the tip vortices and near-wake region are resolved in more detail than with ADM (*Troldborg et al.*, 2015). Notably, the choice of an actuator model does not strongly affect the time cost of one step: ADM performs calculations for more actuator points than ALM, but ALM needs to rotate actuator lines at each step (*Martinez-Tossas et al.*, 2012). However, the total computational time heavily depends on the time step length. For ALM, the time step length is restricted by the tip-speed ratio and should be chosen so that the blade tip passes through no less than a single finite volume cell at each step. Therefore, ALM requires smaller time steps than ADM or more time steps in total for the same period simulated. Nevertheless,

ALM can potentially hold a good agreement to the experimental data even when run on the coarse grid (*Martinez et al.*, 2016).

Further expansion of the actuator line approach is replacing the blade with an actuator surface model (ASM) defined by chord lines at several radial locations (*Shen et al.*, 2007). ASM allows for improved prediction of flow behavior near blade tips and resolves tip vortices shed along the blade but requires additional airfoil data, such as pressure and friction distribution over the surface.

Due to associated computational costs and complexity, ASM has yet to be widely implemented in numerical simulation codes. Hence, most codes use either ADM or ALM and their modifications. A compromise between ADM and ALM is the actuator disk model with rotation (ADM-R) (Fig. 2.7). ADM-R considers a non-uniform force distribution and disk rotation, effectively mitigating the drawbacks of both ADM and ALM: unresolved tip vortices and longer computational time, respectively (*Porté-Agel et al.*, 2011; *Dörenkämper et al.*, 2015). Instead of distributing the forces uniformly, ADM-R splits the rotor disk into annular areas and calculates forces per unit rotor area for each. The lift and drag forces are then calculated using BEM theory (Sect. 2.2.5), with each blade element assuming a two-dimensional airfoil of the corresponding blade section.

A comparison between ADM, ADM-R, and ALM shows that regular ADM leads to an underprediction of the velocity deficit. Accounting for the rotation effects in ADM-R or using ALM returns better agreement with wind tunnel experiments and wind farm measurements (*Porté-Agel et al.*, 2011; *Wu and Porté-Agel*, 2011).

Reference wind turbines

Several reference wind turbines exist for numerical simulations as well as validation and verification of new rotor models (Table 2.3).

Table 2.3: Parameters of the reference wind turbines

Name	Size, m		Wind speed, m/s			Source
	Rotor diameter	Hub height	Cut-in	Rated	Cut-out	
DTU 10MW	178.3	119	4	11.4	25	*Bak et al.* (2013)
LEANWIND 8MW	164	110	4	12.5	25	*Desmond et al.* (2016)
NREL 5MW	126	90	3	11.4	25	*Jonkman et al.* (2009)
NREL 15MW	240	150	3	10.6	25	*Gaertner et al.* (2020)

The NREL 5MW wind turbine is implemented into most numerical simulation codes (HAWC2, SOWFA, LESGO, PALM); the NREL 15MW turbine is also being added to allow simulation of large modern wind turbines. The DTU 10MW reference wind turbine is included in codes developed by DTU Wind Energy (HAWC2, Ellipsys3D). Several codes, e.g., PALM, allow changing parameter files to include a particular turbine provided that its blade geometry and generator characteristics are known.

3 Data and models

Table 3.1: Overview of the observational data and models used in the papers. The exact Gaussian models are listed in Sect. 3.2

Paper	Observational data	Models
I	–	PALM v6.0
II	FINO1 (sonic anemometer)	PALM v21.10
III	FINO1 (cup anemometer, vane)	WRF, PALM v21.10
IV	–	Gaussian models, WRF, PALM v21.10
V	FINO1 (lidar, cup anemometer, vane)	Gaussian models, PALM v6.0
VI	FINO1 (lidar, cup anemometer, vane), SCADA	–

3.1 Observational data

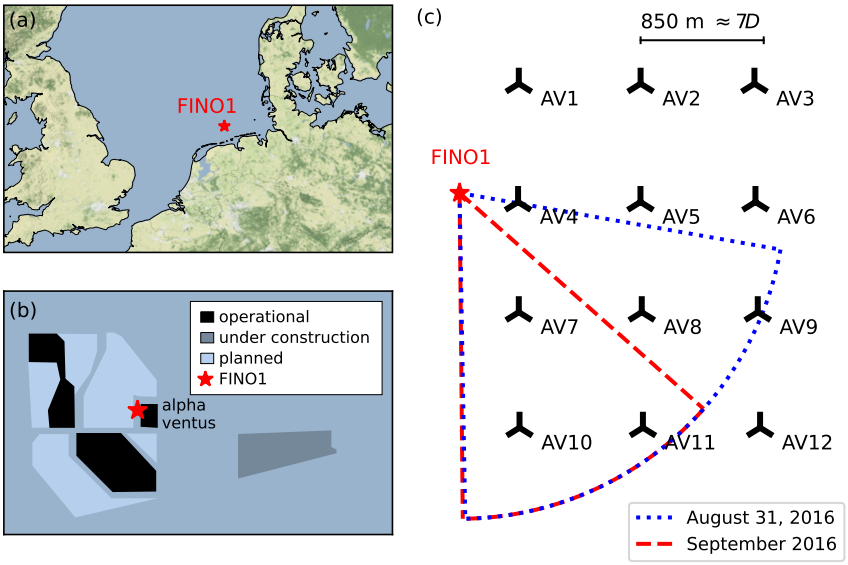

Figure 3.1: A scheme showing (a) the FINO1 location, (b) nearby wind farms, and (c) scan sectors of the lidars installed at FINO1 during the OBLEX-F1 campaign.

The papers in this thesis primarily use lidar data and anemometer time series obtained during the Offshore Boundary-Layer Experiment at FINO1 (OBLEX-F1) campaign in 2015–2016 (*The Offshore Boundary-Layer Observatory (OBLO)*, 2015). The FINO1

platform is located in the southern North Sea at 54° 00′ 53.5″N, 6° 35′ 15.5″E, 45 km north of the German island of Borkum. The nearby Alpha Ventus wind farm consists of 12 wind turbines arranged in a 4×3 rectangular pattern. The turbines are abbreviated as AV plus index of the turbine. Six turbines in two top rows (AV1−AV6) are of the type Repower 5M with a hub height of 92 m and a rotor diameter of 126 m; six turbines in two bottom rows (AV7−AV12) are of the type AREVA M5000 with a hub height of 91.5 m and a rotor diameter of 116 m. The AV4 turbine is the closest to the FINO1 platform and is located at 400 m to the east.

The FINO1 mast has cup anemometers installed at 33, 40, 50, 60, 70, 80, 90, and 100 m above sea level and vanes installed at 33, 40, 50, 60, 70, 80, and 90 m above sea level (*Fischer*, 2006; *Beeken*, 2008). Wind speed and direction times series are averaged to 10-minute periods. The gaps encountered in the regarded periods are filled with linear interpolation.

A scanning Doppler wind lidar (Leosphere WindCube 100S) was installed at the FINO1 platform at 23.5 m above sea level and was oriented towards the Alpha Ventus wind farm. Operating in the PPI mode, the lidar took scans in the inclined plane so that wind turbines AV7, AV10, and AV11 were captured in a scan. The elevation angle of the scanning plane varied with time. On August 31, 2016, the lidar performed scans under the constant elevation angle of 0.5° and scanned a sector between 100° and 180° azimuth angles. The elevation pattern was changed after August 31, 20:00 UTC+0 to the following: during the first 20 minutes of each hour, the lidar scanned at a constant elevation angle of 4.6° so that AV7 is scanned near the hub height; for the remaining 40 minutes, the lidar performed alternating scans at three elevation angles of 0.5°, 4.6°, and 9.0°. The scanned sector was also decreased to the range of 131.5° and 180° azimuth angles. This pattern remained unchanged during September 2016.

Several papers used additional datasets. The LES in Paper II was set up to generate mean wind speed and turbulence profiles similar to 1 Hz sonic anemometer time series processed by *Nybø et al.* (2019, 2020). Lidar retrieval results described in Paper VI required verification with the observational data. Besides FINO1 series, data from the Supervisory Control and Data Acquisition (SCADA) system were also utilized, particularly, wind speed and direction time series from the AV7 turbine. SCADA series were recorded with a higher frequency than 10-minuted averaged FINO1 series and contained longer gaps of up to one day. Therefore, no gap filling was performed for the SCADA series; the cross-comparison considered only those entries that had FINO1, SCADA data, and a successful lidar retrieval.

The comparison between wind direction measured at FINO1 and the estimated AV7 wake direction (Paper V) or AV7 SCADA data (Paper VI) revealed a consistent offset of approximately 10°. The offset is seemingly unaffected by the wind direction and is too large to be attributed solely to the measurement uncertainty. The comparison of wind direction recorded by SCADA system for other turbines revealed different but also consistent offset values. Therefore, it is plausible that the offset is partially caused by flow rotation and partially by technical reasons, e.g., an orientation error of the measurement instruments. With the data available, it is impossible to separate the effects of atmospheric stability, Coriolis force, wind turbine control and instrumental errors. Therefore, the observed offset was only reported in the respective papers but has yet to be analyzed thoroughly.

3.2 Gaussian wake models

Although Gaussian models can be reduced to the same formulation in Eq. (2.23), each model introduces its own corrections to the Gaussian function and amplitude affecting the final shape of the distribution. The models are also at different stages of development and complexity. Thus, implementing them in the thesis papers required a preliminary analysis of their interpretation of the wake. Paper I compared the BPA, Jensen-Gaussian, Ishihara, and double Gaussian models. Subsequent Paper VI selected the BPA and Jensen-Gaussian models as the most suitable for the coefficient re-fitting and added the super-Gaussian model that was not yet described at the time Paper I was written.

3.3 PALM Model System configuration

The LESs for this thesis were performed using PALM Model system v6.0 (*Maronga et al.*, 2020) and later – v21.10. The model upgrade was primarily dictated by technical reasons in order to retain compatibility with the Fram SIGMA2 computational cluster. The version difference did not affect the underlying equations relevant to the wake simulations and contained mostly quality-of-life improvements. For example, PALM v6.0 had no built-in function to include surface cooling for SBL simulations, so it had to be provided via user code. The function was fully implemented so that the surface cooling could be defined via regular input parameters in PALM v21.10.

LES of the Alpha Ventus wind farm or a stand-alone wind turbine used the NREL 5 MW reference wind turbine (Table 2.3, *Jonkman et al.* (2009)); its parameters were set to a rotor diameter of 126 m and a hub height of 90 m.

All simulations were performed assuming offshore conditions, i.e., low roughness length with the order of $z_0 \sim 10^{-3}$ m. The dynamic surface roughness due to the wave formation was not considered, as the corresponding module for PALM is still in development.

The PALM LESs for Papers I−III were run as a precursor-main run scheme in which a turbulent flow was first simulated in a precursor domain until a steady state. Although LESs for Paper III did not contain wind turbines, the precursor-main run approach was also used to ensure the same stability conditions and initial flow for nested and non-nested domain configurations.

3.4 Code repositories

During the research conducted for the thesis, several codes were produced to implement the regarded data processing methods. The codes and respective repositories are listed in this section. Additional documentation for each code is available within the repository.

The scripts require Python 3.8 with Jupyter notebook support. Standard libraries should be installed for running: `os`, `numpy`, `matplotlib`, `scipy`, `pandas`, `datetime`. In addition, `netcdf4` should be installed to read PALM output or lidar data. *Crameri* (2023) scientific color maps are preferable, although the scripts may run without them and switch to the standard Matplotlib colors. Additional libraries are listed in the respective code section.

PALM high-frequency data processing

The repository contains PALM high-frequency output for Paper II and routines to reproduce the plots from it. The code is strongly optimized for the specific output and simulations, so it is not recommended to run it as a standalone program.

Repository: Krutova, M. (2023). PALM v21.10 self-nested LES for three stability conditions (1.1.1). Zenodo. https://doi.org/10.5281/zenodo.7886678

Analytical wake model fitting

The repository contains functions to run several analytical wake models provided that the thrust coefficient C_T and ambient turbulence intensity I_a are known. The main code fits the selected models to wind field before and during the OCC event described in Paper III and Paper IV. The code allows selection of the fitting modes not mentioned in Paper IV, such as perform fitting only for one wake and ignore merging; alter wake length and width for which the fitting is performed or select models not mentioned in Paper IV. The results visualization is optimized for three models regarded at once.

Repository: Krutova, M. (2023). Gaussian wake model fitting to a transient event simulated with WRF-LES (1.0.1). Zenodo. https://doi.org/10.5281/zenodo.8139536

Wake identification and characterization via automatic thresholding method

The repository contains codes from Paper V to perform wake identification via thresholding and wake characterization from the thresholded shapes. Supplementary codes allow comparing the result to wake characterization via fitting a Gaussian function. The provided data provided contain LES and lidar wind fields as examples.

Additional Python libraries: `sklearn` (for finding the wake centerline via linear regression), `scikit-image` (for pre-processing), `holoviews`, `panel`, `param` (interactive dashboard for the manual threshold selection, not required to run the main script).

Repository: Krutova, M. (2022). Adaptive Thresholding Segmentation (ATS) for wake identification and characterization (0.5.1). Zenodo. https://doi.org/10.5281/zenodo.6997975 (Access by request due to the usage of unpublished lidar data)

2D-VAR method for elevated scans

The repository contains code implementing 2D-VAR method as described in *Cherukuru et al.* (2017); *Cherukuru* (2017) and corrections introduced in Paper VI. The SCADA data are excluded because of the non-disclosure agreement.

The main lidar retrieval script re-uses several functions from the wake identification repository to mask wakes in a lidar scan. The `inpaint` function used for gap filling in the lidar scans is provided with the repository since it does not exist as a Python library.

Repository: Krutova, M. (2023). 2D-VAR lidar retrieval method for low-elevation scans (1.0.0). Zenodo. https://doi.org/10.5281/zenodo.10226071 (Access by request due to the usage of unpublished lidar data)

4 Introduction to the papers

Paper I: Evaluation of Gaussian wake models under different atmospheric stability conditions: Comparison with large eddy simulation results

Krutova, M., Bakhoday-Paskyabi, M., Nielsen, F. G., and Reuder, J., Journal of Physics: Conference Series, ***1669(1)****, 012016 (2020)*

Objectives

1. Provide an overview of the Gaussian wake models available at the time the study was conducted.

2. Explore the accuracy of the models in the near and far wake against a single turbine wake simulated with the LES code PALM.

Summary

Currently, there exist numerous Gaussian wake models, and new ones are continuously being proposed. Some models approximate the far wake better than the near wake, while others aim to resolve the full wake. This paper compares how existing Gaussian models perform on wakes from a high-fidelity simulation.

Main findings

Single Gaussian models estimate the far wake ($x/D > 6$) better than the near wake. This observation is in line with the primary application of the analytical models – estimate the wake effect on the downstream turbine. The double Gaussian models are still in early development and are not consistent enough.

The number of tunable coefficients in models varies. Although the coefficients of some models, e.g., *Ishihara and Qian* (2018), are found by fitting, they are sensitive to attempts to re-fit their values.

Paper II: Self-nested large-eddy simulations in PALM model system v21.10 for offshore wind prediction under different atmospheric stability conditions

Krutova, M., Bakhoday-Paskyabi, M., Reuder, J., and Nielsen, F. G., Geoscientific Model Development, ***16(12)****, 3553–3564 (2023)*

Objectives

1. Perform LES with the PALM model system under different stability conditions and nesting modes at the wind speed typical for wind power production.
2. Explore the effect of the nesting modes on the simulated flow depending on the stability conditions.
3. Evaluate simulations based on the turbulence characteristics: spectral density, coherence, co-coherence and phase.

Summary

LES approximates turbulent scales smaller than the grid spacing and resolves the rest. Wind turbine wakes are more turbulent than free flow and contain small turbulent scales. Hence, one would be interested in keeping the grid spacing low to improve LES accuracy. Low grid spacing is often undesirable with respect to computational resources, as it leads to increased simulation time. The solution is to refine the grid locally with a nested domain. A new type of domain boundary and interpolation to the refined grid and back inevitably leads to new approximations in the flow. The effects of the nesting on zero to low wind speeds are documented. The secondary circulation was observed occurring in the two-way nested domain for buoyancy-driven flows, the circulation becomes evident when the flow is averaged for a period of several hours. The paper examines how the PALM nesting modes affect the flow at a wind speed of 12.5 m/s - the order of wind speeds usually encountered in wind energy research. The LESs are performed for true neutral, stable, and unstable conditions and compared to the 1 Hz sonic anemometer time series of the wind speed components.

Main findings

Simulating a strong wind flow in non-neutral conditions with PALM produced a slowdown in the nested domain with a consequent acceleration after exiting the nested domain. The slowdown effect appears nearly immediately after the time required for the flow to pass the outermost domain once. This drawback makes the two-way nesting mode inapplicable for non-neutral conditions, even though it would allow accounting for the effect of a better-resolved wake downstream. Notably, the effect also appears in any PALM simulation that is not set to true neutral explicitly, i.e., as long as the temperature term is considered in the equation.

Despite nesting effects, the LESs fairly reproduce turbulence characteristics as seen in the observational data. Although decreasing the grid spacing to 1.25 m still does not resolve all turbulence scales, the width of the resolved inertial subrange increases visibly with the grid refinement. Compared to the one-way nesting mode, the spectra of wind speed components lay closer to each other in two-way nesting due to the solution exchange between child and parent nested domains.

Paper III: **Multiscale simulation of offshore wind variability during frontal passage: Brief implication on turbines' wakes and load**

Bakhoday-Paskyabi, M., Krutova, M., Bui, H., and Ning, X., Journal of Physics: Conference Series, ***2362****, 012003 (2022)*

Objectives

1. Set up a multi-scale modeling framework by combining WRF capability of simulating complex atmospheric processes and PALM resolution of turbulent micro-scales to investigate structural response with NREL FAST.

2. Perform a WRF-PALM simulation of a transient event near FINO1 platform and Alpha Ventus wind farm – the OCC event occurred in the Southern North Sea on November 22−24, 2015.

3. Analyze changes in the wake behavior and turbines' load response for the Alpha Ventus wind farm.

Summary

A series of cascading nested domains is set up for the simulation. The outermost domain in WRF simulation covers the area above Northern Europe with a grid spacing of 9 km. In the same simulation, the domain is locally refined with several intermediate nested domains to 1 km grid spacing. The LES proceeds with the grid refinement until the innermost domain with a spacing of 10 m containing area around the Alpha Ventus wind farm. The WRF simulation is initialized with ERA5 reanalysis data and runs for the period of November 22−24, 2015. Its results are passed to the LES as a dynamic input. Considering the results from Paper II, the one-way nesting mode was used for the grid refinement in PALM to avoid alteration of the wind field caused by the two-way nesting mode. Wind fields 20 minutes before and after the beginning of the OCC event at Alpha Ventus are selected for aero-elastic analysis with NREL FAST.

Main findings

The WRF simulation shows the OCC structures forming at 100 m level, meaning that changes in the wind flow affect wind turbines in the Southern North Sea. While the WRF simulation captures the variability of the flow during the OCC event, the follow-up PALM LES details the wakes. The performed WRF-PALM simulation reveals strong alteration of the wake behavior from wide meandering wakes prior to the OCC event to narrow straight wakes in the OCC cell. The aero-elastic analysis of the LES output shows increased oscillations in the rotor speed during the OCC event. The induced oscillations make the control system act accordingly and adjust the pitch angle.

The paper successfully demonstrates a multi-scale modeling chain which links large-scale atmospheric processes and a dynamic load response of the turbines.

Paper IV: Gaussian wake model fitting in a transient event over Alpha Ventus wind farm

Krutova, M. and Bakhoday-Paskyabi, M., Wind Energy Science Discussions ***[preprint]****, (2023)*

Objectives

1. Evaluate the behavior of selected Gaussian models for wakes in a transient event – the OCC event occurred in the Southern North Sea on November 22−24, 2015.

2. Apply models to calculate the deficit of merging wakes and evaluate their accuracy.

Summary

Gaussian wake models are applied to 10-minute averaged periods before and after the OCC event simulated with WRF-PALM described in Paper III. Models' coefficients are also re-fitted to evaluate whether each model could have described the wakes better. The coefficient re-fitting is performed to minimize the RMSE for all wake cross-sections regarded in one period. The models for this study are selected by their response to coefficients re-fitting as observed in Paper I. Thus, the Jensen-Gaussian and BPA models are chosen; the recently emerged super-Gaussian model is also added.

Main findings

The 10-minute period corresponding to the peak of the transient event is the most challenging for all models. The complication is primarily the ambiguity of the free-flow wind speed: a part of an averaged wake forms under increased flow speed while the far wake is still unaffected.

Single Gaussian models confirm an existing problem of overestimating the velocity deficit in the near wake, especially if the deficit distribution has a double peak shape. However, the Jensen-Gaussian model being defined with only one tunable coefficient is not flexible enough and requires re-assessment of the coefficient depending on the atmospheric conditions. The Gaussian model in *Niayifar and Porté-Agel* (2015) definition responds to the changing flow better, although it may fail for the very near wake of $x/D \leq 2.5$. The super-Gaussian model shows good agreement with the velocity deficit distribution without an additional adjustment and interprets merged wakes particularly well. This result calls for further study of the model on wake-wake interactions in the observational data.

Paper V: **Development of an automatic thresholding method for wake meandering studies and its application to the data set from scanning wind lidar**

Krutova, M., Bakhoday-Paskyabi, M., Reuder, J., and Nielsen, F. G., Wind Energy Science, ***7(2)****, 849–873 (2022)*

Objectives

1. Develop a novel method for wake identification via automatic thresholding.
2. Develop routines to characterize wake after the thresholding is performed: find the wake centerline.
3. Verify the developed methods with LES and lidar data.

Summary

This paper proposes a novel method to perform automatic thresholding based on image processing techniques. The method is first demonstrated on the LES wake to prove the concept and is then applied to a lidar dataset of the Alpha Ventus wind field with the lidar installed at the FINO1 platform. The method's accuracy is verified by visually comparing identified wakes and comparing the detected centerline to the Gaussian method results.

Main findings

The automatic thresholding method proved to perform well on wide and prominent wakes, which appear in a lidar scan when the line-of-sight is close to the wind direction. It is more challenging to separate wakes from the background flow when the wind direction is perpendicular to the line-of-sight – a case where the regular Gaussian method may also fail.

The comparison revealed an offset of $5-10^{\circ}$ between FINO1 wind direction and estimated wake direction. While the yaw deflection and Coriolis effect can partially explain it, the offset is seemingly independent of the wind speed and direction. The offset is attributed to a combined effect of the Coriolis force and a possible lidar orientation error. This issue requires further investigation.

Paper VI: Validation of the 2D-VAR lidar retrieval algorithm for non-homogeneous wind fields using FINO1 and SCADA data

Krutova, M., Bakhoday-Paskyabi, M., and Reuder, J., Authorea, ***[preprint]*** *(2023)*

Objectives

1. Independently implement a proposed method for the 2D-VAR lidar retrieval and validate it on a larger dataset with an addition of the SCADA data.

2. Explore the method's sensitivity to the initial guess and weights used in the optimization.

Summary

Scanning lidars do not measure the wind speed explicitly but only its line-of-sight projection. Therefore, lidar data have to be processed in order to retrieve the original wind speed values. The existing methods are either developed for homogeneous flows or require a complex processing procedure. The wake field is non-homogeneous and requires fast processing for short-term forecasting. To fill the gap, a 2D-VAR lidar retrieval method was proposed by *Cherukuru et al.* (2017). However, the method was only validated on a one-day dataset for horizontal scans near the bottom tip wakes. The setup made it impossible to compare results to the turbine's hub-height data and study the algorithm performance for different flow conditions. In this paper, the algorithm is independently implemented and applied for a larger dataset that covers more wind speed and direction pairs and allows comparison to SCADA data.

Main findings

When verified on the same one-day dataset, the independently reproduced algorithm shows a small discrepancy with the original study. The discrepancy may be attributed to the lack of details describing the preparatory steps which lead to different processing and optimization routines chosen. When run for a larger dataset, the scanning was performed under a different elevation angle, capturing wakes across the hub-height plane. Because of larger differences between the free-flow and wake velocities, the algorithm produced an unnatural wind speed increase along the wakes. The effect was mitigated by wake masking via the automatic thresholding described in Paper V. A comparison of the retrieved wind speed to the time series from FINO1 mast and SCADA data showed that the wind speed upstream of the turbine tends to the SCADA data. It is possible that the retrieval result tunes to the initial guess of the wind speed and direction – this issue requires further investigation. Among the weights used during the optimization, only the weight assigned to the residuals affects the final result most.

5 Conclusions and Outlook

This thesis approached several aspects of studying wind turbine wakes: observation processing, analytical and numerical modeling. The multi-scale modeling framework was established and demonstrated throughout Papers II−IV. Paper II explored the nesting modes in the chosen LES model and highlighted the problems arising from the two-way nesting mode. Although this mode should theoretically improve LES accuracy in the nested area for all simulation domains, it leads to a strong flow slowdown for non-neutral LES at wind speeds typical for wind energy research ($\sim 10\,\mathrm{m/s}$). Weak secondary circulation was reported before but for a near-zero wind speed and shear. PALM's behavior for higher wind speeds means that the two-way nesting mode is currently unsuitable for wind turbine simulations; the one-way nesting mode is preferable. Therefore, one-way nested domains were chosen for the LES part of the multi-scale simulation performed in Paper III. Several simulations were performed in the preparation of Paper III; one of them was used for the analytical models fitting to wakes in Paper IV. The analytical models and coefficient fitting were previously explored in Paper I. The updated framework was carried over to Paper IV with an addition of another wake model, the super-Gaussian model, and a code update to account for the wake merging. Paper IV showed promising results for the super-Gaussian model, which performed comparably before and after the beginning of the OCC event.

In parallel, a novel method for wake identification and characterization was suggested in Paper V. Since image processing techniques such as dynamic thresholding are new to the wake research, the article presented an extensive study on the novel method's capabilities. The dynamic thresholding method requires further development to improve its performance for lidar data. Nevertheless, it was possible to demonstrate a usage case as a sub-routine in the lidar retrieval algorithm studied in Paper VI. The regarded retrieval algorithm was proposed by (*Cherukuru et al.*, 2017). The new paper aimed to validate it on a larger dataset and additional observational data. During the validation, it was found that the algorithm's performance declines in the presence of prominent wind turbine wakes in the scan. The side effect was successfully mitigated by using the thresholding method from Paper V to identify and mask wakes.

Overall, the research carried out for this thesis settled a base for further study of wake meandering and transient events.

5.1 Further work

There is always room for improvement of existing and newly developed methods: optimizing the algorithm, increasing performance in complex cases, and mitigating errors and uncertainties.

The slowdown of the flow in the two-way nesting mode is not unique to PALM and was reported for other LES approaches. When LES were run for Paper II with various combinations of input parameters, the cause of the slowdown effect was narrowed down to a few functions responsible for the data exchange between nested domains. Although the slowdown effect may be not removed completely, it is worth studying whether it can be mitigated significantly to allow usage of the two-way nesting modes for wind turbine

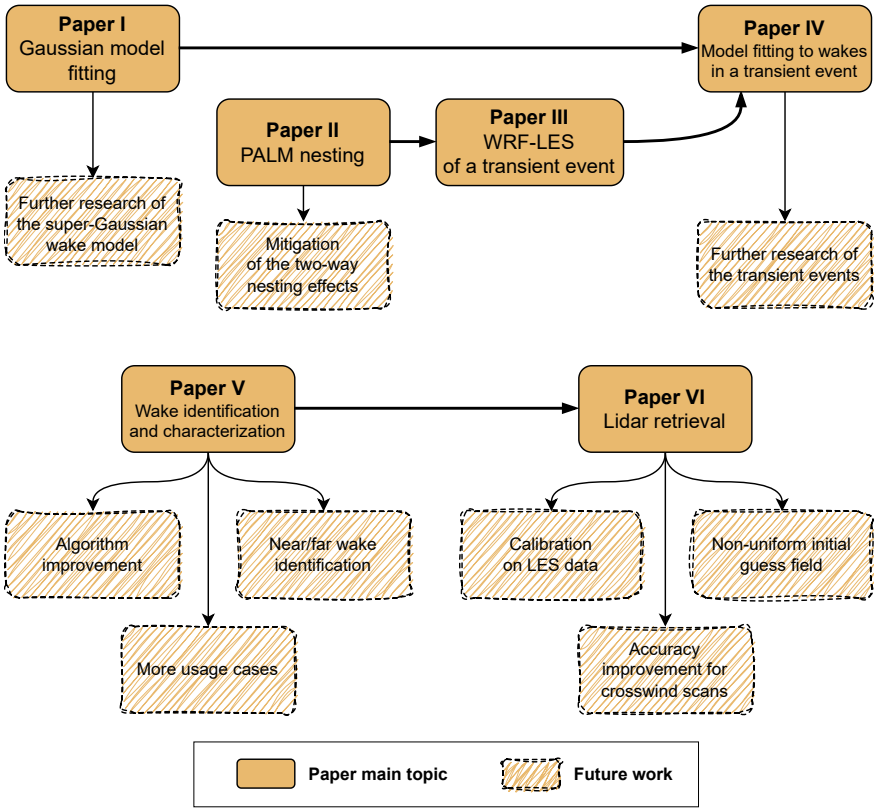

Figure 5.1: Planned work

simulations.

Paper IV observed a good performance of the super-Gaussian model on describing merged wakes and reacting to the transient flow. This finding calls for further validation of the model in other transient events to obtain more data for analysis. The transient event can be also studied with other simplified models. For example, the curled wake model was developed with wind farm control strategies in mind (*Martínez-Tossas et al.*, 2019, 2021), which makes it relevant for an application in a transient event. Considering that this model was tested in steady conditions, it is still an open question how it would behave in a transient flow.

During the development of the wake identification method in Paper II and its application for the wake masking in Paper VI, it was found that the wake identification under-performs for the crosswind scans and often cannot separate the full wake from the free flow. Considering that the wakes are still visible in the crosswind scans, the dynamic thresholding algorithm requires fine-tuning for such cases. As of now, the algorithm performs best for simulated wakes or lidar scans taken when wind direction approaches the lidar's line of sight – both cases also allow using fitting methods to identify a wake. Thus, the thresholding method does not have a big advantage except that it identifies wake points directly, which simplifies wake masking. The algorithm tuning may go as far as replacing the criteria for finding the threshold while leaving the general framework the

same. During the algorithm development, a possibility to separate near and far wake was found but left aside due to the amount of results already presented in Paper V. The follow-up paper, if focused not just on the algorithm update, should also demonstrate new usage cases for wake identification via thresholding.

The validation of the lidar retrieval algorithm left a question of how much is the final result affected by the initial guess and weights chosen for the optimization function. Considering that the true velocity is unknown when working with lidar data, the retrieval algorithm for non-homogeneous fields should be additionally validated on the LES wind field with a virtual lidar. If the result is too sensitive to the initial guess, new ways of defining it can be suggested, e.g., by constructing an approximated field based on mast and SCADA data for the wind speed.

6 Scientific papers

Paper I

Evaluation of Gaussian wake models under different atmospheric stability conditions: Comparison with large eddy simulation results

Krutova, M., Bakhoday-Paskyabi, M., Nielsen, F. G., and Reuder, J.
Journal of Physics: Conference Series, **1669(1)**, 012016 (2020)

Evaluation of Gaussian wake models under different atmospheric stability conditions: Comparison with large eddy simulation results

Maria Krutova, Mostafa Bakhoday Paskyabi, Finn Gunnar Nielsen, Joachim Reuder

Geophysical Institute, University of Bergen and Bergen Offshore Wind Centre, Bergen, Norway

E-mail: Maria.Krutova@uib.no

Abstract. The calculation of the velocity deficit in the wake of individual wind turbines is a fundamental part of the wind farm analysis. A good approximation of the wake deficit behind a single wind turbine will improve the power estimation for downwind turbines. Large-eddy simulation (LES) is a research tool widely used in studying the velocity deficit and turbulence intensity in the wake. However, the computational cost of the LES prevents its application in wind farm performance analysis and control. Existing analytical wake models provide a fast estimation of the velocity deficit and the wake expansion rate downstream from the rotor. The Gaussian wake models use a Gaussian distribution to improve the prediction of the wake velocity deficit. With the number of analytical models available, an extensive evaluation of their performance under different flow parameters is needed. In this work, we simulate a wake of a single wind turbine using the LES code PALM (Parallelized LES Model) combined with an actuator disc model with rotation. We compare the computed flow field with the predictions made by Gaussian models and fit their parameters to obtain the best possible fit for the wake field data as computed by LES.

1. Introduction

Inside a wind farm, the wind turbines are subjected to the influence of upstream turbines. The wake, an area with reduced mean velocity and increased turbulence intensity, is formed behind a working wind turbine due to the extraction of kinetic energy from the flow. Far downstream, the wake velocity eventually recovers to the free-flow velocity. However, the distances between wind turbines in a wind farm are usually shorter than needed for the full recovery. Therefore the wind turbines subjected to a wake operate under reduced wind speed. Since the available wind power is proportional to the cube of wind speed U^3, it is crucial to predict the wake velocity deficit accurately.

Wake models range from simple analytical expressions to complex Computational Fluid Dynamic (CFD) codes. One of the latter, the large-eddy simulation (LES), is widely used in atmospheric boundary layer studies. LES resolves large turbulence scales directly and simulates subgrid scales and therefore is capable of handling turbulent flows such as wind turbine wakes. The LES can reproduce wake field characteristics in detail but requires grid resolution fine enough to resolve all turbulence scales of interest. The high-fidelity LES demands a significant amount of time and computational resources. Analytical wake models are less demanding but simplify

the wake shape and wake velocity distribution. The simplest analytical models (Jensen [1], Frandsen [2]) assume a top-hat distribution of the wake deficit at each cross-section. A recent development in the analytical wake models, Gaussian models, suggests improving the wake-deficit distribution estimation by replacing the top-hat distribution with a Gaussian distribution.

In this study, we use the LES code PALM [3] to generate wind turbine wake fields at $U_\infty = 10\,\mathrm{m/s}$ and $15\,\mathrm{m/s}$. We then assign this data as an input field to four Gaussian models: Bastankhah & Porté-Agel [4], Jensen-Gaussian [5], Ishihara [6], and Double Gaussian [7] models. In Section 2, we briefly describe the models, their governing equations, special features, and select the parameters to fit the simulated wake field data. Section 3 introduces the LES code PALM and the configuration used to simulate a wind turbine wake under neutral and stable atmospheric conditions. We evaluate the parameters of Gaussian models by fitting them to various data slices of the LES wake flow fields. Applying fitted parameters, we compare the models' capability to predict the full LES wake and discuss the results in Section 4. We give a summary of the findings in Section 5.

2. Methodology

To calculate the wake field with an analytical wake model, we use the Cartesian coordinate system (x, y, z) centered at the foundation of a wind turbine so that the x-axis is aligned with the wind direction and z-axis is positive upwards.

The analytical wake models describe the wake velocity U_w or the normalized wake velocity deficit $\Delta U = 1 - U_w/U_\infty$ based on the following characteristics: downstream distance x from the turbine, wind turbine diameter D, and hub height z_h. Besides the wind turbine characteristics, the wake models also use the thrust coefficient C_T and the ambient turbulence intensity I_a estimated upwind of the rotor plane. Each model has one or more parameters to define the wake shape and/or expansion rate. The axisymmetric models regarded in this study implicitly assume that the wake does not interfere with the lower boundary, represented by the land or sea surface. The effect of vertical shear in the incident wind field is not considered.

2.1. Top-hat analytical models

While the top-hat analytical models are not the focus of this research, their concepts are borrowed and extended by the Gaussian wake models. Hence we provide a short description of the Jensen and Frandsen models.

2.1.1. The Jensen model [1] assumes linear expansion of a fully turbulent wake and equal velocity deficit in the cross-section of the wake (top-hat distribution). The expansion coefficient k defines the increase of the wake diameter D_w with the downstream distance x as follows

$$D_w(x) = D + 2kx. \tag{1}$$

The velocity deficit is calculated as

$$\Delta\overline{U} = \left(1 - \sqrt{1 - C_T}\right) \left(\frac{D}{D_w}\right)^2. \tag{2}$$

While several methods to define k are suggested, we use the one that allows linking wake expansion with ambient turbulence intensity: $k \approx 0.4 I_a$ [8].

2.1.2. The Frandsen model [2] also assumes an equal velocity deficit in the cross-section of the wake but uses a different approach to calculate the wake diameter.

$$D_w(x) = D\left(\beta + \alpha \cdot x/D\right)^{1/2} \tag{3}$$

where the induction factor α is determined experimentally or corrected from the wake growth rate k in the Jensen model. The coefficient β is related to the thrust coefficient C_T by

$$\beta = \frac{1}{2} \cdot \frac{1 + \sqrt{1 - C_T}}{\sqrt{1 - C_T}}. \tag{4}$$

The wake deficit also depends on C_T and is calculated as follows

$$\Delta\overline{U} = \frac{1}{2} - \frac{1}{2}\sqrt{1 - 2\left(\frac{D}{D_w}\right)^2 C_T}. \tag{5}$$

2.2. Gaussian wake models
The general form of a Gaussian wake model is given by

$$\Delta\overline{U} = A \cdot F(x, C_T, I_a) \cdot G\left(r, \sigma(x)\right) \tag{6}$$

where

- $\Delta\overline{U} = 1 - U_w/U_\infty$ is the normalized wake velocity deficit;
- A is an optional scaling constant;
- $F(x, C_T, I_a)$ is an amplitude function which defines the maximum normalized velocity deficit at the wake centerline;
- $G(r, \sigma(x))$ denotes a Gaussian function;
- $r^2 = y^2 + (z - z_h)^2$ is a radial coordinate;
- $\sigma = \sigma(x)$ is the standard deviation of a Gaussian function, defining the wake width.

2.2.1. The Bastankhah & Porté-Agel model , further referred to as BPA, exists in several formulations. In this study, we use the axisymmetric version of the model that includes ambient turbulence intensity [4].

The BPA model retains the linear expansion of the wake similar to the Jensen model (Eq. (1)) but introduces a different coefficient – the growth rate of the wake k^* – so that the standard deviation $\sigma(x)$ of the Gaussian distribution is

$$\frac{\sigma}{D} = k^* \frac{x}{D} + \varepsilon, \tag{7}$$

where the growth rate of the wake k^* is a linear function of turbulence intensity [4]:

$$k^* = 0.003678 + 0.3837 I_a, \tag{8}$$

and ε can be expressed as $\varepsilon = 0.2\sqrt{\beta}$ [9], where β is defined in Eq. (4).

The normalized wake velocity is then given by the BPA model as

$$\Delta\overline{U} = \left(1 - \sqrt{1 - \frac{C_T}{8(\sigma/D)^2}}\right) \times \exp\left(-\frac{r^2}{2\sigma^2}\right). \tag{9}$$

In our study, we preserve the linear function as $k^* = k_1^* + k_2^* I_a$ where the parameters k_1^* and k_2^* are to be identified by fitting $\Delta\overline{U}$ to the simulation data.

2.2.2. The Jensen-Gaussian model [5] is a modification of the Jensen model.

The wake radius is calculated similarly to the Jensen model (Eq. 1) with the expansion coefficient k corrected for turbulence intensity:

$$r_x = r_1 + k_{wake}(k, C_T, I_a)x, \tag{10}$$

where $r_1 = r_d\sqrt{(1-a)/(1-2a)}$ is the original rotor radius corrected for the axial induction [5].

Furthermore, the top-hat distribution of the wake deficit is replaced by the Gaussian distribution to satisfy the following conditions:

(i) 99% of the Gaussian distribution lies within the wake radius r_x (Eq. 10), i.e., the corresponding quantile for the Gaussian distribution is $z_{0.99} = 2.58$ from which the standard deviation should be $\sigma = r_x/2.58$.

(ii) The wind velocity outside the wake radius r_x is set equal to the free stream velocity U_∞.

(iii) The model has the same mass flow as the Jensen model.

Applying the above assumptions will lead to the following expression for the normalized wake velocity deficit:

$$\Delta\overline{U} = \left[1 - \frac{5.16}{\sqrt{2\pi}} \cdot \overline{U}^*(x, k_{wake}(k, C_T, I_a))\right] \times \exp\left(-\frac{r^2}{2\sigma^2}\right),\ \sigma = r_x/2.58 \tag{11}$$

The exact definitions of functions $k_{wake}(k, C_T, I_a)$ and $\overline{U}^*(x, k_{wake})$ are omitted for brevity and can be found in the original study [5].

As seen from Eq. (10) and (11), the wake expansion coefficient k is included in the Jensen-Gaussian model through the function k_{wake}. The initial value of k is defined as in the Jensen model: $k = 0.4I_a$ (Section 2.1.1 and [8]).

2.2.3. The Ishihara model [6] proposes a general expression for the normalized velocity deficit of the full-wake:

$$\Delta\overline{U} = (a + b \cdot x/D + p)^{-2} \times \exp\left(-\frac{r^2}{2\sigma^2}\right). \tag{12}$$

The standard deviation σ is defined as in the BPA model Eq. (7). The coefficients k^* and ε are calculated from thrust coefficient C_T and ambient turbulence intensity I_a as given in [6]:

$$k^* = 0.11C_T^{1.07}I_a^{0.20},\ \varepsilon = 0.23C_T^{-0.25}I_a^{0.17}. \tag{13}$$

The coefficients a and b are in turn dependent on k^* and ε as

$$a = 4C_T^{-0.5}\varepsilon,\ b = 4C_T^{-0.5}k^*. \tag{14}$$

The dimensionless coefficient p in Eq. (12) is expressed through another coefficient c as

$$p = \frac{c}{(1 + x/D)^2},\ c = 0.15C_T^{-0.25}I_a^{-0.7}. \tag{15}$$

The coefficient p performs a near-wake correction for the amplitude function $F(x, C_T, I_a)$ (Eq. 6). The role of the correction coefficient is detailed further in Section 2.3.

According to Eq. (13) and (15), k^*, ε and c of the Ishihara model are represented as functions of C_T, I_a, and three tunable parameters for each function:

$$k^* = k_1C_T^{k_2}I_a^{k_3},\ \varepsilon = \varepsilon_1C_T^{\varepsilon_2}I_a^{\varepsilon_3},\ c = c_1C_T^{c_2}I_a^{c3}. \tag{16}$$

Overall, there are nine parameters to be identified: k_1, k_2, k_3, ε_1, ε_2, ε_3, c_1, c_2 and c_3.

2.2.4. The Keane Double Gaussian model [7] extends the BPA model's approach to account for the two peaks often present in the wake measurements near the wind rotor:

$$\Delta\overline{U} = A \cdot F(\sigma(x), C_T) \cdot G(r, \sigma(x)). \tag{17}$$

The double Gaussian function $G(r, \sigma(x))$ describes the axisymmetric wake as

$$G(r, \sigma(x)) = \frac{1}{2}\left(e^{W_+} + e^{W_-}\right),\ W_\pm = -\frac{(r \pm r_0)^2}{2\sigma^2(x)}, \tag{18}$$

where r_0 is the radial position of the extremum of a Gaussian function. For $r_0 = 0$, the function collapses to a single Gaussian function. For $r_0 > 0$, a double peak appears in a wake profile. The estimation $r_0 = 0.75D/2$, or 75% of the rotor radius, is suggested by the original study as a good approximation.

The standard deviation σ characterizes the width of each of the two Gaussian profiles as

$$\sigma(x) = k^* x^{1/3} + \varepsilon. \tag{19}$$

The Double Gaussian model does not include turbulence intensity I_a in the formulation, i.e., the amplitude function is expressed only by the standard deviation and the thrust coefficient as

$$F(\sigma(x), C_T) = \frac{M - \sqrt{M^2 - \frac{1}{2}NC_TD^2}}{2N}, \tag{20}$$

where erf is the error function and

$$\tau = r_0/\sigma, \tag{21}$$

$$M = 2\sigma^2 \exp\left(-\frac{1}{2}\tau^2\right) + \sqrt{2\pi} r_0 \sigma [\mathrm{erf}\left(\tau/\sqrt{2}\right) - 1], \tag{22}$$

$$N = \sigma^2 \exp\left(-\tau^2\right) + \frac{1}{2}\sqrt{\pi} r_0 \sigma [\mathrm{erf}\left(\tau\right) - 1]. \tag{23}$$

It should be noted that the original form of the Double Gaussian model probably has a typo in the expressions for M and N (page 3 in [7]). The expressions provided here are corrected according to the model output under default parameters compared to the original work.

In this study, we choose variables k^*, ε, and A as fitting parameters. Unlike the previous models, the Double Gaussian model does not have universal parameters. We select two sets of the original study parameters that correspond to free-flow speeds of $10-12\,\mathrm{m/s}$ and $16-18\,\mathrm{m/s}$ (Table 1 in [7], note that ε has to be additionally multiplied by the rotor diameter D). The selected parameters are used as initial guesses for the $U_\infty = 10\,\mathrm{m/s}$ and $U_\infty = 15\,\mathrm{m/s}$ simulations, respectively.

2.3. Overview of the Gaussian wake models

The characteristics of the Gaussian wake models are summarized in Table 1. The recommended parameters provided in the original formulation of each wake model are used as initial guesses for the fitting function and are further referred to as default parameters. All tunable parameters are constrained to a specific range to keep the values physically sensible and to avoid curve fitting failure.

The sample flow fields are calculated with each Gaussian model for the thrust coefficient $C_T = 0.763$ and turbulence intensity $I_a = 6.6\%$. The normalized velocity deficit distribution at the hub height $z_h = 102\,\mathrm{m}$ is shown in Fig. 1.

Table 1. Gaussian wake models.

Model	# of parameters	Recommended values	I_a included
BPA (I_a)	2	$k_1^* = 0.003678, k_2^* = 0.3837$	Yes
Ishihara	9	Yes, see Eq. (13), (15)	Yes
Jensen Gaussian	1	$k = 0.4I_a$	Yes
Double Gaussian	3	N/A	No

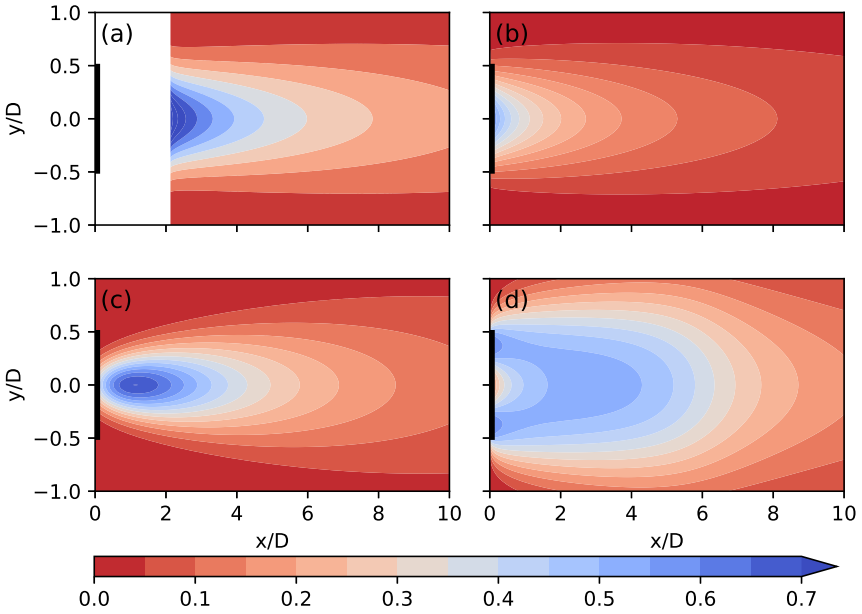

Figure 1. The normalized wake velocity deficit in a horizontal section at the hub height, calculated using Gaussian models with default parameters for $C_T = 0.763, I_a = 6.6\%$. (a) BPA, (b) Jensen-Gaussian, (c) Ishihara, (d) Double Gaussian

The BPA model (Fig. 1a) predicts a slowly expanding wake for the selected conditions. However, the BPA model cannot resolve a wake for $x/D \leq 2$ and high thrust coefficient because of the negative value under the square root $\sqrt{1 - \frac{C_T}{8(\sigma/D)^2}}$. Nevertheless, the unresolved region is not a critical flaw of the model, since the main interest is predicting wake influence on the downwind turbines.

The Jensen-Gaussian model (Fig. 1b) predicts a short near-wake. Without a comparison to a reference wake field, it is difficult to determine whether the initial guess of $k = 0.4I_a$ is correct or should be approximated better. Yet, it is possible to say that the Jensen-Gaussian model is rather sensitive to its only tunable parameter k. Decreasing k brings the wake growth rate closer to linear and delays wake recovery. Judging from the wake shape, it may be expected that the Jensen-Gaussian and the BPA models can give similar predictions as the parameters

k, and k_1^* and k_2^* are adjusted accordingly.

The Ishihara model (Fig. 1c) places a region of the high velocity deficit at $x/D \approx 1$. At the same time, the near-wake is narrower than predicted by other models. The far-wake grows slightly faster than in the BPA and Jensen-Gaussian models for the same conditions.

As follows from Eq. (12) the Gaussian function of the Ishihara model does not affect the velocity deficit at the centerline $r = 0$. Therefore, we can review the influence of the correction coefficient p on the centerline velocity deficit. An example amplitude function at the centerline is plotted in Fig. 2. Since p is inverse proportional to the normalized downstream distance x/D, the correction effect decreases with an increase of the downstream distance. As shown in Fig. 2, the coefficient p has a strong influence at the downstream distance $x/D \leq 2$. For $x/D \to \infty$, the value of p becomes negligible; the amplitude function with and without the correction coincide.

If no correction coefficient is present for the near-wake, i.e., $p = 0$ ($c = 0$) regardless of the downstream distance, the velocity deficit may exceed 1 near the center of the rotor. The velocity deficit $\Delta\overline{U} > 1$ corresponds to $U_w/U_\infty < 0$, or the wake velocity $U_w < 0$, i.e., reverse flow. Therefore, the coefficients p and c must be positive to avoid non-physical values of the velocity deficit in the near-wake.

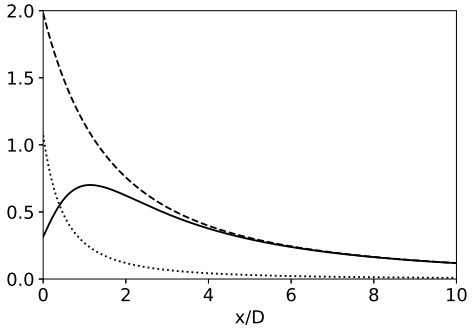

Figure 2. The effect of the near-wake correction on the amplitude function of the Ishihara model, calculated for NBL $U_\infty = 10\,\mathrm{m/s}, C_T = 0.763, I_a = 6.6\%$.
—— amplitude function with a correction, - - - - amplitude function without a correction, ····· correction coefficient p.

The Double Gaussian model (Fig. 1d) stands out by predicting significantly larger wake width compared to other models. The parameter k^* of the Double Gaussian model affects the width of each of the Gaussian distributions. Decreasing k^* reduces the overall width of the wake but delays merging of the two profiles. Other parameters of the Double Gaussian model provide little effect on the predicted wake width.

3. PALM LES

3.1. Model description

PALM is an open-source Fortran LES code developed at the University of Hanover and capable of simulating turbulent atmospheric processes. The wind turbine simulation is performed using a supplementary module written by the research group from the University of Oldenburg. The module implements an actuator disk model with rotation (ADM-R) to simulate a wind turbine rotor [10]. The model is based on the concept suggested by Wu and Porté-Agel [11]. The original actuator disk model without a rotation (ADM) assumes a uniform distribution of the thrust force across the disc and does not consider the effect of turbine-induced rotation. ADM-R

includes rotation into the model to improve the predictions. In ADM-R, the actuator disc is first split into annular areas. The lift and drag forces in each area are calculated using the blade element momentum theory. Each blade element assumes a 2D airfoil of the corresponding blade section. As shown in [11], ADM-R improves the agreement with wind tunnel measurements compared to ADM, especially in the near-wake. Additionally, ADM-R performs comparably to a more complex actuator line model (ALM) [12]. The effect of the nacelle and the wind tower effect can be taken into account through the drag coefficients.

Comparisons with FINO1 lidar measurements [13][14] confirmed that ADM-R captures the features of a near-wake rather well and has a reasonable agreement on the width and velocity deficit value in the far-wake. For the full description of the current wind turbine model implementation, we refer to Section 3.7 of the PALM overview [3].

3.2. LES configuration

LES are carried out in PALM for a single NREL 5 MW wind turbine [15] with a diameter of $D = 126\,\mathrm{m}$ and horizontal wind speed of $U_\infty = 10\,\mathrm{m/s}$ (near rated) and $15\,\mathrm{m/s}$ (above rated) at the hub height $z_h = 102\,\mathrm{m}$. Two stability conditions are simulated for each wind speed: neutral boundary layer (NBL) and stable boundary layer (SBL). Offshore conditions are assumed by a roughness length of $z_0 = 0.0005\,\mathrm{m}$ for all cases. The domain size and the grid resolution Δ are chosen in accordance with the existing PALM simulations of wind turbines for different atmospheric stabilities [16].

Each simulation consists of two stages: the precursor run to let the turbulence develop, and the main run using the precursor run as an input for the larger domain with one wind turbine (Table 2). The grid cell is stretched vertically to reduce the number of cells in the z-direction. The stretching factor of 1.04 is applied after reaching the height h_z above the surface. The maximum possible height of a grid cell is capped with a value twice of the original resolution Δ. The height of the boundary layer in each stability case remains lower than h_z.

The geostrophic wind velocity is one of the initialization parameters for LES. Since the simulations are performed at the latitude 54°N, a correction is introduced for the geostrophic wind components U_g and V_g to compensate for the Coriolis effect and obtain the required horizontal free-flow wind speed U_∞ at the hub height. The corrections depend on the stability conditions and are listed in Table 3. The lateral velocity of the free-flow at the hub height stays within $V_\infty < 0.05\,\mathrm{m/s}$ and may cause a small deflection of the wake. An additional NBL simulation for $U_\infty = 10\,\mathrm{m/s}$ is performed on a $\Delta = 4\,\mathrm{m}$ grid to reduce deflection. Furthermore, the LES of NBL $U_\infty = 10\,\mathrm{m/s}$ implies the simulation on a finer grid ($\Delta = 4\,\mathrm{m}$), while the LES of NBL $U_\infty = 15\,\mathrm{m/s}$ is still performed on a coarser grid ($\Delta = 6\,\mathrm{m}$).

Table 2. Domain size.

Case	Δ, m	Precursor run, points	Main run, points	h_z
Stable	4	$384 \times 384 \times 160$	$1792 \times 384 \times 160$	500 m
Neutral	4	$576 \times 576 \times 160$	$2304 \times 576 \times 160$	500 m
Neutral	6	$384 \times 384 \times 192$	$1536 \times 384 \times 192$	800 m

All precursor runs start with the surface temperature of $T_s = 277\,\mathrm{K}$ and the vertical temperature gradient $1\,\mathrm{K/m}$. For the simulation of the stable conditions, the surface is cooled down at a constant rate. The cooling rate is chosen in a way to avoid low-level jets in the upper part of the rotor disk, as they are not a focus of this study. The cooling rate is listed in Table 3 along with other parameters specific to each run.

Table 3. Initialization parameters for LES.

Case	U_∞, m/s	U_g, m/s	V_g, m/s	surface cooling rate, K/h
Neutral ($\Delta = 4$ m)	10	10.544	-2.614	-
Neutral ($\Delta = 6$ m)	10	10.539	-2.590	-
Neutral ($\Delta = 6$ m)	15	16.412	-4.130	-
Stable	10	10.584	-3.530	0.15
Stable	15	16.034	-5.769	0.25

Each precursor run takes approximately 5 days (NBL) or 30 hours (SBL) of simulation time to reach the steady-state representation of the flow field. The main run uses the temperature gradient and the velocity profile from the precursor run as starting values.

3.3. Comparison of analytical models with LES

In this study, we fit the analytical wake models using the least-squares to the 10-minute average of normalized wake deficit $\Delta\overline{U}$, which is calculated from PALM LES data. We consider the following data slices:

(i) *cross-section profiles*: the analytical models are fitted to profiles at $x/D = 1, 2, ..., 10$ in the xy-plane at hub height;

(ii) *vertical profiles*: the analytical models are fitted to profiles at $x/D = 1, 2, ..., 10$ in the xz-plane passing through the rotor center;

(iii) *centerline*: the analytical models are fitted to the velocity deficit at the centerline, starting from $x/D = 0, 1$ and 4 for comparison;

(iv) *xy-plane* at hub height: fitting to two-dimensional data is expected to provide higher accuracy and is used to evaluate the profile fits.

A sub-domain of length $20D$ and square cross-section $1.5 \times 1.5D$ centered at the wind rotor center is cut from the LES data for fitting with the Gaussian wake models. A coarse detection of wake shape is performed for the LES data to exclude occasional velocity fluctuations in the free-flow from the fitting process. We consider that a point belongs to the wake if the velocity at the point is lower than free-flow velocity by at least 2.5%, i.e., $\Delta\overline{U} < 0.025$.

4. Results

Based on the LES for NBL conditions at $U_\infty = 10$ m/s and $I_a = 6.6\%$ (Fig. 3a) we define three regions inside a wake: the near-wake ($x/D \leq 4$) where the wake deficit distribution is most complex, the middle wake ($4 < x/D \leq 7$), and the far-wake ($x/D > 7$) where the wake speed is recovering to the free-flow speed.

As seen from Fig. 3, the double peak in the near-wake velocity deficit is prominent for $U_\infty = 10$ m/s. In the case of higher free-flow velocity, $U_\infty = 15$ m/s, the velocity deficit distribution is closer to a single Gaussian throughout the wake. The wake deficit is slightly higher for SBL conditions than for NBL conditions at the same downstream distances. Overall, the stability conditions affect the wake shape less than the free-flow velocity magnitude. A small wake deflection may be observed, due to the free-flow not perfectly aligned with the x-axis after the Coriolis force correction is applied.

The thrust coefficient and the turbulence intensity calculated in each case are provided in Table 4. The thrust coefficient for NBL conditions at $U_\infty = 10$ m/s varies with grid cell size

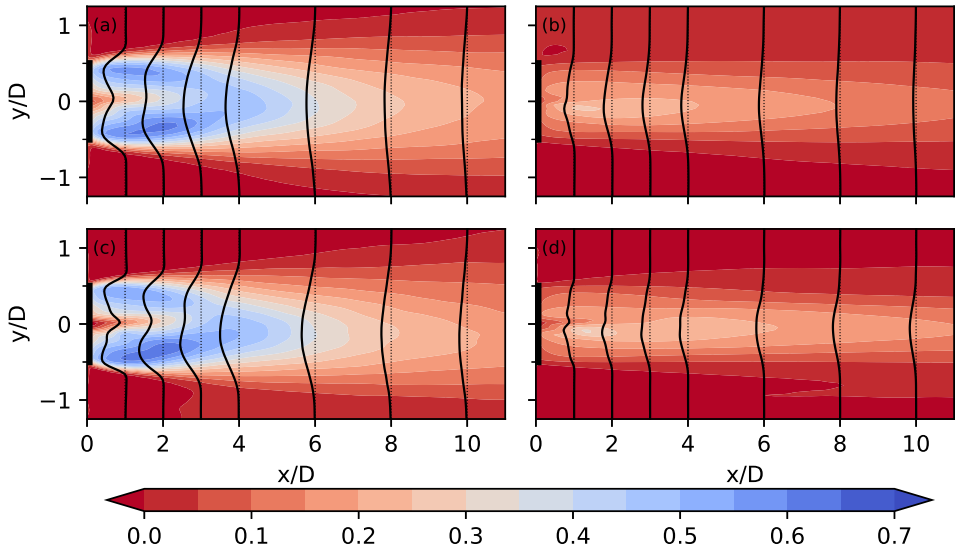

Figure 3. Normalized wake velocity deficit distribution $\Delta\overline{U}$ in the horizontal plane at hub height, LES 10-minute average. Solid lines mark the velocity deficit at selected distances x/D. The scale of the velocity deficit is the same for both plots. (a) NBL $U_\infty = 10\,\mathrm{m/s}$, (b) NBL $U_\infty = 15\,\mathrm{m/s}$, (c) SBL $U_\infty = 10\,\mathrm{m/s}$, (d) SBL $U_\infty = 15\,\mathrm{m/s}$.

due to the different number of grid points in the rotor area. The turbulence intensity is almost unaffected by the grid cell size.

Table 4. Flow parameters at $z_h = 102\,\mathrm{m}$ from the LES data.

Case	U_∞, m/s	C_T	I_a
Neutral ($\Delta = 4\,\mathrm{m}$)	10	0.763	6.6%
Neutral ($\Delta = 6\,\mathrm{m}$)	10	0.713	6.5%
Neutral ($\Delta = 6\,\mathrm{m}$)	15	0.205	5.8%
Stable	10	0.725	7.4%
Stable	15	0.217	4.3%

The models are compared based on how well they predict the wake in the hub height plane after the fitting. The results are provided in Tables 5−8 based on the lowest RMSE for a wake calculated in the hub height plane with the fitted parameters. The best fit out of profiles and centerline fits is marked in bold. In case of equal RMSEs with respect to round up to the fourth digit, the fit to a cross-section profile is given a priority. Fits to the horizontal plane at the hub height (column "HH plane" in tables) are performed only as a reference and are not considered in a comparison between best fits. As can be seen, identifying model parameters on a limited data set may show the results comparable to the fitting to two-dimensional data.

The BPA model returns an incorrect fit to the hub height plane for $U_\infty = 10\,\mathrm{m/s}$, as the model cannot resolve the wake at $x/D \leq 2$ for a high thrust coefficient. This fit is not included in Tables 5−6.

Table 5. Best fits for NBL and $U_\infty = 10\,\mathrm{m/s}$. RMSE is calculated for the wake in the horizontal plane at hub height using the fitted parameters.

Fitted to:	cross-section profile		vertical profile		centerline		HH plane	Default
Model	x/D	RMSE	x/D	RMSE	x/D	RMSE	RMSE	RMSE
BPA	9	0.0316	**9**	**0.0311**	4	0.0325	N/A	0.0428
Jensen-Gaussian	**10**	**0.0784**	10	0.0786	4	0.0785	0.0784	0.0864
Ishihara	2	0.1194	2	0.1192	**4**	**0.0731**	0.0662	0.0951
Double Gaussian	7	0.0814	6	0.0667	**0**	**0.0622**	0.0603	0.0757

Table 6. Best fits for SBL and $U_\infty = 10\,\mathrm{m/s}$. RMSE is calculated for the wake in the horizontal plane at hub height using the fitted parameters.

Fitted to:	cross-section profile		vertical profile		centerline		HH plane	Default
Model	x/D	RMSE	x/D	RMSE	x/D	RMSE	RMSE	RMSE
BPA	**6**	**0.0382**	5	0.0384	4	0.0390	N/A	0.0489
Jensen-Gaussian	**2**	**0.0844**	8	0.0844	4	0.0845	0.0844	0.0940
Ishihara	2	0.1155	2	0.1106	**0**	**0.099**	0.0728	0.0904
Double Gaussian	7	0.0909	6	0.0646	**0**	**0.0644**	0.0627	0.0742

Table 7. Best fits for NBL and $U_\infty = 15\,\mathrm{m/s}$. RMSE is calculated for the wake in the horizontal plane at hub height using the fitted parameters.

Fitted to:	cross-section profile		vertical profile		centerline		HH plane	Default
Model	x/D	RMSE	x/D	RMSE	x/D	RMSE	RMSE	RMSE
BPA	**4**	**0.0181**	4	0.0181	4	0.0181	0.0181	0.0274
Jensen-Gaussian	**10**	**0.0241**	10	0.0241	1	0.0244	0.0241	0.0369
Ishihara	**2**	**0.0154**	10	0.0154	0	0.0171	0.0140	0.0160
Double Gaussian	**2**	**0.0322**	3	0.0538	0	0.0474	0.0320	0.0856

4.1. Fitting to velocity deficit profiles

The velocity deficit distribution in the horizontal plane at hub height provides the essential information on the wake shape. The cross-section profiles in the horizontal plane are usually

Table 8. Best fits for SBL and $U_\infty = 15\,\mathrm{m/s}$. RMSE is calculated for the wake in the horizontal plane at hub height using the fitted parameters.

Fitted to:	cross-section profile		vertical profile		centerline		HH plane	Default
Model	x/D	RMSE	x/D	RMSE	x/D	RMSE	RMSE	RMSE
BPA	**5**	**0.0240**	6	0.0240	1	0.0240	0.0240	0.0309
Jensen-Gaussian	10	0.0242	10	0.0245	**1**	**0.0238**	0.0236	0.0394
Ishihara	9	0.0212	4	0.0216	**1**	**0.0184**	0.0168	0.0194
Double Gaussian	**3**	**0.0401**	1	0.0658	0	0.0608	0.0402	0.0888

close to symmetric and can be fitted with a Gaussian wake model. The velocity profiles in the vertical plane are affected by surface friction. We account for the wind shear by subtracting the averaged free-flow profile $U_\infty(z)$ from the vertical wake profile. We then fit the resulting profile with a Gaussian wake model.

The models split into two groups. The BPA and Jensen-Gaussian models fit the far-wake rather well and are further referred to as far-wake models. For each of these models, the coefficients obtained from fitting to any profile in the far-wake ($x/D > 7$) have a good agreement from case to case and show little differences in the RMSE. For the BPA model, the best fit may also be found in the middle wake ($4 < x/D \leq 7$). The RMSE returned by the BPA model is always lower by half compared to the RMSE of the Jensen-Gaussian model for the same far-wake profile-fit combination.

The other two models (Ishihara and Double Gaussian), further referred to as full-wake models, perform worse during the profile fitting. Both models aim to describe the near-wake's particular features: the high velocity deficit at the centerline (Ishihara) or the double peak in the velocity deficit cross-section profiles (Double Gaussian). Fitted to a single profile, they lack the information on the wake structure and return high RMSE.

Fitting the Ishihara model to a single velocity deficit profile sets the coefficient c and, consequently, the near-wake correction p to zero (Eq. 15). This result suggests that the model regards the whole wake as a far-wake when it receives the information on the velocity deficit of a single cross-section profile. The Ishihara model fitted to a near-wake profile overestimates the wake velocity in the far-wake. When fitted to a far-wake profile, the Ishihara model predicts negative velocity values (i.e. reverse flow) with an RMSE up to 0.5 in the near-wake.

The Double Gaussian model fitted to a near-wake profile captures the double peak well. The double peaks are also present in the far-wake, and the predicted velocity deficit is noticeably high for downstream distances $x/D \geq 7$. Fitting the Double Gaussian model to a far-wake profile improves the full-wake's prediction as reflected by best fits in Tables 5−8. In this case, the double peak is still predicted for the near-wake, although the wake velocity deficit is underestimated compared to LES. The RMSE for the near-wake cross-sections is comparable to the corresponding RMSEs of single Gaussian models (BPA and Jensen-Gaussian).

Full-wake models perform better in the case of strong wind, when the wake shape is smoother, and show an improvement of RMSEs compared to default parameters.

4.2. Centerline fitting

Fitting to the rotor centerline is essentially the fitting of an amplitude function of a Gaussian wake model. The centerline wake velocity deficit predicted by the LES has a convex shape (concave for the wake velocity), which lies in the $0 \leq x/D \leq 4$ range (Fig. 4a). The convexity

is especially emphasized for $U_\infty = 10\,\mathrm{m/s}$. This shape provides a challenge for far-wake models (BPA, Jensen-Gaussian) that assume monotonic recovery of the wake velocity. Besides $x/D \geq 0$ fit (entire centerline), we perform two supplementary fits to the partial centerline. A fit to the centerline segment $x/D \geq 1$ imitates missing data in the very near-wake area (centerline with data loss). A different fit to the segment $x/D \geq 4$ allows comparing the performance of the far-wake models (monotonic segment fit).

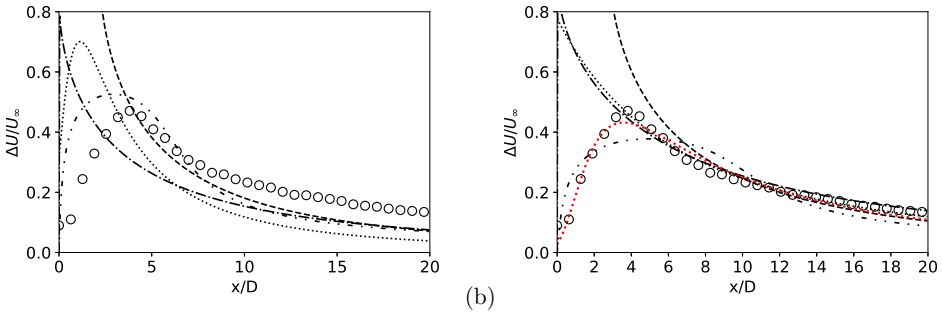

Figure 4. Normalized wake velocity deficit at the rotor centerline for NBL conditions with $U_\infty = 10\,\mathrm{m/s}$. (a) Default parameters, (b) Best overall fits to 10-minute average according to Table 5. ○ – LES data, - - - - BPA, — · — Jensen-Gaussian, ····· Ishihara, ·····(red) Ishihara for $x/D \geq 0$, — · · — Double Gaussian

As seen from Tables 5−8, far-wake models tend to have the best fit for a part of the centerline segment, starting from $x/D \geq 4$. The parameters fitted to the monotonic centerline segment and the RMSE are close to the ones obtained from best fits to profiles.

Full-wake models (Ishihara, Double Gaussian) capture the centerline velocity profile's features more precisely. In general, fitting full-wake models to the entire centerline or the centerline with data loss returns noticeably different parameters, but rather close RMSEs for single profiles and horizontal wake. Fitting full-wake models to the monotonic segment usually increases RMSE for near-wake profiles.

The Ishihara model may show low RMSE when fitted to the monotonic section. In this case, the fitted model predicts an extremely high velocity deficit in the near-wake (Fig. 4) and sets the near-wake coefficient p to zero. At the same time, the full centerline fit returns comparable RMSE for the Ishihara model, but completely different parameters. Therefore, the RMSE criterion alone is not enough to identify the best fit for the Ishihara model.

The Double Gaussian model improves its accuracy when fitted to the centerline at $U_\infty = 10\,\mathrm{m/s}$ and shows RMSE close to the control fit to the horizontal plane at hub height. Nevertheless, the Double Gaussian significantly overestimates the wake width and velocity deficit.

The comparison of cross-section profiles of velocity deficit in the far-wake at $x/D = 8$ is presented in Fig. 5 for NBL conditions with $U_\infty = 10\,\mathrm{m/s}$. The predictions calculated with default parameters underestimate the wake velocity deficit (Fig. 5a). The default BPA model has the closest match in terms of wake shape and deficit value. After the fitting (Fig. 5b), the BPA model follows the LES data most precisely but overestimates the centerline velocity deficit more than the Jensen-Gaussian and Ishihara models.

The parameters of each Gaussian model are identified for a 10-minute average velocity field. We provide best fits to a 1-hour average velocity field for NBL conditions with $U_\infty = 10\,\mathrm{m/s}$ for comparison (Fig. 5c). For a 1-hour average velocity field, the maximum wake deficit at $x/D = 8$

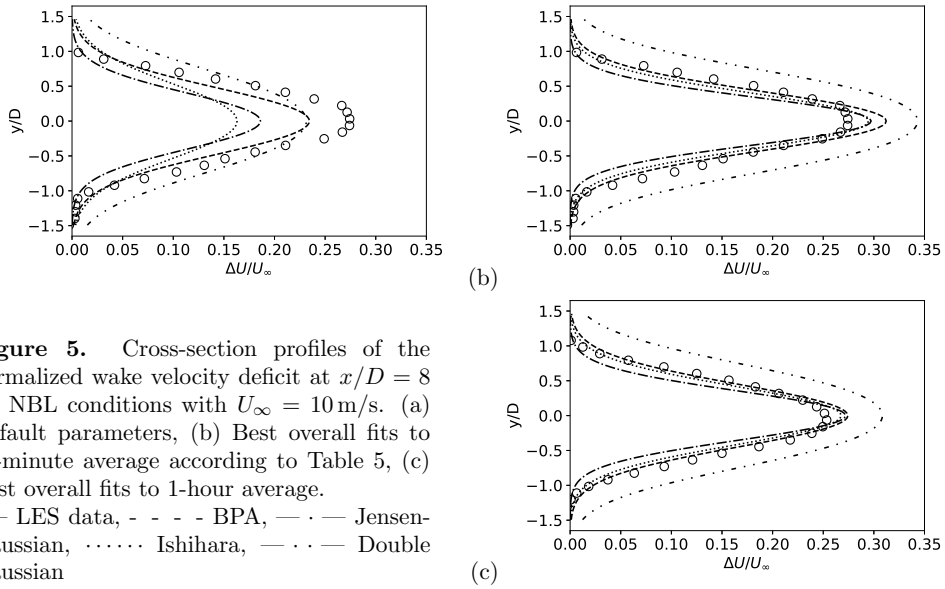

Figure 5. Cross-section profiles of the normalized wake velocity deficit at $x/D = 8$ for NBL conditions with $U_\infty = 10\,\mathrm{m/s}$. (a) Default parameters, (b) Best overall fits to 10-minute average according to Table 5, (c) Best overall fits to 1-hour average.
○ – LES data, - - - - BPA, — · — Jensen-Gaussian, ····· Ishihara, — · · — Double Gaussian

slightly decreases; all models except for the Double Gaussian show good agreement between LES data and each other.

In the case of SBL conditions with $U_\infty = 15\,\mathrm{m/s}$ (Fig. 6), the Double Gaussian model shows the highest discrepancy between the LES wake before and after fitting. Other models, particularly the Ishihara model, have a better agreement.

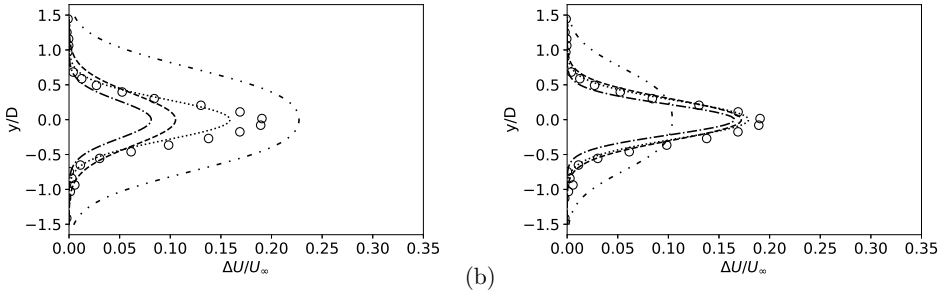

Figure 6. Cross-section profiles of the normalized wake velocity deficit at $x/D = 8$ for SBL conditions with $U_\infty = 15\,\mathrm{m/s}$. (a) Default parameters, (b) Best overall fits according to Table 8.
○ – LES data, - - - - BPA, — · — Jensen-Gaussian, ····· Ishihara, — · · — Double Gaussian

The Double Gaussian model is the only one among the regarded models which fully parametrizes the standard deviation. Therefore, it does not depend on the flow characteristics directly. It may be one of the reasons the model often overestimates the wake width compared to the one predicted by the LES and the other Gaussian wake models. A recent paper on the Double Gaussian model pointed out the momentum conservation issues of the original model and suggested a modification to resolve them [17].

5. Conclusion

Our main objective was a model-based study. We attempted to fit analytical models to the simulated data and observed their behavior. The comparison with observations is beyond the scope of this paper and will be performed in another independent research study.

In this study, we classified Gaussian wake models into two groups. We showed that the far-wake models (BPA, Jensen-Gaussian) did not accurately describe the near-wake, but they performed well in the far-wake. Both far-wake models showed a good agreement with the LES far-wake.

The full-wake models (Ishihara, Double Gaussian) attempt to describe the whole wake. When fitted to a single profile, they often do not predict the structure of the wake correctly. In some cases, fitting a full-wake model to the wind turbine centerline improved the predictions and gave RMSE comparable to the map fit to the horizontal plane at the hub height. Best fits for the BPA and Ishihara models usually followed the shape of the LES wake rather closely; the Jensen-Gaussian model predicted narrower width than the other models, but still got the wake shape right. Nevertheless, there was always a discrepancy between the peak deficit in a profile predicted by the LES and Gaussian models. The Double Gaussian model showed the worst agreement with the LES data compared to other models.

Considering that the far-wake approximation possesses more interest in wind farm applications, the use of far-wake models at the cost of the unresolved or poorly resolved near-wake can be justified.

Acknowledgments

The simulations were performed on resources provided by UNINETT Sigma2 - the National Infrastructure for High Performance Computing and Data Storage in Norway.

References

[1] Jensen N O 1983 *A note on wind generator interaction,* (Roskilde: Risø National Laboratory)
[2] Frandsen S, Barthelmie R J, Pryor S C, Rathmann O, Larsen S, Højstrup J and Thøgersen M 2006 *Wind Energy* **9(1–2)** 39–53
[3] Maronga B et al 2020 *Geosci. Model Dev.* **13(3)** 1335–1372
[4] Niayifar A and Porté-Agel F 2016 *Energies* **9(9)** 1–13
[5] Gao X, Yang H and Lu L 2016 *Appl. Energy* **174** 192–200
[6] Ishihara T and Qian G-W W 2018 *J. Wind Eng. Ind. Aerodyn.* **177** 275–292
[7] Keane A, Aguirre P E O, Ferchland H, Clive P and Gallacher D 2016 *J. Phys.: Conf. Series.* **753(3)** 32-39
[8] Göçmen T, Van Der Laan P, Réthoré P-E, Diaz A P, Larsen G C and Ott S 2016 *Renew. Sustain. Energy Rev.* **60** 752–769
[9] Bastankhah M and Porté-Agel F 2014 *Renew. Energy* **70** 116–123
[10] Dörenkämper M, Witha B, Steinfeld G, Heinemann D and Kühn M 2015 *J. Wind Eng. Ind. Aerodyn.* **144** 146–153
[11] Wu Y-T and Porté-Agel F 2011 *Boundary-Layer Meteorology* **138(3)** 345–366
[12] Porté-Agel F, Wu Y-T, Hao L and Conzemius R J 2011 *J. Wind Eng. Ind. Aerodyn.* **99(4)** 154–168
[13] Vollmer L et al. 2015 *J. Phys.: Conf. Series.* **625(1)** 012001
[14] Vollmer L, Steinfeld G and Kühn M 2017 *Wind Energ. Sci.* **2(2)** 603–614
[15] Jonkman J, Butterfield S, Musial W and Scott G 2009 *Definition of a 5-MW Reference Wind Turbine for Offshore System Development* (USA: National Renewable Energy Laboratory)
[16] Witha B, Steinfeld G, Dörenkämper M and Heinemann D 2014 *J. Phys.: Conf. Series.* **555** 012108
[17] Schreiber J, Balbaa A, and Bottasso C L 2020 *Wind Energ. Sci.* **5(1)** 237–244

Paper II

II

Self-nested large-eddy simulations in PALM model system v21.10 for offshore wind prediction under different atmospheric stability conditions

Krutova, M., Bakhoday-Paskyabi, M., Reuder, J., and Nielsen, F. G.
Geoscientific Model Development, **16(12)**, 3553–3564 (2023)

Geosci. Model Dev., 16, 3553–3564, 2023
https://doi.org/10.5194/gmd-16-3553-2023

Geoscientific Model Development
Open Access
EGU

Self-nested large-eddy simulations in PALM model system v21.10 for offshore wind prediction under different atmospheric stability conditions

Maria Krutova[1,2], **Mostafa Bakhoday-Paskyabi**[1,2], **Joachim Reuder**[1,2], **and Finn Gunnar Nielsen**[1,2]

[1]Geophysical institute, University of Bergen, Allégaten 70, 5007 Bergen, Norway
[2]Bergen Offshore Wind Centre, University of Bergen, Allégaten 55, 5007 Bergen, Norway

Correspondence: Maria Krutova (maria.krutova@uib.no) and Mostafa Bakhoday-Paskyabi (mostafa.bakhoday-paskyabi@uib.no)

Received: 25 October 2022 – Discussion started: 11 November 2022
Revised: 2 May 2023 – Accepted: 29 May 2023 – Published: 28 June 2023

Abstract. Large-eddy simulation (LES) resolves large-scale turbulence directly and parametrizes small-scale turbulence. Resolving micro-scale turbulence, e.g., in wind turbine wakes, requires both a sufficiently small grid spacing and a domain large enough to develop turbulent flow. Refining a grid locally via a nesting interface effectively decreases the required computational time compared to the global grid refinement. However, interpolating the flow between nested grid boundaries introduces another source of uncertainty. Previous studies reviewed nesting effects for a buoyancy-driven flow and observed a secondary circulation in the two-way nested area. Using a nesting interface with a shear-driven flow in LES, therefore, requires additional verification. We use PALM model system 21.10 to simulate a boundary layer in a cascading self-nested domain under neutral, convective, and stable conditions and verify the results based on the wind speed measurements taken at the FINO1 platform in the North Sea.

We show that the feedback between parent and child domains in a two-way nested simulation of a non-neutral boundary layer alters the circulation in the nested area, despite spectral characteristics following the reference measurements. Unlike the pure buoyancy-driven flow, a non-neutral shear-driven flow slows down in a two-way nested area and accelerates after exiting the child domain. We also briefly review the nesting effect on the velocity profiles and turbulence anisotropy.

1 Introduction

Large-eddy simulation (LES) allows performing a detailed process study for areas and situations where we lack appropriate field measurements. For this reason, LES is widely used for high-fidelity simulations of wind flows in wind energy applications. When considering the turbulent flow, the grid resolution should be sufficiently high to resolve the relevant turbulence scales (Wurps et al., 2020). Increased grid resolution comes at the cost of gradually increased computational time. The overall computational time can be reduced by refining a grid locally through the nesting interface. While improving the grid resolution, a nesting interface introduces new uncertainties in the simulation. Such nesting effects are documented for buoyancy-driven flows, with the strongest influence observed for the two-way nesting mode (Moeng et al., 2007; Hellsten et al., 2021). A buoyancy-driven flow develops a secondary circulation and decreased velocity inside the nested area – the effect becomes prominent for the data averaged over several hours. However, buoyancy-driven flows are characterized by near-zero wind speed, while the wind energy research primarily deals with wind speeds of 5–25 $\mathrm{m\,s^{-1}}$. Therefore, shear-driven LES with the nesting interface requires additional verification.

We use the Fortran-based LES code PALM 21.10 (Maronga et al., 2020) to simulate wind flow with a speed of 12.5 $\mathrm{m\,s^{-1}}$ at the reference height of 119 m for three stability conditions: true neutral (NBL), convective (CBL), and stable (SBL) boundary layers. The initial velocity and turbulence intensity profiles are defined to match 1 h averages

of the sonic anemometer time series as processed by Nybø et al. (2019). The domain is simulated for a non-nested grid and nested grids with one-way or two-way nesting modes. The resulting turbulence statistics are then compared with the measurements to evaluate the model's performance.

2 Data

The reference measurements contain wind speed directional components u, v, and w recorded with sonic anemometers during the Offshore Boundary-Layer Experiment at FINO1 (OBLEX-F1) campaign in 2015–2016 in the North Sea. The meteorological mast is installed on the FINO1 platform located in the North Sea at 54°00′53.5″ N, 6°35′15.5″ E, 45 km to the north of the German island of Borkum.

The sonic anemometers were installed at the meteorological mast at 40, 60, and 80 m. The measurements were processed by Nybø et al. (2019) and organized into 1 h time series of 1 Hz frequency. Each processed series corresponds to different pairs of a stability condition and mean wind speed at the reference height of 119 m. This height was chosen as an outlook into future wind turbine development and corresponds to a hub height of the DTU reference 10 MW turbine (Bak et al., 2013). The reference height unifies different stability conditions under the assumption of a similar flow speed. Due to the computational time restrictions, we simulate only those conditions where the horizontal wind speed reaches approximately $\overline{U}_{119} = 12.5\,\mathrm{m\,s^{-1}}$ at the reference height (Table 1).

The wind speed $\overline{U}_{119}$ at the reference height was estimated from the measurement data. Since the measurements are originally available only for three levels, the mean wind speed profile was approximated by Nybø et al. (2020) by fitting the logarithmic law

$$\overline{u}(z) = u_{\mathrm{F1}} \left[\frac{\ln\left(\frac{z}{z_0} - \psi\right)}{\ln\left(\frac{z_{\mathrm{F1}}}{z_0} - \psi\right)} \right], \tag{1}$$

where the wind speed u_{F1} measured at FINO1 is taken for the highest available level $z_{\mathrm{F1}} = 80$ m, and the stability correction function ψ is defined as in Stull (1988):

$$\psi = \begin{cases} 0 & \text{– NBL,} \\ -2\ln\frac{1+x}{2} - \ln\frac{1+x^2}{2} + 2\arctan x - \frac{\pi}{2} & \text{– CBL,} \\ 4.7\zeta & \text{– SBL,} \end{cases} \tag{2}$$

where $x = (1 - 15\zeta)^{1/4}$. The stability parameter ζ is derived from the height above the surface z and Obukhov length L as

$$\zeta = \frac{z}{L}. \tag{3}$$

The roughness length z_0 in Eq. (1) is, therefore, a fitting parameter to be found. The estimation is based on the assumption that the boundary layer extends beyond 119 m so that the logarithmic law can be applied to the mean wind profile. During the simulation, we attempt to match the mean wind profile, including the estimated wind speed at 119 m and turbulence intensity calculated for levels 40, 60, and 80 m.

3 Methodology

3.1 PALM LES model

We perform a free-flow large-eddy simulation (LES) using the Fortran code PALM developed at Leibniz Universität Hannover (Maronga et al., 2020). PALM utilizes a staggered Arakawa C grid: the velocity components are defined at the grid cell edges and are shifted by a half-grid spacing; the scalar variables are defined at the center of a grid cell. The subgrid-scale fluxes are resolved via the Deardorff 1.5-order closure model.

By default, PALM solves prognostic equations for the velocity components u, v, and w and potential temperature θ. If the stability condition is set to true neutral, the temperature is considered constant, and the corresponding equation is not solved. Buoyancy terms are also not considered in a true neutral simulation

A nested simulation in PALM consists of at least one child domain inside a parent domain. Each child domain can simultaneously be a parent domain for another child domain, thus forming a cascading self-nested structure. The top-level parent domain is further referred to as the root domain to make a distinction from inner parent domains. Overall, PALM supports simulation of one root domain and up to 63 child domains.

The nesting algorithm is constructed in a way to optimize computational time for multiple child domains (Hellsten et al., 2021). The nested domains communicate via interpolation which is performed just before the pressure-correction step, so that the time-consuming pressure solver is run only once per the time step. The solution at the nested boundaries of a parent domain – velocity components and scalar quantities, e.g., temperature and humidity – is linearly interpolated to all nested boundaries, except the bottom surface, as boundary conditions. The bottom surface is always located at a zero level as in the root domain and utilizes Dirichlet or Neumann boundary conditions as prescribed in the corresponding child domain input files.

After the interpolation, the prognostic equations are solved for a child domain. In the case of cascading nesting, the procedure is repeated until the solution is found for all nested domains at the current step. In a one-way nesting case, the simulation proceeds to the pressure-correction step, so the solution in parent domains remains unaffected by the solution in child domains. In a two-way nesting case, PALM uses an anterpolation scheme – a term suggested by Sullivan et al. (1988) and first described by Clark and Farley (1984).

Table 1. Aggregated statistics of 1 h sonic anemometer time series.

Stability	$\overline{U}_{119}$, $m\,s^{-1}$	TI_{80}, %	L, m	ζ	ψ	1 h period start, UTC
NBL	12.41	6.6	2753	0.043	0	18 April 2016 04:30
CBL	12.58	6.1	−451	−0.263	0.528	22 February 2016 19:00
SBL	12.14	3.2	158	0.753	−3.540	2 June 2016 16:30

The technical details behind the implementation in PALM are explained in Hellsten et al. (2021). Each child domain anterpolates its solution via first-order integration to the respective parent domain before the pressure-correction step. Therefore, the two-way nested solution remains similar in the nested area, while the one-way nested solution may eventually diverge for parent and child domains.

3.2 Precursor and main LES run parameters

One of the ways PALM can simulate a turbulent flow is a precursor scheme, which does not require complex dynamic input data and effectively reduces the domain size required for turbulence development (Witha et al., 2014). First, a small precursor domain is simulated with cyclic boundaries until the flow reaches a steady state. The resulting mean wind speed and temperature profiles are then copied over the larger main domain to set up an initial non-cyclic flow with a developed turbulence. Provided that the main run is simulated with the same forcing as the precursor, the mean profiles in the main run remain stationary.

The size of the precursor domain is usually smaller than for the main run, and the y-shift procedure is performed at left/right cyclic boundaries to avoid non-physical regularity of the flow (Munters et al., 2016). The y-shift procedure is also applied in the main run for an additional disruption of regularity. Using the precursor scheme also ensures that an idealized input flow remains the same within a stability case regarded.

The grid characteristics of the root and innermost child domain in the PALM simulation were selected to closely match the SOWFA simulation in Nybø et al. (2020). The ratio between the parent and child domains' grid spacing, thus, would reach 8 (from 10 to 1.25 m for NBL and CBL cases) or 4 (from 5 to 1.25 m for SBL case). As shown by Hellsten et al. (2021), the discrepancy with a fine-grid simulation in PALM increases if the grid spacing ratio is 4 or higher. Therefore, we add intermediate child domains and reduce the grid spacing by a factor of 2 until the desired refinement is reached. Hence, NBL and CBL simulations contain three child domains, while the SBL simulation has two (Tables 2 and 3, Fig. 1).

We perform one-way and two-way nested simulations. To evaluate the nesting effect, we also simulate domains without nested grids using the same precursor flow. Due to high computational time and memory requirements, we only simulate non-nested domains for the grid spacing of $\Delta_x = 10$ and 5 m.

Table 2. Grid parameters for NBL and CBL nested domains (Fig. 1a).

					Bottom-left corner	
Domain	N_x	N_y	N_z	Δ_x, m	x, m	y, m
Precursor	256	256	160	10	–	–
Precursor	512	512	256	5	–	–
Root	1024	512	160	10	–	–
Child #1	384	192	128	5	4480	2080
Child #2	640	256	192	2.5	4640	2240
Child #3	1024	256	256	1.25	4800	2400

Table 3. Grid parameters for SBL nested domains (Fig. 1b).

					Bottom-left corner	
Domain	N_x	N_y	N_z	Δ_x, m	x, m	y, m
Precursor	512	288	160	5	–	–
Root	1920	384	160	5	–	–
Child #1	640	256	192	2.5	3840	640
Child #2	1024	256	256	1.25	4000	800

The precursor profiles undergo development during a simulation and thus may deviate from the initial profiles. The precursor's input parameters are then selected so that the resulting steady-state profiles of mean wind speed and turbulence intensity follow the values estimated from the measurements, particularly the wind speed at the reference height. The Coriolis force is switched off; hence the required wind speed and turbulence intensity profiles in the precursor run are enforced by a combination of the parameters: the initial mean wind $\overline{U}_0$, the pressure gradient forcing $\mathrm{d}p/\mathrm{d}x$, and the roughness length z_0. The NBL case is run as the true neutral flow with no heat flux. The CBL case is defined via the positive heat flux $\overline{w'\theta'}$ in addition to the parameters mentioned above. The SBL case uses surface cooling over time $\mathrm{d}T_\mathrm{s}/\mathrm{d}t$ instead of the heat flux (Wurps et al., 2020). NBL and SBL cases start with zero temperature gradient; the CBL case has an initial temperature gradient of $1\,\mathrm{K}\,(100\,\mathrm{m})^{-1}$. The surface temperature T_s is varied to match the conditions ob-

Table 4. Input parameters of the precursor runs.

	$\overline{U}_0$, $m\,s^{-1}$	dp/dx, $Pa\,m^{-1}$	z_0, m	T_s, K	$\overline{w'\theta'}$, $K\,m\,s^{-1}$	dT_s/dt, $K\,s^{-1}$	Run time, s
NBL (coarse)	13.8	-2×10^{-4}	1.2×10^{-3}	300	0	–	144 000
NBL (fine)	14.0	-2×10^{-4}	1.6×10^{-3}	300	0	–	172 800
CBL	11.5	-1×10^{-4}	5×10^{-4}	281	0.015	–	525 600
SBL	13.0	-5×10^{-4}	8×10^{-4}	300	–	−0.2	259 200

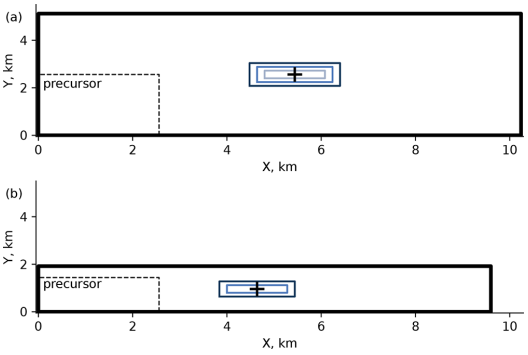

Figure 1. Nested domains schematic. **(a)** NBL and CBL domains and **(b)** SBL domains.

Table 5. Steady state of the precursor runs – turbulent inflow for the main run.

	$\overline{U}_{119}$, $m\,s^{-1}$	TI_80, %	T_s, K	L, m	Capping inversion, $K\,(100\,m)^{-1}$
NBL (coarse)	12.3	7.5	300	10^6	0
NBL (fine)	12.6	7.7	300	10^6	0
CBL	12.1	6.2	295	−333	7.4
SBL	12.8	4.6	291	529	9

served during the reference meteorological measurements at FINO1. The precursor domain characteristics and input parameters are listed in Tables 2–4.

During the precursor simulation, the initial profiles are altered due to the influence of pressure forcing and heat fluxes. The resulting precursor profiles are provided in Table 5; the same profiles are used to initialize the main run.

We run main simulations for 3 h with a dynamic time step selected by the model. The simulation is then continued for another hour with the fixed time step of $\Delta t = 0.05$ s to obtain a high-frequency output. Then, we probe time series of each wind speed component at the center of the innermost child domain and the corresponding points of the parent domain (Fig. 1). The high-frequency time series are further used to compare turbulence statistics with the measurements. Spatial averages (cross-sectional flows, profiles) are calculated for 10 min periods.

3.3 Turbulence characteristics

We evaluate the model performance based on turbulence characteristics: power spectrum, coherence, co-coherence, and phase. The coherence represents a correlation between time series $a(t)$ and $b(t)$ at two points separated by a certain distance δ and is calculated as follows

$$\mathrm{Coh}_{ab} = \frac{S_{ab}}{\sqrt{S_{aa}S_{bb}}}, \tag{4}$$

where S_{aa} and S_{bb} are the spectral densities of $a(t)$ and $b(t)$, while S_{ab} is the cross-spectrum of the same series.

The co-coherence represents the real part of the coherence

$$\mathrm{Co}_{ab} = Re\ \mathrm{Coh}_{ab} = Re\ \frac{S_{ab}}{\sqrt{S_{aa}S_{bb}}}. \tag{5}$$

The phase ϕ_{ab} shows the level of synchronicity between time series $a(t)$ and $b(t)$

$$\phi_{ab} = \arctan\frac{Re\ \mathrm{Coh}_{ab}}{Im\ \mathrm{Coh}_{ab}}. \tag{6}$$

Since the measurement time series are available only for three levels, 40, 60, and 80 m, the spectra are calculated and compared at $h = 80$ m for the total horizontal $U = \sqrt{u^2 + v^2}$ and vertical w wind speed. The co-coherence is calculated for two vertical separations of $\delta = 20$ m (between levels 60 and 80 m) and $\delta = 40$ m (between levels 40 and 80 m). The sampling frequency for the LES time series matches the output frequency $f_s^{\mathrm{LES}} = 1/0.05\,\mathrm{s} = 20$ Hz, and the segment length is chosen as 60 s. The sampling frequency for the measurement time series is lower, $f_s^{\mathrm{mast}} = 1/0.1\,\mathrm{s} = 10$ Hz, although the segment length is left the same.

3.4 Flow characteristics for load analysis

We also review flow characteristics relevant to the turbine performance analysis: power law coefficient and turbulence anisotropy.

The power law is commonly applied to assess wind resources at the hub height from near-surface wind speed measurements.

$$U(z) = \overline{U}_{10}\left(\frac{z}{10}\right)^{\alpha}, \tag{7}$$

where $\overline{U}_{10}$ is the wind speed at $z = 10$ m and α is the power law exponent. The power law exponent is sensitive to atmospheric conditions and is usually approximated with a constant; e.g., $\alpha = 1/7$ is applicable to neutral onshore sites but not other stabilities (Touma, 1977). Often, the approximations do not reflect seasonal and diurnal variations in mean wind profiles (Bratton and Womeldorf, 2011; Jung and Schindler, 2021). Hence, simulating a long time series with the LES gives a possibility to study wind profiles in detail.

The anisotropic turbulence naturally develops in a simulation with an anisotropic grid resolution (Haering et al., 2019) but may also occur in isotropic grids, such as those used in this study. The anisotropic turbulence affects wind turbine loads, particularly fatigue loads. Therefore, it is important to evaluate its strength in the simulation (Dimitrov et al., 2017). We estimate turbulence anisotropy by comparing spectra of velocity components for the normalized frequency $f_n = fz/U_z$, where $z = 80$ m and U_z is the horizontal velocity at this level. We compute ratios S_{vv}/S_{uu} and S_{ww}/S_{uu} for all regarded cases at $f_n \approx 1$. The closer both ratios are to the theoretical value of $4/3 = 1.333$, the more isotropic the simulated turbulence is (Weiler and Burling, 1967; Smedman et al., 2003).

4 Results

4.1 Nesting effects

All LESs are run at 1024 cores for each case with a time step of $\Delta t = 0.05$ s; the required simulation times for each scenario are summarized in Table 6. Since the domains vary in size and number of grid points, we compare not the total CPU time but the CPU time per second of the simulated time. The non-nested coarse domain ($\Delta_x = 10$ m) is not computationally demanding, regardless of the stability case. However, the required CPU time gradually increases if the grid spacing is reduced globally for the whole domain. As could be seen for the NBL case, the CPU time per second of the simulated time increases from 5.1 s for $\Delta_x = 10$ m to 31.7 s for $\Delta_x = 5$ m, respectively. Refining the grid locally by adding child domains increases the CPU time compared to the coarse reference non-nested grid ($\Delta_x = 10$ m). Still, the nested simulation finishes faster than the globally refined non-nested simulation ($\Delta_x = 5$ m), while allowing better a local grid refinement up to $\Delta_x = 1.25$ m.

Both NBL and CBL simulations have the same domain structure and grid spacing (Table 2). However, CBL simulations require more CPU time compared to the respective NBL (true neutral) simulations due to solving the temperature equation. SBL simulations use CPU time comparable to NBL simulations due to having one child domain less and a smaller root domain size – and thus a lower overall number of the grid points (Table 3).

Table 6. CPU time in seconds used per second of simulated time. All simulations run at 1024 cores with a time step of $\Delta t = 0.05$ s.

Stability	Δ_x, m	Non-nested	One-way	Two-way
NBL	10	5.1	18.4	20.9
NBL	5	31.7	–	–
CBL	10	7.9	28.8	30.8
SBL	5	4.5	25.1	28.7

Two-way nested simulations require additional ~ 2–3 s of the CPU time per simulated time step to anterpolate the child domain solution back to the parent domain. This results in about 10 % increase in the CPU time compared to one-way nesting.

It should be noted that, unless obtaining high-frequency time series is the main goal of a simulation, the time step can be gradually increased for non-nested runs in order to speed up the computation. The computational time will, nevertheless, increase in a similar proportion with the global grid refinement. The time step in nested runs is still limited by the lowest grid spacing in child domains. For example, the dynamic step in the regarded configuration does not exceed 0.075 s to satisfy Courant–Friedrichs–Lewy condition.

Depending on the simulation conditions, LES produces different results in the nested area. If the true neutral case is defined in PALM explicitly via setting a corresponding flag, the one-way and the two-way nested simulations behave similarly with respect to grid spacing and feedback between domains (Fig. 2). Switching on the true neutral flag means that the temperature equation and buoyancy terms are not considered in the calculations. As long as those terms are introduced for non-neutral simulations, the two-way nested simulation results in a decreased flow speed in child domains.

Since the child domains anterpolate their solution back to the parent domain, the area of reduced flow speed spreads to the root domain. While the effect is less prominent for the instantaneous fields, it becomes apparent in the 10 min averaged flow (Fig. 3). The induction of downward vertical wind in two-way nested simulations was already described by Hellsten et al. (2021) for the 5 h averaged buoyancy-driven flow in PALM. Hellsten et al. (2021) argued that the effect of the secondary circulation described by Moeng et al. (2007) was caused solely by the insufficient domain size and explained it with the different grid spacing and subsequent divergence of the vertical heat flux in the parent and child domains. The researchers hypothesized that the secondary circulation was an inevitable side effect of the two-way nesting solution due to the better resolution of the turbulence mixing in child domains. In the case of the shear-driven flow, we observe that the slowing effect is more prominent and develops faster. The effect emerges in the beginning of the simulation within 20 min – an approximate time required for the precursor flow to pass the main run domain. In addition, some

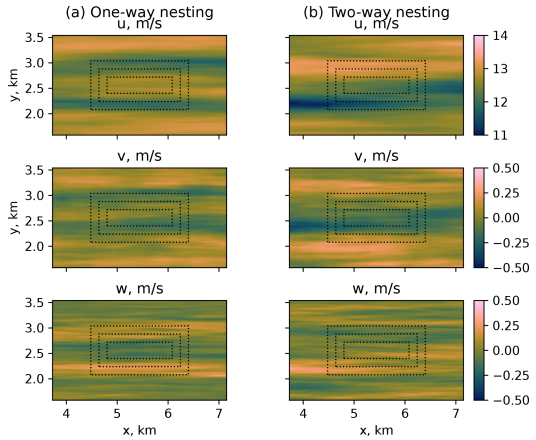

Figure 2. NBL, flow at the reference height of 119 m for different wind speed components: **(a)** one-way nesting and **(b)** two-way nesting.

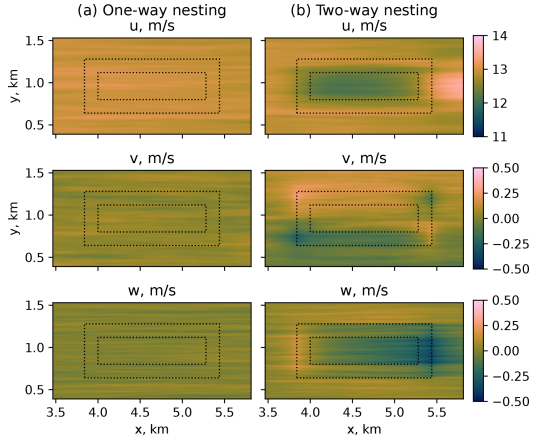

Figure 3. SBL, flow at the reference height of 119 m for different wind speed components: **(a)** one-way nesting and **(b)** two-way nesting.

of the quantities of a shear-driven flow, mainly the vertical velocity w, are not uniformly distributed inside the child domains (Fig. 4).

4.2 Subgrid scales

LES resolves scales larger than the grid spacing directly but approximates smaller scales. In a well-resolved flow, the unresolved (subgrid) scales should not exceed the resolved ones. This relation holds for all simulations performed, implying that the grid spacing of $\Delta = 10$ m is already small

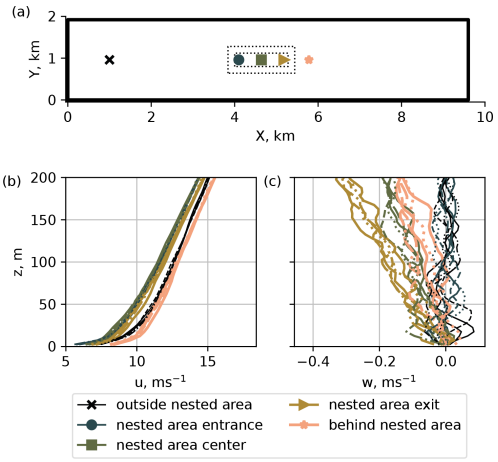

Figure 4. The 10 min average profiles, SBL two-way nested case. **(a)** Sampling points; **(b)** the mean flow is slowed down in the nested area; **(c)** the vertical flow near the entrance of the nested area remains weak but becomes stronger as the flow passes through the nested area.

enough for the given flow (Fig. 5). The grid refinement does not strongly affect momentum fluxes, except for the CBL case (Fig. 5b), where turbulent eddies are generally larger than in the NBL and SBL cases. The effect from the nesting mode is also the most pronounced in CBL simulations (Fig. 5b). The resolved $\overline{wu}$ and $\overline{wv}$ fluxes remain stationary in the one-way nesting mode but decrease over time in the two-way nesting mode and eventually merge.

The subgrid-scale fluxes consistently remain near zero for all levels except near-surface cells, where the turbulence intensity is expected to be high due to the surface influence (Fig. 6). Consequently, the near-surface subgrid-scale fluxes are comparable to resolved-scale fluxes. However, the subgrid-scale fluxes at lower levels tend to zero faster as the grid spacing is refined. Unlike the one-way nesting mode, the resolved fluxes in the two-way nesting mode show a non-monotonic behavior near the surface in the intermediate child domains. The effect is observed in all two-way simulations, including true neutral conditions. Therefore, it cannot be solely caused by the flow difference in the nested and non-nested areas, despite the flux profiles being time and spatial averages. The occurring non-monotonic behavior can be rather attributed to the way PALM performs anterpolation from a child to the parent domain.

4.3 Turbulence characteristics

Since the flow is driven by the pressure gradient instead of the Coriolis force, the flow is aligned with the x axis, and the wind direction remains nearly constant. The fluctuations

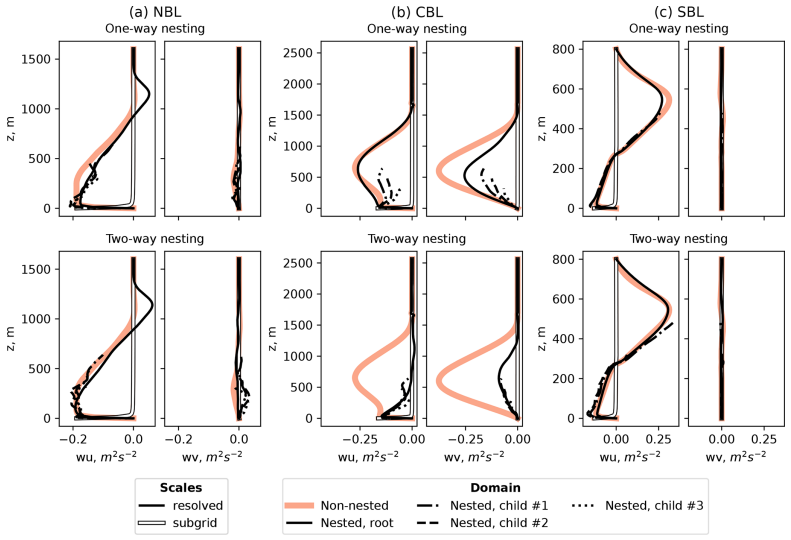

Figure 5. Comparison of resolved and subgrid-scale momentum fluxes for different stability simulations and nesting modes.

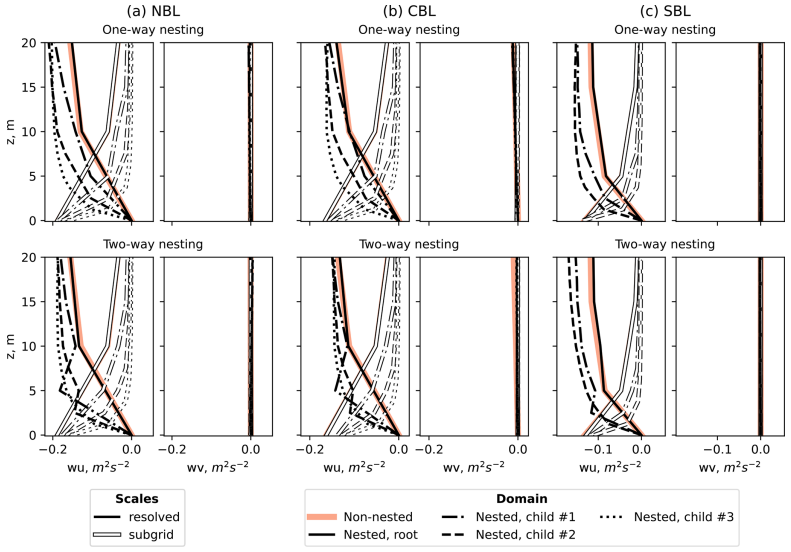

Figure 6. Comparison of near-surface resolved and subgrid-scale momentum fluxes for different stability simulations and nesting modes.

of the lateral component v are stronger for the measurement time series. Therefore, we compare turbulence statistics of the horizontal wind speed u from the LES results to the total horizontal flow in the measurements $U = \sqrt{u^2 + v^2}$ and omit the lateral component v for the LES data.

In one-way nested simulations, the parent domain does not receive feedback from the child domain. Consequently, the spectral characteristics of non-nested domains with the grid spacing of $\Delta_x = 10\,\mathrm{m}$ (NBL and CBL) and 5 m (SBL) match the characteristics of the corresponding domain in a one-way nesting simulation (Figs. 7 and 8). The individual

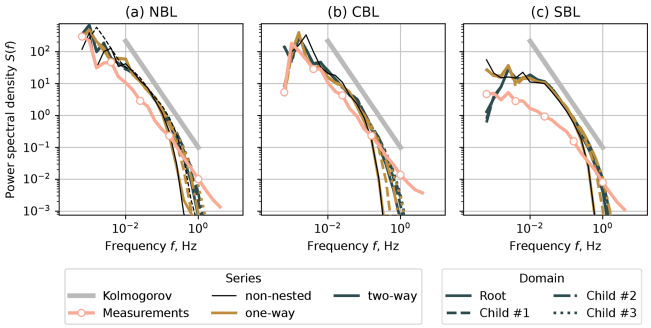

Figure 7. Spectra for the horizontal velocity u at the height $z = 80$ m. **(a)** NBL case, **(b)** CBL case, and **(c)** SBL case.

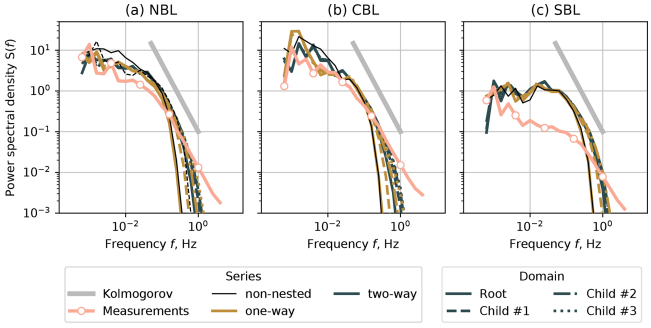

Figure 8. Spectra for the vertical velocity w at the height $z = 80$ m. **(a)** NBL case, **(b)** CBL case, and **(c)** SBL case.

spectra of the nested domains lie apart from each other but show improvement as the grid spacing is reduced. The inertial subrange resolved by LES widens as the grid becomes more refined; however, it is not fully resolved despite the grid spacing being reduced to $\Delta_x = 1.25$ m.

The two-way nesting mode ensures feedback between the nested domains. Therefore, the root and child domain spectra lie closer to each other and to the one-way spectra of the most refined child domain ($\Delta_x = 1.25$ m). Despite the exchange between domains in the two-way nested case, the spectral characteristics do not coincide perfectly. The inertial subrange being shorter for $\Delta_x = 10$ m than for the refined domains implies that the grid resolution is the limiting factor, and the solution for the root domain cannot be improved further even in the two-way nesting case.

Despite the NBL case being simulated as a true neutral condition, it showed good agreement with the measurements on par with the CBL case. The result suggests that it is possible to omit a weak heat flux in neutral cases to save computational time and avoid secondary circulation in the two-way nesting mode.

The SBL simulations largely overestimate the energy contained in low-frequency eddies. The inertial subrange of the corresponding measurement time series also starts at higher frequencies, unlike in the NBL and CBL cases. The LES does not fully resolve high frequencies despite gradually reduced grid spacing. Hence the overall agreement for the SBL case is worse than for NBL and CBL. When comparing available measurement profiles for the specific period of SBL time series, we did not observe anomalies or irregularities, such as reported by Kettle (2014), which could be studied as a possible cause of a discrepancy. The existing studies on SBL simulations with PALM (Beare et al., 2006; Wurps et al., 2020) do not compare simulated spectra against measurements but evaluate other aspects, such as fluxes and grid resolution influence. Hence, simulating SBL in PALM may require additional studies focusing on turbulence characteristics.

In order to match the SBL spectra shape, we performed a short SBL simulation with lower forcing, which led to a decreased turbulence intensity but stronger mean profile shear. The results are provided in Appendix.

The coherence, co-coherence, and phase are plotted against the reduced frequency:

$$f_\mathrm{r} = \frac{f\delta}{\overline{u}}, \tag{8}$$

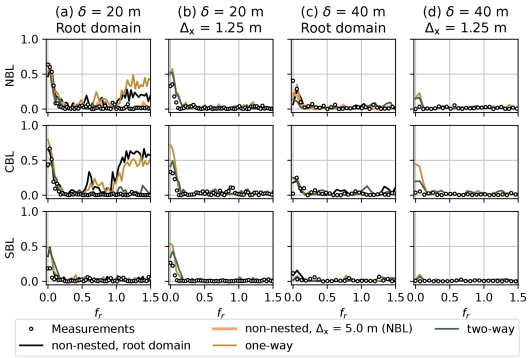

Figure 9. Coherence for the horizontal velocity u and different stability cases. **(a)** Root domain ($\Delta_x = 10$ m for NBL and CBL, $\Delta_x = 5$ m for SBL), vertical separation $\delta = 20$ m. **(b)** Innermost child domain ($\Delta_x = 1.25$ m, all cases), vertical separation $\delta = 20$ m. **(c)** Root domain ($\Delta_x = 10$ m for NBL and CBL, $\Delta_x = 5$ m for SBL), vertical separation $\delta = 40$ m. **(d)** Innermost child domain ($\Delta_x = 1.25$ m, all cases), vertical separation $\delta = 40$ m.

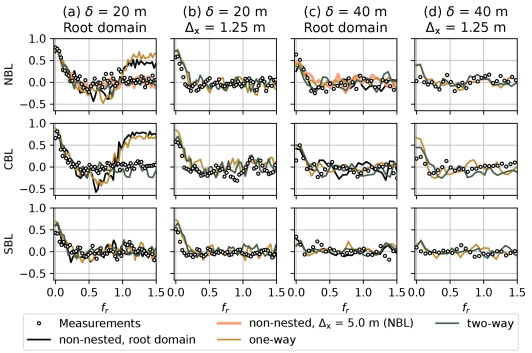

Figure 10. Co-coherence for the horizontal velocity u and different stability cases. **(a)** Root domain ($\Delta_x = 10$ m for NBL and CBL, $\Delta_x = 5$ m for SBL), vertical separation $\delta = 20$ m. **(b)** Innermost child domain ($\Delta_x = 1.25$ m, all cases), vertical separation $\delta = 20$ m. **(c)** Root domain ($\Delta_x = 10$ m for NBL and CBL, $\Delta_x = 5$ m for SBL), vertical separation $\delta = 40$ m. **(d)** Innermost child domain ($\Delta_x = 1.25$ m, all cases), vertical separation $\delta = 40$ m.

where f is the original frequency, δ is the vertical separation distance, and $\overline{u}$ is the mean wind speed of the two regarded levels, 60 and 80 m for $\delta = 20$ m or 40 and 80 m for $\delta = 40$ m.

The coherence and co-coherence calculated for NBL and CBL coarse domains ($\Delta_x = 10$ m) and $\delta = 20$ m show strong deviation from the measurements for the one-way and non-nested simulations at $f_r > 1$ (Figs. 9a and 10a). The tendency to the coherence/co-coherence value of 0.5 suggests that the time series at points separated by $\delta = 20$ m remain partially correlated in the coarse grid, which is not the case for the corresponding measurements. While the most refined child domain ($\Delta_x = 1.25$ m) shows a good match between the LES and measurement series (Figs. 9b and 10b), the agreement already improves for $\Delta_x = 5$ m, and the correlation falls to zero for $f_r > 0.5$. The SBL case shows better agreement for the root domain because of the lower initial grid spacing $\Delta_x = 5$ m. Nevertheless, the coherence is noticeably overestimated for low f_r compared to the measurements (Fig. 9a, b). The time series are generally uncorrelated for the vertical separation of $\delta = 40$ m both for the LESs and measurements (Figs. 9c, d and 10c, d). However, the NBL case does not capture the high coherence value at $f_r = 0$ observed in the measurements.

The phase plots are in line with the coherence. The time series are in phase for $f_r < 0.1$, where the coherence is above zero. The effect is strong for the low vertical separation of $\delta = 20$ m (Fig. 11a, b) and is in good agreement with the measurements. The phase becomes more chaotic as the vertical separation distance increases to $\delta = 40$ m (Fig. 11c, d), while the time series become less correlated (Figs. 9c, d and 10c, d).

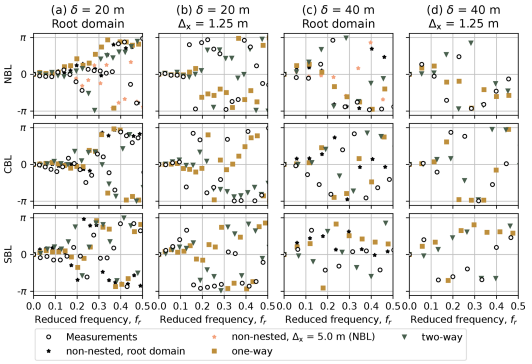

Figure 11. Phase plot for the horizontal velocity u and different stability cases and domains. **(a)** Root domain ($\Delta_x = 10$ m for NBL and CBL, $\Delta_x = 5$ m for SBL), vertical separation $\delta = 20$ m. **(b)** Innermost child domain ($\Delta_x = 1.25$ m, all cases), vertical separation $\delta = 20$ m. **(c)** Root domain ($\Delta_x = 10$ m for NBL and CBL, $\Delta_x = 5$ m for SBL), vertical separation $\delta = 40$ m. **(d)** Innermost child domain ($\Delta_x = 1.25$ m, all cases), vertical separation $\delta = 40$ m.

4.4 Other flow characteristics

4.4.1 Power law

In general, the power law coefficient follows the known trend, also observed in the measurement profile fits (Table 7): high value in the stable layer and low value in the convective layer (Touma, 1977). The discrepancy between exact values of α in measurement and simulated fits is primarily caused by the different way of obtaining U_{10}. For sonic data, U_{10} is

Table 7. Estimated power law coefficient.

Nesting	Δ_x, m	Power law coefficient α		
		NBL	CBL	SBL
non-nested	10	0.111	0.093	–
non-nested	5	0.099	–	0.154
one-way	10	0.112	0.093	–
one-way	5	0.103	0.067	0.156
one-way	2.5	0.092	0.077	0.145
one-way	1.25	0.087	0.073	0.145
two-way	10	0.109	0.089	–
two-way	5	0.095	0.083	0.158
two-way	2.5	0.088	0.080	0.164
two-way	1.25	0.085	0.077	0.172
Measurements		0.061	0.023	0.237

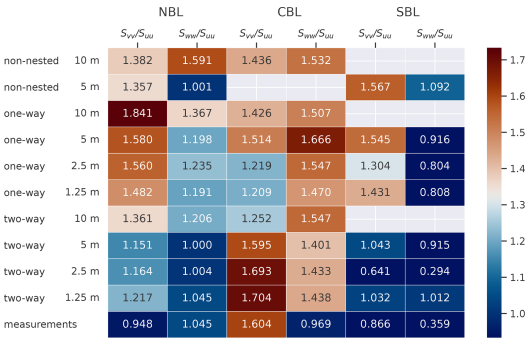

Figure 12. Comparison of anisotropy across the regarded stability and nesting cases. The color map is centered at the value $4/3 = 1.333$.

calculated from the previously estimated profile Eq. (1). The LES returns the full mean profile on the pre-defined grid, so U_{10} can be interpolated to the level of $z = 10$ m. U_{10} derived from LES data consistently deviates from measurements U_{10} by 10 %–20 %, thus affecting the estimation of the power law exponent.

The estimated power law coefficient α shows little variation for the NBL and CBL domains of the same refinement but implies high sensitivity of the SBL profiles. Considering higher shear in the SBL profiles, the grid refinement may affect the estimation of U_{10} more strongly than lower shear NBL and CBL profiles.

4.4.2 Turbulence anisotropy

The anisotropy estimation captures only general trends seen in the measurements with the nesting modes being radically different between each other (Fig. 12). Since the inertial subrange resolved in a one-way nested root domain is slightly shorter than of a two-way root domain (Figs. 7–8), $f_n \approx 1$ may fall outside of the resolved subrange and provide a less precise estimation. The two-way nested cases approach closer to the anisotropy seen in the measurement, although the anisotropy strength may not match the value seen in the measurement data. The divergence is particularly strong for the SBL simulation, primarily caused by the differences in power density spectra discussed in Sect. 4.3.

5 Conclusions

We performed nested LES of three stability cases for the horizontal mean wind speed of 12–13 m s^{-1} at the reference height of 119 m. The simulations were verified by comparing turbulence characteristics to the corresponding measurement time series. The comparison showed that the grid spacing of $\Delta_x = 10$ m was insufficient for NBL and CBL simulations; the spectral and coherence characteristics had improved their agreement with the measurements after the spacing was reduced to $\Delta_x = 5$ m via nesting or a refined non-nested domain simulation. The inertial subrange was not fully resolved despite further refinement and remained narrower than for the measurement time series even at $\Delta_x = 1.25$ m.

We confirmed that the nesting mode does not affect the true neutral simulation, unlike when the temperature equation is solved along with other prognostic equations for CBL and SBL conditions. In the case of CBL or SBL, the flow inside the child domain differed for the one-way and two-way nesting. The two-way nested simulation produced a secondary circulation resulting in a decreased velocity and increased turbulence intensity in the child domains. Due to a strong horizontal shear, the irregularities in lateral and vertical velocity profiles were spread non-uniformly; e.g., the downward flow was stronger at the exit of the nested domain. The horizontal flow accelerated after leaving the nested area so that the mass conservation law was not violated eventually. Unlike the existing research on buoyancy-driven flows, the two-way nesting effects in a shear-driven flow emerged in the first hour of the LES and did not dissipate as the simulation proceeded for 3 more hours.

In theory, the two-way nesting is a good option to refine the grid in the area of interest of a non-homogeneous flow, e.g., wind turbine wakes, as the feedback between parent and child domain allows accounting for the irregularities after the flow exits the nested area. However, the fast development of a secondary circulation in the shear-driven flow limits the two-way nesting application strictly to the true neutral condition. The one-way nested simulation did not add anomalies to the flow; each child domain only refined the grid spacing and resolved small turbulence scales. We, therefore, recommend using the one-way nesting mode for the wind turbine wake simulation. In the case when the two-way nesting mode is preferable, only a true neutral setup does not produce secondary circulation.

Appendix A: SBL simulation with reduced forcing

We performed a test simulation of an SBL precursor for the same wind speed but weaker pressure gradient ($-0.0001\,\mathrm{Pa\,m^{-1}}$ instead of $-0.0005\,\mathrm{Pa\,m^{-1}}$) and slightly stronger surface cooling ($-0.3\,\mathrm{K\,s^{-1}}$ instead of $-0.2\,\mathrm{K\,s^{-1}}$). As a result of the decreased forcing, the developed profiles deviated from the reference measurements and showed stronger shear but lower turbulence intensity (Fig. A1). Due to the computational time constraints we simulate only a non-nested main run for a comparison of spectral characteristics. We observe a better agreement with the measurements spectra (Fig. A2), especially in the w component, whose spectrum does not follow a $-5/3$ theoretical slope. Therefore, we are able to match only one of two – either SBL profiles or SBL spectra – and observe a strong discrepancy in another.

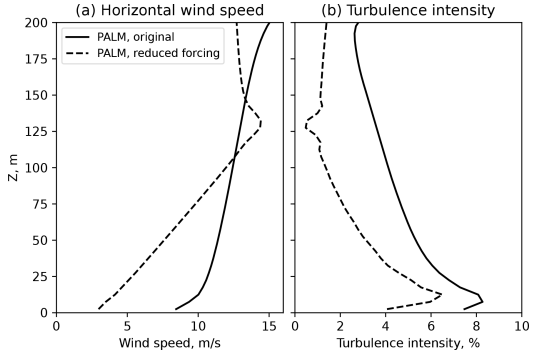

Figure A1. Precursor run profiles with original and reduced pressure forcing. **(a)** Horizontal flow mean profile and **(b)** turbulence intensity profile.

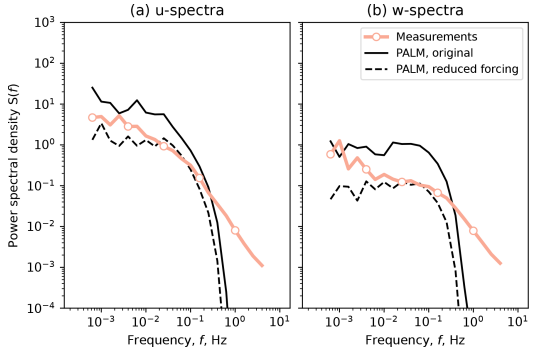

Figure A2. Main run spectra with original and reduced pressure forcing. **(a)** Horizontal velocity spectrum and **(b)** vertical velocity spectrum.

Code and data availability. The PALM model system is freely available at https://gitlab.palm-model.org/releases/palm_model_system/-/releases/v21.10 (Maronga et al., 2020) and distributed under the GNU General Public License v3 (http://www.gnu.org/copyleft/gpl.html, last access: 12 October 2022). The LESs in this article were performed using PALM model system v21.10. The corresponding version is provided at https://doi.org/10.5281/zenodo.7886678 (Krutova, 2022) together with input and output files, as well as post-processing scripts needed to reproduce the figures. The processed high-frequency sonic anemometer data are available upon request after permission from DEWI (Deutsches Windenergie Institut) is granted.

Author contributions. MK performed the LES simulations and analysis in accordance with the plan developed by MPB; JR and FGN provided valuable discussions explaining the discrepancies with the measurement data.

Competing interests. The contact author has declared that none of the authors has any competing interests.

Disclaimer. Publisher's note: Copernicus Publications remains neutral with regard to jurisdictional claims in published maps and institutional affiliations.

Acknowledgements. The authors would like to thank DEWI (Deutsches Windenergie Institut) for providing the FINO1 high-resolution sonic anemometer data and Astrid Nybø from the University of Bergen for the additional information and guidance.

The large-eddy simulations for this study have been performed by using the high-performance-computer facilities of the Norwegian e-infrastructure Uninett Sigma2 (project number NS9696K).

Review statement. This paper was edited by Sylwester Arabas and reviewed by two anonymous referees.

References

Bak, C., Zahle, F., Bitsche, R., Kim, T., Yde, A., Henriksen, L., Hansen, M., Blasques, J., Gaunaa, M., and Natarajan, A.: The DTU 10-MW Reference Wind Turbine, Danish Wind Power Research 2013, Conference, 27–28 May 2013, Fredericia, Denmark, https://orbit.dtu.dk/en/publications/the-dtu-10-mw-reference-wind-turbine (last access: 27 June 2023), 2013.

Beare, R. J., Macvean, M. K., Holtslag, A. A., Cuxart, J., Esau, I., Golaz, J. C., Jimenez, M. A., Khairoutdinov, M., Kosovic, B., Lewellen, D., Lund, T. S., Lundquist, J. K., McCabe, A., Moene, A. F., Noh, Y., Raasch, S., and Sullivan, P.: An Intercomparison of Large-Eddy Simulations of the Stable Boundary Layer, Bound.-Lay. Meteorol., 118, 247–272, https://doi.org/10.1007/S10546-004-2820-6, 2006.

Bratton, D. C. and Womeldorf, C. A.: The wind shear exponent: Comparing measured against simulated values and analyzing the phenomena that affect the wind shear, in: ASME 2011 5th Int. Conf. Energy Sustain. ES 2011, 7–10 August 2011 Washington, DC, USA, PARTS A, B, AND C, American Society of Mechanical Engineers Digital Collection, 2245–2251, https://doi.org/10.1115/ES2011-54823, 2011.

Clark, T. and Farley, R.: Severe downslope windstorm calculations in two and three spatial dimensions using anelastic interactive grid nesting: A possible mechanism for gustiness, J. Atmos. Sci., 41, 329–350, 1984.

Dimitrov, N., Natarajan, A., and Mann, J.: Effects of normal and extreme turbulence spectral parameters on wind turbine loads, Renew. Energ., 101, 1180–1193, https://doi.org/10.1016/j.renene.2016.10.001, 2017.

Haering, S. W., Lee, M., and Moser, R. D.: Resolution-induced anisotropy in large-eddy simulations, Phys. Rev. Fluids, 4, 114605, https://doi.org/10.1103/PhysRevFluids.4.114605, 2019.

Hellsten, A., Ketelsen, K., Sühring, M., Auvinen, M., Maronga, B., Knigge, C., Barmpas, F., Tsegas, G., Moussiopoulos, N., and Raasch, S.: A nested multi-scale system implemented in the large-eddy simulation model PALM model system 6.0, Geosci. Model Dev., 14, 3185–3214, https://doi.org/10.5194/gmd-14-3185-2021, 2021.

Jung, C. and Schindler, D.: The role of the power law exponent in wind energy assessment: A global analysis, Int. J. Energ. Res., 45, 8484–8496, https://doi.org/10.1002/ER.6382, 2021.

Kettle, A. J.: Unexpected vertical wind speed profiles in the boundary layer over the southern North Sea, J. Wind Eng. Ind. Aerodyn., 134, 149–162, https://doi.org/10.1016/j.jweia.2014.07.012, 2014.

Krutova, M.: PALM v21.10 self-nested LES for three stability conditions, Zenodo [data set], https://doi.org/10.5281/zenodo.7886678, 2022.

Maronga, B., Banzhaf, S., Burmeister, C., Esch, T., Forkel, R., Fröhlich, D., Fuka, V., Gehrke, K. F., Geletič, J., Giersch, S., Gronemeier, T., Groß, G., Heldens, W., Hellsten, A., Hoffmann, F., Inagaki, A., Kadasch, E., Kanani-Sühring, F., Ketelsen, K., Khan, B. A., Knigge, C., Knoop, H., Krč, P., Kurppa, M., Maamari, H., Matzarakis, A., Mauder, M., Pallasch, M., Pavlik, D., Pfafferott, J., Resler, J., Rissmann, S., Russo, E., Salim, M., Schrempf, M., Schwenkel, J., Seckmeyer, G., Schubert, S., Sühring, M., von Tils, R., Vollmer, L., Ward, S., Witha, B., Wurps, H., Zeidler, J., and Raasch, S.: Overview of the PALM model system 6.0, Geosci. Model Dev., 13, 1335–1372, https://doi.org/10.5194/gmd-13-1335-2020, 2020.

Maronga, B., Banzhaf, S., Burmeister, C., Esch, T., Forkel, R., Fröhlich, D., Fuka, V., Gehrke, K. F., Geletič, J., Giersch, S., Gronemeier, T., Groß, G., Heldens, W., Hellsten, A., Hoffmann, F., Inagaki, A., Kadasch, E., Kanani-Sühring, F., Ketelsen, K., Khan, B. A., Knigge, C., Knoop, H., Krč, P., Kurppa, M., Maamari, H., Matzarakis, A., Mauder, M., Pallasch, M., Pavlik, D., Pfafferott, J., Resler, J., Rissmann, S., Russo, E., Salim, M., Schrempf, M., Schwenkel, J., Seckmeyer, G., Schubert, S., Sühring, M., von Tils, R., Vollmer, L., Ward, S., Witha, B., Wurps, H., Zeidler, J., and Raasch, S.: PALM model system 21.10, PALM Group, Institute of Meteorology and Climatology of Leibniz Universität Hannover, Germany [code], https://gitlab.palm-model.org/releases/palm_model_system/-/releases/v21.10, (last access: 12 October 2022), 2021.

Moeng, C. H., Dudhia, J., Klemp, J., and Sullivan, P.: Examining two-way grid nesting for large eddy simulation of the PBL using the WRF model, Mon. Weather Rev., 135, 2295–2311, https://doi.org/10.1175/MWR3406.1, 2007.

Munters, W., Meneveau, C., and Meyers, J.: Shifted periodic boundary conditions for simulations of wall-bounded turbulent flows, Phys. Fluids, 28, 025112, https://doi.org/10.1063/1.4941912, 2016.

Nybø, A., Nielsen, F. G., and Reuder, J.: Processing of sonic anemometer measurements for offshore wind turbine applications, J. Phys. Conf. Ser., 1356, 012006, https://doi.org/10.1088/1742-6596/1356/1/012006, 2019.

Nybø, A., Nielsen, F. G., Reuder, J., Churchfield, M. J., and Godvik, M.: Evaluation of different wind fields for the investigation of the dynamic response of offshore wind turbines, Wind Energy, 23, 1810–1830, https://doi.org/10.1002/we.2518, 2020.

Smedman, A.-S., Högström, U., and Sjöblom, A.: A Note on Velocity Spectra in the Marine Boundary Layer, Bound.-Lay. Meteorol., 109, 27–48, https://doi.org/10.1023/A:1025428024311, 2003.

Stull, R.: An Introduction to Boundary Layer Meteorology, Atmospheric and Oceanographic Sciences Library, Springer Netherlands, https://doi.org/10.1007/978-94-009-3027-8, 1988.

Sullivan, P. P., McWilliams, J. C., and Moeng, C.-H.: A grid nesting method for large-eddy simulation of planetary boundary-layer flows, Bound.-Lay. Meteorol., 80, 167–202, https://doi.org/10.1007/BF00119016, 1996.

Touma, J. S.: Dependence of the wind profile power law on stability for various locations, J. Air Pollut. Control Assoc., 27, 863–866, https://doi.org/10.1080/00022470.1977.10470503, 1977.

Weiler, H. S. and Burling, R. W.: Direct Measurements of Stress and Spectra of Turbulence in the Boundary Layer Over the Sea, J. Atmos. Sci., 24, 653–664, https://doi.org/10.1175/1520-0469(1967)024<0653:DMOSAS>2.0.CO;2, 1967.

Witha, B., Steinfeld, G., and Heinemann, D.: High-Resolution Offshore Wake Simulations with the LES Model PALM, Springer, Berlin, Heidelberg, https://doi.org/10.1007/978-3-642-54696-9_26, 2014.

Wurps, H., Steinfeld, G., and Heinz, S.: Grid-Resolution Requirements for Large-Eddy Simulations of the Atmospheric Boundary Layer, Bound.-Lay. Meteorol., 175, 179–201, https://doi.org/10.1007/s10546-020-00504-1, 2020.

Paper III

Multiscale simulation of offshore wind variability during frontal passage: Brief implication on turbines' wakes and load

Bakhoday-Paskyabi, M., Krutova, M., Bui, H., and Ning, X.
Journal of Physics: Conference Series, **2362**, 012003 (2022)

Multiscale Simulation of Offshore Wind Variability During Frontal Passage: Brief Implication on Turbines' Wakes and Load

Mostafa Bakhoday-Paskyabi, Maria Krutova, Hai Bui, and Xu Ning
Geophysical Institute, University of Bergen, and Bergen Offshore Wind Centre, Bergen, Norway

E-mail: Mostafa.Bakhoday-Paskyabi@uib.no

Abstract. Enhancing the performance of offshore wind park power production requires, to a large extent, a better understanding of the interactions of wind farms and individual wind turbines with the atmospheric boundary layer over a wide range of spatiotemporal scales. In this study, we use a multiscale atmospheric model chain coupled offline with the aeroelastic Fatigue, Aerodynamics, Structures, and Turbulence (FAST) code. The multiscale model contains two different components in which the nested mesoscale Weather and Research Forecast (WRF) model is coupled offline with the Parallelized Large-eddy Simulation Model (PALM). Such a multiscale framework enables to study in detail the turbine behaviour under various atmospheric forcing conditions, particularly during transient atmospheric events.

1. Introduction

Offshore wind is one of the key renewable energy resources today and for the years to come. Therefore, a better understanding of wind and its spatiotemporal variability further offshore plays a significant role in future technical and technological developments in offshore wind industries. In some applications, the wind in the boundary layer is described using simple representations, such as power-law or logarithmic profiles. However, these simplified wind profiles cannot always properly capture the vertical distributions of observed wind, particularly, during transient atmospheric events such as Low-Level Jets (LLJs)–during stably stratified conditions, and Open Cellular Convection (OCC)–during convectively unstable conditions. In such conditions, the wind characteristics, such as wind shear, wind veer, and turbulence intensity, depart significantly from those assumed under standard conditions [1, 2, 3]. Furthermore, these transient events modify the performance of wind power generation and structural loading by impacting the turbine wake meandering, evolution, and recovery rates. Therefore, increased knowledge of site-specific characteristics of events like OCCs, their formation mechanisms, and their strengths and impacts are critical to improving farm power generation, turbine performance, and offshore wind turbine load assessments [4].

Areas covered by a large number of wind park clusters experience a large variability of wind speed and farm/turbine power fluctuations during the passage of OCCs. These transient frontal episodes are common atmospheric processes in the North Sea [2]. OCCs are associated with cold air advection over the warmer ocean surface and are visible from the satellite images as honeycomb-like patterns of shallow convective clouds (with 1km-3km thickness) [6, 2]. The

vertical velocity is positive in the updraft regions at the cloudy edges of cells and is negative in the downdraft regions at the cloud-free cell centres. Spatial scales of the cell in the Southern North Sea vary between 7km and 80km with a temporal scale of minutes to hours. The spatiotemporal behaviour of the OCCs at their multiple scales can be efficiently captured by the use of an appropriate atmospheric multiscale modelling system.

Over the last couple of years, numerical research of flow field modelling in the offshore wind energy applications has developed by coupling between the mesoscale Numerical Weather Prediction (NWP) models and microscale high fidelity Large Eddy Simulation (LES) models [1]. NWPs are primarily Reynolds-Averaged Navier–Stokes (RANS) models, in which the turbulence is parameterized based on averaged properties of the flow fields. However, LES models (for example the Parallelized Large-eddy Simulation Model, or PALM) resolve turbulent eddies larger than a spatial lengthscale (large eddies) and parameterize the eddies smaller than the spatial filter lengthscale (subgrid scales) [8, 9]. While LES models have been primarily used in idealised simulations, they can represent realistic flow evolution if the effects of time-varying mesoscale flows along their outermost boundaries are implemented properly through an (one-way) offline nesting approach [10]. PALM system is able to use the mesoscale data from the regional weather prediction model such as Consortium for Small-scale Modeling (COSMO) and the Weather Research and Forecast (WRF) [11] models. The PALM model also contains the implementation of a wind turbine actuator disk parameterization with rotation that enables the multiscale framework to predict more precisely the turbulent flow within the wind park under realistic atmospheric forcing conditions. However, these types of simulations are subjected to several uncertainties associated with the boundary forcing information, the land-use characteristics, the choice of roughness length, etc. [1].

In this work, we develop a multi-scale model chain consisting of the WRF and the PALM models: the WRF model downscales large-scale features and provides the lateral forcing for the PALM model to perform LES simulation using a grid nesting approach. This modelling system provides the LES model with a more realistic time-dependent inflow condition that enables it to capture the variability of a broad range of differently stratified flows. The primary objectives of this study are then:

- to tentatively assess the added value of simulations with the suggested multiscale framework.
- to preliminary study and improve the understanding of the effects of thermally-driven flows on wake evolution and the turbine load behaviour during an OCC event at the area of Alpha Ventus offshore wind park.

While the LES model can provide a non-Gaussian representation of inflow winds, to be used for the load study, we simplify our analysis by assuming that the inflow turbulence field is completely Gaussian by applying a so-called constrained turbulence generator that uses the LES high-frequency time series at a number of separated points.

In this paper, we first introduce the site and its environmental conditions. The methodology is then given in Section 3, and the multiscale model results and structural loading are presented in Section 4. Finally, some conclusions are given in the last section.

2. Observational data and case study

The 100-m tall FINO1 meteorological mast (with coordinates of $54^{o}0'53.5"$N, $6^{o}35'15.5"$E) is located in the Southern North Sea in a water depth of 30m, see Fig. 1. The mast is equipped with various sensors to measure different atmospheric quantities such as wind velocity at 33, 40, 50, 60, 70, 80, 90, and 100 m. High-frequency measurements were collected by sonic anemometers at 40, 60 and 80 m with a sampling frequency of 10 Hz, with an orientation of 308^{o} in order to remove the mast shadow zone during the data analysis step. During the NORCOWE OBLEX-F1 campaign between May 2015 and October 2016 at FINO1, two additional sonic anemometers

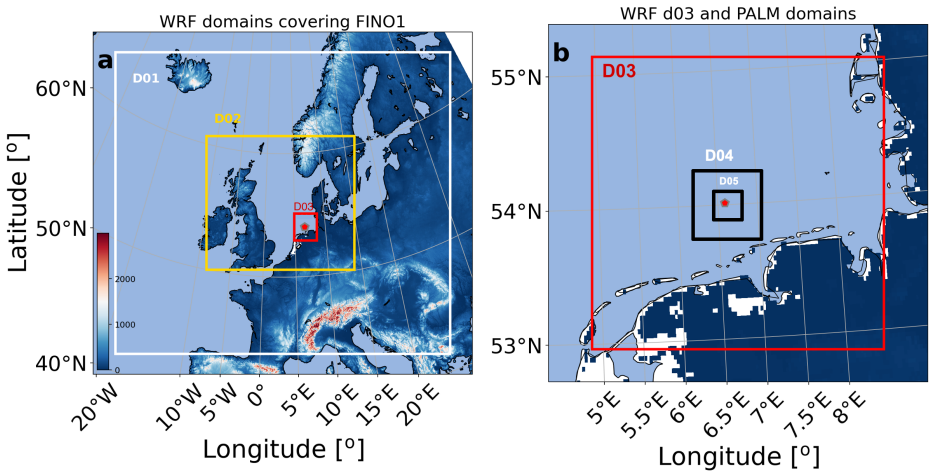

Figure 1. (a) The WRF's nested domains used in this paper with the horizontal resolutions of 9 km (D01), 3 km (D02), and 1 km (D03); and (b) the WRF's 1-km domain (D03) along with the PALM's two nested domains with horizontal resolutions of 375 m (D04) and 10 m (D05). The FINO1 platform is indicated by the red markers in both panels.

with a sampling frequency of 25Hz and an orientation angle of 135° were installed at 15m and 20m above the mean sea level. Waves were measured by a Datawell MKIII buoy deployed in close vicinity of the FINO1 mast.

The Alpha Ventus wind park operating in the vicinity of the FINO1 meteorological mast covers an area of 4km^2 and contains 12 wind turbines (M5000-116) with a hub height of 90 m and rotor top height of 148 m.

Figure 2-a shows a 10-min averaged time series of wind and wave characteristics at FINO1 and the vicinity for a 12-day period in November 2015, when there exhibits a range of variability and fluctuations in wind speed corresponding to several OCC events. The wind speed varies from 2 m/s to nearly 25 m/s with the wave height closely correlated with the wind (i.e. suggesting an almost fully developed sea). During the first period of OCC (between 02 UTC November 22 and 00 UTC November 23), the wave has the heights varying around 3 m and is primarily aligned with the wind (Fig. 2b). The OCC events are characterized by a warmer ocean surface than the overlying air (Fig. 2c). The second strong OCC event occurs between 06 UTC November 23 and 00 UTC November 24 when the wind and wave are even more aligned. Table 1 contains the characteristics of the averaged wind and wave during these two OCC events that occurred during the study period.

3. Methodology

3.1. WRF multiscale simulation setup

The Advanced Research WRF (ARW) version 4.3 is used for the mesoscale simulations of the OCC events and wind farm wakes for areas covering the offshore FINO1 meteorological mast. Figure 1-a represents the three-nested-domain setup of WRF. The outermost parent domain, D01, has a horizontal grid resolution of 9 km; the intermediate and innermost domains, D02 and D03, use 3-km and 1-km horizontal spacing, respectively. We use 60 vertical η-level with

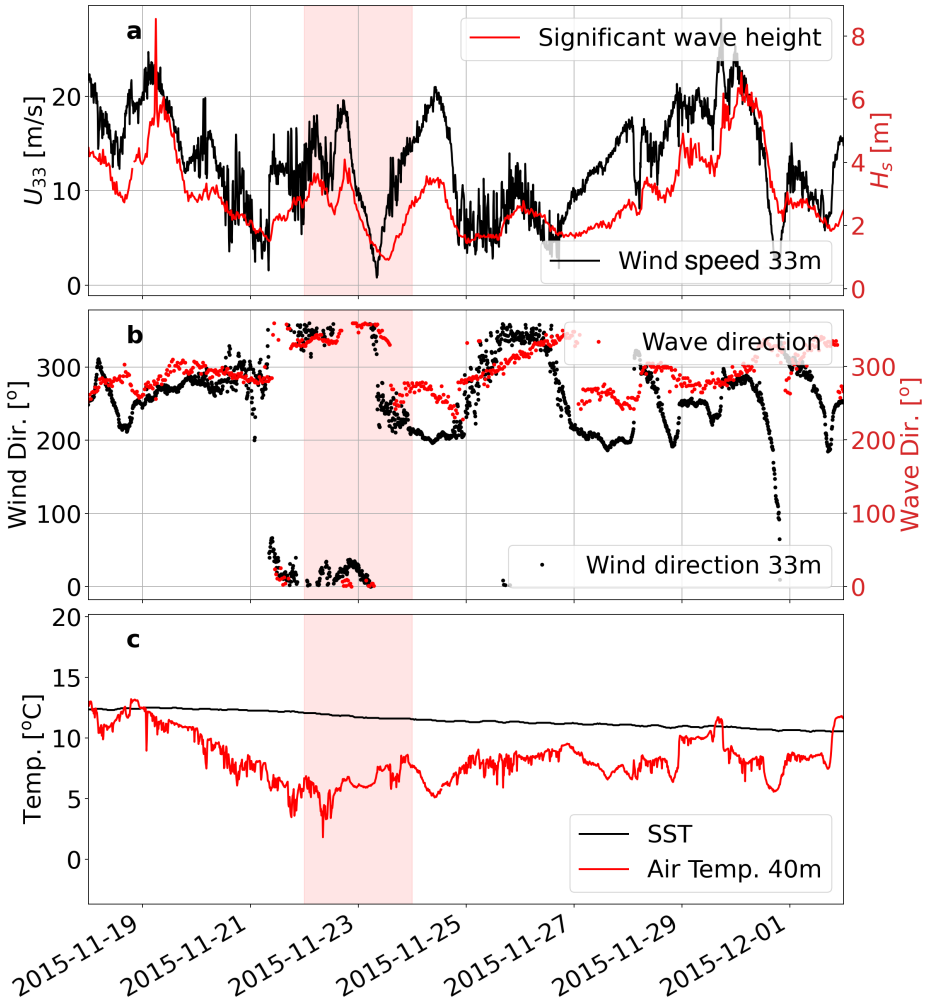

Figure 2. Time series during a 12-day period in November 2015 of (a) 33-wind speed measured by the 33-m height cup anemometer on the FINO1 met-mast (U_{33}, black line) and significant wave height measured by a moored buoy in the vicinity of FINO1 (H_s, red line); (b) wind direction at 33 m height measured by FINO1's wind vane (black dots) and wave direction (red dots); and (c) Sea Surface Temperature (SST) (black line) and air temperature at 40 m (red line). The red shaded area between November 22–24 highlights the WRF simulation period.

the highest vertical grid resolution near the surface for all three domains with 21 levels below 500 m (covering appropriately the measurement heights and the rotor plane area of turbines).

We initialized WRF with ERA5 reanalysis data and conducted a 2-day WRF simulation between November 22 and 24, 2015 (in which convective cells were generated and propagated over the FINO1 and Alpha Ventus wind park regions) using the contiguous US (CONUS) physics

Table 1. Summary of the averaged wind and wave data sets during two OCC events between November 22 and 24 2015. Here, T_p denotes the wave peak period, measured by the buoy nearby the FINO1 location.

Variables	U_{33} [m/s]	Wind direction [°]	H_s [m]	T_p [s]	Wave direction [°]
OCC1	14.3	251.0	3.2	8.4	337.0
OCC2	8.8	212.2	1.5	6.1	259.0

suite configuration. The physics suite contains the microphysics parameterisation developed by Thompson et al. (2008) [12], the Rapid Radiative Transfer Model and Dudhia schemes [13] for longwave and shortwave radiation calculations, the Tiedtke cumulus parameterisation, the eta similarity scheme for the surface layer parameterisation, and the unified Noah land surface model. We considered a spin-up time of 12 h and we did not apply the data assimilation technique in this study. We used the MYNN planetary boundary layer scheme to enable the use of the wind farm parameterization using the Fitch scheme [5]. Furthermore, we use the Met Office's Operational Sea-surface Temperature and Sea Ice Analysis (OSTIA) dataset due to the importance of the SST to study the OCC transient event. The daily OSTIA data are interpolated in time in order to match with hourly ERA5 input data.

3.2. PALM microscale simulation setup

We used the PALM model (version 21.10) to study the flow field variability in the area of the Alpha Ventus wind park and to provide (Gaussian) turbulent inflow boundary information for the wind turbine load study. PALM is an open-source LES code that models both the atmosphere and the ocean and is based on solving the non-hydrostatic incompressible Boussinesq approximation, along with the mass and energy conservation equations [8, 9]. Effects of turbines in the PALM are based on an Actuator Disk Model with Rotation (ADM-R). We used the ADM-R parameters to account for the NREL 5 MW reference turbine and to model the turbine/farm-affected flow fields in the area of Alpha Ventus wind park.

The PALM simulation domains are shown in Fig. 1-b. The parent domain covers the study site with a size of approximately 141 km (east-west)$\times$ 141 km (south-north). The grid sizes of this domain are $\Delta x = \Delta y = 275$ m and $\Delta z = 40$ m. The twelve wind turbines of the Alpha Ventus locates within the child domain with the grid sizes of $\Delta x = \Delta y = 11$ m and $\Delta z = 5m$.

3.3. Meso-to-microscale modeling system

With the offline nesting strategy, non-cyclic boundary conditions are applied to achieve a more realistic meteorological representations inside the PALM domain. Instead, the WRF outputs are used to create lateral and top boundary conditions for PALM, which include [10]: thermodynamics and velocity fields; vertical grid structure; soil information; and some geographical information. The boundary conditions for the PALM's outer domain are updated every 10 minutes, which is the WRF's output frequency. Since the WRF outputs do not contain turbulence, a synthetic turbulence generator is then used to generate the turbulence in time and space.

3.4. Structural analysis code

We conducted aeroelastic simulations based on the open-source software FASTv8 (developed by NREL) to model wind turbine responses during the frontal passage [7]. FAST contains embedded subroutines for the aerodynamic code that works based on the blade element momentum theory and the hydrodynamic module. Using a constraint turbulence generator (here TurbSim) and LES

time series (with a sampling frequency of 25 Hz) at vertical points located at FINO1 distributed over different heights from the near-surface (7.5 m) to below 250 m (so-called constraint points or pattern), we created the (Gaussian) inflow (3D turbulent wind fields) for the FAST program that computes then the time-series of blade momentums and forces. The FAST simulations are made on a 5-MW tripod-foundation wind turbine. The hydrodynamic loads (by HydroDyn FAST) on the supporting structure are modelled for the irregular waves (we use JONSWAP empirical spectrum to reconstruct the irregular waves based on wave bulk parameters measured during the study period).

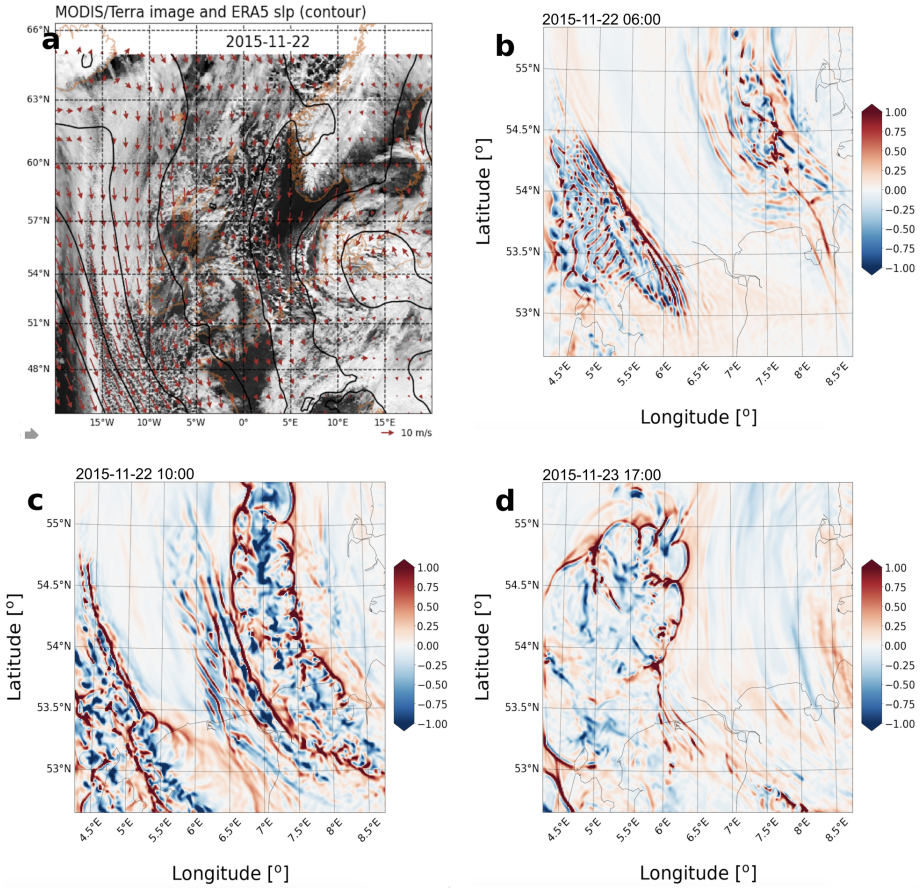

Figure 3. (a) The terra/MODIS satellite cloud image at 00 UTC November 22, 2015, from https://wvs.earthdata.nasa.gov; and the WRF vertical velocities at 100-m height at (b) 06 UTC November 22; (c) 10 UTC November 22; and (d) 17 UTC November 23 respectively.

The stochastic wind was generated by TurbSim on a 16×16 grid with $\sim$ 13-m width. The model uses time series of PALM at the constraint points and coherence parameters from model datasets as inputs. The PALM 25-Hz wind is aligned with the mean wind at each point in space

and the Davenport coherence in the TurbSim simulator, γ, is applied as follows:

$$\gamma(f) = \exp\left(-C\frac{f\delta}{\bar{u}}\right), \tag{1}$$

with the parameters estimated from the coherence in the PALM high-frequency wind data. Here, f denotes frequency, δ is the separation distance between the locations of two given time series, $\bar{u}$ is the mean wind speed, and C represents a decay coefficient (C can be computed separately for each velocity component). The surface roughness, power-law exponent for the wind profile, and wave parameters are found from the wind and wave measurements (see Table 1). In this paper, we used three load quantities calculated by FAST: the rotor speed F_t, the blade pitch, and blade 1 out-of-plane deflection.

4. Results

In this work, we study the OCC event that occurred on November 22, 2015, and Fig. 3-a shows the observed hexagonal cloud patterns of this event from the satellite image over the North Sea. This transient event was the result of a cold air outbreak when the cold and dry air behind an extratropical cyclone was advected from the north-northwest over a relatively warmer ocean surface (see Fig. 2-c). Figure 3-a provides a qualitative impression of the sizes, distributions, and locations of the convective cells over the North Sea and particularly over the study site. The OCC structures are revealed in the snapshots of vertical velocity at 100-m height from the WRF simulation at 1-km resolution (Fig. 3b-d). The wind parks operating in the Southern North Sea may experience substantial and harsh wind speed and wind direction differences during the passage of this front. In such convective conditions, both turbulence vertical/lateral mixing as well as the increase of unstable stratification, lead to narrow updraft edges (positive vertical velocity) and downdraft regions (negative vertical velocity at cell centres). Qualitative and visual comparisons between WRF model results and the satellite image suggest some general similarities in spatial distributions of cells over the North Sea. This event remains strong until approximately 20 UTC November 22, 2015 (Fig. 3-d).

Figures 4a-b show the WRF simulations of horizontal wind speed and vertical velocity extracted at the closest grid point to the FINO1 location (see Section 2 and Fig. 1). Short-timescale fluctuations are produced by WRF for both horizontal and vertical wind components under the OCC, and the patterns of convective circulation are observed clearly through the diverging downdrafts and the converging updrafts. The WRF simulation performed well when we compare the 100-m wind speed with the observation (Fig. 4c). Figure 4c also shows significant fluctuations during the passage of convective cells, where the WRF successfully captures the locations of cells and some of the variations.

For the LES simulation, we coupled WRF with the PALM model through a one-way, offline nesting approach. We first run the mesoscale simulation (i.e. WRF with domains D01–D03) for the entire study period and created the boundary file from the 1-km (D03) resolution results to force the flow fields inside the PALM parent domain (D04), which were then nested onto the innermost domain (D05) through PALM-PALM nesting scheme. We conducted two microscale experiments to simulate high-frequency time series of wind speed at different heights at the location of FINO1 met-mast: (1) before the first frontal passage (starting from 00UTC, November 22) for 20min); and (2) the onset of the first OCC event (starting from 02 UTC, November 22 for 20min). Within D05, we included 12 5-MW NREL wind turbines at geographical locations of Alpha Ventus turbines. Besides the general mean outputs, we included the 25-Hz high-frequency sampling outputs at points covering the rotor area of one turbine in the first row of Alpha Ventus farm to study the non-Gaussian turbulence later on, as well as vertically distributed points at the geographical location of FINO1 to be used in the Gaussian wind generator TurbSim. While the more thorough validation of WRF-PALM results

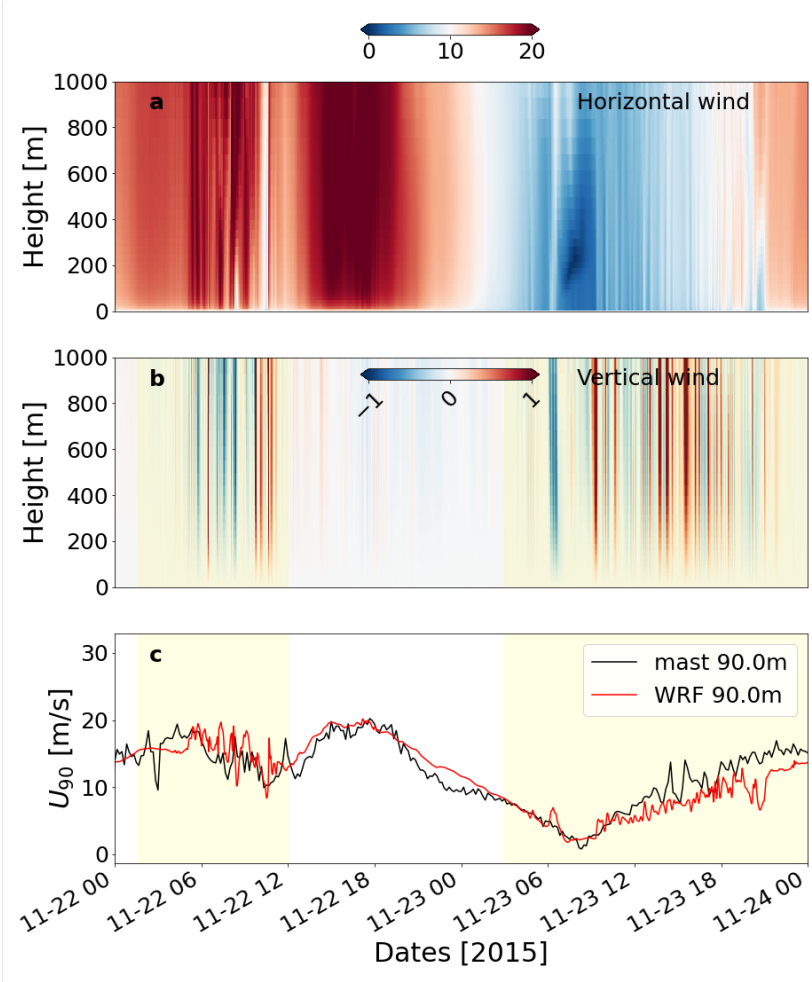

Figure 4. Time-height section at FINO1 over the study period November 22–24 2015 for (a) WRF's horizontal wind speed and (b) WRF's vertical velocity. Panel (c) compares the WRF's wind speed at 50-m height (red line) and measurements from FINO1's cup anemometer (black line). Shaded yellow areas in (b) and (c) show the periods of OCCs.

will be done in our next study, we illustrate the capability of our coupled WRF-PALM system to simulate the wind variability and the turbine wake before and during the OCC passage in Fig. 5. Before the frontal passage, the background flow is almost north-northeasterly which then rotates gradually to north-northwesterly as the front enters the farm region. It is observed that the yaw control of turbines may contribute to the wake meandering by turbines (we do not investigate how well the modelled yawing results match the observed SCADA data in this study).

To construct turbulence velocity fields as inflows of aeroelastic simulations, the necessary

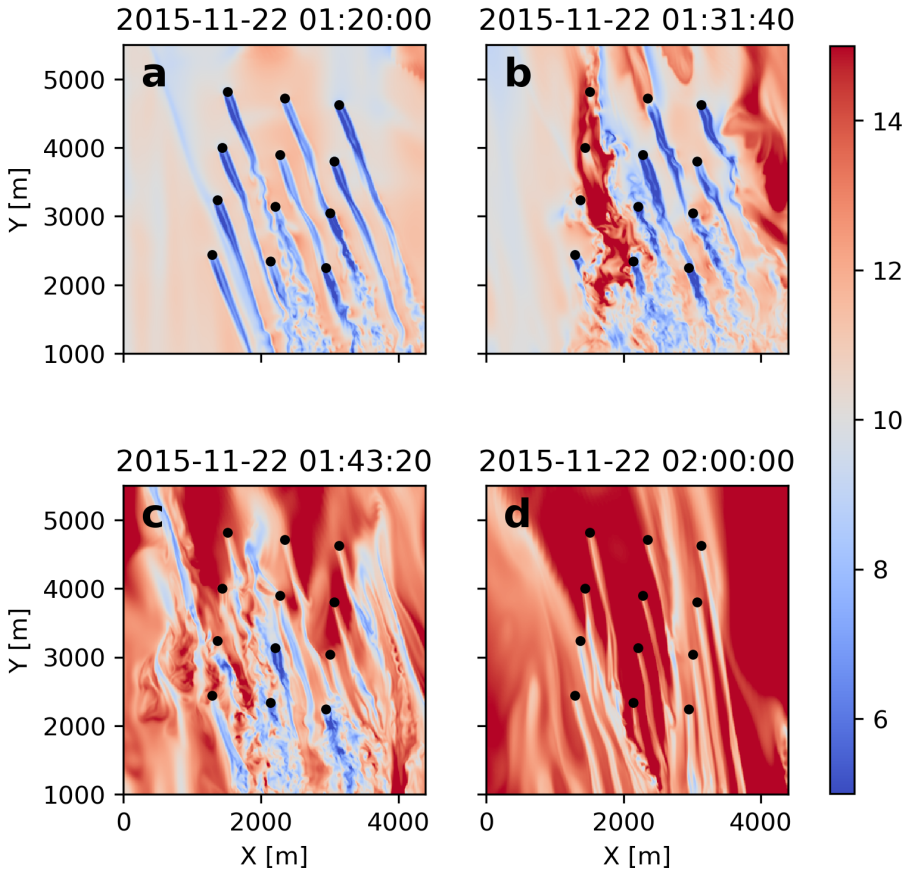

Figure 5. Hub-height wind speed comparison of PALM model results at child domain at the times: (a) before frontal passage; (b) close to the OCC event but still before its passage; (c) when OCC is entering the Alpha Ventus region; and (d) during the OCC event.

parameters of the simulator will be fitted to the measured time series at the given constraint spatial pattern. Figure 6 displays the power spectra of times series at two different heights (7.5 m in the left panels and 147.5 m in the right panels) to examine how large scale turbulent structures, as well as the inertial subrange, are extended before (hence. PREOCC) and during the OCC event. The enhanced variability in the wind energy is pronounced across almost all frequencies during open cells, particularly close to the sea surface.

Two sets of wind fields are generated for the PREOCC and OCC conditions. The 20min wind fields are fitted to the PALM time series at FINO1. Figure 7 shows the generated constraint wind fields by TurbSim simulator (hereafter TIMESER) for two cases. In the Davenport model of the TurbSim, we assumed equal decay parameters for horizontal and vertical separation distances. Note that the PALM generated wind fields may not be appropriately stationary and this will be explored and discussed in our future study.

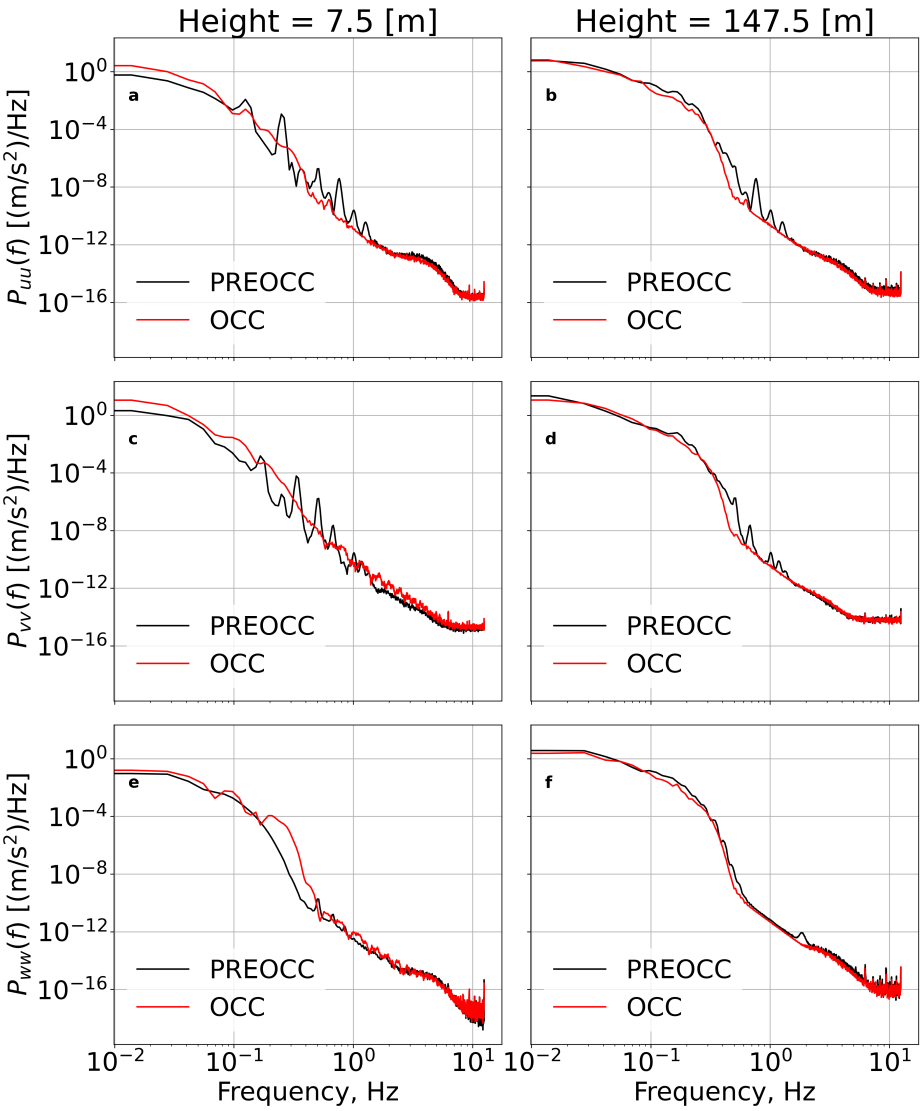

Figure 6. Comparisons of wind power spectra of PREOCC and OCC timeseries at FINO1 location at heights of 7.5m (a,c,e) and 147.5m (b,d,f) above the mean sea level. P_{uu}, P_{vv}, and P_{ww} denote the power spectra of horizontal and vertical wind components, respectively.

We calculate the aerodynamic loads by the use of wind inflows according to TIMESER for PREOCC and OCC conditions. A time step of 0.05 s and a total length of 600s are used in the FAST simulations. We drop the first 200s of simulations as the spin-up time of the model. Figure 8 shows the various response spectra of the following quantities: "OopDefl1" that represents the instantaneous out-of-plane tip deflections of blade 1 relative to the undeflected pitch axis;

"BldPitch1" that indicates the pitch angle of the first blade; and the "RotSpeed" that represents the rotor speed. In Fig. 8-a, the effect of OCC can be observed through its oscillatory behaviour on the out-of-plane blade tip deflection, the rotor speed, and the blade pitch angle (pitch angle during PREOCC is 0 degree and is not shown here). During the transient event, the variation of the wind inflows relative to the rotor induces oscillations in the rotor speed. The control system adjusts then the fluctuating power through the control of blade pitch angle (as shown in Fig. 8b, red line). PSDs in Fig. 8c show very different variations at low frequencies and PSDs in Fig. 8d show very similar behaviour with comparable energy levels at very low frequencies (and elevated energy levels at higher frequencies). The maximum OopDefl1 (of approximately 6m) occurs when wind speed drops and the pitch angle of the blade becomes 0°.

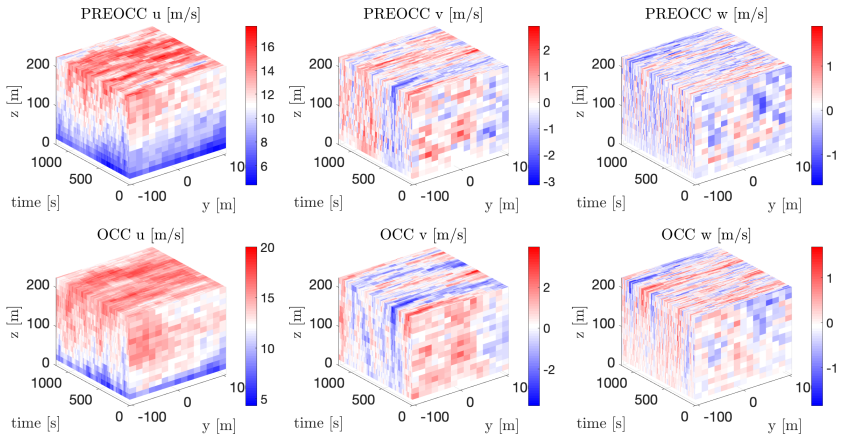

Figure 7. Three-dimensional turbulent wind boxes simulated by TurbSim constrained by 30 vertical points at FINO1 during: (a,b,c) OCC event; and (d,e,f) PREOCC event.

5. Conclusions

In this study, we presented a multi-scale modelling framework to simulate tentatively the propagation of the wind turbine wake as well as structural loads under a thermally-driven transient event (i.e. OCC). We utilized four model components in our model chain including: the WRF mesoscale model with three nested domains; the PALM microscale model with two nested domains combined with the actuator disk model with rotation; the TurbSim model generating the constraint turbulent wind fields; and finally the NREL FASTv8 structural code for investigating very briefly the structural responses of a 5-MW NREL wind turbine.

We implemented the offline nesting approach from the WRF to the PALM and conducted two experiments of WRF-PALM before the OCC (but very close to the onset of the OCC, PREOCC) and during the OCC event respectively. It was shown that the open convective cells modulate strongly the wake spatiotemporal evolution and load behaviour. Results preliminary showed the wake and load variations in the Alpha Ventus wind farm under OCC conditions and underlined the importance of using a multiscale framework to better understand the flow field and its variability, particularly during transient events in the offshore wind park regions.

We further explore the structural responses for the OCC event against another PREOCC event, in which the flow fields and environmental conditions are approximately similar to the

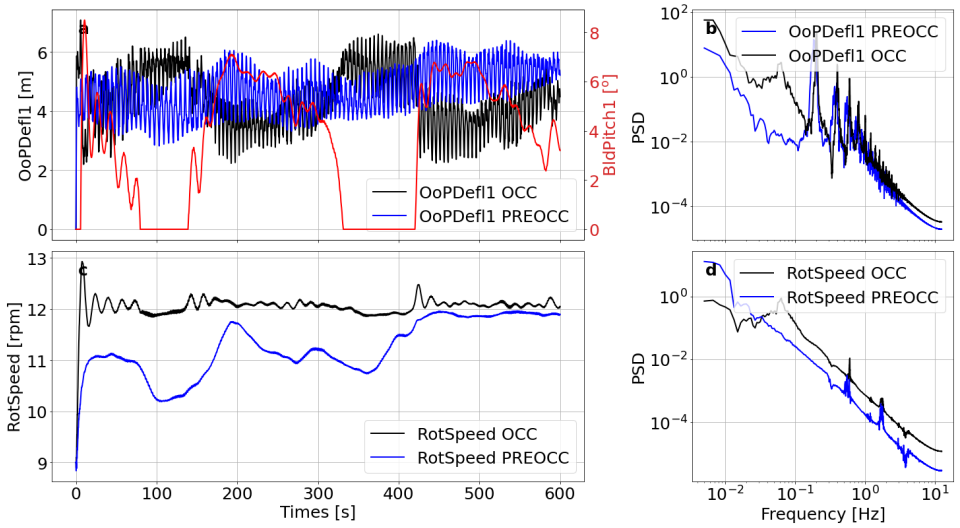

Figure 8. (a,c) Time series of turbine response from FASTv8 model; and (b,d) Power Density Spectra (PSDs) of out-of-plane tip deflections of blade 1 and rotor speeds before (PRECOCC) and during OCC event.

environmental conditions of the OCC.

We need, however, to conduct more comprehensive verification and validation procedures to assure the accuracy and performance of the presented coupled system. Furthermore, the selected PREOCC episode may have been affected by the OCC impacts. This necessitates further elaboration on the event selection.

Acknowledgments

The work is a part of the HIghly advanced Probabilistic design and Enhanced Reliability methods for high-value, cost-efficient offshore WIND (HIPERWIND) project, which has received funding from the European Union's Horizon 2020 Research and Innovation Programme under Grant Agreement No. 101006689. The simulations were performed on resources provided by UNINETT Sigma2 - the National Infrastructure for High Performance Computing and Data Storage in Norway. Some data used in this study are as part of the OBLEX-F1 field campaign that has been performed under the Norwegian Centre for Offshore Wind Energy (NORCOWE) funded by the Research Council of Norway (RCN 193821), the Offshore Boundary Layer Observatory (OBLO) project (project no. RCN 227777) and the Norwegian e-infrastructure NorStore (project no. RCN: NS9060K). OBLEX-F1 was coordinated in collaboration between the University of Bergen (Geophysical Institute) and NORCE Norwegian Research Centre (project executing organization). The Federal Maritime and Hydrographic Agency of Germany (BSH) is acknowledged for providing the FINO1 reference data through the FINO database at http://fino.bsh.de/. The FINO project is funded by the BMU, the German Federal Ministry for the Environment, Nature Conservation, Building and Nuclear Safety in collaboration with Project Management Jülich GmbH (project no. 0325321). The FINO1 meteorological reference data were provided by Deutsches Windenergi Institut (DEWI). We also thank the FINO1 platform operator Forschungs- und Entwicklungszentrum Fachhochschule Kiel GmbH (FuE Kiel

GmbH) for their support (project no. 0329905E).

References

[1] Arthur R S, Mirocha J D, Marjanovic N, Hirth B D, Schroeder J L, Wharton S, and Chow F K, 2020 Multi-Scale Simulation of Wind Farm Performance during a Frontal Passage, *Atmosphere*, **11**, 245, https://doi.org/10.3390/atmos11030245.

[2] Imberger M, Larsén X G, and Davis N, 2021 Investigation of Spatial and Temporal Wind-Speed Variability During Open Cellular Convection with the Model for Prediction Across Scales in Comparison with Measurements, *Boundary-Layer Meteorology*, 179:291–312, https://doi.org/10.1007/s10546-020-00591-0

[3] Bakhoday-Paskyabi M, Flügge M, 2021, Predictive Capability of WRF Cycling 3DVAR: LiDAR Assimilation at FINO1, *J. of Physics: Conference Series*, 1742–6596, http://dx.doi.org/10.1088/1742-6596/2018/1/012006.

[4] Krüger S, Steinfeld G, Kraft M, and Laura Lukassen L J, 2022 Validation of a coupled atmospheric–aeroelastic model system for wind turbine power and load calculations, *Wind Energ. Sci.*, **7**, 323–344, 2022

[5] Fitch A C, Olson J B, Lundquist J K, Dudhia J, Gupta A K, Michalakes J, and Barstad I, 2012, Local and mesoscale impacts of wind farms as parameterized in a mesoscale NWP model, *Mon. Weather Rev.*, **140**, 3017–3038.

[6] Göcmen T, Larśen X G, and Imberger M, 2020 The effects of Open Cellular Convection on Wind Farm Operation and Wakes, *J. Phys.: Conf. Ser.*, **1618**, 062014.

[7] Jonkman J M, Butterfield S, Musial W, and Scott G, 2009 Definition of a 5-MW reference wind turbine for offshore system development. Technical Report NREL/TP-500-38060, *National Renewable Energy Laboratory*, 1617 Cole Boulevard, Golden, Colorado 80401- 3393, February.

[8] Maronga B, Gryschka M, Heinze R, Hoffmann F, Kanani-Sühring F, Keck M, Ketelsen K, Letzel M O, Sühring M, and Raasch S, 2015 The Parallelized Large-Eddy Simulation Model (PALM) version 4.0 for atmospheric and oceanic flows: model formulation, recent developments, and future perspectives. *Geoscientific Model Development*, **8(8)**, 2515–2551.

[9] Maronga B, Banzhaf S, Burmeister C, Esch T, Forkel R, Fröhlich D, Fuka V, Gehrke K F, Geletič J, Giersch, S, Gronemeier T, Groß G, Heldens W, Hellsten A, Hoffmann F, Inagaki A, Kadasch E, Kanani-Sühring F, Ketelsen K, Khan B A, Knigge C, Knoop H, Krč P, Kurppa M, Maamari H, Matzarakis A, Mauder M, Pallasch M, Pavlik D, Pfafferott J, Resler J, Rissmann S, Russo E, Salim, M, Schrempf, M., Schwenkel J, Seckmeyer G, Schubert, S, Sühring M, von Tils R, Vollmer L, Ward S, Witha B, Wurps H, Zeidler J, and Raasch S, 2020 Overview of the PALM model system 6.0, *Geosci. Model Dev.*, **13**, 1335–1372, https://doi.org/10.5194/gmd-13-1335-2020.

[10] Lin D, Khan B, Katurj M, Bird L, Faria R, and Revell L E, 2021 WRF4PALM v1.0: a mesoscale dynamical driver for the microscale PALM model system 6.0, *Geosci. Model Dev.*, **14**, 2503–2524.

[11] Hellsten A, Ketelsen K, Sühring M, Auvinen M, Maronga B, Knigge C, Barmpas F, Tsegas G, Moussiopoulos N, and Raasch S 2021 A nested multi-scale system implemented in the large-eddy simulation model PALM model system 6.0, *Geosci. Model Dev.*, **14**, 3185–3214, https://doi.org/10.5194/gmd-14-3185-2021.

[12] Thompson G, Field P R, Rasmussen R M, and Hall W D, 2008 Explicit forecasts of winter precipitation using an improved bulk microphysics scheme: Part II: implementation of a new snow parameterization, *Mon Weather Rev* **136(12)**, 5095–5115, https://doi.org/10.1175/2008MWR2387.1.

[13] Dudhia J, 1989 Numerical study of convection observed during the winter monsoon experiment using a mesoscale two-dimensional model, *J. Atmos. Sci.*, **46**, 3077–3107.

Paper IV

Gaussian wake model fitting in a transient event over Alpha Ventus wind farm

Krutova, M. and Bakhoday-Paskyabi, M.
Wind Energy Science Discussions **[preprint]**, (2023)

https://doi.org/10.5194/wes-2023-79
Preprint. Discussion started: 31 July 2023

eawe european academy of wind energy
Open Access WIND ENERGY SCIENCE DISCUSSIONS

Gaussian wake model fitting in a transient event over Alpha Ventus wind farm

Maria Krutova[1,2] and Mostafa Bakhoday-Paskyabi[1,2]

[1]Geophysical institut, University of Bergen, Allégaten 70, 5007 Bergen, Norway
[2]Bergen Offshore Wind Centre, University of Bergen, Allégaten 55, 5007 Bergen, Norway

Correspondence: Maria Krutova (maria.krutova@uib.no)

Abstract.

Engineering wake models are defined by mathematical expressions and a set of coefficients. Because of their simplicity, the models may be rigid in transient events such as open cellular convection (OCC), characterized by a strong wind speed and direction change within tens of minutes. We use the results of a multiscale wind-wake modeling during an OCC event at the Alpha Ventus wind farm in the Southern North Sea to study how Gaussian models capture wake deficit variabilities. We find that the Jensen-Gaussian model would benefit from a constant coefficient tuning. On the contrary, the Bastankhah and Porté-Agel model and the super-Gaussian model are consistent without tuning but perform best with different deficit distribution shapes.

1 Introduction

Engineering wake models predict wake deficit with simple analytical expressions and known values of the free-flow characteristics and thrust coefficient. Models' simplicity ensures fast calculation but smooths instantaneous wake features. The wind speed, turbulence intensity and thrust coefficient provide the model with limited capability to adapt to the flow. Since strong changes in the flow may affect the accuracy of the prediction, the model's reaction to transient events has to be studied (Bakhoday-Paskyabi et al., 2022a, b).

Transient events change the flow characteristics within several minutes, which makes numerical simulations unfeasible for real-time control. Although engineering models do not resolve the instantaneous wake structure, they can operate on a steady averaged flow before and after the event.

Open cellular convection (OCC) is a transient event associated with a cold-air outbreak above the warm ocean surface. We regard an OCC event in the Southern North Sea on November 22, 2015, near FINO1 platform (Fig. 1, Sect. 2). We select three Gaussian models (Sect. 3) and evaluate their performance before and after the OCC event based on the accuracy of predicting the 10-minute average normalized wake deficit in the downstream cross-sections (Sect. 4). We also evaluate whether the prediction can be improved if the model's coefficients are corrected by choosing the best fit for the wake deficit.

https://doi.org/10.5194/wes-2023-79
Preprint. Discussion started: 31 July 2023

eawe european academy of wind energy
Open Access WIND ENERGY SCIENCE DISCUSSIONS

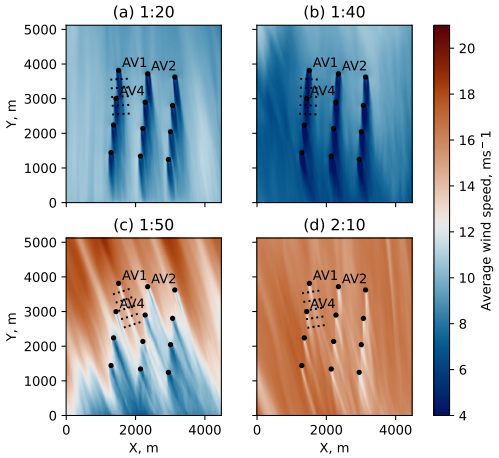

Figure 1. The cross-section of the innermost domain of the WRF-LES containing the Alpha Ventus wind farm. The cross-section shows 10-minute averages of the wind speed at the hub height; time stamps mark the end of each 10-minute period. a) Flow before the OCC event; b) the OCC event is about to begin, the wind farm is not yet affected; c) the flow in the wind farm undergoes radical changes due to the OCC event; d) the convective cell had passed the wind farm, the flow is stabilizing.

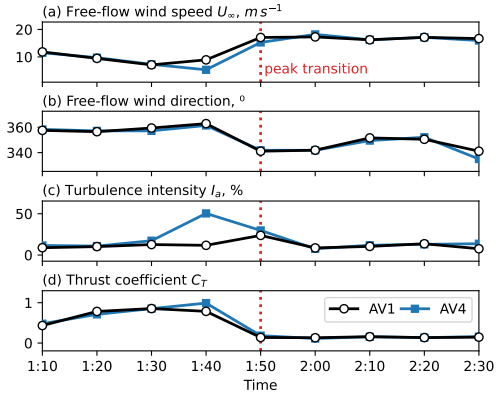

Figure 2. 10-minute averaged inflow characteristics at the hub height $2D$ upstream of AV1 and AV4 (a-c) and the thrust coefficient (d).

https://doi.org/10.5194/wes-2023-79
Preprint. Discussion started: 31 July 2023

eawe european academy of wind energy
Open Access WIND ENERGY SCIENCE DISCUSSIONS

2 Data

The convective cell passed the FINO1 platform and Alpha Ventus wind farm on November 22, 2015 1:40−2:00 AM UTC+0 (Fig. 1). Due to the lack of lidar data for this day, we utilize a high-fidelity numerical simulation to reproduce the flow field (Bakhoday-Paskyabi et al., 2022b). The Weather Research and Forecasting (WRF) model output acts as a dynamic driver input for the large-eddy simulation (LES) PALM model system (Maronga et al., 2020). The LES consists of two nested domains, with the inner domain $4480 \times 5120 \times 320\,\mathrm{m}$ refining the grid around Alpha Ventus to the grid cell size of $\Delta = 10 \times 10 \times 5\,\mathrm{m}$.

The passing open cell affects the flow characteristics changing the wake shapes. We define three phases. The pre-OCC phase covers time stamps 1:10−1:40 and is characterized by low wind speed but high thrust (Fig. 1ab); the wakes are wide and merge for turbines of the same column. A short transition phase takes about 10-minutes and is most prominent at 1:50 time stamp (Fig. 1c). The post-OCC phase starts at 2:00 time stamp and is characterized by low thrust, but high wind speed (Fig. 1d); the wakes become narrow and do not merge anymore. The turbulence intensity fluctuates withing $7 - 11\%$ for both phases, the wind direction changes by $10-15°$ between phases.

The Alpha Ventus wind farm consists of 12 wind turbines of two types arranged in a rectangular pattern, with the turbine AV1 located in the northwest corner. All turbines are approximated as the NREL 5MW reference turbine (Jonkman et al., 2009) and actuator disc model with rotation (Witha et al., 2014); the turbines are set to the same hub height z_h of 90 m and rotor diameter D of 126 m.

3 Methodology

3.1 Model fitting

Model fitting is performed by taking WRF-LES results as a true value. We choose the turbine AV1 as a reference for the regarded wake models since AV1 is the least affected by the nearby wakes due to the northwest wind. To extract the cross-sectional velocity U in xy-plane, we define a local coordinate system with a center at the AV1 position so that the x-axis always follows a 10-minute average wind direction. The downstream cross-sections are regarded in a range of $x/D = 2..10$ with a step of 0.5 – totaling 17 cross-sections. The local coordinates for each cross-section are represented by a radial distance r varying in the range of $r/D = -2..2$ from the rotor axis. The 10-minute average inflow characteristics – wind speed $\overline{U}_0$, wind direction, and turbulence intensity I_a – are estimated by probing the free flow at $2D$ upstream of AV1. The PALM LES output contains the thrust force T for each turbine; hence, the thrust coefficient C_T is derived as

$$C_T = \frac{T}{0.5 \cdot \rho A \overline{U}_0^2} \tag{1}$$

where $\rho = 1.17\,\mathrm{kg/m^3}$ is the constant air density as returned by the WRF-LES, $A = \pi(D/2)^2$ is the rotor area.

The wake from AV4 appears in AV1 cross-sections starting from $x/D = 6.5$. The inflow probes for AV4 generally return similar values, except for the time stamp 1:40 (Fig. 2) – the wind speed and turbulence intensity near AV4 are strongly affected

https://doi.org/10.5194/wes-2023-79
Preprint. Discussion started: 31 July 2023

eawe european academy of wind energy
Open Access WIND ENERGY SCIENCE DISCUSSIONS

Table 1. Gaussian wake models and their original coefficients.

Model	Coefficients
BPA	$k_1^* = 0.003678$, $k_2^* = 0.3837$
Jensen Gaussian	$k = 0.05$
Super-Gaussian	$a_s = 0.17$, $b_s = 0.005$, $c_s = 0.2$

by the direct hit from AV1 wake. Overall, this similarity allows using AV1 inflow characteristics and thrust coefficient to estimate wakes for both turbines. An ensemble wake is calculated by summing up the normalized wake deficit from the AV1 wake at the regarded cross-section and the deficit at the respective cross-section of the AV4 wake.

We also tune coefficients of each model to find the best fit to WRF-LES results. Overall, we regard the following cases:

- **default model** – a wake model uses coefficients suggested by its authors and relies only on C_T and I_a to calculate wake deficit.
- **corrected fit** – model's coefficients are fitted for the first 10-minute period of the pre-OCC and post-OCC phases – periods ending at 1:10 and 2:00, respectively – and remain fixed for the further periods of the phase.
- **best fit** – model's coefficients are re-fitted to each new 10-minute period. The fit uses already known simulation data for the passing period, so while not being practical, it shows whether the model could have described the wake better.

The best fit is optimized for all cross-sections in a 10-minute period to avoid tuning models to a specific part of the wake. To evaluate the models' performance, we also compare root mean square errors (RMSE) for the normalized wake deficit of each cross-section separately.

3.2 Gaussian wake models

We apply engineering wake models to calculate normalized wake deficit $\Delta\overline{U} = 1 - U/U_0$. Since we are interested in how well wake models approximate the wake shape and flow characteristics, we select wake models that suggest a Gaussian distribution of the deficit. The three Gaussian models regarded in this study are chosen based on their flexibility and possibility to re-fit the parameters (Krutova et al., 2020). When choosing which values to fit, we prefer the coefficients fitted by the original authors (Table 1).

3.2.1 BPA Gaussian model

One of the first Gaussian models was developed by Bastankhah and Porté-Agel, further referred to as the BPA model (Bastankhah and Porté-Agel, 2014). We utilize Niayifar and Porté-Agel (2016) version of the model, which parameterizes the

https://doi.org/10.5194/wes-2023-79
Preprint. Discussion started: 31 July 2023

eawe european academy of wind energy
Open Access WIND ENERGY SCIENCE DISCUSSIONS

growth rate of the wake k^* as a linear function of the turbulence intensity I_a:

$$k^* = k_1^* + k_2^* I_a, \tag{2}$$

where k_1^* and k_2^* are the coefficients to fit. Then the standard deviation σ of the Gaussian function depends on the diameter D and downstream distance x as

$$\sigma = k^* x + \varepsilon D, \tag{3}$$

$$\varepsilon = 0.2\sqrt{\beta},\ \beta = \frac{1}{2}\frac{1+\sqrt{1-C_T}}{\sqrt{1-C_T}} \tag{4}$$

The normalized wake deficit is then given as

$$\Delta\overline{U} = \left(1 - \sqrt{1 - \frac{C_T}{8(\sigma/D)^2}}\right) \times \exp\left(-\frac{r^2}{2\sigma^2}\right) \tag{5}$$

3.2.2 Jensen-Gaussian model

Gao et al. (2016) replaced a top-hat distribution in the Jensen wake model (Jensen, 1983) with a Gaussian.

$$\Delta\overline{U} = \left[1 - \frac{5.16}{\sqrt{2\pi}} \cdot \overline{U}^*(x, k_w)\right] \times \exp\left(-\frac{r^2}{2\sigma^2}\right) \tag{6}$$

$$\sigma = r_x/2.58 \tag{7}$$

where $r_x(C_T, k_w)$ is the wake radius, $\overline{U}^*(x, k_w)$ and $k_w(k, C_T, I_a)$ are new functions omitted here for the sake of brevity. The full definition can be found in the original study (Gao et al., 2016).

The only coefficient to fit, the wake decay coefficient k, is defined similarly to the Jensen model and is then corrected with the function $k_w(k, C_T, I_a)$. We choose the starting value $k = 0.05$ as suggested by the model's authors for offshore wind farms.

3.2.3 Super-Gaussian model

A regular Gaussian model uses the order of $n = 2$. Increasing this value leads to the tendency for a flat peak of the distribution. Blondel and Cathelain (2020) proposed a super-Gaussian model with varying n. Although another version of this model exists (Cathelain et al., 2020), it mainly improves the wake deficit prediction for $x/D < 5$, which we already found satisfactory for our purposes. Hence, we prefer the first version with less parameterized coefficients.

The super-Gaussian model expands the BPA model and alters the order n depending on the downstream distance x

$$\Delta\overline{U} = C(x) \exp\left(-\frac{|r|^{n(x)}}{2\sigma^2}\right) \tag{8}$$

where $C(x)$ is defined via $n(x)$ as

$$C(x) = 2^{2/n-1} - \sqrt{2^{4/n-2} - \frac{nC_T}{16\Gamma(2/n)\sigma^{4/n}}} \tag{9}$$

https://doi.org/10.5194/wes-2023-79
Preprint. Discussion started: 31 July 2023

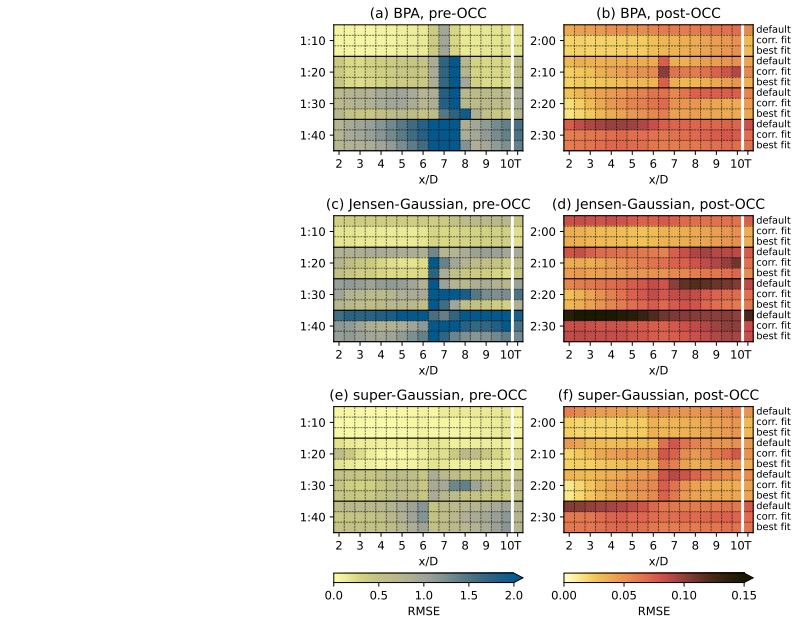

Figure 3. RMSE of the Gaussian models calculated for each cross-section. The label 'T' stands for the total RMSE normalized by the number of cross-sections to allow comparison. The results for the peak transition time 1:50 are excluded since the RMSE is not representative there.

and collapses to the multiplier in Eq. (5) for $n = 2$.

The standard deviation σ in this model is defined as

$$\sigma = (a_s I_a + b_s) + c_s \sqrt{\beta} \tag{10}$$

Here, β follows Eq. (4) of the BPA model with $c_s = 0.2$. a_s and b_s are defined differently despite being used similarly to k_2^* and k_1^* in Eq. (2). We fit these three coefficients (Table 1).

The super-Gaussian model proposes two method of finding $n(x)$: root-solving and analytical. The analytical method adds three more coefficients; therefore, we choose the root-solving method and find $n(x)$ from the equation

$$C(x)^2 - 2^{2/n} C(x) + \frac{nC_T}{16\Gamma(2/n)\sigma^{4/n}} = 0 \tag{11}$$

4 Results

The general behavior of all models follows similar trends (Fig. 3). The agreement to WRF-LES is good for the stabilized flow in the pre-OCC phase but declines as the convective cell approaches the wind farm. During the peak transition phase at 1:50,

https://doi.org/10.5194/wes-2023-79
Preprint. Discussion started: 31 July 2023

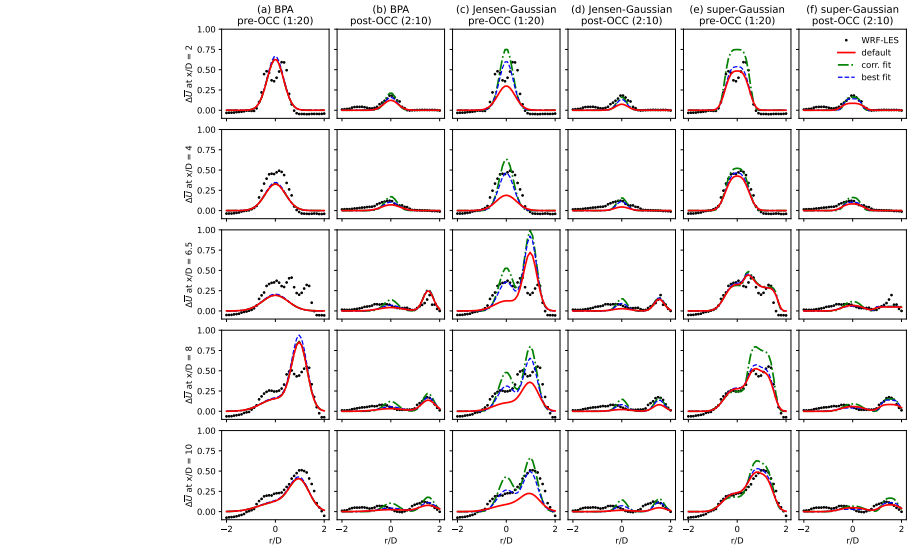

Figure 4. Gaussian wake models applied to the normalized wake deficit at the various downstream distances. For $x/D \geq 6.5$, two wakes are present in a cross-section.

the free-flow wind speed becomes ambiguous. The near wake may already be affected by the convective cell – probing the flow upstream would return the correct free-flow wind speed for the near wake. At the same time, the effects of the accelerated flow had not yet reached the far wake (Fig. 1c) – the upstream flow characteristics are not relevant. Probing the free flow at a distance parallel to the wake is not accurate enough due to wake effects from the nearby turbines. Model fitting for the period ending on 1:50 returns unrealistic coefficients, e.g., a negative wake decay coefficient k for the Jensen-Gaussian model.

The post-OCC phase is less challenging for the models because the wakes no longer merge due to the changed wind direction and narrower wake deficit distribution. However, despite the averaging, the deflection effect becomes more prominent in the far wake. We did not account the deflection, hence, the radial positions of the wake deficit maximums do not perfectly match maximums extracted in cross-sections for the time stamp 2:30. The discrepancy between maximums positions leads to increased RMSEs, although the agreement in earlier periods was acceptable.

Depending on C_T and I_a, the BPA model may not resolve the near wake ($x/D < 3$) due to a negative value occurring under the square root in Eq. (5). While this is not crucial for the AV1 wake, the model may miss the influence from the AV4 wake for several cross-sections leading to an increased RMSE for $x/D \geq 6.5$ (Fig. 3a, 4a). This complicates searching for a best fit – the coefficients fitted for the BPA model do not deviate much from the original values, and the best fits do not gradually improve RMSEs compared to the default model. Overall, the BPA model tends to overestimate the maximum deficit in the near wake, especially if the wake deficit distribution has a double peak shape.

https://doi.org/10.5194/wes-2023-79
Preprint. Discussion started: 31 July 2023

eawe european academy of wind energy
Open Access WIND ENERGY SCIENCE DISCUSSIONS

The Jensen-Gaussian model benefits from correcting the wake decay coefficient k similarly as the Jensen model requires adjustments for better prediction (Peña et al., 2016). The chosen value of $k = 0.05$ underestimates the pre-OCC wake deficit implying that the initial choice requires re-evaluation based on the observed wake deficit (Fig. 4c). The corrected fit may follow the wake deficit better but tends to a narrow distribution underestimating the wake width and overestimating the maximum wake deficit. Despite dependencies on the thrust coefficient and turbulence intensity, having only one adjustable coefficient limits the flexibility of the Jensen-Gaussian model. In addition, the only coefficient is sensitive to short-term fitting: k varied between -0.01 and 0.03 for the regarded periods, although showing a tendency for $k = 0.01$ in both phases.

Both Jensen-Gaussian and BPA models are subjected to increased RMSE for $x/D \geq 6.5$ in the pre-OCC phase when the wake from AV4 enters the AV1 downstream cross-section. The models either overestimate the deficit in the AV4 wake or underestimate it in the AV1 wake. A notable exception is the super-Gaussian model, which follows the complex shape of the merging pre-OCC wakes well (Fig. 4e).

The tendency for a flat distribution in the super-Gaussian model smooths the double peak in the near wake and resolves a single peak in the far wake equally well. Consequently, the RMSE of individual cross-sections is rather uniform for the super-Gaussian model (Fig. 3e). Unlike other models, the super-Gaussian model does not benefit from re-fitting the coefficients in the pre-OCC phase – new fits either only slightly deviates from the default model or noticeably overestimates the near wake deficit. On the other hand, a flat peak hinders the super-Gaussian performance in the post-OCC phase (Fig. 4f) – sharp but low distribution peaks are captured by the super-Gaussian model worse than by other models (i.e., BPA and corrected Jensen-Gaussian). It should be noted that the calibrated super-Gaussian model (Cathelain et al., 2020) slightly increases the maximum wake deficit predicted in the post-OCC near wake, but underestimates it compared to other models.

5 Conclusions

We performed a WRF-LES of a transient event and studied how the Gaussian models describe the 10-minute average wake deficit before and after the event. The transient period remained challenging for all models due to the ambiguity in the free-flow wind speed.

Having only one coefficient, the Jensen-Gaussian model is simple to fit. Moreover, correcting the coefficient based on the flow characteristics and wind farm site conditions is preferable before working with the model. However, adjusting to short averaging periods may not produce a stable coefficient value. While the Jensen-Gaussian consistently showed an improved RMSE with the best fit, this approach is not feasible since all flow characteristics should be known in advance. We do not recommend using this model for short periods during transient events.

The default definitions of BPA and super-Gaussian models kept a good agreement with the changing flow and did not benefit from the coefficient tuning. While the BPA model could occasionally return better RMSE with the re-fitted coefficients, the default values performed more consistently. Due to how these models interpret the distribution peak, they work better with different wake shapes. The BPA model approximates well a single sharp peak and may result in an increased RMSE when two wakes are present in a cross-section. The super-Gaussian model smooths the distribution peak, which appears to be a

https://doi.org/10.5194/wes-2023-79
Preprint. Discussion started: 31 July 2023

eawe european academy of wind energy
Open Access WIND ENERGY SCIENCE DISCUSSIONS

good approximation of a double peak or merging wakes. Still, the model underperformed in the post-OCC phase with low and uniform wake deficit.

The super-Gaussian model's capability to capture wake merging accurately is promising for applications where the wake deficit distribution is important. Considering that the model also reacts well to changing conditions, this calls for further model validation in complex wake-wake interaction cases.

Code and data availability. The simulation data and the Python code to reproduce the figures are available at https://doi.org/10.5281/zenodo.8135542 (Krutova, 2023).

Author contributions. MK wrote the code for model fitting and processed the results, MBP selected the OCC event to design the WRF-LES setup and provided valuable discussion on the findings.

Competing interests. The authors declare that they have no conflict of interest.

Acknowledgements. The WRF-LES for this study have been performed as a part of the HIghly advanced Probabilistic design and Enhanced Reliability methods for the high-value, cost-efficient offshore WIND (HIPERWIND) project, which has received funding from the European Union's Horizon 2020 Research and Innovation Programme under Grant Agreement No. 101006689. Resources for simulations were provided by UNINETT Sigma2 – the National Infrastructure for High Performance Computing and Data Storage in Norway (project number NS9696K)

https://doi.org/10.5194/wes-2023-79
Preprint. Discussion started: 31 July 2023

eawe european academy of wind energy
Open Access WIND ENERGY SCIENCE DISCUSSIONS

References

Bakhoday-Paskyabi, M., Bui, H., and Penchah, M. M.: Atmospheric-Wave Multi-Scale Flow Modelling, Delivery report, HIPERWIND EU project, No. 101006689, https://www.hiperwind.eu/publications, Accessed: July 4, 2023, 2022a.

Bakhoday-Paskyabi, M., Krutova, M., Bui, H., and Ning, X.: Multiscale Simulation of Offshore Wind Variability During Frontal Passage: Brief Implication on Turbines' Wakes and Load, Journal of Physics: Conference Series, 2362, 012 003, https://doi.org/10.1088/1742-6596/2362/1/012003, 2022b.

Bastankhah, M. and Porté-Agel, F.: A new analytical model for wind-turbine wakes, Renewable Energy, 70, 116–123, https://doi.org/10.1016/j.renene.2014.01.002, 2014.

Blondel, F. and Cathelain, M.: An alternative form of the super-Gaussian wind turbine wake model, Wind Energy Science, 5, 1225–1236, https://doi.org/10.5194/wes-5-1225-2020, 2020.

Cathelain, M., Blondel, F., Joulin, P., and Bozonnet, P.: Calibration of a super-Gaussian wake model with a focus on near-wake characteristics, Journal of Physics: Conference Series, 1618, 062 008, https://doi.org/10.1088/1742-6596/1618/6/062008, 2020.

Gao, X., Yang, H., and Lu, L.: Optimization of wind turbine layout position in a wind farm using a newly-developed two-dimensional wake model, Applied Energy, 174, 192–200, https://doi.org/10.1016/j.apenergy.2016.04.098, 2016.

Jensen, N. O.: A note on wind generator interaction, Risø-M-2411 Risø National Laboratory Roskilde, pp. 1–16, https://doi.org/Riso-M-2411, 1983.

Jonkman, J., Butterfield, S., Musial, W., and Scott, G.: Definition of a 5-MW Reference Wind Turbine for Offshore System Development, National Renewable Energy Laboratory (NREL), https://doi.org/10.2172/947422, 2009.

Krutova, M.: Gaussian wake model fitting to a transient event simulated with WRF-LES, https://doi.org/10.5281/zenodo.8135543, 2023.

Krutova, M., Paskyabi, M. B., Nielsen, F. G., and Reuder, J.: Evaluation of Gaussian wake models under different atmospheric stability conditions: Comparison with large eddy simulation results, Journal of Physics: Conference Series, 1669, 012 016, https://doi.org/10.1088/1742-6596/1669/1/012016, 2020.

Maronga, B., Banzhaf, S., Burmeister, C., Esch, T., Forkel, R., Fröhlich, D., Fuka, V., Gehrke, K. F., Geletič, J., Giersch, S., Gronemeier, T., Groß, G., Heldens, W., Hellsten, A., Hoffmann, F., Inagaki, A., Kadasch, E., Kanani-Sühring, F., Ketelsen, K., Khan, B. A., Knigge, C., Knoop, H., Krč, P., Kurppa, M., Maamari, H., Matzarakis, A., Mauder, M., Pallasch, M., Pavlik, D., Pfafferott, J., Resler, J., Rissmann, S., Russo, E., Salim, M., Schrempf, M., Schwenkel, J., Seckmeyer, G., Schubert, S., Sühring, M., von Tils, R., Vollmer, L., Ward, S., Witha, B., Wurps, H., Zeidler, J., and Raasch, S.: Overview of the PALM model system 6.0, Geoscientific Model Development, 13, 1335–1372, https://doi.org/10.5194/gmd-13-1335-2020, 2020.

Niayifar, A. and Porté-Agel, F.: Analytical Modeling of Wind Farms: A New Approach for Power Prediction, Energies, 9, 741, https://doi.org/10.3390/en9090741, 2016.

Peña, A., Réthoré, P., and van der Laan, M. P.: On the application of the Jensen wake model using a turbulence-dependent wake decay coefficient: the Sexbierum case, Wind Energy, 19, 763–776, https://doi.org/10.1002/we.1863, 2016.

Witha, B., Steinfeld, G., and Heinemann, D.: High-Resolution Offshore Wake Simulations with the LES Model PALM, Springer, Berlin, Heidelberg, https://doi.org/10.1007/978-3-642-54696-9_26, 2014.

Paper V

Development of an automatic thresholding method for wake meandering studies and its application to the data set from scanning wind lidar

Krutova, M., Bakhoday-Paskyabi, M., Reuder, J., and Nielsen, F. G.
Wind Energy Science, **7(2)**, 849–873 (2022)

Wind Energ. Sci., 7, 849–873, 2022
https://doi.org/10.5194/wes-7-849-2022

WIND ENERGY SCIENCE

Development of an automatic thresholding method for wake meandering studies and its application to the data set from scanning wind lidar

Maria Krutova, Mostafa Bakhoday-Paskyabi, Joachim Reuder, and Finn Gunnar Nielsen

Geophysical institute and Bergen Offshore Wind Centre,
University of Bergen, Allégaten 70, 5007 Bergen, Norway

Correspondence: Maria Krutova (maria.krutova@uib.no) and
Mostafa Bakhoday-Paskyabi (mostafa.bakhoday-paskyabi@uib.no)

Received: 13 August 2021 – Discussion started: 6 September 2021
Revised: 21 January 2022 – Accepted: 3 March 2022 – Published: 8 April 2022

Abstract. Wake meandering studies require knowledge of the instantaneous wake evolution. Scanning lidar data are used to identify the wind flow behind offshore wind turbines but do not immediately reveal the wake edges and centerline. The precise wake identification helps to build models predicting wake behavior. The conventional Gaussian fit methods are reliable in the near-wake area but lose precision with distance from the rotor and require good data resolution for an accurate fit. The thresholding methods, i.e., selection of a threshold that splits the data into background flow and wake, usually imply a fixed value or manual estimation, which hinders the wake identification on a large data set. We propose an automatic thresholding method for the wake shape and centerline detection, which is less dependent on the data resolution and quality and can also be applied to the image data.

We show that the method performs reasonably well on large-eddy simulation data and apply it to the data set containing lidar measurements of the two wakes. Along with the wake identification, we use image processing statistics, such as entropy analysis, to filter and classify lidar scans.

The automatic thresholding method and the subsequent centerline search algorithm are developed to reduce dependency on the supplementary data such as free-flow wind speed and direction. We focus on the technical aspect of the method and show that the wake shape and centerline found from the thresholded data are in a good agreement with the manually detected centerline and the Gaussian fit method. We also briefly discuss a potential application of the method to separate the near and far wakes and to estimate the wake direction.

1 Introduction

A wake is a complex dynamic structure forming behind a wind turbine due to the kinetic energy extraction from the incoming wind flow. The wake region is characterized by decreased wind speed and increased turbulence intensity. The relative velocity deficit, or wake deficit, is strongest right after the wind turbine. Strongly affected by wind turbine rotor, the region extends up to 4–5 rotor diameters depending on the terrain characteristics and stability conditions (Stevens and Meneveau, 2017; Porté-Agel et al., 2020). The wake transitions to the far wake, where the recovery to the free flow is considerably slowed down; at the same time, the wake width increases up to 3 rotor diameters according to observations (Aitken et al., 2014). The turbine spacing in operational wind farms usually reaches 7–10 D (e.g., London Array), although the optimal spacing is estimated to be even higher in order to reduce the wake effect on downstream turbines (Meyers and Meneveau, 2012; Stevens, 2016). Since the generated wind power is proportional to the cube of the wind speed U^3, the power production gradually decreases if the incoming wind speed drops below the rated wind speed. The increased turbulence intensity negatively affects the turbine fatigue loads (Lee et al., 2012). Studying the wake behavior is hence crucial to estimating both the actual power production and the overall lifetime of a wind farm.

Not only does the wake expand, but it is also subjected to wake meandering – oscillations along the rotor axis caused by the movement of large eddies (Larsen et al., 2007, 2008). While the near wake remains primarily stable and follows the wind direction, the far wake oscillates randomly in the horizontal plane with an amplitude exceeding 0.5 D (Howard et al., 2015; Foti et al., 2016). The far wake also oscillates in the vertical plane, although the velocity fluctuations there are weaker (España et al., 2011). As a result, a downstream turbine is exposed to intermittent flow and, consequently, unequal fatigue loads (Muller et al., 2015; Moens et al., 2019). Additionally, the wake in the Northern Hemisphere slightly turns clockwise due to the Coriolis effect (Abkar and Porté-Agel, 2016; van der Laan and Sørensen, 2017), adding more complexity to the wake evolution over time. Knowing only the velocity deficit at a certain downstream distance is insufficient, since the wake meandering strength is characterized by the standard deviation of the wake center. Therefore, the wake meandering analysis requires the knowledge of the wake centerline to quantify the instantaneous wake effect on the downwind structures. An appropriate detection method should be able to perform wake identification by separating the wake from the free flow and wake characterization by estimating the wake centerline and its statistical characteristics (Quon et al., 2020). Method application and capabilities are highly dependent on the input data available.

Measurement campaigns that use scanning lidars provide the most relevant data on the wind flow in a particular wind farm (Bingöl et al., 2010; Trujillo et al., 2011; Herges et al., 2017). Due to the technical restrictions and cost of lidar installation, it is complicated to obtain a three-dimensional scan of the flow around the whole wind farm, although the flow can be reconstructed for a single turbine (Beck and Kühn, 2019). Still, the measurement campaigns span several months and require data preprocessing to sort out invalid measurements. A controlled experiment can be performed on a wind tunnel for model validation or reproduction of specific flow conditions (Snel et al., 2007; Chamorro and Porté-Agel, 2010). The particle image velocimetry (PIV) provides good spatial and temporal resolution of the measured wind field but deals with the scaled models and has to account for their limitations. A different approach is running a large-eddy simulation (LES) of a wind turbine or a wind farm. While LES provides a wide range of possibilities to simulate atmospheric conditions and wind farm configuration, its representation of a wake strongly depends on the implemented turbulence closure (Moriarty et al., 2014; Mehta et al., 2014; Martínez-Tossas et al., 2018) and wind turbine model (Porté-Agel et al., 2011; Martínez-Tossas et al., 2015). A relatively new development is quantitative study of wind farm wakes from satellite data (Ahsbahs et al., 2020). The satellites generally have a lower spatial resolution than scanning lidars and measure wind speed on the horizontal near-surface plane but still provide general information on the flow around wind farms.

Several wake identification methods exist, varying in complexity and input data requirements (Quon et al., 2020). Among the variety of methods, we focus on thresholding and Gaussian fitting because they are applicable to a 2D lidar scan in a horizontal or inclined plane. The most common wake identification method is to fit a one- or two-dimensional Gaussian distribution to the velocity deficit across the wake at various downstream positions and get estimations of the wake center and width from the fitted function (Fleming et al., 2014; Vollmer et al., 2016; Krishnamurthy et al., 2017). This method can be applied to both the averaged and instantaneous wake, although the irregular wake shape of the latter complicates the detection. For better accuracy, the fitting requires wind speed data in a fine spatial resolution. A sufficient spatial resolution is achieved by large-eddy simulation or particle image velocimetry. The Gaussian fit method can also be applied to the scanning wind lidar data, provided the wake region is resolved well enough. Overall, the fitting method efficiency depends on the data quality and spatial resolution. The method also requires the free-flow wind speed to calculate the wake deficit.

Alternatively, a threshold value can be defined. In the simplest case, the threshold splits the range of available values into two: all values below the threshold fall into one group, while the remaining values form the second group. When applied to the wind field for the wake identification, the threshold would split the data into the wake and free-flow points. Thresholding methods depend less on the data resolution and mainly rely on the wind speed values. The simplest thresholding method sets a threshold based on the wind speed ratio in the wake and the free flow. As shown by España et al. (2011), the method is effective for a regular flows, e.g., in a wind turbine: a threshold of 95 % of the free-flow wind speed identified the continuous part of the wake up to the downstream distance of 6–8 D. The resulting shape required smoothing and filtering to reduce the noise. Bastine et al. (2015) used a stricter threshold of 40 % of the maximum wake deficit on the LES data to extract the wake core and perform proper orthogonal decomposition on the processed wind field.

The thresholding method is not widely used due to its restriction: it applies an empirical coefficient that does not account for the data quality and wind speed fluctuations in the flow field, which may be a common issue for a lidar scan. We propose an automated threshold estimation, previously developed for whitecap detection – the adaptive thresholding segmentation (ATS) method (Bakhoday-Paskyabi et al., 2016). We adapt the method for wake identification and develop new routines to estimate the wake centerline without a priori knowledge of the wind direction.

This study focuses on the technical aspect of the ATS method and discusses its advantages and limitations. The method is applied to a scanning lidar data set containing wakes from two wind turbines and various wake–wake interactions. The measurements and LES setup are described

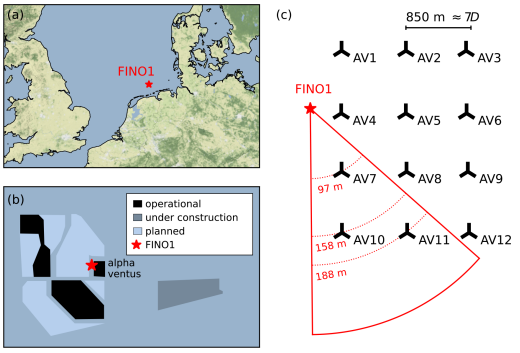

Figure 1. A schematic shows the **(a)** location of FINO1 platform, map made with Natural Earth; **(b)** wind farms and platforms near FINO1, status in 2015–2016; and **(c)** alpha ventus wind farm layout, with maximum lidar scan area and scanning height at the position of each wind turbine.

in Sect. 2. Lidar data required additional preprocessing, described in Sect. 3. In the same section, we preview diagnostic techniques by using image entropy to evaluate and classify the data. The application of the image processing method to the wake identification and characterization is detailed in Sect. 4. We demonstrate our algorithm on the idealized LES data as a proof of concept in Sect. 5. We then apply the same algorithm to the lidar data and compare the result with the manual wake detection, deficit-based thresholding, and Gaussian fit method in Sect. 6. The findings are summarized in Sect. 7. In the Appendix, we briefly discuss the differences between wake identification from the lidar scan data and the respective grayscale image.

2 Data description

2.1 Lidar and reference data

We use measurements of wind speed and wind direction recorded during the Offshore Boundary-Layer Experiment at FINO1 (OBLEX-F1) campaign. The FINO1 platform is located in the North Sea at 54°00′53.5″ N, 6°35′15.5″ E, 45 km to the north of the German island of Borkum. The alpha ventus wind farm is located in the vicinity of FINO1 and consists of 12 wind turbines arranged in a rectangular pattern (Fig. 1). The wind turbines AV1–AV6 are of the type Repower 5M with a hub height of 92 m and a rotor diameter of 126 m; AV7–AV12 are of the type AREVA M5000 with a hub height of 91.5 m and a rotor diameter D of 116 m. The row and column distances between the turbines vary within 800–850 m, approximately 7 rotor diameters, 7 D. The distance between FINO1 and the closest wind turbine, AV4, is 405 m.

The FINO1 meteorological mast has a cup anemometer installed at 90 m above sea level and a vane installed at 100 m a.s.l. (above sea level). The wind speed and direction measured with those instruments are used to characterize the free flow. We will further refer to them as the reference wind speed and direction, respectively.

The scanning Doppler wind lidar Leosphere WindCube 100S installed at FINO1 is oriented towards the alpha ventus wind farm. The closest scanned wind turbine, AV7, is located at 919 m or 7.92 D from FINO1 (Fig. 1c). The lidar is installed at 23.5 m above sea level and operates in a plan position indicator (PPI) scanning mode. In this mode, the azimuth of the lidar beam changes between 131.5 and 179.5° at an elevation angle of 4.62°. The lidar scans the southwestern sector of the alpha ventus wind farm and captures wake patterns from two wind turbines, AV7 and AV10. The third wind turbine, AV11, stays outside of the lidar range in most scans, but a part of its wake is visible for the specific wind directions. The wind turbine AV7 is scanned near the hub height at approximately 97 m. The farther wind turbines AV10 and AV11 are scanned above the top of the blade tip at 158 and 188 m, respectively.

The lidar measurements partially cover 24 September 2016 and capture a variety of wake–wake interactions. The consecutive lidar scans are separated by approximately 45 s – the time required for the lidar to finish one scan. The data set contains 600 lidar scans, which are split into 24 subsets of 25 scans. Each subset contains the first 20–22 min of each hour. For simplicity of presentation and reference, we number the lidar scans from 1 to 600.

The ATS algorithm accepts the input data as a grayscale image. The wind speed data of each lidar scan are normalized by scaling to the range of [0, 1] to imitate the grayscale intensity as

$$I = \frac{U_{\max} - U}{U_{\max} - U_{\min}}, \tag{1}$$

where U is the wind speed measured at a point, and $U_{\min}$ and $U_{\max}$ are minimum and maximum wind speeds registered in a particular lidar scan. For the lowest wind speed $U = U_{\min}$ (potential wake points), $I = 1$ denotes the points with the highest intensity. Similarly, for the highest wind speed $U = U_{\max}$ (free-flow points), $I = 0$ indicates the points with the lowest intensity.

The wake identification is performed on the data stored in a polar coordinate matrix (Fig. 2a). For a better presentation, the resulting data are plotted in the Cartesian coordinates as a scanned sector (Fig. 2b).

2.2 Large-eddy simulation

We also perform a large-eddy simulation to demonstrate and verify the performance of the ATS method and compare it against the Gaussian wake identification and characterization method described further in Sect. 4.3. We use the PALM

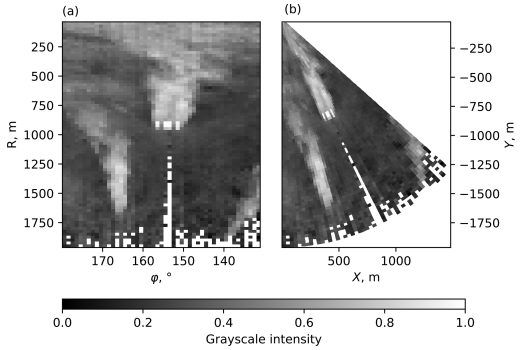

Figure 2. An example lidar scan 497 taken on 24 September 2016 19:18:20 UTC+0 at reference wind speed 7.4 m s^{-1} and reference wind direction 151.14°. The original data are presented in **(a)** the polar coordinates R, φ as stored in the matrix and **(b)** the Cartesian coordinates X, Y.

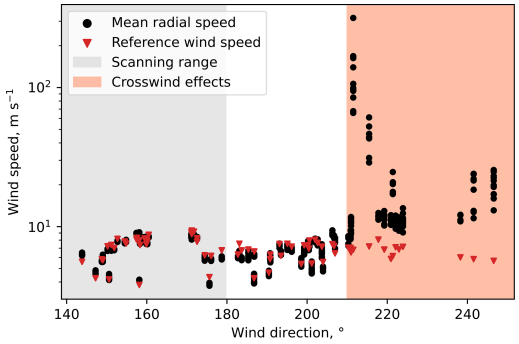

Figure 3. Comparison of the mean radial wind speed and the reference wind direction in the data set.

LES code with a built-in actuator disc with rotation (ADR) wind turbine model (Maronga et al., 2020). The results produced with the model were shown to capture the reduction of the wake deficit with the downstream distance at the rate similar to the accounted for wind turbines (Vollmer et al., 2015, 2017; Doubrawa et al., 2020). The wake recovery aspect is particularly important to test the ATS method performance in the far wake. The currently used polynomial kernel also allows us to fit the Gaussian function to compare it with the ATS method.

The domain contains $2304 \times 576 \times 192$ points and has horizontal grid spacing of 4 m. The vertical spacing below 600 m is also 4 m. Above 600 m, the vertical spacing is stretched with a factor of 1.08, capped at maximum 8 m grid cell height. The roughness length of $z_0 = 0.0005$ m corresponds to the calm sea surface. The Coriolis forcing is enabled for the latitude of 54°, and the wind speed components are set to $u = 10.5\,\mathrm{m\,s^{-1}}$ and $v = -2.6\,\mathrm{m^{-1}}$ so that the flow rotation is compensated for, and the flow is aligned with the x axis, resulting in horizontal speed of $10\,\mathrm{m\,s^{-1}}$ at the hub height. The surface temperature is 277 K and increases by 1 K per 100 m. Neither heat flux nor surface heating are activated. During the simulation the turbulence intensity reaches 6.6 %.

The reference NREL 5 MW wind turbine has a hub height of 102 m and a diameter of $D_\mathrm{r} = 126$ m and is placed in the center of the domain so that the wake length can reach up to 20 D_r.

The LES is used solely to generate idealized wake data. No direct comparison to the lidar data is performed.

3 Lidar data pre-processing and classification

3.1 Data quality

Working with the current data set, we encountered two types of noise affecting the quality of the wake identification through thresholding: small wind speed fluctuations not directly caused by the wake and high wind speed values appearing due to a measurement error.

The measurement errors are primarily caused by the difference between wind direction and lidar orientation. The lidar measures radial velocity, which can be represented through three directional wind speed components u, v, and w, and the information on the line of sight of the lidar beam, given by the azimuth ϕ and elevation angle θ:

$$U = u \sin\phi \cos\theta + v \cos\phi \cos\theta + w \sin\theta. \quad (2)$$

When the wind blows along the lidar's line of sight, the measured radial velocity is essentially the horizontal wind speed. If the wind direction differs from the line of sight, the radial velocity deviates from the actual wind speed magnitude. In the case of crosswind – the wind direction is close to perpendicular to the line of sight – the radial velocity tends to zero and does not represent the actual wind speed. The measurements taken during the crosswind event are more prone to errors compared to other wind directions.

When plotted against the reference wind direction, the reference wind speed and mean radial wind speed of a lidar scan show strong discrepancy for a range of wind directions (Fig. 3). With the lidar scanning in the range of 131.5–179.5°, the crosswind effects can be expected for the wind directions of 221.5–269.5°. As shown in Fig. 3, the crosswind effects already appear for the wind direction above 210°. The scans taken near the crosswind direction show a large number of non-physical wind speed values reaching 100–1000 m s^{-1}. We further refer to these scans as "corrupted".

Occasionally, we also observe weaker spikes in the radial wind speed, most of which are localized at the position of a

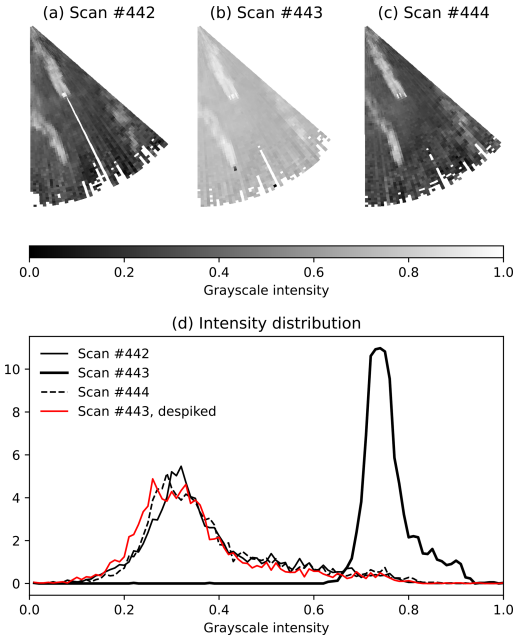

Figure 4. Consecutive lidar scans from the bimodal subset. No outliers are present in scans 442 **(a)** and 444 **(c)**, while scan 443 **(b)** has wind speed spikes near the wind turbine position and in the far range; panel **(d)** shows the intensity distribution for the same scans.

wind turbine AV10, implying a measurement error due to the lidar beam reflection from rotating blades. The reference and mean radial wind speeds remain in good agreement for the wind directions below 210° despite containing spikes in the wind speed data. Nevertheless, the outliers cause an intensity skew when the wind speed data are normalized to the range of [0, 1] (Fig. 4). The intensity distribution peak moves to the right, with the left side containing occasional low bumps caused by the spikes (Fig. 4d).

In the example, the middle scan (Fig. 4b) has a wind speed spike of $15\,\mathrm{m\,s^{-1}}$, while the reference wind speed reaches $5.8\,\mathrm{m\,s^{-1}}$. The radial wind speed magnitude measured in the spike region stays below $7\,\mathrm{m\,s^{-1}}$. The lidar scan after normalization shows less contrast compared to the adjacent lidar scans.

To preserve the uniformity between consequent lidar scans of the same subset, we perform despiking – detection and removal of the spikes. The spikes are detected based on the wind speed value and the difference with the adjacent points. We delete all values higher than $30\,\mathrm{m\,s^{-1}}$ and check the remaining data for the local maximums. An empirically chosen wind speed difference of $7\,\mathrm{m\,s^{-1}}$ proved to be enough to designate a local maximum as a spike. When a spike consists of a single or double point, the values there are deleted, and the resulting gap is filled by interpolation to retain the continuous wind field. Three or more adjacent points designated as spike are considered a noise cluster; in such cases, gap filling after removal is not performed.

Since the lidar is oriented towards the closest wind turbine, a string of missing values – a wind turbine "shadow" – is always present in the lidar scans regardless of the wind direction. The shadow rarely crosses wind turbine wakes and does not noticeably affect the performance of the wake detection methods. Hence we do not perform a gap filling to remove the shadow in addition to the despiking.

3.2 Information entropy and data classification

We introduce entropy criteria as an alternative to using reference wind speed and direction for quality control. The entropy application ranges from finding a threshold (Pun, 1981) to object classification in an image (e.g., satellite map segmentation by Long and Singh, 2013). Here, we calculate it primarily for diagnostic purposes and data classification into subsets.

The information entropy is a measure of noise in the data. It can be calculated for the whole data set as well as across the rows or columns of a rectangular matrix containing 2D data. We apply Shannon entropy S (Shannon, 1948) as follows:

$$S = -\sum_{i=1}^{n} P(x_i)\log_2 P(x_i), \tag{3}$$

where $P(x_i)$ is the probability density function (PDF) of the variable x_i (here intensity) to occur in the data. If the entropy tends to zero, it indicates uniform data. A high entropy value implies disturbances in the lidar scan due to wakes or noise.

To analyze lidar scan features, we calculate entropy for the partial data instead of the whole scan. We select wind speed values in either the radial or azimuthal direction and calculate a PDF of this sample to pass it to the entropy function. An example is presented in Fig. 5. The top and the left parts of the example scan in polar coordinates do not contain wakes; hence the entropy calculated for the respective rows and columns is lower than for the wake regions. The entropy calculated in the radial direction (Fig. 5a) is higher for columns crossing both wakes instead of one due to a higher disturbance rate. An additional entropy increase near the azimuth of 130–140° can be explained by high noise at the lidar scan border. The entropy calculated in the azimuthal direction (Fig. 5c) shows a peak for the AV7 wake. The AV10 far wake produces a less prominent peak, indicating a wake spread along a longer distance and not aligned with the azimuthal direction.

We calculate the entropy in radial and azimuthal directions for all lidar scans before preprocessing. Combined into two plots, the entropies present an overview of the data set (Fig. 6). The respective wind turbine positions are marked on the right axis. The lower color bar limit is adjusted for better

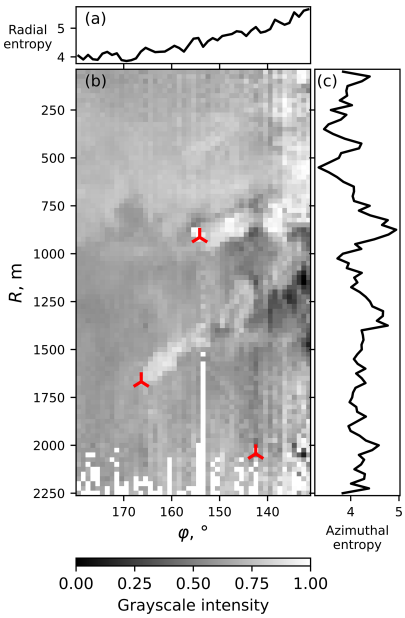

Figure 5. The entropy calculated in the **(a)** radial and **(c)** azimuthal directions of **(b)** the lidar scan 61. Reference wind speed is 7.19 m s^{-1} and reference wind direction is 203.68°.

presentation of the features contained in non-corrupted scans. For the scans with low noise, the entropy values fall into the range of 4–5 in both the azimuthal and radial directions. The entropy calculated in the azimuthal direction highlights several lidar scans with a substantial entropy decrease (Fig. 6a) – the value drops below 2 and tends to zero. The same scans are also characterized by the measurements corrupted due to the crosswind effect. The spiked data in non-corrupted scans lead to a local entropy decrease, seen as occasional blue dots mostly at the location of AV10. Series of such points can be seen for scans 176–200 and 401–410.

Non-corrupted subsets show similar entropy distribution in the azimuthal direction (Fig. 6a). A wake from the wind turbine AV7 can be seen as an increase in entropy near the turbine's location. A weaker increase in entropy can also be seen for AV10, for example, in scans 51–175.

The entropy calculated in the radial direction is distributed uniformly for the corrupted subsets (Fig. 6b) but otherwise does not have as strong of a difference to non-corrupted data as the entropy in the azimuthal direction (Fig. 6a). Some non-corrupted scans (51–300 and 376–425) show a gradient-like pattern caused by the absence of wakes in the 170–180° sector (low entropy) and wakes and border noise in the 130–140° sector (high entropy). The pattern is weaker for scans 176–250, where the border noise is absent and wakes are aligned along the line connecting wind turbines, thus disturbing a smaller area of a lidar scan. The scans 426–600 combined demonstrate a horizontal stripe pattern, caused by the wind blowing towards the lidar. Wakes forming across the scanned azimuths cause the entropy increase in the radial direction matching the positions of AV7 and AV10, as marked on the graphs.

The low entropy criterion agrees well with the crosswind criterion on which scans are likely to contain a high amount of corrupted data. In general, the scans with a high corruption rate can be identified based on the percentage of the data points exceeding a specific wind speed limit. Since the reference wind speed does not exceed 10 m s^{-1}, we consider the wind speeds above 30 m s^{-1} to be a likely measurement error. The corrupted scans consistently have at least 1 % of points exceeding this limit. The percentage drops to 0 %–0.05 % for the rest scans and corresponds to the occasional spikes.

The number of corrupted scans is 125, i.e., about one-fifth of the total number of scans. Classification of the remaining valid scans requires either a priori knowledge of the reference wind direction (which may be unavailable if we work with image data) or visual evaluation of the wake features (which may be complicated for a large data set). Entropy criteria can simplify the classification by presenting a condensed overview of the data set. Using the entropy and intensity histograms, we classify the subsets into the following groups.

1. *Parallel-wake subset*, Fig. 8a. The wakes do not interact with each other. Some noise may occur at the lidar scan's border due to the wind direction approaching the value where the crosswind effects start. Since the wakes propagate towards this border and add to the disturbance, the entropy calculated in the radial direction shows a consistent increase near the azimuth of 131°. The entropy calculated in the azimuthal direction shows a strong increase near the location of AV7 due to the wake and a weaker disturbance caused by AV10. The intensity histogram of an averaged subset tends to be more symmetrical than in other subsets and has a peak close to the intensity of 0.5. The intensity histogram of a single scan has a peak deviating from the center depending on the amount of noise. Parallel wakes are the most common case for this data set.

2. *Aligned-wake subset*, Fig. 8b. The wind blows along the line connecting wind turbines AV7 and AV10 so that the former is subjected to a wake. The entropy patterns are generally similar to the parallel-wake subset, except that a footprint of the AV10 wake is no longer visible for the entropy calculated in the azimuthal direction. The wind direction is closer to the scanned azimuth range, and measurements have less noise compared to the parallel subset. Hence the scans show slightly lower entropy. Compared to the parallel-wake subset, the histogram peak is shifted to the left. The histogram peak may split

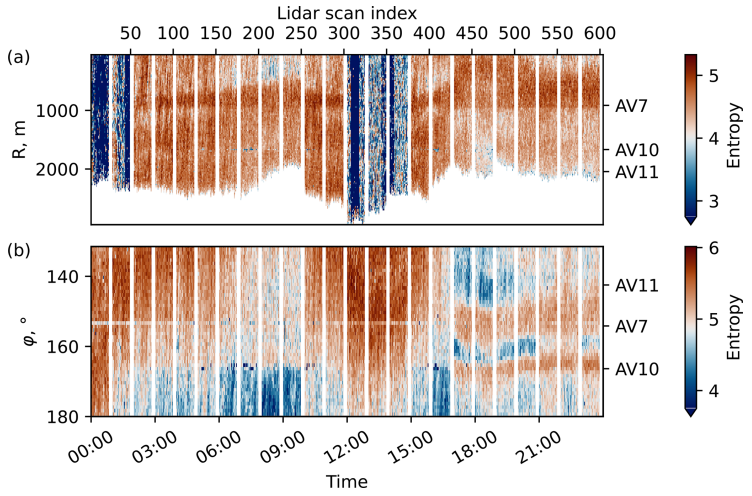

Figure 6. Entropy of the raw lidar data with all 600 lidar scans combined: **(a)** azimuthal entropy and **(b)** radial entropy.

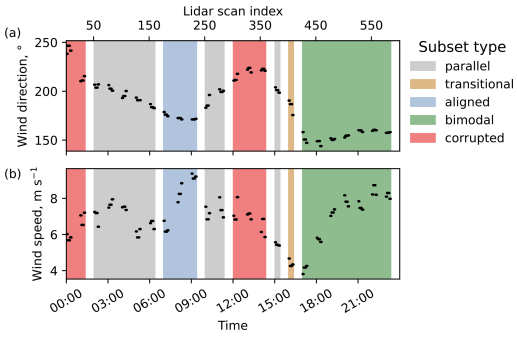

Figure 7. Classification of the subsets and overview of the reference wind direction **(a)** and wind speed **(b)**.

into two small peaks located close to each other when the wakes are not perfectly aligned.

3. *Transitional subset*. The wind direction changes, so both parallel and aligned wakes can be observed in the subset. This behavior is observed for a single subset containing scans 401–425. The transition to slightly lower entropy can be seen for the entropy calculated in the radial direction at azimuths 130–150° (Fig. 6b).

4. *Bimodal subset*, Fig. 8c. The wind blows along the lidar beam. Two long wakes are formed behind the wind turbines and merge in the lidar near range. Since the near range is scanned at a high resolution (Fig. 2), the far wake is represented by a larger percentage of points compared to the other subsets. Consequently, the intensity histogram approaches a bimodal distribution, which is especially prominent for the averaged subset. The larger peak represents the free flow, while the smaller peak corresponds to the far wakes of AV7 and AV10. The two peaks may merge resulting in one flat peak. The scans have little noise; the increase in entropy, especially in the radial direction, highlights the presence of the wakes.

5. *Corrupted subset*, Fig. 8d. The lidar scan is characterized by the number of non-physical measurements (wind speed higher than $30\,\mathrm{m\,s^{-1}}$) exceeding 1 % of the lidar scan points. While the valid measurements still take the largest share of a single scan, they are now considered "low" wind speeds in a comparison to the maximum value. Due to the normalization (Eq. 1) that converts low values into light pixels, the histogram tends to the far right side, forming a sharp peak in intensity values between 0.9 and 1.0. The entropy in the azimuthal direction is lower than in other subsets and approaches zero, while the entropy in the radial direction tends to be more uniform than in non-corrupted scans and does not react to the presence of a wake.

The overview of the subsets and reference values is presented in Fig. 7 and Table 1, containing wind speed, wind direction, and entropy averaged over each subset. A sample histogram averaged for a typical subset from each group is shown in Fig. 8 together with a single-scan histogram from the same subset.

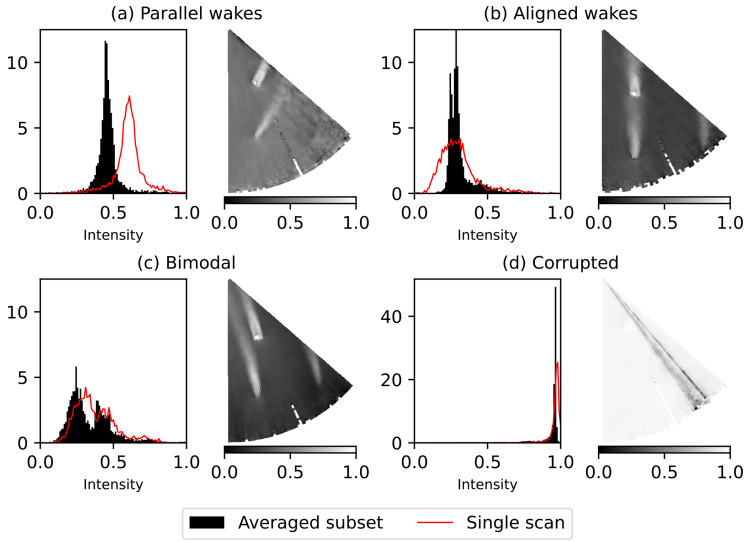

Figure 8. Sample averaged subsets and intensity histograms corresponding to the averaged subset and a single scan within the subset. The wind speed data are normalized to imitate the grayscale intensity. Despiking and removal of non-physical wind speeds are not performed to preserve the characteristics before preprocessing.

Table 1. Overview of the lidar data subsets.

Data type	Subset	Scans	WSPD, $m\,s^{-1}$	WDIR, °	Entropy	% of data
Parallel wakes	3	51–75	6.99	205.3	5.11	33.3
	4	76–100	7.71	202.7	5.29	
	5	101–125	7.48	196.0	5.38	
	6	126–150	6.05	191.4	5.35	
	7	151–175	6.58	184.0	5.01	
	11	251–275	7.10	187.8	5.12	
	12	276–300	7.41	200.2	5.37	
	16	376–400	5.45	200.9	5.02	
Transitional	17	401–425	4.38	184.5	4.76	4.2
Aligned wakes	8	176–200	6.32	176.2	4.69	12.5
	9	201–225	8.30	172.2	5.28	
	10	226–250	9.19	171.3	5.30	
Bimodal	17	426–450	4.11	151.5	5.44	29.2
	18	451–475	5.71	147.3	5.31	
	19	476–500	7.22	150.9	5.72	
	20	501–525	7.83	154.2	5.67	
	21	526–550	7.52	159.4	5.64	
	22	551–575	8.46	160.1	5.72	
	23	576–600	8.16	157.7	5.70	
Corrupted	1	1–25	5.80	243.3	1.54	20.8
	2	26–50	6.85	212.1	2.31	
	13	301–325	7.27	213.4	1.53	
	14	326–350	7.06	222.2	2.64	
	15	351–375	6.41	222.0	2.52	

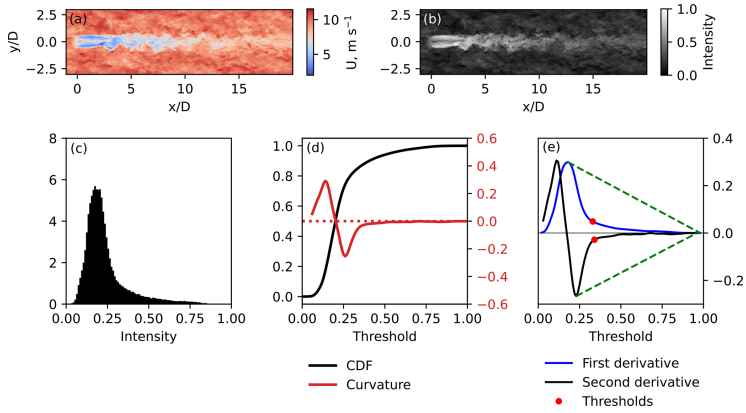

Figure 9. Sample LES wake and threshold detection. **(a)** Original instantaneous flow, **(b)** same flow normalized to the range of [0, 1], **(c)** the intensity histogram of the normalized data, **(d)** CDF of the normalized data and CDF plot curvature, and **(e)** first and second derivatives of the CDF and the estimated thresholds.

4 Methodology

Wake detection includes two stages (Quon et al., 2020): wake identification (a separation of the wake from the free flow) and wake characterization (further analysis of the identified wake). We focus on the wake identification methods, particularly an identification method using thresholding, and also provide an algorithm for the wake characterization through centerline detection from the thresholded data.

4.1 Wake identification using automatic threshold detection

The thresholding methods split an image into background (in our case – free flow) and foreground (wake). Despite lidar data having a considerable number of disturbances in the free flow, the wind speed distribution in a lidar scan tends to have one peak, either sharp or flattened (Fig. 8). The wake points take a small share of the lidar scan stored in polar coordinate matrix, while the remaining points belong to the free flow – i.e., the most prominent peak contains free-flow points. The exception is the bimodal subset, where the far wakes are characterized by high number of points (Fig. 2). As a result, the histogram of a scan from the bimodal subset may have two peaks depending on the intensity of the far wakes. To make our wake identification method universal, we build it upon threshold detection from a single histogram peak. The specifics of the wake identification in the bimodal case are further described in Sect. 6.4 and in the Appendix.

A single peak limits the applicability of the common thresholding methods that search for the local minimum of a bimodal histogram (Otsu, 1979). The lidar scan structure has similarities with ocean surface images: a background with small disturbances and bright whitecaps. Bakhoday-Paskyabi et al. (2016) described three methods of an automated threshold detection for the whitecaps. We choose an adaptive thresholding segmentation (ATS) method identified to be fast and reliable by the original study. The basic principles of the ATS method are introduced here on a test example of an instantaneous LES wake.

Figure 9a and b show the wind speed field of an instantaneous LES wake and the same data normalized to the range of [0, 1]. A threshold T is an intensity value in the range [0, 1] that separates free flow and wake points. After the threshold is applied to the normalized wind field, a binary matrix **WP** is constructed from the grayscale intensity matrix **I** as follows:

$$\mathbf{WP}(i,j) = \begin{cases} 0: & \mathbf{I}(i,j) \le T - \text{free-flow point}, \\ 1: & \mathbf{I}(i,j) > T - \text{wake point}. \end{cases} \quad (4)$$

The intensity threshold can be converted back to the radial velocity threshold U_{th} by reverting the normalization expression Eq. (1) as

$$U_{\text{th}} = U_{\max}(1-T) + U_{\min}T. \quad (5)$$

The normalized wind speed data are represented as an intensity histogram (Fig. 9c). Let $H(x)$ for $k \in [0,1]$ be the cumulative distribution function (CDF) of the intensity data. Then $H'(k)$ and $H''(k)$ are its first and second derivatives, respectively. With respect to the definition of intensity I in Eq. (1), the wake points are located in the histogram's tail, while the free-flow points form a peak on the left side. The transition region where the peak tends to the tail is a good choice to search for a suitable threshold. We detect the threshold at the point where the CDF slope is close to constant; i.e., the curvature $C(k)$ approaches zero.

$$C(k) = H''(k)\left[1 + H'(k)^2\right]^{-3/2} \quad (6)$$

The curvature graph tail (Fig. 9d) may fluctuate and complicate the detection of the zero curvature. Instead, we look at the first and second derivatives $H'(k)$ and $H''(k)$ separately. The threshold value T_2 is selected as an inflection point at the right side of the second derivative graph (Fig. 9e). A similar point in the first derivative graph T_1 is used as a control value. We select the threshold as an average value between first and second derivative inflection points to smooth the threshold detection outcome. If the points initially lay close to each other, the averaged threshold $T = (T_1 + T_2)/2$ would not deviate too far from T_2. If the difference between T_1 and T_2 is high, the smoothing prevents the threshold from being too strict and leaving weak wakes undetected.

In the case of the lidar data, the derivative plots have strong oscillations. Therefore, we fit a polynomial function on the range between intensity I_k, corresponding to the most prominent local extremum and maximum intensity $I_{\max} = 1$. We fit a function $F(k) = a_1 + a_2/k^5$, since the corresponding fit returned low root-mean-square error (RMSE) while not altering the inflection point location significantly.

After the threshold is found, we apply it to the data as described in Eq. (4) and obtain a binary matrix **WP** that represents thresholded data. Each matrix point corresponds to an image pixel. Because of the wake irregularity, especially in the lidar scan, the method usually detects several clusters of high-intensity points. Any cluster may be a part of a wake as well as falsely detected noise. We do not yet distinguish between wake and noise and refer to all detected clusters as "wake shapes". Due to the code implementation, the detected points belong to the same shape as long as the constituting points are adjacent in the matrix **WP**. The shapes touching only by the corners are considered to be separate shapes.

4.2 Wake characterization from the data thresholded by the ATS method

For the wake characterization, we detect the centerline of a wake shape. The centerline search method starts with extracting a contour of a wake shape; the further algorithm is based upon the geometrical properties. It should be noted that the centerline search algorithm does not strictly depend on the ATS method and can be used as a stand-alone algorithm that requires thresholded data as an input.

To start the centerline search method, we require a procedure to determine which shapes were correctly identified as a wake. The ATS method searches for the high-intensity points corresponding to the highest wake deficit. Containing the highest wind speed decrease, the near-wake region perfectly satisfies this condition. Therefore, it can be expected that the near wake will be one of the largest continuous shapes among those detected and will contain a wind turbine within or near it. The borderline contour of such a shape is extracted for further analysis. The wake centerline is then defined as a centerline of the extracted contour.

Assuming the outline of the shape as wake boundaries, we estimate the wake centerline using the following algorithm.

1. The algorithm starts by drawing a circle of radius 1 D around the wind turbine and marks points where the circle crosses the borders of the wake shape. If the circle appears to lie within the wake shape completely, the initial radius is increased until intersections are found.

2. The midpoint of the arc inside the wake contour indicates the wake direction and is stored as the centerline midpoint.

3. The circle diameter is increased by a pre-defined step, e.g., 0.1 D, and the steps 1–2 are repeated until the end of the wake shape is reached.

This short algorithm works as it is for an ideal case of a smooth wake contour and known wind direction matching the wake direction. However, the circular lines may cross the irregular wake contour several times. Considering the near wake to be wide and continuous, we expect the centerline point to lie within the wake shape. We also assume that the wake does not turn gradually further downstream. Therefore, the segment between the last known and unknown midpoint should turn by a relatively small angle compared to the previous segment. The wind or wake direction is advantageous to distinguish wake shapes from noise, as it allows us to narrow the search by disregarding shapes detected in the upwind direction as false detection.

Procedure 1 Automatic threshold detection

Input: U(r, ϕ) {raw lidar data}
despike U(r, ϕ)
Input: $k \in [0, 1]$ step 0.01
$I \leftarrow (U_{\max} - U)/(U_{\max} - U_{\min})$
$H \leftarrow f(I, k)$ {get the intensity histogram}
$H_1 \leftarrow \partial H/\partial k$
smooth H_1 with moving average $n = 4$
$H_2 \leftarrow \partial^2 H/\partial k^2$
smooth H_2 with moving average $n = 4$
normalize H_1 and H_2
$P_1 \leftarrow$ fit $F(k) = a_1 + a_2/k^5$ on $[k(\max H_1), 1]$
$P_2 \leftarrow$ fit $F(k) = a_1 + a_2/k^5$ on $[k(\min H_2), 1]$
$T_1 \leftarrow P_1$ inflection
$T_2 \leftarrow P_2$ inflection
Output: $T \leftarrow (T_1 + T_2)/2$
{threshold data as $WP(r, \phi)$}
if $I(r, \phi) < T$ **then**
$WP(r, \phi) \leftarrow 0$ {free-flow point}
else
$WP(r, \phi) \leftarrow 1$ {wake point}
end if

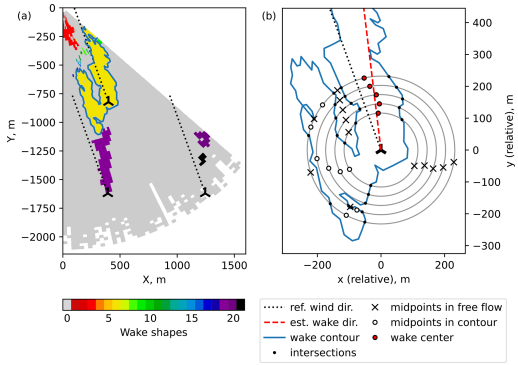

Figure 10. An example wake centerline detection in an ambiguous case.

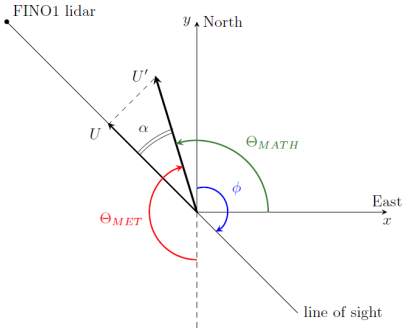

Figure 11. The relation between radial wind speed U, actual wind speed U', azimuth angle ϕ, and meteorological and mathematical wind directions Θ_{MET} and Θ_{MATH}.

The currently used centerline search algorithm 2 provided further includes these and several other rules for selection of a wake point when an ambiguity is present. Figure 10 shows an example of resolved ambiguity based on the wind direction. If the wind direction was not available, an estimated wake direction could be used instead with the same outcome.

Generally, this centerline search method does not require a priori knowledge of the wind direction. However, it may be difficult to resolve the ambiguity on the first step, if the wind direction is unknown. For example, the aligned-wake subset (Fig. 8b) and, to a certain extent, also the bimodal subset (Fig. 8c) introduce ambiguity in the wake direction for the downstream wind turbine AV7. A circle drawn around AV7 may cross the detected wake in at least four points. The algorithm will in turn identify downstream and upstream points as potential centerline points. To continue the search, the algorithm has to select only one direction. In the absence of the reference wind direction, the ambiguity can be resolved by approximating the wake direction first.

The procedure to approximate the wake direction runs similarly to the centerline search, with a few alterations. First, the step is increased, but the algorithm is run for a shorter length until 4 D downstream, so only the most well-resolved part is processed. All midpoints laying inside the wake contour are accepted, since there is no way to make a distinction between them as of yet. A linear function $y(x) = ax$ is then fit to the identified midpoints. If the coefficient of determination is negative ($R^2 < 0$), the fit is too inaccurate, and the procedure is repeated for another wind turbine.

The intercept value a of the best fit is the arctangent of the mathematical wind direction (Fig. 11). The approximated meteorological wind direction is then

$$\Phi_{\mathrm{MET}} = \frac{3}{2}\pi - \Phi_{\mathrm{MATH}} = \frac{3}{2}\pi - \arctan a. \tag{7}$$

The approximated wake direction may strongly deviate from the actual wake direction, so it is only used to resolve ambiguity. The actual wind direction is estimated from the full centerline. We convert the coordinates of the centerline points for the AV7 and AV10 wakes to the Cartesian system and subtract the respective wind turbine positions to get a set of the relative centerline coordinates. We assume a centered data set and add a point (0, 0) corresponding to the relative wind turbine position. The wake from the wind turbine AV11 is prominent only for the bimodal subset and is too short and easily confused with the noise in the other subsets. We do not consider this wake in our analysis due to the little information it can provide compared to the other two wakes. The composed data set is fitted with the linear regression, and the fitted line indicates the estimated wake direction.

4.3 Wake identification and characterization using the Gaussian method

The wake deficit distribution is similar to the Gaussian distribution in the far wake (Ainslie, 1988) and often shows a double Gaussian peak in the near wake (Magnusson, 1999). The similarity to the Gaussian distribution makes a base for a widely used method to detect wake boundaries and centerline (Vollmer et al., 2016; Krishnamurthy et al., 2017). The method requires the data in a two-dimensional horizontal plane, which makes it versatile and practical to use for wake identification and characterization.

Due to the lidar elevation angle, AV10 is scanned near the top tip and does not show a double wake. The scan resolution near AV7 is not always sufficient to resolve a pronounced double wake. Therefore, we fit the wake deficit distribution with a single Gaussian function:

$$F(y) = A \exp\left(-\frac{(y-\mu)^2}{2\sigma^2}\right), \tag{8}$$

where the amplitude A, mean value μ, and standard deviation σ are the parameters to fit; the variable y is a coordinate on a line perpendicular to the wind direction. The fitting

Procedure 2 Wake centerline detection

$N(r,\phi) \leftarrow$ label $WP(r,\phi)$ {enumerate detected shapes}
Input: (x_w, y_w) or (r_w, ϕ_w) {wind turbine coordinates}
if $WP(r_w,\phi_w) = 1$ **then**
$n \leftarrow WP(r_w,\phi_w)$ {select a wake shape containing the wind turbine}
else
find $n \in N$ and R {select the largest detected shape near the wind turbine location}
end if
$L \leftarrow$ boundary contour of the wake shape n
for $d = 1$ to $15D$ step $0.1D$ **do**
$C \leftarrow$ contour of a circle with radius r centered at (x_w, y_w)
$p^i \leftarrow$ intersect L and C
calculate midpoints on the arc between (p^i, p^{i-1})
$N_p \leftarrow$ number of midpoints inside the wake shape n
if $N_p == 0$ **then**
$(x_c^r, y_c^r) \leftarrow$NaN {the circle does not cross the wake contour}
else if $N_p == 1$ **then**
$(x_c^r, y_c^r) \leftarrow$ midpoint p_1, p_2 {centerline point is the only midpoint inside a wake}
else
{ambiguous centerline point, limit the search}
$\alpha \leftarrow$ deviation from the know wind or wake direction for each valid midpoint
$(x_c^r, y_c^r) \leftarrow \min(\alpha^{(x_c^r, y_c^r)})$
end if
end for
Output: X_c, Y_c

starts from 1 D to avoid uncertainties caused by a weak double wake observed for AV7. We attempt fitting for the wake deficit profiles up to 15 D downstream distance, covering the length of most wakes in the lidar data set.

For a wake deficit distribution, the fitted Gaussian function $F(y)$ reaches its maximum at $y = \mu$; i.e., the estimated mean μ gives the wake center position. The wake boundaries are defined through the mean value μ and the standard deviation σ as $\mu \pm 2\ln 2\sigma$ so that the velocity deficit at the wake boundaries is 5 % of the velocity deficit at the wake center (Aitken et al., 2014).

The Gaussian function is fitted to the wake deficit of $\Delta U(y) = 1 - U/U_0$; thus knowledge of the free-flow wind speed U_0 is also required. Since the background flow is rather non-uniform in the lidar scans, we probe the velocity at each cross section at 1.6 D from the rotor axis (Krishnamurthy et al., 2017). The LES data use the wind speed at the hub height as the free-flow wind speed.

We run the Gaussian method in an automatic mode. The method should be applied to the data extracted along the straight line perpendicular to a pre-defined search direction. The algorithm thus requires knowledge of the wind direction before the fitting. The algorithm is also dependent on the accuracy of the wind direction measurements and the similarity between reference wind and actual wake direction. During our analysis, we observed an offset of about 5° between the directions, which caused fitting errors for otherwise clear wake. To reduce the influence of a possible discrepancy between wind and wake direction, we recalculate the search direction every five points by fitting the linear function to the previously found center points.

The wake deficit profiles extracted for fitting have a width of 2.5 D, except for the bimodal subset. There, the profile width is decreased to 1.75 D after reaching the downstream distance of 6 D. The correction is active only for the scans after 500 where the AV10 far wake and the AV7 wake come close enough but do not yet merge completely and allow separation. If the Gaussian function is fit to a wider profile there, the fitting would mistake higher deficit in the AV7 near wake for the center of the AV10 wake. Reducing the extracted wake profile width improves the centerline detection in the AV10 far wake and delays the first occurrence of this error, although it does not always prevent it.

4.4 Deficit-based wake identification

In addition to the Gaussian fit, we apply a threshold based on the wake deficit criterion. The method assumes that a point belongs to the wake if the wind speed there is less than or equal to 95 % of the free-flow wind speed (España et al., 2011), here the reference wind speed.

The lidar measures radial velocity U (Eq. 2). If the wind direction differs from the scanned azimuths, the reference wind speed measured by a cup anemometer noticeably deviates from the free-flow radial velocity. Normally, a lidar retrieval procedure should be performed to reconstruct the actual wind field. Since we are only interested in the wind speed values, but not the local flow direction, we apply a simple expression to re-project the radial velocity and take the magnitude of the calculated wind speed.

$$U'_{\mathrm{r},\phi} = \frac{U_{\mathrm{r},\phi}}{\cos\alpha}, \tag{9}$$

where $U_{\mathrm{r},\phi}$ is the measured radial velocity at the beam range r and azimuth ϕ, $U'_{\mathrm{r},\phi}$ is the estimated magnitude of the real velocity, and α is the angle between the radial and actual wind speed vectors (Fig. 11). Equation (9) assumes that the flow moves in the reference wind direction at each scanned point regardless of the wake influence and other flow disturbances.

The angle α is calculated as the difference between reference wind direction Θ_{MET}, given according to the meteorological convention, and the azimuth ϕ (Fig. 11). That is, Eq. (9) changes to

$$U'_{\mathrm{r},\phi} = \frac{U_{\mathrm{r},\phi}}{\cos\alpha} = \frac{U_{\mathrm{r},\phi}}{\cos\left(\Theta_{\mathrm{MET}} - \phi\right)}. \tag{10}$$

Since the normalization (Eq. 1) is not performed, the deficit-based method does not necessarily require despiking – all high-value outliers would be assigned to the background flow by the threshold condition. However, the method requires additional information on the free flow, such as the wind speed and direction, to perform the simple retrieval.

The threshold is applied to the wind speed field recalculated with Eq. (10) instead of the original radial velocity field used for the ATS method. Therefore direct comparison of the thresholds is complicated. Instead, we compare the thresholded images and evaluate the detection accuracy against the manual wake identification.

4.5 Manual wake identification and characterization

We perform a manual segmentation to select an optimal threshold for each lidar scan and use it as a "true" identification. The manual threshold is defined in a way to represent the minimum threshold required to identify a wake shape suitable for the automatic centerline detection as described in Sect. 4.2. The comparison against manual wake identification then would show whether the ATS method is capable of automatizing the threshold selection and improving its flexibility compared to the deficit-based thresholding.

Since the available scans represent different wake–wake interactions, the criteria for a reasonable threshold vary over the subsets. In order to reduce human error, we use the following qualitative criteria:

1. The shape of the wake should be distinguishable enough not to be misinterpreted as noise.
2. The noise should be reduced near wind turbines AV7 and AV10 but is allowed near AV11 since its wake has low importance in this study.
3. The identified wakes from AV7 and AV10 should not merge to ease the centerline detection.

We also perform a manual centerline detection. A centerline is drawn over the lidar scan as a line or series of points. For further comparison with other wake characterization methods, it is converted to the Cartesian coordinates using a plot digitizer. Unlike the manual threshold detection, the manual wake characterization is more prone to errors, especially in the far-wake region, where the wake becomes less distinguishable from the free flow. Due to ambiguity and complexity of the manual centerline detection, we select only a few lidar scans to demonstrate the methods' performance in the parallel, aligned, and bimodal subsets.

For brevity, the wake identification and characterization methods are further referred to as listed in Table 2.

5 Proof of concept: wake identification and characterization from the LES data

In this section, we demonstrate the performance of the ATS method in application to the LES data and compare the result to the Gaussian method.

An instantaneous LES wake reveals complex spatial features to be detected, although its intensity histogram remains rather smooth (Fig. 9b). The ATS method detects a continuous structure in the near wake and the beginning of the far wake, while the wake at $x/D > 10$ is represented as series of small disconnected structures (Fig. 12b and c). The ATS method does not capture the wake expansion, but only a trail of the low-wind-speed areas.

Since the ATS method extracts the outer contour of a shape, small holes inside the detected wake are automatically filled and do not affect the intersection-based centerline search (Fig. 13a). The current algorithm processes only the first continuous wake shape. Extending the centerline downstream requires a procedure to identify which of the small detected shapes actually belong to the far wake and the connection order. The former problem is more relevant for a lidar scan, which has less uniform background flow compared to the LES data.

Table 2. Summary of the wake detection methods.

Name	Main characteristics
Manual	Input data: radial velocity field. Identification: threshold value based on the visual evaluation. Characterization: digitized centerline drawn over the lidar scan. Automation: no. Flexibility: yes.
Deficit-based	Input data: retrieved velocity field, Eq. (9), reference wind speed. Identification: threshold value based on the wake deficit compared to the free flow. Characterization: not performed. Automation: yes. Flexibility: no.
Gaussian	Input data: radial velocity field, wind direction, and wind turbine locations. Identification: Gaussian function fitted to the wake profile. Characterization: performed simultaneously with the wake identification. Automation: yes. Flexibility: partial.
ATS	Input data: radial velocity field, wind direction (optional), and wind turbine locations. Identification: threshold value from the intensity histogram. Characterization: midpoints of the concentric arcs crossing the wake contour. Automation: yes. Flexibility: partial.

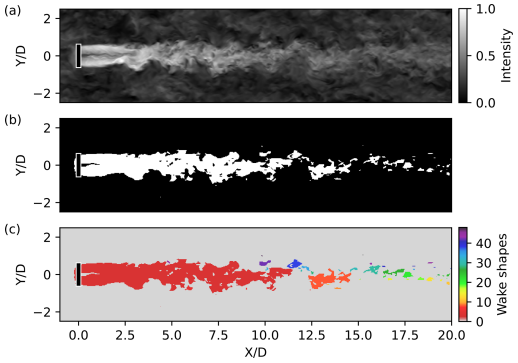

Figure 12. Wake and centerline identification for a sample instantaneous LES wake: **(a)** normalized flow field, same as Fig. 9b; **(b)** thresholded flow field; and **(c)** wake shapes color-coded to show connectivity.

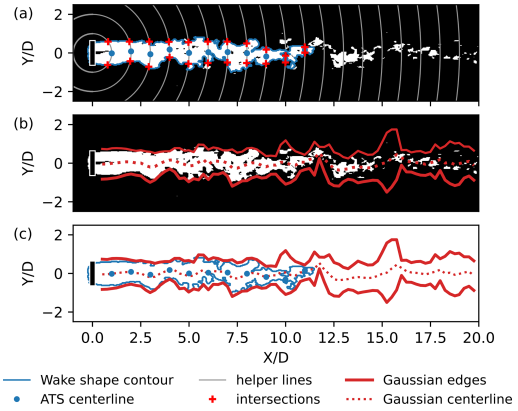

Figure 13. Sample wake identification and characterization using idealized LES data. **(a)** Thresholded data overlaid with the contour of the wake shape; **(b)** thresholded data overlaid with the wake boundaries and centerline detected by the Gaussian method; and **(c)** ATS and Gaussian wake detection results, overlaid.

Figure 13c compares the wake centerline and edges detected by the Gaussian and ATS methods. Both methods perform well in the range of $1 < x/D < 10$ and show good agreement on the same distance (Fig. 13c). Downstream ($x/D > 10$), the wake becomes weaker as it recovers to the free flow. If the wake deficit function becomes too flat to fit accurately, the fitting result may place the wake center incorrectly or overestimate the standard deviation and, consequently, the wake width. The ATS method detects only disconnected structures in the far wake. Nevertheless, those structures primarily lie within the wake edges detected by the Gaussian method. The Gaussian centerline also passes through the centers of the ATS-detected structures. A good agreement between methods can be explained by the fact that the ATS method searches for regions of high intensity, i.e.,

low wind speed. At the same time, the Gaussian method approximates a wake center at the point of high wake deficit, which also corresponds to low wind speed.

Overall, the Gaussian and ATS centerline search methods show complementary flaws. The Gaussian method may estimate the wake center correctly on a weak wake profile but returns a large standard deviation, leading to an overestimation of the wake width. The Gaussian method does not always interpret strong wake meandering correctly and mistakes a wake turn for a wide wake. Conversely, the ATS method is capable of discerning a complex wake shape but has problems with the centerline detection if the wake shape is too irregular due to wake merging or mixing with noise.

6 Results

For the lidar data, we perform an extensive comparison to the manual wake identification and characterization and evaluate the accuracy of the ATS method. We further compare the performance of the ATS and Gaussian methods and discuss the application of the ATS method in the centerline detection. We show both ensemble statistics and demonstrate the methods' performance on sample scans showing each of the most represented non-corrupted subsets: parallel, aligned, and bimodal.

6.1 Comparison of the ATS wake identification against the manual identification and deficit-based thresholding

We construct a confusion matrix to assess the performance of the methods for a single lidar scan. The 2×2 confusion matrix describes the comparison of the automatic thresholding methods (deficit-based or ATS; see Table 2) against the manual method and contains the following outcomes.

- True positive (TP) – the point is detected as a wake point by both manual and automatic identification.
- True negative (TN) – the point is detected as a free-flow point by both manual and automatic identification.
- False positive (FP) – the point is detected as a wake point by the automatic method but is a free-flow point in the manual identification.
- False negative (FN) – the point is detected as a free-flow point by the automatic method but is a wake point in the manual identification.

If the automatic identification is accurate with respect to the manual identification, TP and TN values tend to 100 %, while FP and FN are close to zero.

The bimodal subset can be considered the most convenient for the manual threshold segmentation. It utilizes the strict criterion for the manual threshold that the wake shapes should not merge (Fig. 14d). In the example, the ATS method

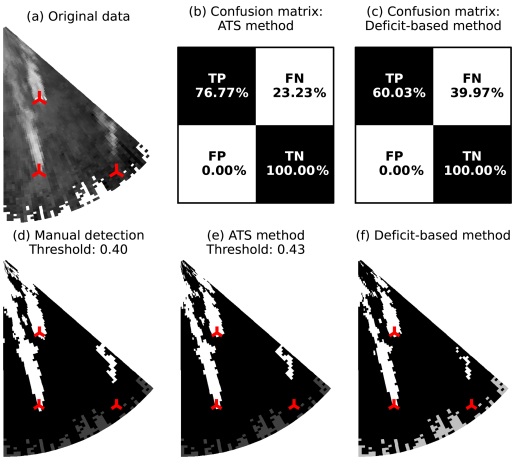

Figure 14. Scan 599 (bimodal subset), wake identification. **(a)** The original data in the Cartesian coordinates, **(b, c)** confusion matrices for the ATS and deficit-based methods, **(d)** manual threshold selected in a way to separate the two wakes, and **(e, f)** thresholds estimated by the ATS and deficit-based methods.

sets the threshold higher compared to the manual identification (Fig. 14e). Hence the far-wake area is slightly reduced. The deficit-based method (Fig. 14f) produces a similar result.

The aligned-wake subset utilizes the same manual threshold criteria for the wake splitting as the bimodal subset (Fig. 15), although the condition may be harder to fulfill. For some lidar scans, the far wake from the turbine AV10 and the near wake from AV7 cannot be separated, unless the threshold is increased so that the far wake is not identified (Fig. 15d). In this case, detecting a general shape of the wake takes priority. The manual threshold is then more subjective than that of the bimodal subset. The deficit-based method underestimates the threshold more significantly than in the bimodal case and produces larger percentage of false positives than the ATS method (Fig. 15f).

The parallel-wake subset is the most challenging, for both the manual identification and the automatic methods (Fig. 16). The wind direction in the subset is approaching 210°, where the crosswind effects start (Fig. 3) and noise appears at the border of a lidar scan. Unlike the corrupted scans with a high number of non-physical wind speed values, the region around the wind turbines AV7 and AV10 contains valid measurements and still allows us to perform wake identification with relative success. However, the wake identification accuracy declines due to the border noise, and only one wake can be extracted well enough to perform the analysis on the wake centerline and shape evolution. If the threshold is increased to distinguish wakes and noise, the wake from AV10 remains nearly undetected as can be seen from Fig. 16d. The ATS method returns a lower threshold that im-

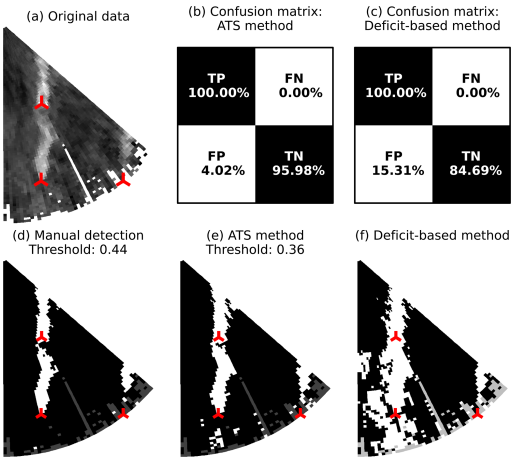

Figure 15. Scan 221 (aligned-wake subset), wake identification. **(a)** The original data in the Cartesian coordinates, **(b, c)** confusion matrices for the ATS and deficit-based methods, **(d)** manual threshold selected in a way to separate the two wakes, and **(e, f)** thresholds estimated by the ATS and deficit-based methods.

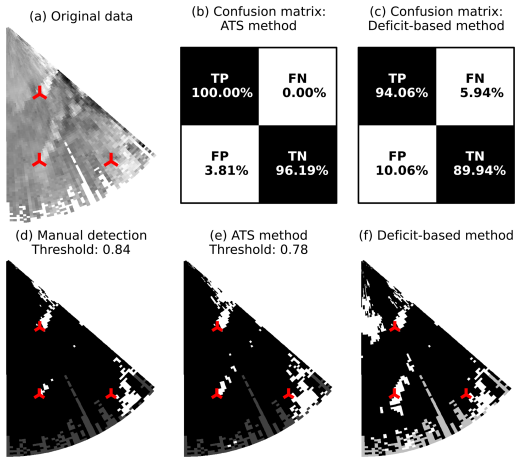

Figure 16. Scan 60 (parallel-wake subset), wake identification. **(a)** The original data in the Cartesian coordinates, **(b, c)** confusion matrices for the ATS and deficit-based methods, **(d)** manual threshold selected in a way to reduce noise but keep a general shape of the wakes, and **(e, f)** thresholds estimated by the ATS and deficit-based methods.

proves the distinguishing of the shape of the AV10 wake but falsely detects noise as a part of the AV7 wake (Fig. 16e). The deficit-based method estimates the threshold rather accurately but may detect additional false positives near wind turbines (Fig. 16f).

We summarize the comparison of true negative and true positive detections in the box plots (Fig. 17) for the different subsets.

Due to the amount of noise, the parallel-wake subset is challenging for both methods. Nevertheless, the ATS method approaches manual identification rather effectively, while the deficit-based method leaves a decent amount of noise which may alter the identified wake shape (Fig. 16f).

Both methods score nearly 100 % for the true positive detections in the aligned subset (Fig. 17b). The result is caused by the criterion for the manual threshold: separate two different wakes. The criterion is too strict for both automatic methods to achieve; therefore, they always underestimate the threshold. Still, the ATS method gets closer to the manual threshold, which is reflected in lower variation in true negative detections compared to the deficit-based threshold.

The deficit-based and ATS wake identifications behave rather similarly for the bimodal subset (Fig. 17c) with respect to the manual wake identification. The variations in the bimodal subset are primarily caused by the wakes forming in the lidar near range, which is scanned at higher resolution than the rest of a scan. That is, any small threshold change affects more points at the wake edges than it would for the parallel or aligned subsets and results in stronger fluctuations in TP–FN values.

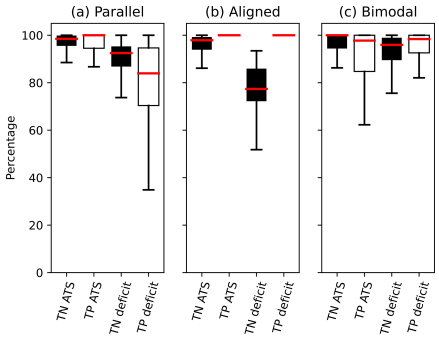

Figure 17. Ensemble statistics of true negative and true positive detections within the subsets.

To reduce the influence of ambiguity of the manual detection, we construct a confusion matrix for each subset of 25 consecutive lidar scans instead of single scans. The corrupted scans are excluded from the comparison, since high noise prevented the manual detection for most of the scans. Table 3 summarizes the detection outcomes for each subset. The ATS and deficit-based method perform comparably in terms of true positives in the aligned and bimodal subsets. However, the number of false positives for the deficit-based method indicates a high probability of identifying noise as a wake. Additionally, the percentage of false positives strongly

Table 3. Comparison of the thresholding methods' performance against the manual wake identification.

			Manual–deficit, %				Manual–ATS, %			
Data type	Subset	Scans	TP	FN	FP	TN	TP	FN	FP	TN
Parallel wakes	3	51–75	55	45	5	95	80	20	2	98
	4	76–100	69	31	4	96	97	3	4	96
	5	101–125	76	24	9	91	91	9	4	96
	6	126–150	85	15	9	91	95	5	4	96
	7	151–175	96	4	23	77	98	2	3	97
	11	251–275	95	5	22	78	99	1	4	96
	12	276–300	71	29	7	93	93	7	2	98
	16	376–400	80	20	6	94	96	4	3	97
Transitional	17	401–425	93	7	19	81	87	13	0	100
Aligned wakes	8	176–200	99	1	28	72	98	2	1	99
	9	201–225	100	0	13	87	100	0	10	90
	10	226–250	100	0	23	77	98	2	3	97
Bimodal	17	426–450	88	12	2	98	82	18	0	100
	18	451–475	83	17	1	99	89	11	0	100
	19	476–500	97	3	5	95	96	4	4	96
	20	501–525	97	3	7	93	85	15	2	98
	21	526–550	99	1	15	85	90	10	5	95
	22	551–575	100	0	20	80	90	10	8	92
	23	576–600	85	15	2	98	94	6	4	96

fluctuates within the same type of the subset, making the fixed threshold method unreliable.

While the number of true positives for the ATS method may drop to 80 % for a complex subset, the number of true negatives consistently stays near 95 % – the background flow is mostly detected correctly regardless of the subset type, which is an improvement compared to the deficit-based method. Compared to manual detection, the ATS method does not always separate wake and noise correctly, particularly for the parallel-wake subset (Fig. 15) and thus requires additional filtering. For the aligned and bimodal subsets, the ATS method is capable of detecting the general wake shape rather similarly to the manual detection.

It should be noted that the deficit-based wake identification requires a free-flow wind speed to define the threshold and an additional preprocessing of a lidar scan – a correction based on the wind direction or a more complex lidar retrieval method. The ATS method runs solely on the lidar data and does not require information besides what is already contained in a lidar scan.

6.2 Comparison of the wake characterization using Gaussian and ATS methods

We perform the wake characterization by searching for the wake centerline from the thresholded image produced with the ATS method as described in Sect. 4.2 or by applying the Gaussian method as described in Sect. 4.3. First, we provide a comparison of selected scans against the manual wake characterization from the lidar scan image as described in Sect. 4.5. The found centerlines are compared by fitting the regression lines to the relative coordinates, so that each local coordinate system is centered at a selected wind turbine.

The parallel-wake subset (Fig. 18) contains a short but pronounced wake from the wind turbine AV7 and a long weaker wake from the wind turbine AV10. Since the AV10 wake is frequently detected as a series of small disconnected structures, the current ATS method detects the centerline only for the first continuous shape, which rarely extends beyond the near-wake region. The manual and Gaussian wake characterization can be carried further into the far-wake region but become rather uncertain as the far wake recovers to the free flow or mixes with the border noise. Considering the problems that the border noise poses for the wake identification in less clean scans (Fig. 16), the characterization outcome can be improved by excluding the near-border sector of 1–2° width from the identification process.

The aligned-wake subset (Fig. 19) shows a distinctive feature: the wakes are aligned along the line connecting two wind turbines, resulting into the merge of the AV10 far wake and the AV7 near wake. Additionally, the connecting line is parallel to the Y axis in Cartesian coordinates, so the centerline tends to $X = \text{const}$ when the wakes are perfectly aligned. Hence, the coefficient of determination R^2 either approaches zero or becomes negative and does not indicate the quality of the regression fit.

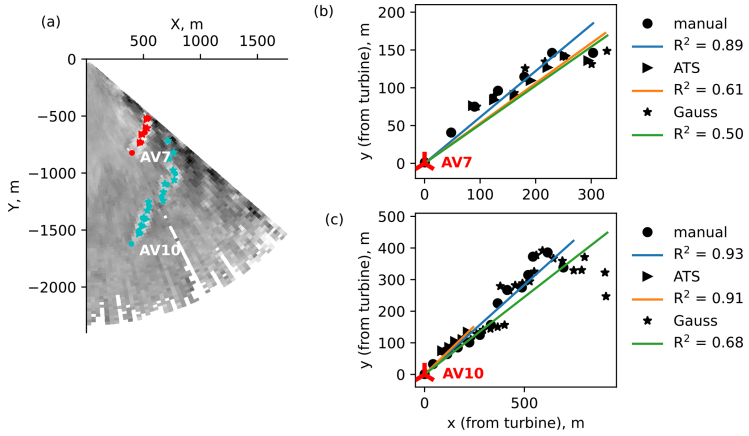

Figure 18. Scan 59 (parallel-wake subset). **(a)** An overview of the detected centerlines and regression fits for **(b)** AV7 and **(c)** AV10.

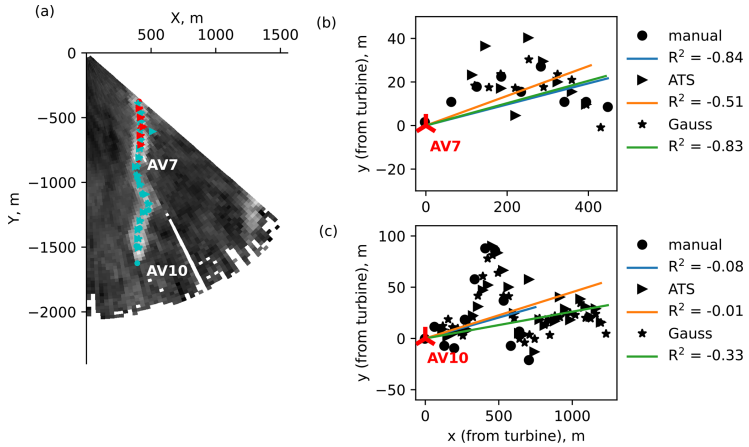

Figure 19. Scan 221 (aligned-wake subset). **(a)** An overview of the detected centerlines and regression fits for **(b)** AV7 and **(c)** AV10.

The bimodal subset (Fig. 20) has the longest wakes in the data set. The wake identification in the far wake (i.e., lidar near range) is hindered by wake merging and the narrowness of the scanned area. For example, the ATS method may underestimate the threshold and detect merging wakes as a single shape. The ATS-based threshold can be adjusted to guarantee the wake splitting. The adjustment is performed automatically by increasing the threshold with an increment of 0.05 until the stopping criterion – the wind turbines belong (or are located near) to different wake shapes – is reached.

The merging wakes also affect the accuracy of the Gaussian method: high wake deficit in the neighboring wake may lead to an incorrect detection of a wake center after the fitting. The characterization inaccuracy in the lidar near range is compensated for by a higher overall number of data points available for fitting, compared to the other subsets.

Figure 21 shows an example of wake identification performed on a lidar scan from the aligned-wake subset. The subset is characterized by the wake merging near AV7. The formed structure proves to be challenging for a Gaussian method, as the centerline point and far-wake width for AV10 are estimated incorrectly.

The ATS method detects wakes as a single shape. Unlike the bimodal subset, the merging wakes in the aligned-wake subset do not necessarily worsen the performance of the centerline detection method. The centerline is first detected for the AV10 wake, from which the wake direction can be estimated. Since the wakes are merged, the centerline detection

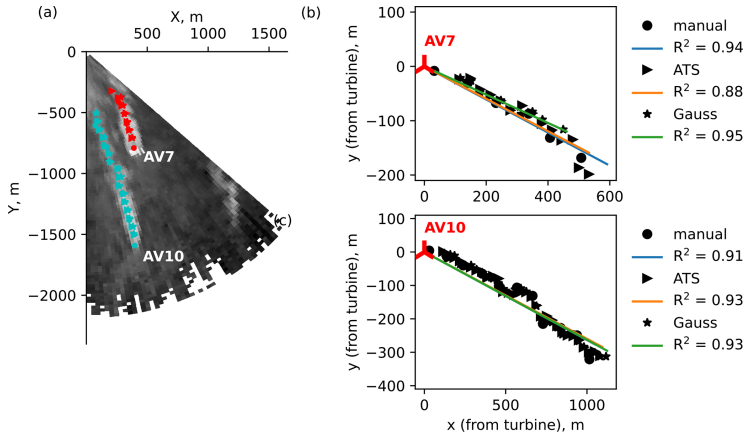

Figure 20. Scan 599 (bimodal subset). **(a)** An overview of the detected centerlines and regression fits for **(b)** AV7 and **(c)** AV10.

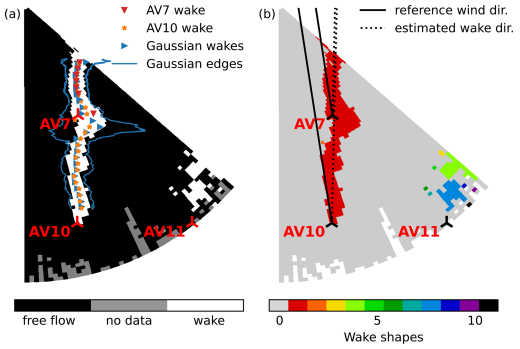

Figure 21. Scan 222 (aligned-wake subset) sample wake identification and characterization showing **(a)** comparison of the ATS and Gaussian methods, **(b)** wakes identified by the ATS method after the threshold is applied, and wind and wake direction.

for AV10 continues in the AV7 wake. The centerline search for AV7 starts at the corresponding turbine location and is performed in the direction of the AV10 wake, thus excluding the merge region from the search. Thus the centerline of the AV7 wake gets detected twice if no stopping criterion (e.g., the AV10 centerline passes the AV7 location) is activated. Both detected centerlines agree in the AV7 wake region and follow the Gaussian centerline rather well. Near-border wake centers of the AV7 wake deviate from the presumed centerline because border noise is erroneously attributed as a part of the wake.

When it comes to the comparison of wake characterization over the whole data set, the effect of weak wakes or merging on the Gaussian method performance complicates a direct comparison. Due to the errors, the Gaussian centerline cannot be taken as a "true" value and requires verification on its own.

Table 4. Rules for scoring Gaussian and ATS centerline search method performance.

Score	Gaussian method	ATS centerline search
0	The method failed to find the wake at all, or less than 10 % of the visible wake was identified.	
0.5	The centerline loosely matches the wake centerline, but the wake width is overestimated or undefined.	The wake shape is readable from the thresholded image, but the centerline is incomplete or erroneous.
1	The method had correctly identified at least 75% of the visible wake and its centerline.	

Instead, we perform a visual comparison of the Gaussian and ATS centerline search methods to score their success rate. The performance of both methods rather differs along the wake; therefore we evaluate the detection result on two segments: $l \leq 4\,D$ and $l > 4\,D$ from the wind turbine. The $l \leq 4\,D$ segment usually covers the most well-resolved part of the wake in non-corrupted scans; we attribute it as the near wake. The rest of the wake would be then referred to as the far wake and characterized by lower wake deficit. Next, we score the success rate based on whether the method was able to identify both wake shape and centerline, failed on one of the tasks, or did not distinguish the wake at all (Table 4).

As mentioned for the LES wake identification and characterization (Sect. 5), the ATS and Gaussian methods are prone to errors in different aspects. A partial success for the Gaussian method would usually mean a centerline estimated with

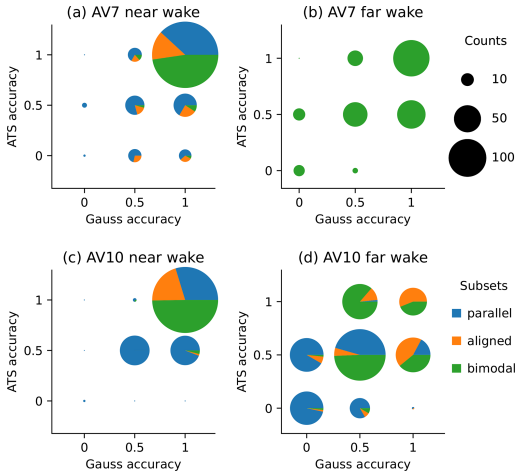

Figure 22. Overview of the Gaussian and ATS method performance on the wake detection and characterization.

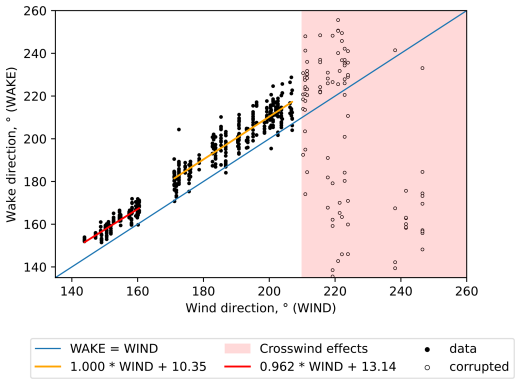

Figure 23. Comparison between reference wind direction (WIND) and estimated wake direction (WAKE).

a large standard deviation, while a partial success for the ATS method would be the detection of the wake shape but not the full centerline.

A summary for the data set excluding corrupted scans is presented in Fig. 22 by showing the counts for each outcome and their distribution between the subsets.

The near wakes are well resolved and show a high number of outcomes where both methods succeed. The partial detections are spread differently. The non-perfect outcomes for the AV7 near wake are spread rather equally (Fig. 22a). The increased error rate of the ATS method in the AV7 near wake is caused by either strong border noise (parallel subset) or strong upstream wake influence (aligned subset) – both distort the detected wake shape.

Due to the studied wind directions, the AV10 near wake is not subjected to the upstream turbine influence. The wake is very clear and poses problems mainly for the ATS method in the parallel subset, when it cannot be identified as a continuous shape. Hence, the ATS method under-performs and stops at the wake identification, while the Gaussian method can succeed in both aspects (Fig. 22c).

The comparison of AV7 far wake accuracy (Fig. 22b) is relevant only for the bimodal subset, where the corresponding wake reaches the required length. Detection outcomes for the AV7 far wake follow a pattern that resembles the other cases: very low counts of partial or full success when one of the methods fails and higher counts for partial and full success of both methods.

The exception from this pattern is the AV10 far wake (Fig. 22d). Both methods achieve partial success most often. The decreased success rate is primarily caused by the wake merging in bimodal and aligned subsets. When it comes to the parallel-wake subset, both methods are likely to fail. The weak AV10 far wake limits efficiency of both methods: the threshold is not enough to separate the wake from the free flow, and the fitting cannot be carried on to the nearly flat wake deficit function.

The low count of (0, 1) pairs throughout the comparison indicates that none of the methods outperform the others in any part of the wake. If one method fails, the other usually fails too or achieves only a partial success.

6.3 Wind and wake direction

The regression line fitted to the ATS-detected centerline also indicates the wake direction. A strong mismatch between reference wind direction and wake direction can be seen for most lidar scans from the data set (Fig. 23b).

Comparing the directions for the whole data set, we observe a clear trend for the wake direction deviating clockwise from the reference wind direction until the crosswind effects start at 210° (Fig. 23).

The valid points for the reference wind directions less than 210° group into two distinct clusters (Fig. 23). The leftmost cluster corresponds to the bimodal subset and lies within the range of wind directions of 140–170°. Another cluster contains the results for the aligned, transitional, and parallel-wake subsets and covers the range of wind directions of 170–210°. Fitting a linear regression to each group returns a similar slope but a different intercept value. Although the fitted line slope is not equal to one, the regression fit on the selected range shows a nearly constant offset between wind and wake direction, with the bimodal subset having noticeably lower difference than other subsets.

The vertical veer and clockwise rotation of the wake in the Northern Hemisphere due to the Coriolis force are known effects causing wake rotation and were confirmed by observations and LES studies of wind farms (Magnusson and Smed-

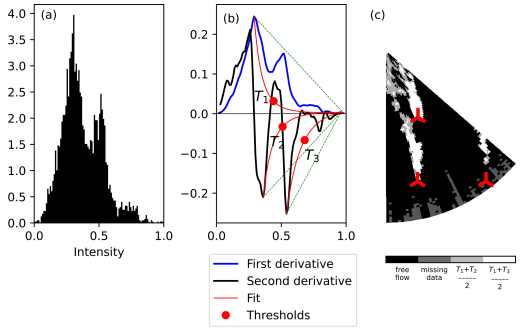

Figure 24. Scan 553 (bimodal subset). **(a)** Intensity histogram of the normalized data, **(b)** the ATS method search for the thresholds, and **(c)** thresholded image.

man, 1994; Abkar and Porté-Agel, 2016; van der Laan and Sørensen, 2017). The wind turbine AV7, closest to the lidar, is scanned nearly at the hub height, while the farther wind turbines, AV10 and AV11, are scanned near the top-tip height (Fig. 1). Due to the elevation and vertical veer, the wind and wake direction discrepancy is the strongest for AV10 and AV11. Nevertheless, we also observe a deflection for the near wake of AV7, although the noticeable effects of the Coriolis force are usually recorded for the downwind distance of 6 D or higher. The additional discrepancy can be explained by the yaw misalignment (Bromm et al., 2018), reference measurement uncertainty (Gaumond et al., 2014), and lidar installation's imperfection. The wake direction variation for the bimodal subset (reference wind direction 140–160°) was possibly reduced because of the longer wakes and, consequently, more precise estimation of the wake direction. We do not have additional data to distinguish these factors and leave it for a future study.

The outliers showing strong differences between wind and wake direction highlight the lidar scans where the wake identification and characterization were hindered by noise or strong irregularity of the wake. The wind–wake direction plot can be used for diagnostic purposes to select the lidar scans that require additional processing prior to the wake identification.

6.4 Wake identification in the bimodal subset using the ATS method

Bimodal subsets often have a distinctive double peak in the intensity histogram (Fig. 24a). The highest histogram peak corresponds to the free flow. The second peak forms due to a long far wake from AV10 and subsequent merging of the two wakes.

The double peak from the histogram translates into two local minimums in the second derivative graph (Fig. 24b). The occasions of two local maximums in the first derivative were rarer in the regarded data set. Applying the ATS method to both second derivative minimums provides a unique opportunity to estimate two thresholds T_2 and T_3 in addition to the threshold T_1 from the first derivative. The final threshold values either separate the full wake from the free flow ($(T_1 + T_2)/2$) or extract only the most intense part of the wake ($(T_1 + T_3)/2$) (Fig. 24c). The splitting point falls approximately at the downstream distance of 4–5 D, marking a transition from the near to far wake.

We ran the ATS method without subset-specific parameters, meaning that it always estimated only one threshold for the wake identification. During the threshold estimation (Sect. 4.1), the current algorithm selects the global maximum or minimum of the first and second derivatives, respectively. The free-flow histogram peak usually results in the global maximum of the first derivative in our data set and does not affect the performance of the ATS method. However, the local minimum values of the second derivative appear to be more sensitive to the intensity distribution. Relying on the global minimum may lead to selecting a stricter threshold T_3 (Fig. 24b). A strict threshold does not detect most of the far wake, as shown in Fig. 24c.

A less strict threshold T_2 could be chosen based on the proximity to T_1 as a control value. However, it would require an automatic check of whether another local minimum can produce a valid threshold. The implementation posed a challenge if the current algorithm ran without subset-specific parameters and produced erroneous threshold estimation for other scans. We refrained from using a more complex approach in the bimodal subset for now. The current ATS method, therefore, overestimated the threshold and did not identify the full wake in about 8 % of the bimodal cases.

7 Conclusions

We developed a set of methods to analyze lidar scans for wake identification and characterization. During the study, we focused on the procedures that would automatically process a large data set and primarily rely on the information contained in the lidar data or site characteristics such as lidar and wind turbine positions. To structure the analysis of the results, we split our data set into several subsets, grouping the scans with similar characteristics. While the classification could be performed based on the wind direction or visual inspection, we introduced entropy as a criterion to reflect the flow characteristics. When calculated in the azimuthal or radial direction, Shannon entropy is sensitive to the disturbances caused by wakes and allows scan classification if the wind direction is unknown. The entropy values also highlighted the lidar scans that were unsuitable for the analysis due to the high number of non-physical measurements caused by the crosswind effects. The classification by entropy criteria introduced in the study was not yet used to apply scan-specific corrections during the thresholding.

An existing automatic thresholding method, the deficit-based method as referred to in the study, thresholds the wind speed data at 95 % of the free-flow wind speed and was initially suggested for more regular wind tunnel wakes. The reliance on the actual wind speed hinders the deficit-based method performance on the lidar data – a retrieval procedure should be applied to the measured radial velocity to reconstruct the wind field. Additionally, the fixed ratio of 95 % does not regard the quality of a lidar scan. To overcome these disadvantages, we proposed an automatic thresholding method for wake identification, the ATS method, based on the method for whitecap detection on the ocean surface. The method did not require knowledge of the actual wind speed and could be applied to the radial velocity data. The preparatory step applied normalization through scaling data to the range of [0, 1], thus requiring the removal of outliers during the lidar scan preprocessing.

The comparison to the manual thresholding showed that the ATS method generally performed better than the deficit-based method and on the par with manual wake identification, which opened a possibility to use it when manual thresholding is infeasible.

We also described an automatic method for the wake centerline search from the thresholded data. The centerline search could run without wind direction provided by making a rough approximation of the wake direction. However, the current algorithm processes only the first continuous shape, limiting the application to the wind fields with little noise and obstructing the wake identification.

We compared the centerline found from the thresholded data to the Gaussian fit method. Although the Gaussian method performance on the lidar scans was not as good as on the LES data, the wake characterization in the near-wake region showed an agreement between the methods with respect to the manual centerline detection. At the same time, the accuracy of both Gaussian and ATS-based methods decreased in the far-wake region, especially for noisy data or in the case of wake–wake interaction. In the latter case, the ATS method often identified two wakes as a single shape, affecting the centerline search algorithm. The algorithm performs better when the wake directly hits the downstream wind turbine – the merged wakes can be considered one wake and have a common centerline. When the wakes are forming side by side and get close to each other, the threshold may need additional adjustment until the identified wake shape is split.

The results showed that automatic thresholding from the intensity histogram was viable for the wake identification not only for the LES but also lidar data. We see a potential to improve the wake characterization algorithm to detect the centerline of the whole wake and plan to present it in future studies.

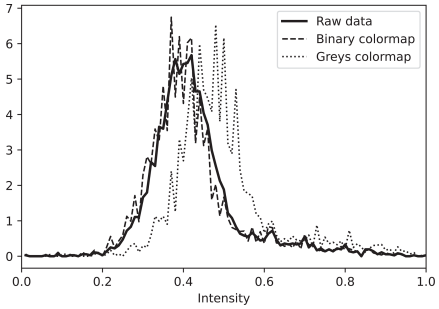

Figure A1. Comparison of the intensity distribution in the original (raw) data and image plotted using Python Matplotlib with different grayscale color maps.

Appendix A: Image data processing

An image has several properties which may affect the algorithm performance compared to the use of the raw wind speed data.

1. *Image resolution in dots per inch (dpi)*. The resolution of 72 dpi transforms an original data point into an image pixel as one-to-one approximately. Higher resolution increases the number of pixels per data point. Lower resolution merges several data points into one pixel.

2. *Color map*. The ATS method relies on the image grayscale intensity as an input. A non-grayscale image can be desaturated, but the color map of the original image then should be sequential rather than perceptually uniform or diverging. For the latter, the conversion to the grayscale gradually reduces the contrast between high and low values, making the wake identification impossible. Additionally, several grayscale color maps exist. Depending on the color map, the intensity histogram of an image may shift to the left or right compared to the raw data. We observed this effect when the "Greys" color map of the Python Matplotlib (Caswell et al., 2021) library was used. This color map emphasizes light tones; as a result, the intensity histogram peak slightly shifts to the right, although the general shape of the peak is preserved (Fig. A1). The color maps "binary" or "gray" from the same library return the result that follows the original data.

3. *Image intensity*. As processed by Python, the values are rounded up to second digits, and some are assigned to different bins compared to the original data. The histogram and CDF have stronger oscillations than the raw data (Fig. A1) and require smoothing before the application of the ATS method.

Running an automated threshold detection on the image raises another question: how much does the image resolution

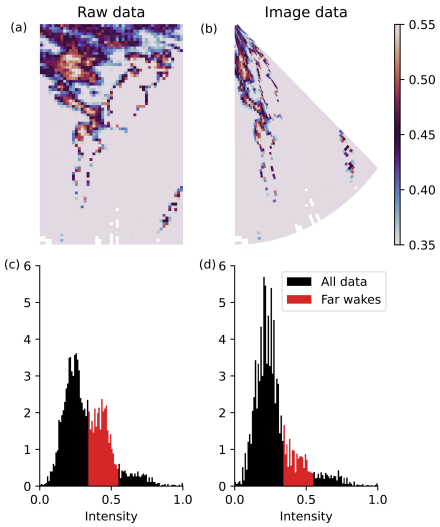

Figure A2. **(a, b)** Normalized wind speed data with far wakes highlighted and **(c, d)** corresponding grayscale intensity histograms of the lidar scan 551.

affect the identification accuracy compared to the raw data. We apply the ATS algorithm to raw and image data under different resolutions: 72, 150, and 300 dpi. We observe little influence from the image resolution, except for a few LES cases, where the low resolution of 72 dpi affected the threshold detection. In those cases, the detected threshold is lower than in fine-resolution cases, and, therefore, a larger shape is identified as a wake. The image resolution of 150 dpi and above agrees well with the wake identification from the raw data. The general shape of an image intensity histogram does not depend on the image resolution. The image resolution of 150 dpi or higher is recommended for use, although 72 dpi also produces good detection results.

In the case of lidar measurements, the wake identification from the image data can be performed in two ways: by plotting the original data in either polar or Cartesian coordinates. The wake identification from the polar coordinate image does not bear a notable difference from the raw data, apart from the aforementioned specifics of the image resolution and intensity. However, if the lidar data are plotted in the Cartesian coordinates as a scanned sector, the lidar close and far ranges get distorted, affecting the percentage of the area covered by the wakes and, consequently, the histogram shape.

The effect is most pronounced when the wind blows towards the lidar. As described in the subset overview in Sect. 3.2, this wind direction and wake behavior result in the bimodal intensity histogram. The leftmost high peak contains points from the free flow, while the second low peak accumulates points from the far wake. The second peak gets smoothed when the input data are changed from the normalized wind speed to the grayscale image plotted in Cartesian coordinates. As can be seen from the comparison (Fig. A2), the lower peak corresponds to the data in the lidar's close range. After the conversion to the Cartesian coordinates, the close range area shrinks significantly, while the free-flow area on the far lidar range enlarges. The transition between coordinate systems changes the balance between wake and free-flow pixels and virtually increases the share of the latter.

Code and data availability. The Python code for wake identification using the ATS method, centerline detection and a sample lidar data set are available upon request at https://doi.org/10.5281/zenodo.5888236 (Krutova, 2022b).

Video supplement. The videos https://doi.org/10.5446/54055 (Krutova, 2021) and https://doi.org/10.5446/56710 (Krutova, 2022a) demonstrates wake identification results for all lidar scans in the data set. No post-processing is performed after running the ATS algorithm.

Author contributions. MK adapted the image processing algorithm developed by MBP to the wake identification, expanded the algorithm with the centerline characterization code, and performed analysis of the wake identification and characterization. MBP provided further guidance on the image processing techniques. JR provided information on the lidar setup and explanation of the discrepancies between reference and lidar data. FGN consulted on the method practical application. All authors contributed to the proofreading and correcting the article draft.

Competing interests. The contact author has declared that neither they nor their co-authors have any competing interests.

Disclaimer. Publisher's note: Copernicus Publications remains neutral with regard to jurisdictional claims in published maps and institutional affiliations.

Acknowledgements. The LESs for the study have been performed by using the high-performance- computer facilities of the Norwegian e-infrastructure Uninett Sigma2 (project number NS9506K).

The authors would like to thank Martin Flügge for providing the lidar data.

Financial support. The OBLEX-F1 field campaign has been performed under the Norwegian Centre for Offshore Wind Energy (NORCOWE), funded by the Research Council of Norway (RCN) under project number 193821. The scanning Doppler wind lidar system (Leosphere WindCube 100S), used for this study,

has been made available via the National Norwegian infrastructure project OBLO (Offshore Boundary Layer Observatory) also funded by RCN under project number 227777.

Review statement. This paper was edited by Rebecca Barthelmie and reviewed by three anonymous referees.

References

Abkar, M. and Porté-Agel, F.: Influence of the Coriolis force on the structure and evolution of wind turbine wakes, Phys. Rev. Fluids, 1, 1–14, https://doi.org/10.1103/physrevfluids.1.063701, 2016.

Ahsbahs, T., Nygaard, N. G., Newcombe, A., and Badger, M.: Wind Farm Wakes from SAR and Doppler Radar, Remote Sens., 12, 462, https://doi.org/10.3390/rs12030462, 2020.

Ainslie, J.: Calculating the flowfield in the wake of wind turbines, J. Wind Eng. Ind. Aerodynam., 27, 213–224, https://doi.org/10.1016/0167-6105(88)90037-2, 1988.

Aitken, M. L., Banta, R. M., Pichugina, Y. L., and Lundquist, J. K.: Quantifying Wind Turbine Wake Characteristics from Scanning Remote Sensor Data, J. Atmos. Ocean. Tech., 31, 765–787, https://doi.org/10.1175/JTECH-D-13-00104.1, 2014.

Bakhoday-Paskyabi, M., Reuder, J., and Flügge, M.: Automated measurements of whitecaps on the ocean surface from a buoy-mounted camera, Meth. Oceanogr., 17, 14–31, https://doi.org/10.1016/j.mio.2016.05.002, 2016.

Bastine, D., Witha, B., Wächter, M., and Peinke, J.: Towards a Simplified DynamicWake Model Using POD Analysis, Energies, 8, 895–920, https://doi.org/10.3390/en8020895, 2015.

Beck, H. and Kühn, M.: Reconstruction of three-dimensional dynamic wind-turbine wake wind fields with volumetric long-range wind doppler LiDAR measurements, Remote Sens., 11, 2027–2055, https://doi.org/10.3390/rs11222665, 2019.

Bingöl, F., Mann, J., and Larsen, G. C.: Light detection and ranging measurements of wake dynamics part I: one-dimensional scanning, Wind Energy, 13, 51–61, https://doi.org/10.1002/we.352, 2010.

Bromm, M., Rott, A., Beck, H., Vollmer, L., Steinfeld, G., and Kühn, M.: Field investigation on the influence of yaw misalignment on the propagation of wind turbine wakes, Wind Energy, 21, 1011–1028, https://doi.org/10.1002/we.2210, 2018.

Caswell, T. A., Droettboom, M., Lee, A., Sales de Andrade, E., Hunter, J., Hoffmann, T., Firing, E., Klymak, J., Stansby, D., Varoquaux, N., Hedegaard Nielsen, J., Root, B., May, R., Elson, P., Seppänen, J. K., Dale, D., Lee, J.-J., McDougall, D., Straw, A., Hobson, P., Gohlke, C., Yu, T. S., Ma, E., Vincent, A. F., Silvester, S., Moad, C., Kniazev, N., Ernest, E., and Ivanov, P.: matplotlib/matplotlib: REL: v3.4.0, Zenodo [code], https://doi.org/10.5281/zenodo.4638398, 2021.

Chamorro, L. P. and Porté-Agel, F.: Effects of Thermal Stability and Incoming Boundary-Layer Flow Characteristics on Wind-Turbine Wakes: A Wind-Tunnel Study, Bound.-Lay. Meteorol., 136, 515–533, https://doi.org/10.1007/s10546-010-9512-1, 2010.

Doubrawa, P., Quon, E. W., Martinez-Tossas, L. A., Shaler, K., Debnath, M., Hamilton, N., Herges, T. G., Maniaci, D., Kelley, C. L., Hsieh, A. S., Blaylock, M. L., Laan, P., Andersen, S. J., Krueger, S., Cathelain, M., Schlez, W., Jonkman, J., Branlard, E., Steinfeld, G., Schmidt, S., Blondel, F., Lukassen, L. J., and Moriarty, P.: Multimodel validation of single wakes in neutral and stratified atmospheric conditions, Wind Energy, 2665, we.2543, https://doi.org/10.1002/we.2543, 2020.

España, G., Aubrun, S., Loyer, S., and Devinant, P.: Spatial study of the wake meandering using modelled wind turbines in a wind tunnel, Wind Energy, 14, 923–937, https://doi.org/10.1002/we.515, 2011.

Fleming, P. A., Gebraad, P. M., Lee, S., van Wingerden, J. W., Johnson, K., Churchfield, M., Michalakes, J., Spalart, P., and Moriarty, P.: Evaluating techniques for redirecting turbine wakes using SOWFA, Renew. Energy, 70, 211–218, https://doi.org/10.1016/J.RENENE.2014.02.015, 2014.

Foti, D., Yang, X., Guala, M., and Sotiropoulos, F.: Wake meandering statistics of a model wind turbine: Insights gained by large eddy simulations, Phys. Rev. Fluids, 1, 044407, https://doi.org/10.1103/physrevfluids.1.044407, 2016.

Gaumond, M., Réthoré, P.-E. E., Ott, S., Peña, A., Bechmann, A., and Hansen, K. S.: Evaluation of the wind direction uncertainty and its impact on wake modeling at the Horns Rev offshore wind farm, Wind Energy, 17, 1169–1178, https://doi.org/10.1002/we.1625, 2014.

Herges, T. G., Maniaci, D. C., Naughton, B. T., Mikkelsen, T., and Sjöholm, M.: High resolution wind turbine wake measurements with a scanning lidar, J. Phys.: Conf. Ser., 854, 012021, https://doi.org/10.1088/1742-6596/854/1/012021, 2017.

Howard, K. B., Singh, A., Sotiropoulos, F., and Guala, M.: On the statistics of wind turbine wake meandering: An experimental investigation, Phys. Fluids, 27, 075103, https://doi.org/10.1063/1.4923334, 2015.

Krishnamurthy, R., Reuder, J., Svardal, B., Fernando, H. J., and Jakobsen, J. B.: Offshore Wind Turbine Wake characteristics using Scanning Doppler Lidar, Energy Procedia, 137, 428–442, https://doi.org/10.1016/j.egypro.2017.10.367, 2017.

Krutova, M.: Automatic thresholding method for the wake detection, TIB AV-Portal [video supplement], https://doi.org/10.5446/54055, 2021.

Krutova, M.: Automatic thresholding method for the wake detection – comparison of the methods, TIB AV-Portal [video supplement], https://doi.org/10.5446/56710, 2022a.

Krutova, M.: Adaptive Thresholding Segmentation (ATS) for wake identification and characterization (0.5), Zenodo [code], https://doi.org/10.5281/zenodo.5888236, 2022b.

Larsen, G., Madsen Aagaard, H., Bingöl, F., Mann, J., Ott, S., Sørensen, J., Okulov, V., Troldborg, N., Nielsen, N., Thomsen, K., Larsen, T., and Mikkelsen, R.: Dynamic wake meandering modeling, no. 1607(EN) in Denmark, Forskningscenter Risoe, Risoe-R, Risø National Laboratory, 978-8755036024, https://orbit.dtu.dk/en/publications/dynamic-wake-meandering-modeling (last access: 6 April 2022), 2007.

Larsen, G. C., Madsen, H. A., Thomsen, K., and Larsen, T. J.: Wake meandering: a pragmatic approach, Wind Energy, 11, 377–395, https://doi.org/10.1002/we.267, 2008.

Lee, S., Churchfield, M., Moriarty, P., Jonkman, J., and Michalakes, J.: Atmospheric and Wake Turbulence Impacts on Wind Turbine Fatigue Loadings, in: 50th AIAA Aerosp. Sci. Meet. Incl. New Horizons Forum Aerosp. Expo., American

Institute of Aeronautics and Astronautics, Reston, Virigina, https://doi.org/10.2514/6.2012-540, 2012.

Long, D. and Singh, V. P.: An entropy-based multispectral image classification algorithm, IEEE T. Geosci. Remote, 51, 5225–5238, https://doi.org/10.1109/TGRS.2013.2272560, 2013.

Magnusson, M.: Near-wake behaviour of wind turbines, J. Wind Eng. Ind. Aerodynam., 80, 147–167, https://doi.org/10.1016/S0167-6105(98)00125-1, 1999.

Magnusson, M. and Smedman, A.-S.: Influence of Atmospheric Stability on Wind Turbine Wakes, Wind Eng., 18, 139–152, 1994.

Maronga, B., Banzhaf, S., Burmeister, C., Esch, T., Forkel, R., Fröhlich, D., Fuka, V., Gehrke, K. F., Geletič, J., Giersch, S., Gronemeier, T., Groß, G., Heldens, W., Hellsten, A., Hoffmann, F., Inagaki, A., Kadasch, E., Kanani-Sühring, F., Ketelsen, K., Khan, B. A., Knigge, C., Knoop, H., Krč, P., Kurppa, M., Maamari, H., Matzarakis, A., Mauder, M., Pallasch, M., Pavlik, D., Pfafferott, J., Resler, J., Rissmann, S., Russo, E., Salim, M., Schrempf, M., Schwenkel, J., Seckmeyer, G., Schubert, S., Sühring, M., von Tils, R., Vollmer, L., Ward, S., Witha, B., Wurps, H., Zeidler, J., and Raasch, S.: Overview of the PALM model system 6.0, Geosci. Model Dev., 13, 1335–1372, https://doi.org/10.5194/gmd-13-1335-2020, 2020.

Martínez-Tossas, L. A., Churchfield, M. J., and Leonardi, S.: Large eddy simulations of the flow past wind turbines: Actuator line and disk modeling, Wind Energy, 18, 1047–1060, https://doi.org/10.1002/we.1747, 2015.

Martínez-Tossas, L. A., Churchfield, M. J., Yilmaz, A. E., Sarlak, H., Johnson, P. L., Sørensen, J. N., Meyers, J., and Meneveau, C.: Comparison of four large-eddy simulation research codes and effects of model coefficient and inflow turbulence in actuator-line-based wind turbine modeling, J. Renew. Sustain. Energy, 10, 033301, https://doi.org/10.1063/1.5004710, 2018.

Mehta, D., van Zuijlen, A. H., Koren, B., Holierhoek, J. G., and Bijl, H.: Large Eddy Simulation of wind farm aerodynamics: A review, J. Wind Eng. Ind. Aerodynam., 133, 1–17, https://doi.org/10.1016/j.jweia.2014.07.002, 2014.

Meyers, J. and Meneveau, C.: Optimal turbine spacing in fully developed wind farm boundary layers, Wind Energy, 15, 305–317, https://doi.org/10.1002/we.469, 2012.

Moens, M., Coudou, N., and Philippe, C.: A numerical study of correlations between wake meandering and loads within a wind farm, J. Phys.: Conf. Ser., 1256, 012012, https://doi.org/10.1088/1742-6596/1256/1/012012, 2019.

Moriarty, P., Rodrigo, J. S., Gancarski, P., Chuchfield, M., Naughton, J. W., Hansen, K. S., Machefaux, E., Maguire, E., Castellani, F., Terzi, L., Breton, S.-P., and Ueda, Y.: IEA-Task 31 WAKEBENCH: Towards a protocol for wind farm flow model evaluation. Part 2: Wind farm wake models, J. Phys.: Conf. Ser., 524, 012185, https://doi.org/10.1088/1742-6596/524/1/012185, 2014.

Muller, Y.-A., Aubrun, S., and Masson, C.: Determination of real-time predictors of the wind turbine wake meandering, Exp. Fluids, 56, 53, https://doi.org/10.1007/s00348-015-1923-9, 2015.

Otsu, N.: A Threshold Selection Method from Gray-Level Histograms, IEEE Trans. Syst. Man. Cybern., 9, 62–66, https://doi.org/10.1109/TSMC.1979.4310076, 1979.

Porté-Agel, F., Wu, Y. T., Lu, H., and Conzemius, R. J.: Large-eddy simulation of atmospheric boundary layer flow through wind turbines and wind farms, J. Wind Eng. Ind. Aerodynam., 99, 154–168, https://doi.org/10.1016/j.jweia.2011.01.011, 2011.

Porté-Agel, F., Bastankhah, M., and Shamsoddin, S.: Wind-Turbine and Wind-Farm Flows: A Review, Bound.-Lay. Meteorol., 174, 1–59, https://doi.org/10.1007/s10546-019-00473-0, 2020.

Pun, T.: Entropic thresholding, a new approach, Comput. Graph. Image Process., 16, 210–239, https://doi.org/10.1016/0146-664X(81)90038-1, 1981.

Quon, E. W., Doubrawa, P., and Debnath, M.: Comparison of Rotor Wake Identification and Characterization Methods for the Analysis of Wake Dynamics and Evolution, J. Phys.: Conf. Ser., 1452, 012070, https://doi.org/10.1088/1742-6596/1452/1/012070, 2020.

Shannon, C. E.: A Mathematical Theory of Communication, Bell Syst. Tech. J., 27, 379–423, https://doi.org/10.1002/j.1538-7305.1948.tb01338.x, 1948.

Snel, H., Schepers, J. G., and Montgomerie, B.: The MEXICO project (Model Experiments in Controlled Conditions): The database and first results of data processing and interpretation, J. Phys.: Conf. Ser., 75, 012014, https://doi.org/10.1088/1742-6596/75/1/012014, 2007.

Stevens, R. J.: Dependence of optimal wind turbine spacing on wind farm length, Wind Energy, 19, 651–663, https://doi.org/10.1002/we.1857, 2016.

Stevens, R. J. and Meneveau, C.: Flow Structure and Turbulence in Wind Farms, Annu. Rev. Fluid Mech., 49, 311–339, https://doi.org/10.1146/annurev-fluid-010816-060206, 2017.

Trujillo, J.-J., Bingöl, F., Larsen, G. C., Mann, J., and Kühn, M.: Light detection and ranging measurements of wake dynamics. Part II: two-dimensional scanning, Wind Energy, 14, 61–75, https://doi.org/10.1002/we.402, 2011.

van der Laan, M. P. and Sørensen, N. N.: Why the Coriolis force turns a wind farm wake clockwise in the Northern Hemisphere, Wind Energ. Sci., 2, 285–294, https://doi.org/10.5194/wes-2-285-2017, 2017.

Vollmer, L., van Dooren, M., Trabucchi, D., Schneemann, J., Steinfeld, G., Witha, B., Trujillo, J., and Kühn, M.: First comparison of LES of an offshore wind turbine wake with dual-Doppler lidar measurements in a German offshore wind farm, J. Phys.: Conf. Ser., 625, 012001, https://doi.org/10.1088/1742-6596/625/1/012001, 2015.

Vollmer, L., Steinfeld, G., Heinemann, D., and Kühn, M.: Estimating the wake deflection downstream of a wind turbine in different atmospheric stabilities: an LES study, Wind Energ. Sci., 1, 129–141, https://doi.org/10.5194/wes-1-129-2016, 2016.

Vollmer, L., Steinfeld, G., and Kühn, M.: Transient LES of an offshore wind turbine, Wind Energ. Sci., 2, 603–614, https://doi.org/10.5194/wes-2-603-2017, 2017.

Paper VI

Validation of the 2D-VAR lidar retrieval algorithm for non-homogeneous wind fields using FINO1 and SCADA data

Krutova, M., Bakhoday-Paskyabi, M., and Reuder, J.
Authorea, **[preprint]** (2023)

Received: Added at production | Revised: Added at production | Accepted: Added at production

DOI: xxx/xxxx

RESEARCH ARTICLE

Validation of the 2D-VAR lidar retrieval algorithm for non-homogeneous wind fields using FINO1 and SCADA data

Maria Krutova* | Mostafa Bakhoday-Paskyabi | Joachim Reuder

[1]Geophysical Institute and Bergen Offshore Wind Center (BOW), University of Bergen, Allégaten 77, Bergen 5007, Vestlandet, Norway

Correspondence
*Maria Krutova, Geophysical Institute and Bergen Offshore Wind Center, University of Bergen, Allégaten 77, Bergen 5007, Vestlandet, Norway Email: Maria.Krutova@uib.no

Abstract

A scanning lidar measures a projection of the actual wind speed to the line-of-sight. Reconstruction of the original field is possible via various retrieval algorithms, especially if several lidars are deployed in the area. However, this may not be the case due to financial constraints. Additionally, conventional algorithms like Volume Velocity Processing (VVP) do not perform well for non-homogeneous flow fields, e.g., smooth wind turbine wakes in a retrieved field. A 2D-VAR algorithm using VVP as an intermediate step was suggested allowing the retrieval for consecutive scans at a low elevation angle. We validate this algorithm for scans containing prominent wakes under elevation angles within 5° using FINO1 mast and supervisory control and data acquisition (SCADA) data.

We show that prominent wakes scanned at the hub height introduce substantial disturbances in the VVP retrieval output and affect the retrieved field. The unwanted disturbance may be overcome by masking the wakes. In point measurements, the wind speed magnitude is retrieved with an acceptable accuracy, but the wind direction appears to be sensitive to the weights and initial guess chosen. According to our sensitivity analysis, the weight assigned to the radial velocity residuals affects the outcome most, while other weights act as corrections.

KEYWORDS:
lidar retrieval; wind turbine wake; wind farm

1 | INTRODUCTION

Wind lidar systems, with their capability to measure the wind field remotely, have become a common measurement technology in atmospheric boundary layer research[1,2,3]. In particular, the wind energy meteorology has utilized this measurement technology extensively during the last decade[4]. The potential of lidar application is already shown for wake dynamic studying[5], turbulence[6,7] and power curve measurements[8,9] or data assimilation for a WRF model[10]. Processing the data in real-time opens a possibility of using lidars in short-term forecasting, e.g., for pitch[11] or yaw[12] control. 2D velocity fields obtained with a scanning lidar are particularly interesting for wake identification and characterization[13,14] or validation of large-eddy simulations (LES)[15].

Unlike sonic or cup anemometers, scanning lidars do not measure the wind speed directly but only its projection to the line-of-sight – the radial velocity. Hence, characterizing wakes with a scanning lidar without additional processing is effective only if the wakes are aligned with the lidar's line-of-sight. Retrieving the original wind speed and direction may be complicated when only one lidar is deployed at the site. Certain widely used algorithms require a specific scanning procedure not compatible with a 2D plane scanning. E.g., Velocity Azimuth Display (VAD) operates on conical 360° scans[16]. Its derivative, Doppler Beam Swinging (DBS), fetches the radial velocity from beams shoot in four directions at 30° angle from vertical. Another algorithm, Volume Velocity Processing (VVP), may be used with a scanning lidar for retrieval[17] but assumes a homogeneous flow

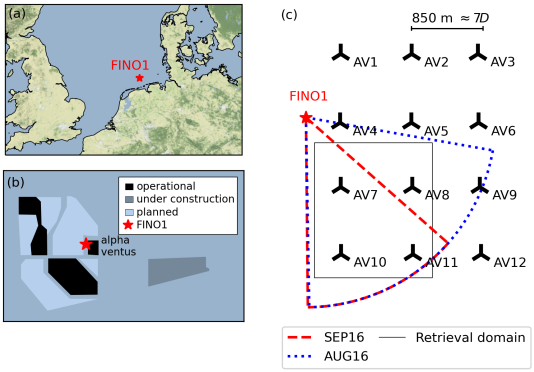

Figure 1 Map indicating the location of the FINO1 platform in the North Sea (a), the surrounding wind farms during the measurement period in September 2016 (b), and the layout of the Alpha Ventus research wind farm with the scanning angles for the PPI scans in this study (c). The retrieval is performed within the retrieval domain; here – pictured in a size used for SEP16 scans.

and does not adequately resolve heterogeneous structures, such as wakes. Complex algorithms, e.g., 4D-VAR and its derivatives, perform better on heterogeneous flows but may be time-consuming to allow real-time processing [18]. 4D-VAR method are mostly developed for weather prediction models [19,20], their capability to estimate thermodynamic quantities may be excessive for a smaller scale wind energy research. An alternative, the 2D-VAR algorithm, was suggested to preserve advantages of the 4D-VAR method and overcome complications caused by heterogeneous wake fields [21]. The algorithm performs a retrieval from a set of consecutive lidar scans taken at a low elevation angle provided that the time interval between two scans is small enough ($\Delta t \sim 60\,\mathrm{s}$) to assume weak changes in the flow.

The 2D-VAR algorithm was validated on a one-day dataset from August 31, 2016. Due to the limited period, the validation covered only a narrow range of wind speeds (2−6.5 m/s) and directions (150−265°). Additionally, the regarded lidar scans were taken at a nearly horizontal plane and captured the flow at the bottom tip of the wind turbines. Consequently, the results could be validated only with FINO1 data. We perform a new validation on the extensive dataset spanning the whole month of September 2016. The scans from that period allow studying the algorithm's performance for a higher elevation angle. The lidar, therefore, scans one turbine at the hub height allowing a comparison to the supervisory control and data acquisition (SCADA) data for this turbine, which was not possible in the original study.

2 | DATA

2.1 | Description of the datasets

The meteorological and lidar data were obtained during the Offshore Boundary-Layer Experiment at FINO1 (OBLEX-F1) campaign in 2015−2016. The FINO1 platform is located in the North Sea at 54° 00′ 53.5″N, 6° 35′ 15.5″E, 45 km north of the German island of Borkum. The Alpha Ventus wind farm is located east of the FINO1 platform and consists of 12 wind turbines arranged in a rectangular pattern (Fig. 1). The wind turbines AV1−AV6 are of the type Repower 5M with a hub height of 92 m and a rotor diameter of 126 m; AV7−AV12 are of the type AREVA M5000 with a hub height of 91.5 m and a rotor diameter D of 116 m. The construction of the Borkum Riffgrund II wind farm south of the Alpha Ventus wind farm was completed in 2018 and did not affect the flow during the measurement period.

The scanning Doppler wind lidar (Leosphere WindCube 100S) was installed at the FINO1 platform at 23.5 m above sea level and was oriented towards the Alpha Ventus wind farm. The lidar operates in PPI mode. The 2D-VAR algorithm was validated on the data from a single day of August 31, 2016. On that day, the lidar performed scans under the elevation angle of 0.5°. The elevation angle remained constant for 20 hours, which resulted in nearly 1500 scans. The lidar scanned a sector between 100° and 180° azimuth angles, so that four wind turbines (AV7, AV8, AV10, AV11) and their bottom tip wakes were present in the scanned sector. We consider this one-day dataset for a comparison to the original results [21,22] and refer to it as AUG16.

During September 2016, the lidar performed azimuth scans between 131.5° and 180° in the following elevation pattern: during the first 20 minutes of each hour, the lidar scanned at a constant elevation angle of 4.6° so that AV7 is scanned near the hub height; for the remaining 40 minutes, the lidar performed alternating scans at three elevation angles of 0.5°, 4.6°, and 9.0°. The interval between two scans is approximately 51 s.

The 2D-VAR retrieval algorithm requires scans taken at the same elevation angle with a sufficiently high temporal resolution that allows assuming weak changes in flow. Hence, we perform a lidar retrieval only for the scans taken during the first 20 minutes of each hour when the elevation angle is fixed at 4.6°. Those selected scans cover about 34% duration of September 2016. Due to an inclined scanning plane and smaller sector scanned, only the wakes from wind turbines AV7 and AV10 are always captured well in the September 2016 scans. The wakes from other wind turbines appear only for the specific wind directions. We use this one-month dataset to perform an extensive validation of the 2D-VAR algorithm and refer to it as SEP16.

Depending on weather conditions, the lidar's beam range varies and may reach up to 3 km. The far range experiences data losses frequently and thus poses little interest for the retrieval. When processing lidar data, we limit the beam range to 2.25 km for the sake of the dataset uniformity and exclusion of the area with a large percentage of missing data points.

The 10-minute averaged time series from the FINO1 mast are used as an initial guess for the retrieval algorithm and as the reference data for validation. The wind speed is measured with cup anemometers installed at 33, 40, 50, 60, 70, 80, 90, and 100 m above sea level; the mast shadow affects wind speed measurements for the wind direction of 290−330°. The wind direction is measured with vanes installed at 33, 40, 50, 60, 70, 80, and 90 m above sea level; the mast shadow affects measurements for the wind direction of 110−150° (Fig. 2a).

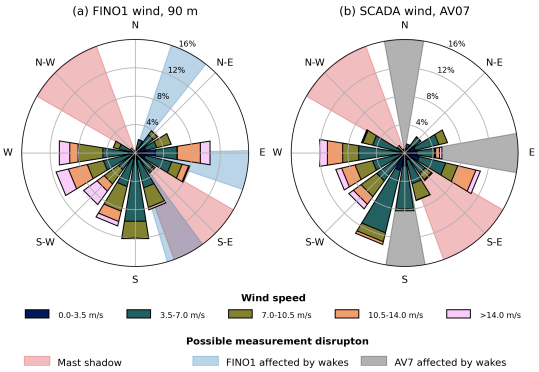

Figure 2 Wind roses for 10-minute averages of FINO1 (90−100 m measurements) and SCADA of the AV7 turbine. The wind roses consider only the periods for which both FINO1 and SCADA data are available

Since the FINO1 mast is located at a distance from the Alpha Ventus wind farm and local measurements do not represent the actual wind flow near the wind turbines, we utilize SCADA data to verify the retrieved flow near the AV7 turbine. The SCADA data consist of 1 Hz wind speed and direction time series.

FINO1 and SCADA data may differ when AV7 is affected by the wake while the FINO1 mast remains in the free flow or vice versa. The wind roses for FINO1 and SCADA data show a discrepancy in the wind speed distribution for southerly directions (160−200°): the wind turbine AV7 is affected by the wake from AV10. Another strong difference is the easterly direction: AV7 is hit directly by the wake from AV8. Being shifted slightly to the North, the FINO1 mast is less affected by the wake from AV4. Hence, the AV7 inflow wind speeds are generally lower than registered at FINO1 (Fig. 2b). The adjacent sector of 140−160° represents cases when the FINO1 mast is affected by the far wake from AV7, reducing the wind speed. The discrepancy between FINO1 and SCADA data there is noticeable but less prominent than for southerly and easterly winds.

The FINO1 mast data are used to define an initial guess for the retrieval algorithm. Since the FINO1 time series is nearly continuous and has little missing data in the regarded period (Table 1), we fill the gaps with a linear interpolation to obtain reference wind speed and direction values for all lidar scans. Due to larger gaps in the SCADA data and its lower importance for the 2D-VAR algorithm, we do not perform a similar interpolation for the SCADA time series. Hence, the cross-comparison for FINO1, SCADA and retrieval results (e.g., wind roses) does not consider time stamps where SCADA data are missing.

The lidar and SCADA data are recorded roughly in 1-minute intervals as opposed to 10-minute averages from FINO1. During the retrieval phase, we consider 10-minute averages from the FINO1 mast for all lidar scans in 5-minute intervals before and after the respective time stamp in the

Table 1 Data availability for the SEP16 dataset. Only scans separated by $\Delta t < 60\,\mathrm{s}$ are considered.

Dataset	Subset	Missing data, %
FINO1 mast	wind speed	0.03
	wind direction	0.08
SCADA	wind speed	1.07
	wind direction	4.05
Lidar	whole scan	1.68
	retrieval domain	0.66

mast data, to comply with the higher time resolution of the lidar data. When comparing the results, we average the retrieval and SCADA series over the corresponding 10-minute periods.

2.2 | Pre-processing of the lidar scans

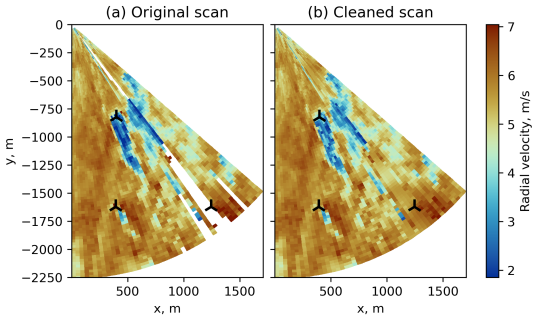

Figure 3 Pre-processing of the lidar scan taken at 2016-09-05 00:08:33. a) Original scan, b) Spike removal and gap filling

The performance of the retrieval algorithm strongly depends on the lidar scan quality. The scans may contain spikes near the wind turbine position because of the lidar beam hitting the rotating blades. We identify spikes by fitting a normal, log-normal, or Weibull distributions to the radial velocity distribution within a scan. The points falling outside the best fit's confidence interval of 99.9% are regarded as spikes and removed from the scan. The gaps, both the ones in the original data set and the ones added by the spike removal, are filled with the Gaussian kernel inpainting algorithm[23] (Fig. 3b).

Occasionally, the lidar may not complete the scan correctly, resulting in missing data that cannot be restored accurately by the gap filling. A high percentage of missing data renders the scan unsuitable for the retrieval. Therefore, we only perform the lidar retrieval if more than 50% of the scanned sector is available within the retrieval domain defined as a rectangle (Fig. 1c). The discarded scans constitute less than 1% of the SEP16 dataset and occur only on certain days (Table 1). The threshold of 50% data losses is enough to ensure that the flow is resolved at least near AV7. The data around AV10 may still be missing in scans with medium data losses (20−50%). Occurrences of medium data losses are scattered across the dataset with a large cluster localized on September 19−21, characterized by low wind speed of 0−5 m/s and wind direction of 0−120° (Fig. 4).

The 2D-VAR retrieval algorithm requires an estimation of various derivatives. Due to a small azimuth step of $1° \approx 0.174\,\mathrm{rad}$ and the discrete nature of a scanned flow field, the derivative $\partial V_r/\partial\theta$ may return values of a higher order than the derivatives taken along the Cartesian grid or the time derivative. The derivative spikes are most likely to occur at the boundary between wakes and free-flow. These effects are mitigated by applying a Gaussian filter to the V_r field before taking a derivative.

After the cleaning, the lidar data coordinates are converted from a polar (r, θ) to a Cartesian grid (x, y). The coordinate center is located at FINO1, with the x-axis being positive in the East direction and the y-axis being positive in the North direction. The retrieval is performed for a rectangular domain, interpolated to an equidistant Cartesian grid. The selected retrieval domain contains enough space around AV7 to resolve

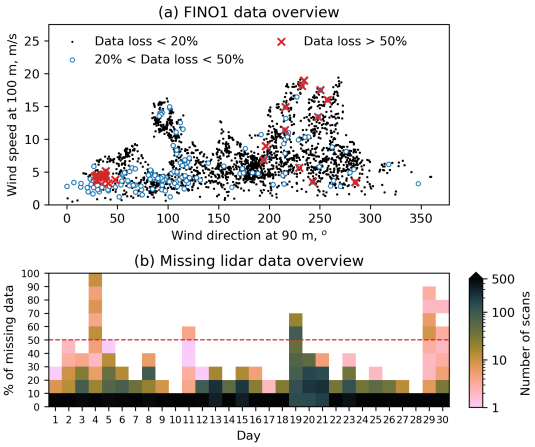

Figure 4 Overview of the missing scan data in SEP16. a) Occurrences of missing data with respect to FINO1 wind speed and direction measurements, b) number of lidar scans with a certain percentage of missing data by day.

the near wake and provide the inflow wind speed. Following the original study[21], we perform the retrieval for AUG16 in a rectangular domain $1500 \times 1200\,\mathrm{m}^2$ with a bottom left corner located at $x = 100\,\mathrm{m}$, $y = -1700\,\mathrm{m}$ and a Cartesian grid spacing of $\Delta x = \Delta y = 30\,\mathrm{m}$. We extend the retrieval domain for SEP16 to capture an additional area around AV10 in case of northerly winds. SEP16, therefore, uses the retrieval domain of $1600 \times 1400\,\mathrm{m}^2$ with a bottom left corner located at $x = 100\,\mathrm{m}$, $y = -1700\,\mathrm{m}$. The Cartesian grid spacing is increased to $\Delta x = \Delta y = 35\,\mathrm{m}$.

3 | METHODOLOGY

The 2D-VAR algorithm[21] consists of two steps. In the first step, the background flow is estimated with a simplified VVP retrieval algorithm. The directional wind speed components from the retrieved background flow (u_b, v_b) are then used in the second step, among with other input data, to optimize the cost function.

3.1 | VVP retrieval to estimate the background flow

The lidar measures the radial velocity V_r, i.e., the projection of the 3D wind vector on the measurement line-of-sight of the lidar:

$$V_r = u \sin\theta \cos\varphi + v \cos\theta \cos\varphi + w \sin\varphi \tag{1}$$

where u, v, and w are the directional components of U; θ is the azimuth angle, and φ is the elevation angle of the lidar beam. The lidar scans AV7 near the hub height at an elevation angle of $\varphi = 4.6° = 0.08\,\mathrm{rad}$, which is small enough to approximate $\cos\varphi$ as 1 and $\sin\varphi$ as φ. Considering that the vertical component w is generally small, the last term of Eq. (1) can be neglected: $w \sin\varphi \approx w\varphi \approx 0$. Then, Eq. (1) is reduced to

$$V_r = u \sin\theta + v \cos\theta \tag{2}$$

The difference between the retrieved field (u, v) and the measured radial velocity V_r can be then presented as a function $F(u, v)$:

$$F(u, v) = u \sin\theta + v \cos\theta - V_r \tag{3}$$

Eq. (3) would have several solutions for $F(u, v) = 0$ if solved for a single point. Instead, we optimize $F(u, v)$ for a fetch area around the target point and find the solution via a least squares method assuming that (u, v) components remain the same within this area. The fetch area size is selected so that the variation in radial velocity is not confused with random fluctuations caused by turbulence[24]. We pass an initial guess as directional components (u_0, v_0) calculated from FINO1 reference wind speed U and direction Φ. Since the wind direction is defined in a meteorological sense, it has to be converted to the mathematical direction as $1.5\pi - \Phi$ to obtain wind speed components via projection to x- and

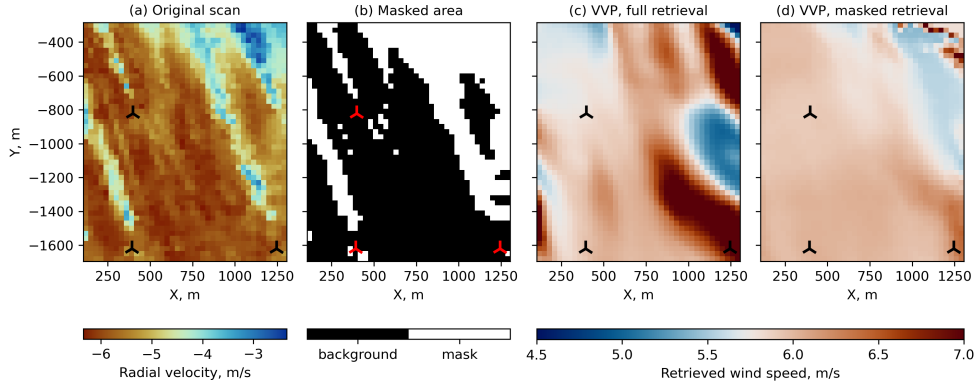

Figure 5 VVP retrieval results for an example scan from AUG16 dataset. (a) A lidar scan taken at 20160831 2:15:46 UTC+0 at the elevation angle of $\varphi = 0.5°$. FINO1 wind speed 5.8 m/s, wind direction 147°. (b) Wake mask. (c) The VVP algorithm without wake masking produces structures of increased wind speed in the far range. (d) The VVP retrieved field with wake masking is more homogeneous.

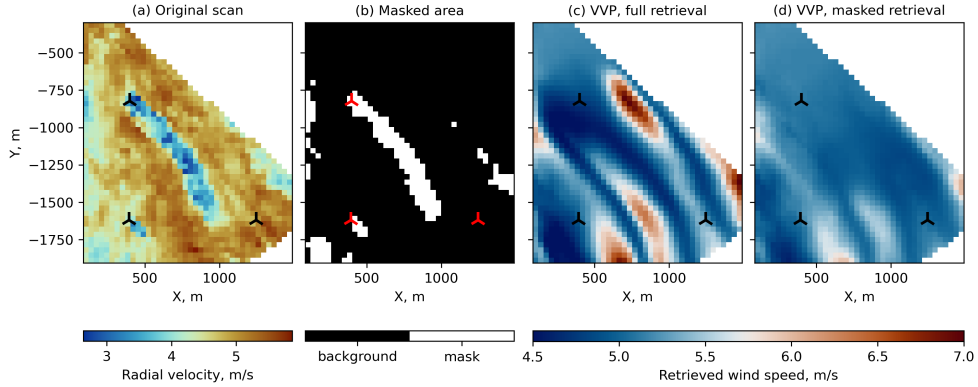

Figure 6 VVP retrieval results for an example scan from SEP16 dataset. (a) A scan taken at 20160904 21:15:22 UTC+0 at the elevation angle of $\varphi = 4.6°$. FINO1 wind speed 5.3 m/s, wind direction 309°. (b) Wake mask. (c) The VVP retrieved field without wake masking is strongly heterogeneous but does not represent the actual wakes. (d) Wake masking smooths the retrieved field, particularly the high-speed structures along wakes.

y-axes.

$$u_0 = U\sin(1.5\pi - \Phi), v_0 = U\cos(1.5\pi - \Phi) \tag{4}$$

In the original study, the VVP algorithm was applied to horizontal scans at $\varphi = 0.5°$, capturing the flow at the bottom tip of the wind turbines (Fig. 5a). Since the VVP algorithm assumes homogeneous wind flow but is solved locally, the retrieved field tends to overestimate the wind speed along the wakes to compensate for the wake deficit. Although the wakes captured at this level are weak and narrow, the VVP algorithm occasionally produces high-speed structures in the far range (Fig. 5c). When scanned at a higher elevation angle ($\varphi = 4.6°$), the wakes occupy a larger part of the lidar scan and show a stronger wake deficit than the bottom tip wakes (Fig. 6a). Consequently, the VVP retrieval produces high-speed structures along the AV7 wake (Fig. 6c). This disturbance has to be mitigated so that it is not carried over to the next step of the 2D-VAR algorithm.

We identify and mask the wakes using an automatic thresholding algorithm that splits the radial velocity field into wake and free-flow points [14]. The identified wake points are not considered in the fetch area during the VVP retrieval (Fig. 5b, 6b). Since the equation $F(u, v) = 0$ is solved for

an area, running an optimization function around a masked point still fetches enough non-masked points for the solution. The masked points are then replaced with the optimization result, and the retrieved field becomes more homogeneous than the non-masked solution (Fig. 5d, 6d).

We apply masking only in the case of prominent wakes, i.e., when the reference wind speed is above the cut-in wind speed of 3.5 m/s and the lidar beam is aligned with the reference wind direction. If the angle between the lidar beam and wind direction are close to perpendicular, a so called crosswind, the radial component of the wind speed tends to zero. Despite the actual magnitude of wind speed, the crosswind wakes become less distinguishable from the free flow in a lidar scan; the radial velocity appears to be more homogeneous and poses less problem for the VVP retrieval.

Originally, the radius of the fetch area was chosen as $r = 200\,\mathrm{m}$ [21] to retrieve the (u, v) field reliably when using the VVP algorithm. We increase this value to $r = 300\,\mathrm{m}$ to ensure that the masked area is always filled in the case of wide or merging wakes.

3.2 | Cost function optimization for the detailed retrieval

The second step of the 2D-VAR algorithm optimizes a cost function J. The cost function introduces several constraints to the background flow to allow a single solution[1]:

- A – the deviation between calculated and observed radial velocities defined from Eq. (5)

$$A = (u \sin\theta + v \cos\theta) - V_r \tag{5}$$

- B – the deviation from the constant wind defined via an unknown value P

$$B = (u \cos\theta - v \sin\theta) - W_{b2} \frac{\partial V_r}{\partial \theta} + P \tag{6}$$

  We alter the definition of the term by adding a weight W_{b2} to allow an additional control of the derivative $\partial V_r/\partial\theta$. When $W_{b2} \neq 1$, the discrepancies with the actual derivative are then accumulated in the term P.

- C – the radial velocity advection equation. This term assumes that the radial velocity is stationary between two consecutive scans.

$$C = \frac{\partial V_r}{\partial t} + u\frac{\partial V_r}{\partial x} + v\frac{\partial V_r}{\partial y} \tag{7}$$

- D – the deviation from the background flow (u_b, v_b), which is estimated in the previous step using the VVP algorithm.

$$D_a = u - u_b,\ D_b = v - v_b \tag{8}$$

The weighted constraints are optimized for the whole retrieval domain defined on the Cartesian grid (x, y).

$$J(u, v, P) = \frac{1}{2\Omega} \int (W_a A^2 + W_b B^2 + W_c C^2 + W_d D_a^2 + W_d D_b^2) d\Omega \tag{9}$$

where W_a, W_b, W_c, and W_d are the weights that could be either constant or dynamic [22]. We utilize the suggested dynamic definition of the weights and provide a brief comparison to the constant weights when analyzing the results.

By the proposed definition, W_a is the only constant weight over the whole retrieval domain. The original study [22] suggests the value of $W_a = 1$. Other weights are defined to adapt to local features of the flow. The weights, W_b and W_d, are complementary so that $W_b + W_d = 1$. They indicate whether the variability of radial velocities was accounted for.

$$W_d(x, y) = 1 - \frac{\sum (V_r^{VVP} - V_r^{obs})^2}{\sigma_{V_r}^2}\bigg|_{(x,y)} \tag{10}$$

where $V_r^{VVP} = u_b \cos\theta + v_b \sin\theta$ is the radial velocity calculated from the retrieved field using Eq. (2). $\sigma_{V_r}^2$ is the variance of the measured radial velocity in the same fetch area around the point (x, y) as in the VVP retrieval, i.e., a circular area with the radius of $r = 300\,\mathrm{m}$. The weight W_b is then $W_b = 1 - W_d$.

The weight W_c ensures that the advection equation is solved only for the points where the assumption of a stationary radial velocity would be valid. I.e., the advection distance Δr between two consecutive scans is

$$\Delta r = V_T \times \Delta t \tag{11}$$

where Δt is the time interval between the measurements at the same point in two consecutive scans, V_T is the tangential velocity

$$V_T = \frac{\partial V_r}{\partial \theta} = u_b \sin\theta + u_b \cos\theta \tag{12}$$

[1]The original study aligns x-axis and respective u-component with the North direction. To comply with the meteorological notation where x-axis is aligned with the East, we had to switch u and v-components where it was relevant

Then, taking λ as $1-2$ times the grid spacing, the weight W_c is defined as a binary matrix

$$W_c = \begin{cases} 0; & \text{for } \Delta R > \lambda \\ 1; & \text{for } \Delta R \leq \lambda \end{cases} \tag{13}$$

We observed an improvement of the retrieved flow structure in SEP16 if more weight is given to W_a, which we discuss further in the sensitivity analysis of the 2D-VAR algorithm. We also set $W_{b2} = 1$ and apply a Gaussian filter with the standard deviation of $\sigma = 4$ to the gap-filled radial velocity V_r prior of calculation of the derivative $\partial V_r/\partial\theta$ in Eq. (6). Time and spatial derivatives in the advection component Eq. (7) are calculated for the original field with the gaps filled to avoid over-smoothing of the input data. Hence, we define our weight set as follows

$$W_a = 5,\ W_b = 1 - W_d,\ W_{b2} = 1,\ W_c \text{ as in Eq. (13)}, W_d \text{ as in Eq. (10)} \tag{14}$$

Since the cost function is optimized for the whole area at once and attempts to retrieve the original non-homogeneous flow, the wake masking is not applied here. An initial guess utilizes a constant field (u_0, v_0) as defined in Eq. (4) from the FINO1 mast data. The initial deviation from the constant flow is set to zeroes matrix $\mathbf{P_0} = 0$.

3.3 | Validation

We consider two aspects when evaluating the retrieval accuracy: whether the virtual lidar field modeled from the retrieved flow correspond to the FINO1 lidar measurement and whether the local retrieved wind characteristics agree with FINO1 and SCADA time series.

The modelled radial velocity V_r^{mod} is calculated from the retrieved field (u^{ret}, v^{ret}) using Eq. (2). The divergence from the observed radial velocity V_r^{obs} is evaluated based on the mean and standard deviation of the residuals ΔV_r.

$$\Delta V_r = V_r^{obs} - V_r^{mod} = V_r^{obs} - (u^{ret}\cos\theta + v^{ret}\sin\theta) \tag{15}$$

The retrieved wind speed and direction are compared against FINO1 and SCADA data. We use different approaches depending on the lidar's elevation angle. For the nearly horizontal scans in the AUG16 dataset taken at the elevation angle of 0.5°, only the comparison to FINO1 measurements near the height of 33 m would be relevant. The wind speed components $(u_{xy}^{ret}, v_{xy}^{ret})$ are extracted from the top left corner of the retrieval domain – the probe point closest to the FINO1 mast, excluding the border points, or $x_p = 130\,\text{m}$, $y_p = -330\,\text{m}$.

The SEP16 dataset with scans taken at the elevation angle of 4.6° provides a different option for the comparison – the time series at AV7 hub height. The inflow wind speed and direction for the AV7 turbine are probed dynamically so that the probe point is always located at $1D$ upstream of AV7. The wind speed components are calculated as mean values in a circular area with a radius of $1D$ around the probe point.

For the comparison, the retrieval and SCADA time series are averaged to the same 10-minute periods as the FINO1 time series. The root mean square errors (RMSE) of wind speed ΔU and direction $\Delta\phi$ estimation are then calculated as follows:

$$\Delta U = \sqrt{\frac{1}{N}\sum_{i=1}^{N}(U_1 - U_2)^2},\ U_{(1,2)} = \sqrt{u_{(1,2)}^2 + v_{(1,2)}^2} \tag{16}$$

$$\Delta\phi = \sqrt{\frac{1}{N}\sum_{i=1}^{N}\left[\arccos\left(\frac{u_1u_2 + v_1v_2}{U_1 \cdot U_2}\right)\right]^2} \tag{17}$$

where the indices (1, 2) mark values from respective time series U_1 and U_2 and N is the number of valid values.

4 | RESULTS

4.1 | Comparison to the original study, August 31, 2016 (AUG16)

Since we are implementing the 2D-VAR retrieval algorithm anew, we verify how our implementation performs compared to the original study[21,22]. The 2D-VAR retrieved time series follows the FINO1 time series regardless of the wake masking. In contrast, the VVP series deviate stronger from FINO1 for certain wind directions when the retrieval is run without wake masking (Fig. 7).

The new implementation achieves good agreement for scans taken after 15:00. Those scans are characterized by crosswind directions and wind speeds close to cut-in wind speed. I.e., the flow is nearly homogeneous. Consequently, the new implementation and VVP retrieval show little divergence from the reference data and from each other.

We observe similar errors in the wind speed estimation between our and original implementation, but a larger error in the wind direction (Table 2). The wind direction error is also larger for the VVP retrieval. Considering that the VVP algorithm returns a rather stable solution, the difference in wind direction errors may be caused by different pre-processing and solving procedures that were not detailed in the original study.

Table 2 Results reproduction for AUG16 dataset.

Study	Algorithm	Wind speed error	Wind speed correlation coefficient	Wind direction error	Wind direction correlation coefficient
Original†	2D-VAR	0.383 m/s	0.96	-1.4°	0.98
	VVP	0.29 m/s	0.98	4.3°	0.99
Reproduced	2D-VAR	0.334 m/s	0.96	6.06°	0.96
	VVP	0.375 m/s	0.96	7.61°	0.96

†Cherukuru, N. W., Calhoun, R., Krishnamurthy, R., Benny, S., Reuder, J. and Flügge, M.: 2D VAD single Doppler lidar vector retrieval and its application in offshore wind energy, Energy Procedia, 137, 497–504, 2017.

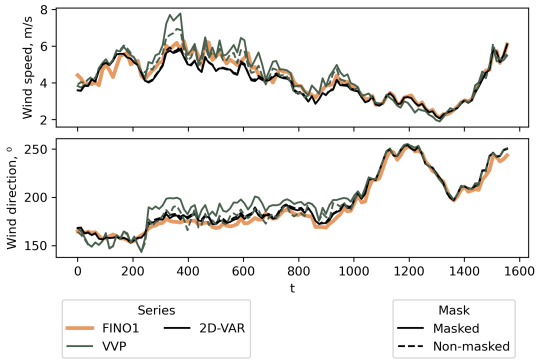

Figure 7 Comparison of the retrieval results and FINO1 data for the AUG16 dataset.

4.2 | Comparison to the new dataset, September 2016 (SEP16)

SEP16 dataset provides an additional possibility for the validation provided that SCADA data are available. FINO1 vs. SCADA comparison is then taken as a reference – the retrieved series should not perform worse than it.

The retrieval time series shows good agreement with FINO1 and SCADA data, especially for the wind speed estimation (Fig. 10ab). Several outliers in wind direction cannot be explained only by being close to 0° or 360°. When highlighted by the wind speed value, the irregular outliers correspond to wind speeds below 1 m/s. The uncertainty of the instantaneous measurements can then explain the discrepancy during low wind. The directional components both in measured and retrieved time series are prone to uncertainty error. Consequently, the wind direction may be estimated incorrectly for low wind even if the wind speed magnitude is similar. Hence, we consider the retrieval results unreliable for FINO1 or SCADA wind speeds below 1 m/s and do not include them in the comparison and error calculation.

The scatter of retrieved wind direction is smaller for the 2D-VAR vs. FINO1 comparison than for 2D-VAR vs. SCADA (Fig. 10ab). In addition, the scatter in 2D-VAR vs. SCADA plot resembles FINO1 vs. SCADA comparison (Fig. 10c) despite the values being probed closer to AV7, SCADA measurement location, than FINO1. A better agreement with FINO1 implies that the cost function optimization may be tuned to the initial guess (u_0, v_0) calculated from FINO1 data. We perform a sensitivity analysis to determine, which factors affect the 2D-VAR algorithm.

4.2.1 | Sensitivity to the input data

The 2D-VAR algorithm consists of two optimization steps. Both steps require an initial guess of the horizontal wind field (u_0, v_0). In the first step, the VVP retrieval is run locally point by point. The VVP solution via least-squares minimization is rather stable and does not noticeably depend on an initial guess. The solution can be affected slightly by altering the grid spacing or retrieval domain size. Stronger alteration can be achieved if some points are deliberately excluded from the minimization, i.e., by applying the wake masking (Fig. 11).

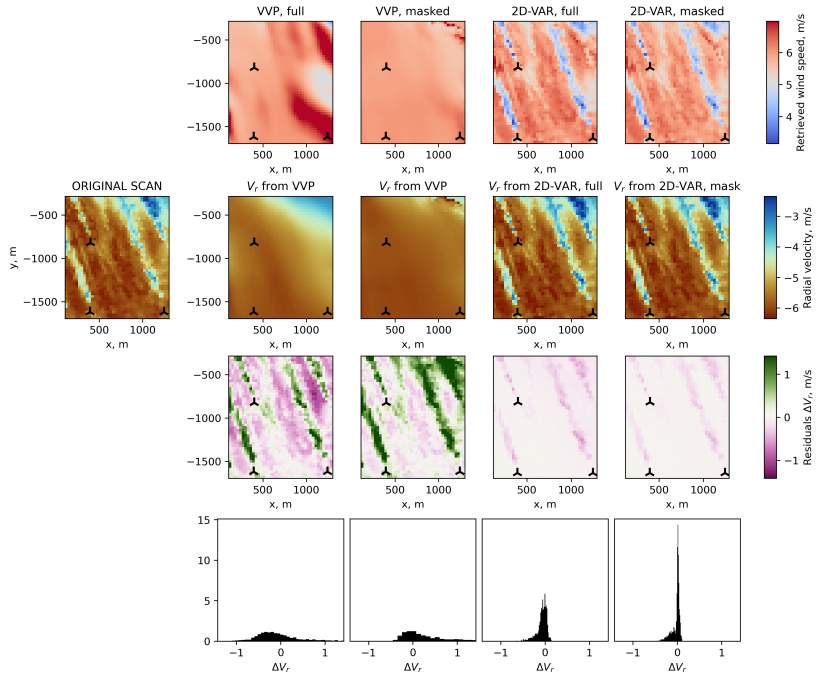

Figure 8 Example of the retrieval performed for the scan from AUG16 taken at 20160831 02:15:46 UTC+0. FINO1 wind speed 5.6 m/s, wind direction 155°.

The VVP field is then used in the cost function optimization in the term D (Eq. (8)) and the weight W_d, if the dynamic definition Eq. (10) is applied. Hence, strong non-physical disturbances in the VVP solution are carried over to the next optimization step. Figure 11 shows an example of the retrieval performed for a lidar scan with long prominent wakes present. If the VVP retrieved field is obtained without the wake masking, the 2D-VAR solution gets a non-uniform wind speed increase along the wind turbines. Consequently, radial velocity residuals have a higher standard deviation and bias compared to the solution where the wakes were masked for the VVP algorithm. The residuals of the non-masked solution tend to have lower bias and standard deviation.

For the first step of the 2D-VAR algorithm, the accuracy of wake masking becomes more important for the VVP solution than the initial guess. If the wakes cannot be identified reliably, e.g., in the crosswind conditions, it is preferable to proceed without masking. Wake masking is the most efficient when the lidar captures wide and long strong wakes, i.e., when the lidar beam and wind direction are aligned (Fig. 11). Due to the FINO1 relative position to AV7 and with the respect to the lidar orientation, such alignment occurs only in the north-western and south-eastern sectors. Although not many events are registered for those sectors, the agreement to the SCADA wind rose (Fig. 9b) is better when the wake masking is applied (Fig. 9c) as opposed to non-masked wakes (Fig. 9d). The improvement leads to a slight reduction of RMSE when the wake masking is applied compared to non-masked retrieval (Fig. 12).

The second step of the 2D-VAR algorithm relies on optimizing the cost function calculated over the whole area. Despite the 2D-VAR algorithm using the FINO1 data as an initial guess, the retrieved data's wind speed and direction distribution (Fig. 9c) are closer to the SCADA wind rose rather than FINO1. If the algorithm is run with the SCADA data as an initial guess, the agreement between the SCADA data and retrieved inflow gradually increases (Table 3, Fig. 12). On the contrary, the solution diverges from FINO1 mast data at the hub height showing wind direction errors similar to the comparison between FINO1 and SCADA.

Nevertheless, the wind field estimated with FINO1 has a smaller gap between wind direction errors for FINO1 or SCADA data comparison. A good agreement implies that the retrieved wind field near AV7 tends to the actual wind field, provided that the initial guess is still close to it.

Table 3 Validation of the retrieval time series for the SEP16 dataset. Bold font marks the smallest error of wind speed and direction.

Series	Wind speed error (RMSE)		Wind direction error (RMSE)	
	VVP	2D-VAR	VVP	2D-VAR
FINO1 mast data as initial guess				
Retrieval vs. FINO1 (60 m)	0.89 m/s (0.976)	0.80 m/s (0.981)	12.16° (0.975)	10.08° (0.980)
Retrieval vs. FINO1 (hub height)	1.04 m/s (0.967)	**0.67 m/s (0.988)**	14.51° (0.981)	11.68° (0.976)
Retrieval vs. SCADA	1.22 m/s (0.954)	1.08 m/s (0.976)	7.46° (0.988)	**7.46° (0.988)**
SCADA AV7 data as initial guess				
Retrieval vs. FINO1 (60 m)	0.88 m/s (0.975)	1.13 m/s (0.976)	12.71° (0.975)	12.23° (0.975)
Retrieval vs. FINO1 (hub height)	1.03 m/s (0.966)	1.08 m/s (0.976)	15.16° (0.976)	13.74° (0.977)
Retrieval vs. SCADA	1.31 m/s (0.949)	**0.74 m/s (0.980)**	8.44° (0.976)	**5.85° (0.983)**
Reference comparison				
FINO1 vs. SCADA	1.43 m/s (0.961)		12.69° (0.979)	

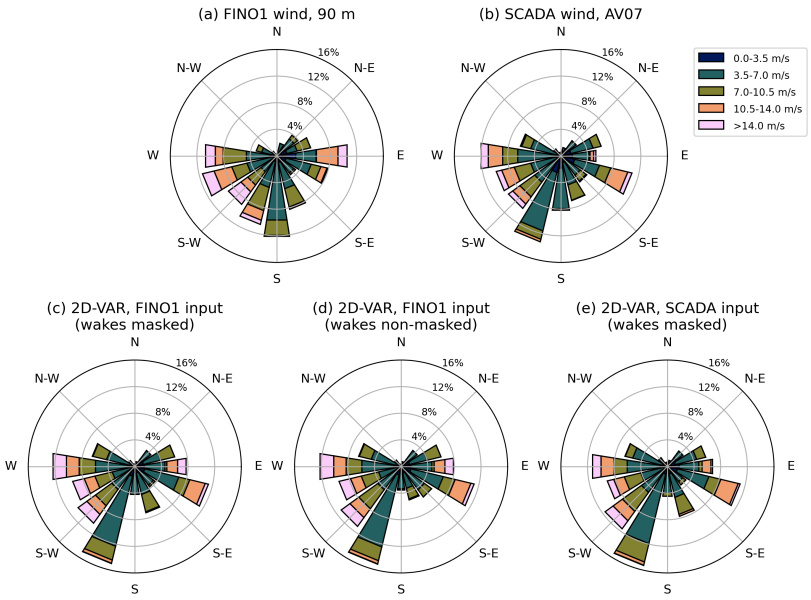

Figure 9 Wind roses for SEP16 for the inflow probe $1D$ upstream of AV7, 2D-VAR input sensitivity. Only scans valid for retrieval and are considered. a) FINO1 data, b) SCADA data, c) 2D-VAR retrieval, FINO1 data as initial guess, wakes are masked at VVP step, d) 2D-VAR retrieval, FINO1 data as initial guess, wakes are not masked at VVP step, e) 2D-VAR retrieval, SCADA data as initial guess, wakes are masked at VVP step

4.2.2 | Sensitivity to the weights

We alter the weights W_a, W_{b2}, W_c, and W_d to analyze their effect on the final solution. We do not regard the weight W_b separately since it is linked to W_d.

The weight W_a adjusts the cost function term A, which reduces the discrepancy between the lidar data and radial velocity calculated from the retrieved field as defined in Eq. (5). Empirically, this weight should remain at $W_a = 1$. However, we observed a non-physical wind speed increase at the wake boundaries in the retrieved flow when using this value for SEP16 scans. Increasing the weight puts more emphasis on reducing the

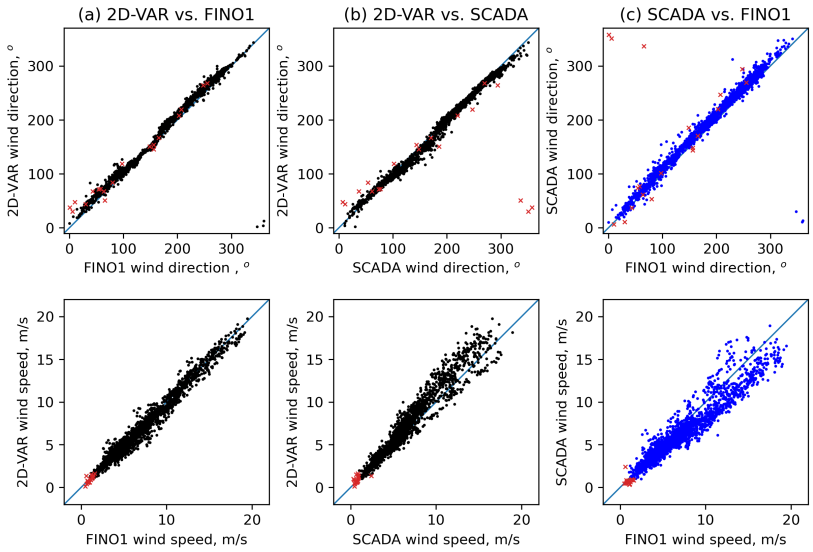

Figure 10 Wind speed and direction comparison for the 2D-VAR retrieval data at AV7 inflow. a) 2D-VAR vs. FINO1, b) 2D-VAR vs. SCADA, c) SCADA vs. FINO1

discrepancy in radial velocity residuals but leads to a bias in the residuals. The residuals for $W_a = 1$ are more symmetrical than with the increased weight and have a higher standard deviation (Fig. 13). While a further increase of W_a gradually decreases the residuals, it strongly affects wind roses for the AV7 inflow (Fig. 14ef), and they diverge from the reference FINO1 and SCADA wind roses (Fig. 14ab). Considering RMSE and correlation coefficient trends for $W_a < 10$ and $W_a \geq 10$, we suggest that using $W_a = 1$ is preferable to reduce the bias in radial velocity residuals, although the retrieved flow may occasionally produce small irregular structures. $W_a = 5$ is a good choice to remove those structures at the cost of increasing the bias in wake and free-flow residuals. We do not recommend using higher values of W_a. As shown in Fig. 13, the high weight of $W_a = 20$ may force the algorithm to stay at the initial guess field, because other components would not contribute comparably to the cost function. Small weights $W_a < 1$ should not be considered, as they lead to increased residuals.

We introduced an additional weight W_{b2} to the term B of the cost function Eq. (6). This weight may be left at $W_{b2} = 1$, provided the radial velocity field was filtered before estimating a derivative $\partial V_r/\partial\theta$. If the original radial velocity field is used, leaving the weight at $W_{b2} = 1$ results in erroneous retrieval due to the high value of derivative (Fig. 16). Decreasing the weight to $W_{b2} = 0.1$ performs nearly equally for filtered and original radial velocities but slightly increases noisiness in the retrieved field. The residuals distribution in the case of reduced weight generally remains similar to the base case: $W_{b2} = 1$ and filtered radial velocity.

Being complementary, the weights W_b and W_d behave in a similar way. We alter the weight W_d and calculate the other weight as $W_b = 1 - W_d$. Effectively, the dynamic weight W_d defined in Eq. (10) acts similarly to the wake masking while also providing local weighting for the background flow. If Eq. (10) cannot be implemented, the wake mask can be re-used in the cost function optimization. However, the wakes cannot be identified reliably in the crosswind with the current masking algorithm. W_d may be set to a constant value as an alternative. Constant weight $W_d = 0.5$ provides an equal weighting to the wake and free-flow points and slightly decreases the bias Eq. (10). Setting $W_d = 1$ may shift the bias within the wakes but does not remove it completely.

The weight W_c is defined dynamically as a binary matrix. Since W_c strongly depends on the flow speed and grid resolution, the matrix may be filled with ones in the case of the low radial velocity, e.g., weak actual flow or crosswind. Setting W_c to a constant value of one for all cases does not strongly alter the final solution. Moreover, W_c would have to be increased by several orders for the residuals to become noticeably affected.

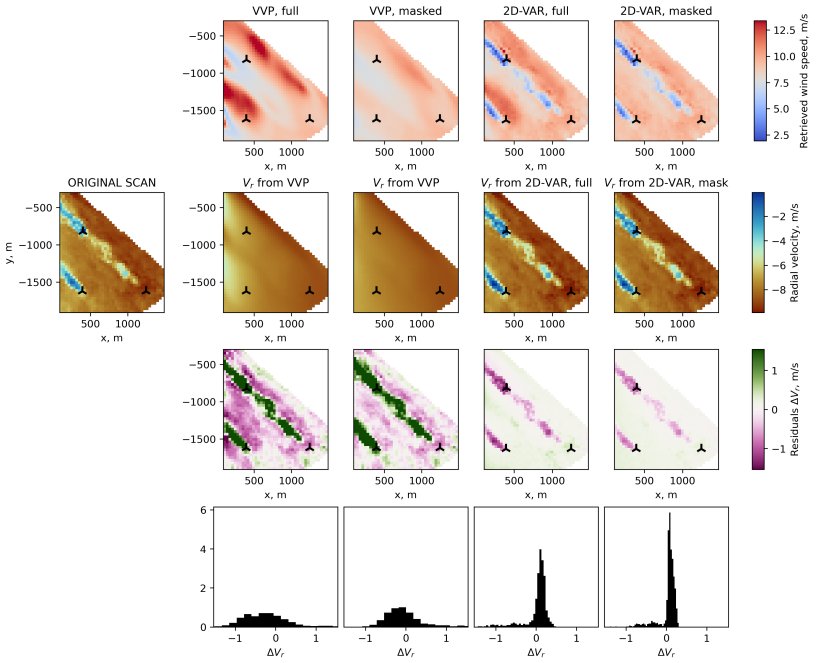

Figure 11 Example of the retrieval performed for the scan from SEP16 taken at 20160911 23:00:03 UTC+0. FINO1 wind speed 8.8 m/s, wind direction 121°.

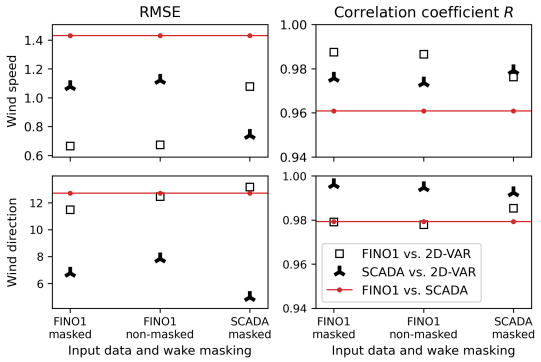

Figure 12 Wind speed and direction RMSE depending on an initial guess of the cost optimization function and wake processing for the VVP algorithm

5 | CONCLUSIONS

We independently reproduced the 2D-VAR algorithm for lidar retrieval for the August 31, 2016 dataset. While we got a similar error in the wind speed estimation, our implementation returned higher offset in the wind direction compared to the original study. We attribute the mismatch to different pre-processing procedures and optimization algorithms used and the overall sensitivity of the wind direction to the retrieval.

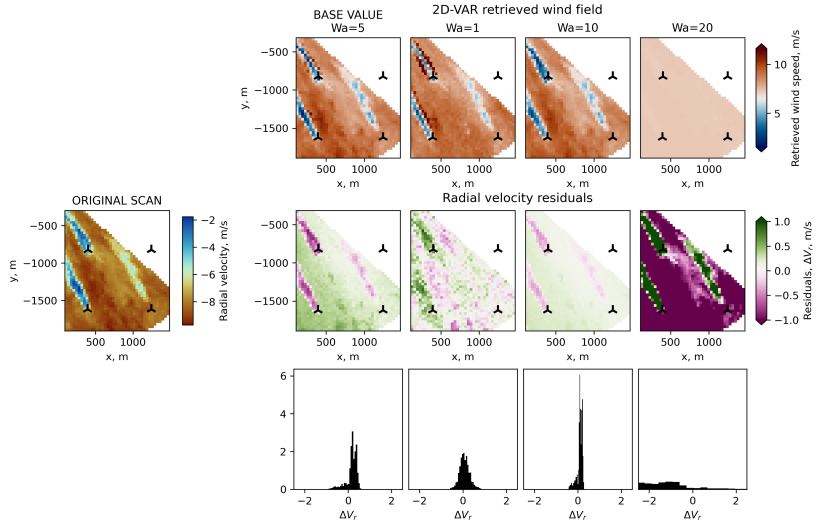

Figure 13 2D-VAR retrieved field and radial velocity residuals depending on the choice of weight W_a. Scan taken at 20160912 2:07:43 UTC+0. FINO1 wind speed 7.2 m/s, wind direction 138°.

We performed an extended validation with the September 2016 dataset and SCADA data for the same period. Due to a higher lidar elevation angle, the scans were capturing wakes near the hub height. We observed an increased heterogeneity in the first step of the 2D-VAR algorithm – an estimation of the background flow with the VVP algorithm. The effect primarily appears in the case of large and strong wakes, which are observed when the wind direction is aligned with the lidar beam. The unwanted heterogeneity was mitigated by masking the wakes with an automatic thresholding algorithm to exclude them from the VVP solution.

Besides the background flow from the VVP algorithm, the cost function optimization in the second step of 2D-VAR algorithm is found to be sensitive to weights and the initial wind field. Defining the initial wind field based on FINO1 or SCADA data tunes the resulting field to the initial values. Nevertheless, the retrieval algorithm tends to the actual flow in both cases – the agreement between wind direction retrieved near AV7 and SCADA series is always better than to FINO1 data. FINO1 data can still be used as an initial guess, when SCADA data are not available. However, if both datasets are accessible, using SCADA data becomes preferable to reconstruct the wind field near the corresponding wind turbine.

Of the weights regarded, the weight W_a is directly connected to the radial velocity residuals and, therefore, affects the residuals and the flow structure most. Other main weights – W_b, W_c, and W_d – have weaker effect on the retrieval result, although they may cause local changes in the retrieved flow. A supplementary weight W_{b2} was introduced primarily for an additional control over the $\partial V_r/\partial\theta$ derivative. Smooth derivative along azimuth θ is more important than W_{b2} in the case of a small azimuth step.

The retrieved flow behaves differently when the wakes are parallel or perpendicular. It is possible that the accuracy of 2D-VAR retrieval may be increased by adjusting the cost function depending on the wind direction relative to the scanned azimuths. Since a comparison to the 'true' flow is complicated for the lidar data, we plan to explore the 2D-VAR algorithm performance on LES generated wakes and virtual lidar in order to improve the retrieval result.

ACKNOWLEDGMENTS

The OBLEX-F1 field campaign was performed under the Norwegian Centre for Offshore Wind Energy (NORCOWE), funded by the Research Council of Norway (RCN) under project number 193821. The scanning Doppler wind lidar system (Leosphere WindCube 100S) has been made available via the National Norwegian infrastructure project OBLO (Offshore Boundary Layer Observatory) also funded by RCN under project number 227777.

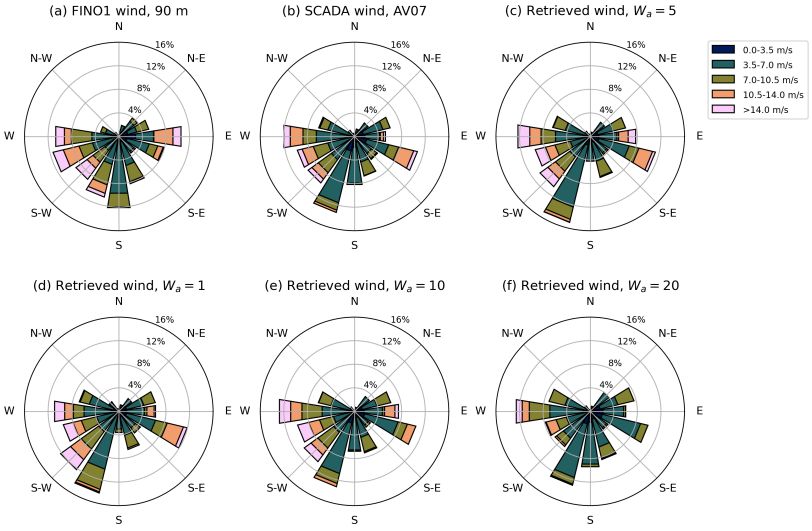

Figure 14 Wind roses for inflow probe at AV7, W_a sensitivity. Only scans valid for retrieval are considered. a) FINO1 data, b) SCADA data, c) 2D-VAR retrieval, $W_a = 1$, d) 2D-VAR retrieval, $W_a = 5$ – default parameter in this study, e) 2D-VAR retrieval, $W_a = 10$

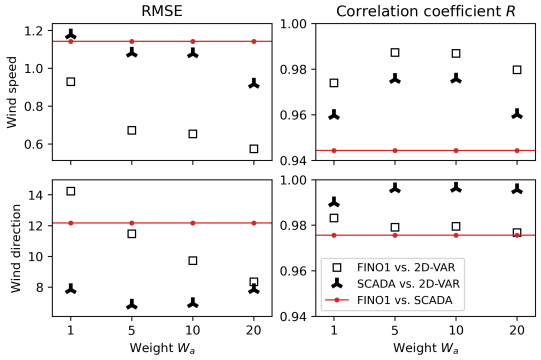

Figure 15 Wind speed and direction RMSE depending on the choice of weight W_a

Wind speed and direction data at FINO1 were made available by the RAVE (Research at Alpha Ventus) initiative, which was funded by the German Federal Ministry of Economic Affairs and Energy on the basis of a decision by the German Bundestag and coordinated by Fraunhofer IWES (see: www.rave-offshore.de).

This work was partly supported by the Research Council of Norway through "Research on smart operation control technologies for offshore wind farms (CONWIND)" project, ENERGIX, with grant number 304229.

References

1. Lothon M, Lenschow DH, Mayor SD. Coherence and scale of vertical velocity in the convective boundary layer from a Doppler lidar. *Boundary-Layer Meteorology* 2006; 121: 521-536. doi: 10.1007/S10546-006-9077-1/METRICS

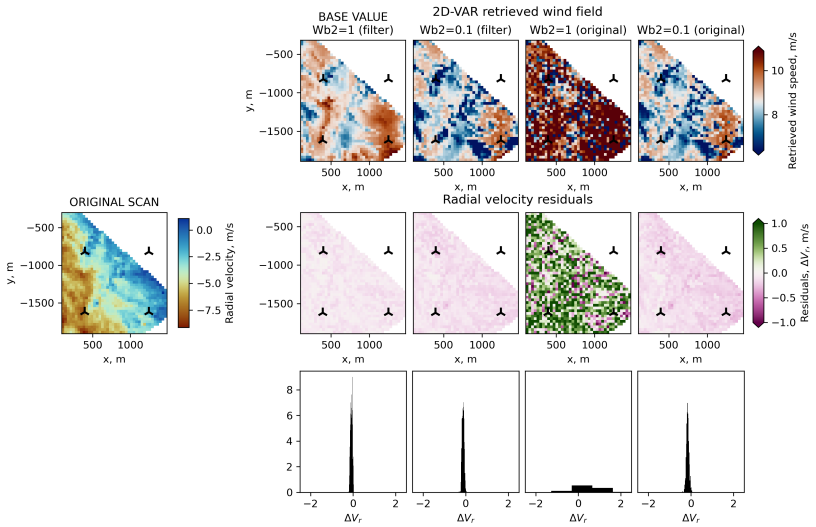

Figure 16 2D-VAR retrieved field and radial velocity residuals depending on the choice of weight W_{b2} in Eq. (6). Scan taken at 20160911 00:01:45 UTC+0. FINO1 wind speed 9.7 m/s, wind direction 201°.

2. Manninen AJ, Marke T, Tuononen M, O'Connor EJ. Atmospheric Boundary Layer Classification With Doppler Lidar. *Journal of Geophysical Research: Atmospheres* 2018; 123: 8172-8189. doi: 10.1029/2017JD028169

3. Liu Z, Barlow JF, Chan PW, et al. A Review of Progress and Applications of Pulsed Doppler Wind LiDARs. *Remote Sensing 2019*, *Vol. 11*, *Page 2522* 2019; 11: 2522. doi: 10.3390/RS11212522

4. Reuder J, Cheynet E, Clifton A, et al. Recommendation on use of wind lidars. https://doi.org/10.5281/zenodo.4672351; 2021

5. Trabucchi D, Trujillo JJ, Schneemann J, Bitter M, Kühn M. Application of staring lidars to study the dynamics of wind turbine wakes. *Meteorologische Zeitschrift* 2015; 24: 557-564. doi: 10.1127/METZ/2014/0610

6. Courtney M, Wagner R, Lindelöw P. Testing and comparison of lidars for profile and turbulence measurements in wind energy. *IOP Conf. Ser. Earth Environ. Sci.* 2008; 1(1): 012021. doi: 10.1088/1755-1315/1/1/012021

7. Mann J, Sathe A, Gottschall J, Courtney M. Lidar Turbulence Measurements for Wind Energy. In: . 141. Springer Science and Business Media, LLC. 2012 (pp. 263–270)

8. Wagner R, Courtney M, Gottschall J, Lindelöw P. Improvement of power curve measurement with lidar wind speed profiles. In: EWEC 2010 Proceedings online. European Wind Energy Association (EWEA); 2010.

9. Krishnamurthy R, Choukulkar A, Calhoun R, Fine J, Oliver A, Barr KS. Coherent Doppler lidar for wind farm characterization. *Wind Energy* 2013; 16: 189-206. doi: 10.1002/WE.539

10. Bakhoday-Paskyabi M, Flügge M. Predictive Capability of WRF Cycling 3DVAR: LiDAR Assimilation at FINO1. *Journal of Physics: Conference Series* 2021; 2018: 012006. doi: 10.1088/1742-6596/2018/1/012006

11. Raach S, Schlipf D, Haizmann F, Cheng PW. Three Dimensional Dynamic Model Based Wind Field Reconstruction from Lidar Data. *Journal of Physics: Conference Series* 2014; 524: 012005. doi: 10.1088/1742-6596/524/1/012005

12. Dhiman HS, Deb D, Muresan V, Balas VE. Wake Management in Wind Farms: An Adaptive Control Approach. *Energies 2019*, *Vol. 12*, *Page 1247* 2019; 12: 1247. doi: 10.3390/EN12071247

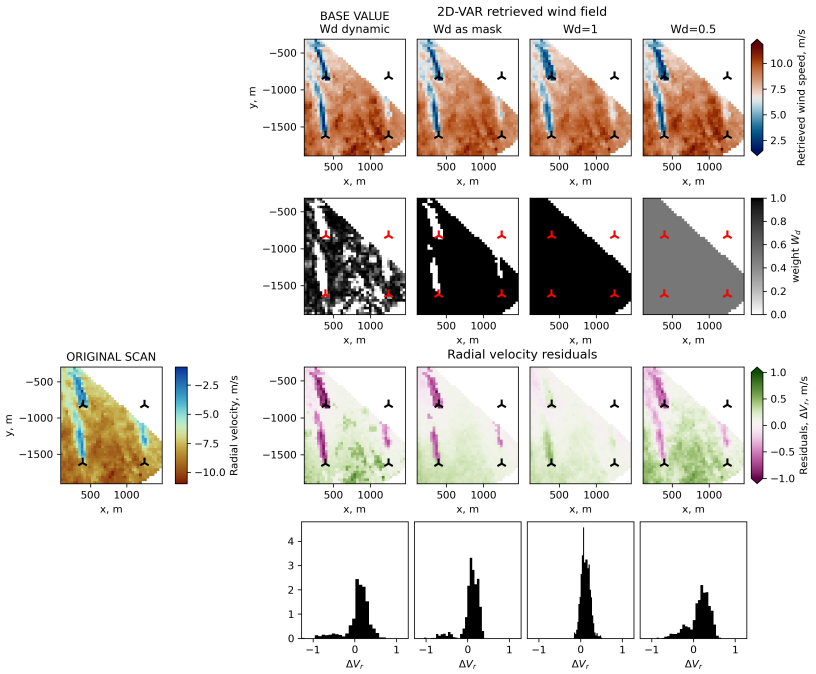

Figure 17 2D-VAR retrieved field and radial velocity residuals depending on the choice of weight W_d. Scan taken at 20160924 21:18:21 UTC+0. FINO1 wind speed 7.4 m/s, wind direction 158°.

13. Krishnamurthy R, Reuder J, Svardal B, Fernando HJ, Jakobsen JB. Offshore Wind Turbine Wake characteristics using Scanning Doppler Lidar. *Energy Procedia* 2017; 137: 428-442. doi: 10.1016/j.egypro.2017.10.367

14. Krutova M, Bakhoday-Paskyabi M, Reuder J, Nielsen FG. Development of an automatic thresholding method for wake meandering studies and its application to the data set from scanning wind lidar. *Wind Energy Sci.* 2022; 7(2): 849–873. doi: 10.5194/wes-7-849-2022

15. Smalikho IN, Banakh VA, Pichugina YL, et al. Lidar Investigation of Atmosphere Effect on a Wind Turbine Wake. *Journal of Atmospheric and Oceanic Technology* 2013; 30: 2554-2570. doi: 10.1175/JTECH-D-12-00108.1

16. Browning KA, Wexler R. The Determination of Kinematic Properties of a Wind Field Using Doppler Radar. *J. Appl. Meteorol.* 1968; 7(1): 105–113. doi: 10.1175/1520-0450(1968)007<0105:TDOKPO>2.0.CO;2

17. Wang H, Barthelmie RJ, Clifton A, Pryor SC. Wind Measurements from Arc Scans with Doppler Wind Lidar. *J. Atmos. Ocean. Technol.* 2015; 32(11): 2024–2040. doi: 10.1175/JTECH-D-14-00059.1

18. Janisková M. Assimilation of cloud information from space-borne radar and lidar: experimental study using a 1D+4D-Var technique. *Quarterly Journal of the Royal Meteorological Society* 2015; 141: 2708-2725. doi: 10.1002/QJ.2558

19. Fielding MD, Janisková M. Direct 4D-Var assimilation of space-borne cloud radar reflectivity and lidar backscatter. Part I: Observation operator and implementation. *Quarterly Journal of the Royal Meteorological Society* 2020; 146: 3877-3899. doi: 10.1002/QJ.3878

20. Janisková M, Fielding MD. Direct 4D-Var assimilation of space-borne cloud radar and lidar observations. Part II: Impact on analysis and subsequent forecast. *Quarterly Journal of the Royal Meteorological Society* 2020; 146: 3900-3916. doi: 10.1002/QJ.3879

21. Cherukuru NW, Calhoun R, Krishnamurthy R, Benny S, Reuder J, Flügge M. 2D VAR single Doppler lidar vector retrieval and its application in offshore wind energy. *Energy Procedia* 2017; 137: 497–504. doi: 10.1016/j.egypro.2017.10.378

22. Cherukuru NW. *Doppler Lidar Vector Retrievals and Atmospheric Data Visualization in Mixed/Augmented Reality*. PhD thesis. Arizona State University, 1151 S Forest Ave Tempe, AZ 85281, USA; 2017.

23. Technariumas . Inpainting Healing algorithm. https://github.com/Technariumas/Inpainting; . Accessed: 2022-09-22.

24. Clifton A, Boquet M, Burin Des Roziers E, et al. Remote Sensing of Complex Flows by Doppler Wind Lidar: Issues and Preliminary Recommendations. Tech. Rep. December, National Renewable Energy Laboratory (NREL); Golden, CO (United States): 2015

How to cite this article: Krutova M., Bakhoday-Paskyabi, M., and Reuder J. (2023), Validation of the 2D-VAR lidar retrieval algorithm for non-homogeneous wind fields, *Wind Energy*, .

Bibliography

Abkar, M., and F. Porté-Agel (2015), Influence of atmospheric stability on wind-turbine wakes: A large-eddy simulation study, *Physics of Fluids*, *27*(3), 035,104, doi:10.1063/1.4913695. 2, 12

Abkar, M., and F. Porté-Agel (2016), Influence of the Coriolis force on the structure and evolution of wind turbine wakes, *Physical Review Fluids*, *1*, 1–14, doi:10.1103/physrevfluids.1.063701. 8

Abkar, M., J. N. Sørensen, and F. Porté-Agel (2018), An analytical model for the effect of vertical wind veer on wind turbine wakes, *Energies*, *11*(7), 1–10, doi:10.3390/en11071838. 20

Adaramola, M., and P. Å. Krogstad (2011), Experimental investigation of wake effects on wind turbine performance, *Renewable Energy*, *36*, 2078–2086, doi:10.1016/j.renene.2011.01.024. 3, 9

Ahsbahs, T., N. G. Nygaard, A. Newcombe, and M. Badger (2020), Wind farm wakes from SAR and doppler radar, *Remote Sensing*, *12*, 462, doi:10.3390/rs12030462. 3

Ainslie, J. (1988), Calculating the flowfield in the wake of wind turbines, *Journal of Wind Engineering and Industrial Aerodynamics*, *27*, 213–224, doi:10.1016/0167-6105(88)90037-2. 20

Akhtar, N., B. Geyer, B. Rockel, P. S. Sommer, and C. Schrum (2021), Accelerating deployment of offshore wind energy alter wind climate and reduce future power generation potentials, *Scientific Reports*, *11*, 11,826, doi:10.1038/s41598-021-91283-3. 3

Alblas, L., W. Bierbooms, and D. Veldkamp (2014), Power output of offshore wind farms in relation to atmospheric stability, *Journal of Physics: Conference Series*, *555*(1), 012,004, doi:10.1088/1742-6596/555/1/012004. 12

Andersen, S. J., J. N. Sørensen, S. Ivanell, and R. F. Mikkelsen (2014), Comparison of engineering wake models with CFD simulations, *Journal of Physics: Conference Series*, *524*, 012,161. 19

Ashton, R., F. Viola, S. Camarri, F. Gallaire, and G. V. Iungo (2016), Hub vortex instability within wind turbine wakes: Effects of wind turbulence, loading conditions, and blade aerodynamics, *Physical Review Fluids*, *1*, 073,603, doi:10.1103/PhysRevFluids.1.073603. 7

Atkinson, B. W., and J. W. Zhang (1996), Mesoscale shallow convection in the atmosphere, *Reviews of Geophysics*, *34*, 403–431, doi:10.1029/96RG02623. 4

Bak, C., F. Zahle, R. Bitsche, T. Kim, A. Yde, L. C. Henriksen, M. H. Hansen, J. P. A. A. Blasques, M. Gaunaa, and A. Natarajan (2013), The DTU 10-MW reference wind turbine. 30

Bakhoday-Paskyabi, M., J. Reuder, and M. Flügge (2016), Automated measurements of whitecaps on the ocean surface from a buoy-mounted camera, *Methods in Oceanography*, *17*, 14–31, doi:10.1016/j.mio.2016.05.002. 15

Bakhoday-Paskyabi, M., H. Bui, and M. M. Penchah (2022), D2.1 - Atmospheric-wave multi-scale flow modelling. Delivery report. HIPERWIND EU project, no. 101006689, available at https://www.hiperwind.eu/publications, Accessed: November 24, 2023. 4

Barthelmie, R., S. Pryor, N. Wildmann, and R. Menke (2018), Wind turbine wake characterization in complex terrain via integrated Doppler lidar data from the Perdigão experiment, *Journal of Physics: Conference Series*, *1037*, 052,022, doi:10.1088/1742-6596/1037/5/052022. 13

Barthelmie, R. J., and L. E. Jensen (2010), Evaluation of wind farm efficiency and wind turbine wakes at the Nysted offshore wind farm, *Wind Energy*, *13*(6), 573–586, doi:10.1002/we.408. 12, 19

Barthelmie, R. J., L. Folkerts, G. C. Larsen, K. Rados, S. C. Pryor, S. T. Frandsen, B. Lange, and G. Schepers (2006), Comparison of wake model simulations with offshore wind turbine wake profiles measured by sodar, *Journal of Atmospheric and Oceanic Technology*, *23*(7), 888–901, doi:10.1175/JTECH1886.1. 19

Barthelmie, R. J., M. J. Churchfield, P. J. Moriarty, J. K. Lundquist, G. S. Oxley, S. Hahn, and S. C. Pryor (2015), The role of atmospheric stability/turbulence on wakes at the Egmond aan Zee offshore wind farm, *Journal of Physics: Conference Series*, *625*(1), 012,002, doi:10.1088/1742-6596/625/1/012002. 11, 12

Bastankhah, M., and F. Porté-Agel (2014), A new analytical model for wind-turbine wakes, *Renewable Energy*, *70*, 116–123, doi:10.1016/j.renene.2014.01.002. 19, 20, 21

Bastine, D., B. Witha, M. Wächter, and J. Peinke (2015), Towards a simplified DynamicWake model using POD analysis, *Energies*, *8*, 895–920, doi:10.3390/en8020895. 15

Basu, S., A. A. M. Holtslag, B. J. H. V. D. Wiel, A. F. Moene, and G.-J. Steeneveld (2008), An inconvenient "truth" about using sensible heat flux as a surface boundary condition in models under stably stratified regimes, *Acta Geophysica*, *56*, 88–99, doi:10.2478/s11600-007-0038-y. 26

Beeken, T. (2008), Five years of offshore measurements at the FINO1 platform in the German Bight, *DEWI Magazine*, *80*, 1–5. 32

Bingöl, F., J. Mann, and G. C. Larsen (2010), Light detection and ranging measurements of wake dynamics part I: one-dimensional scanning, *Wind Energy*, *13*(1), 51–61, doi:10.1002/we.352. 13

Blondel, F., and M. Cathelain (2020), An alternative form of the super-gaussian wind turbine wake model, *Wind Energy Science*, *5*, 1225–1236, doi:10.5194/wes-5-1225-2020. 22

Bodini, N., D. Zardi, and J. K. Lundquist (2017), Three-dimensional structure of wind turbine wakes as measured by scanning lidar, *Atmospheric Measurement Techniques*, *10*, 2881–2896, doi:10.5194/amt-10-2881-2017. 13

Breton, S.-P., J. Sumner, J. N. Sørensen, K. S. Hansen, S. Sarmast, and S. Ivanell (2017), A survey of modelling methods for high-fidelity wind farm simulations using large eddy simulation., *Philosophical transactions. Series A, Mathematical, physical, and engineering sciences*, *375*, doi:10.1098/rsta.2016.0097. 15

Burton, T., N. Jenkins, D. Sharpe, and E. Bossanyi (2011), *Wind Energy Handbook*, 1-952 pp., Wiley, doi:10.1002/9781119992714. 28

Cañadillas, B., M. Beckenbauer, J. J. Trujillo, M. Dörenkämper, R. Foreman, T. Neumann, and A. Lampert (2022), Offshore wind farm cluster wakes as observed by long-range-scanning wind lidar measurements and mesoscale modeling, *Wind Energy Science*, *7*, 1241–1262, doi:10.5194/wes-7-1241-2022. 3

Canuto, V. M., and Y. Cheng (1997), Determination of the smagorinsky–lilly constant cs, *Physics of Fluids*, *9*, 1368–1378, doi:10.1063/1.869251. 23

Chamorro, L. P., R. E. A. Arndt, and F. Sotiropoulos (2011), Turbulent flow properties around a staggered wind farm, *Boundary-Layer Meteorology*, *141*, 349–367, doi:10.1007/s10546-011-9649-6. 3

Chatterjee, T., N. W. Cherukuru, Y. T. Peet, and R. J. Calhoun (2018), Large eddy simulation with realistic geophysical inflow of Alpha Ventus wind farm: a comparison with LIDAR field experiments, *Journal of Physics: Conference Series*, *1037*, 072,056, doi:10.1088/1742-6596/1037/7/072056. 4

Cherubini, A., A. Papini, R. Vertechy, and M. Fontana (2015), Airborne wind energy systems: A review of the technologies, *Renewable and Sustainable Energy Reviews*, *51*, 1461–1476, doi:10.1016/j.rser.2015.07.053. 2

Cherukuru, N. W. (2017), Doppler lidar vector retrievals and atmospheric data visualization in mixed/augmented reality, Ph.D. thesis, Arizona State University, 1151 S Forest Ave Tempe, AZ 85281, USA, available at https://www.proquest.com/dissertations-theses/doppler-lidar-vector-retrievals-atmospheric-data/docview/1896107270/se-2 Accessed: 22-11-2023. 34

Cherukuru, N. W., R. Calhoun, R. Krishnamurthy, S. Benny, J. Reuder, and M. Flügge (2017), 2D VAR single Doppler lidar vector retrieval and its application in offshore wind energy, *Energy Procedia*, *137*, 497–504, doi:10.1016/j.egypro.2017.10.378. 14, 34, 40, 41

Cheynet, E., J. B. Jakobsen, and J. Reuder (2018), Velocity spectra and coherence estimates in the marine atmospheric boundary layer, *Boundary-Layer Meteorology*, *169*, 429–460, doi:10.1007/s10546-018-0382-2. 12

Christiansen, M. B., and C. B. Hasager (2005), Wake effects of large offshore wind farms identified from satellite SAR, *Remote Sensing of Environment*, *98*, 251–268, doi:10.1016/j.rse.2005.07.009. 2

Christiansen, M. B., and C. B. Hasager (2006), Using airborne and satellite SAR for wake mapping offshore, *Wind Energy*, *9*, 437–455, doi:10.1002/we.196. 1, 2

Churchfield, M. J., S. Lee, J. Michalakes, and P. J. Moriarty (2012), A numerical study of the effects of atmospheric and wake turbulence on wind turbine dynamics, *Journal of Turbulence*, *13*, 32, doi:10.1080/14685248.2012.668191. 10, 12

Crameri, F. (2023), Scientific colour maps, doi:10.5281/zenodo.8409685. 33

Crespo, A., J. Hernández, and S. Frandsen (1999), Survey of modelling methods for wind turbine wakes and wind farms, *Wind Energy*, *2*, 1–24, doi:10.1002/(SICI)1099-1824(199901/03)2:1<1::AID-WE16>3.3.CO;2-Z. 8

Dai, J., D. Liu, L. Wen, and X. Long (2016), Research on power coefficient of wind turbines based on SCADA data, *Renewable Energy*, *86*, 206–215, doi:10.1016/J.RENENE.2015.08.023. 2

Deardorff, J. W. (1972), Numerical investigation of neutral and unstable planetary boundary layers, *Journal of the Atmospheric Sciences*, *29*, 91–115, doi:10.1175/1520-0469(1972)029<0091:NIONAU>2.0.CO;2. 11

Deardorff, J. W. (1980), Stratocumulus-capped mixed layers derived from a three-dimensional model, *Boundary-Layer Meteorology*, *18*, 495–527, doi:10.1007/BF00119502. 25

Debnath, M., G. V. Iungo, R. Ashton, W. A. Brewer, A. Choukulkar, R. Delgado, J. K. Lundquist, W. J. Shaw, J. M. Wilczak, and D. Wolfe (2017), Vertical profiles of the 3-D wind velocity retrieved from multiple wind lidars performing triple range-height-indicator scans, *Atmospheric Measurement Techniques*, *10*, 431–444, doi:10.5194/amt-10-431-2017. 13

Desmond, C., J. Murphy, L. Blonk, and W. Haans (2016), Description of an 8 MW reference wind turbine, in *Journal of Physics: Conference Series*, vol. 753, IOP Publishing, doi:10.1088/1742-6596/753/9/092013. 30

Dörenkämper, M., B. Witha, G. Steinfeld, D. Heinemann, and M. Kühn (2015), The impact of stable atmospheric boundary layers on wind-turbine wakes within offshore wind farms, *Journal of Wind Engineering and Industrial Aerodynamics*, *144*, 146–153, doi:10.1016/j.jweia.2014.12.011. xiii, 29, 30

Drew, D. R., J. F. Barlow, and S. E. Lane (2013), Observations of wind speed profiles over greater london, uk, using a doppler lidar, *Journal of Wind Engineering and Industrial Aerodynamics*, *121*, 98–105, doi:10.1016/j.jweia.2013.07.019. 13

Duscha, C., J. Pálenik, T. Spengler, and J. Reuder (2023), Observing atmospheric convection with dual-scanning lidars, *Atmospheric Measurement Techniques*, *16*, 5103–5123, doi:10.5194/amt-16-5103-2023. 13

España, G., S. Aubrun, S. Loyer, and P. Devinant (2011), Spatial study of the wake meandering using modelled wind turbines in a wind tunnel, *Wind Energy*, *14*(7), 923–937, doi:10.1002/we.515. 2, 9, 15

Fielding, M. D., and M. Janisková (2020), Direct 4D-Var assimilation of space-borne cloud radar reflectivity and lidar backscatter. Part I: Observation operator and implementation, *Quarterly Journal of the Royal Meteorological Society*, *146*, 3877–3899, doi:10.1002/qj.3878. 14

Finserås, E., I. H. Anchustegui, E. Cheynet, C. G. Gebhardt, and J. Reuder (2024), Gone with the wind? wind farm-induced wakes and regulatory gaps, *Marine Policy*, *159*, 105,897, doi:10.1016/j.marpol.2023.105897. 3

Fischer, G. (2006), *Installation and Operation of the Research Platform FINO1 in the North Sea*, pp. 237–253, Springer Berlin Heidelberg, Berlin, Heidelberg, doi:10.1007/978-3-540-34677-7_15. 32

Fitch, A. C., J. B. Olson, J. K. Lundquist, J. Dudhia, A. K. Gupta, J. Michalakes, and I. Barstad (2012), Local and mesoscale impacts of wind farms as parameterized in a mesoscale NWP model, *Monthly Weather Review*, *140*, 3017–3038, doi:10.1175/MWR-D-11-00352.1. 24

Fleming, P. A., P. M. Gebraad, S. Lee, J.-W. van Wingerden, K. Johnson, M. Churchfield, J. Michalakes, P. Spalart, and P. Moriarty (2014), Evaluating techniques for redirecting turbine wakes using SOWFA, *Renewable Energy*, *70*, 211–218, doi:10.1016/j.renene.2014.02.015. 3, 9

Foti, D., X. Yang, M. Guala, and F. Sotiropoulos (2016), Wake meandering statistics of a model wind turbine: Insights gained by large eddy simulations, *Physical Review Fluids*, *1*, 044,407, doi:10.1103/physrevfluids.1.044407. 2

Foti, D., X. Yang, and F. Sotiropoulos (2018), Similarity of wake meandering for different wind turbine designs for different scales, *Journal of Fluid Mechanics*, *842*, 5–25, doi:10.1017/jfm.2018.9. 9

Frandsen, S., R. J. Barthelmie, S. C. Pryor, O. Rathmann, S. Larsen, J. Højstrup, and M. Thøgersen (2006), Analytical modelling of wind speed deficit in large offshore wind farms, *Wind Energy*, *9*, 39–53, doi:10.1002/we.189. 19

Froude, R. E. (1889), On the part played in propulsion by differences of fluid pressure, *Trans. Inst. Naval Architects*, *30*, 390–405. 29

Gaertner, E., J. Rinker, L. Sethuraman, F. Zahle, B. Anderson, G. Barter, N. Abbas, F. Meng, P. Bortolotti, W. Skrzypinski, G. Scott, R. Feil, H. Bredmose, K. Dykes, M. Shields, C. Allen, and A. Viselli (2020), Definition of the IEA 15-megawatt offshore reference wind, doi:NREL/TP-5000-75698, Golden, CO, USA: National Renewable Energy Laboratory. 30

Gao, J., M. Xue, S.-Y. Lee, A. Shapiro, Q. Xu, and K. K. Droegemeier (2006), A three-dimensional variational single-Doppler velocity retrieval method with simple

conservation equation constraint, *Meteorology and Atmospheric Physics*, *94*, 11–26, doi:10.1007/s00703-005-0170-7. 14

Gao, X., H. Yang, and L. Lu (2016), Optimization of wind turbine layout position in a wind farm using a newly-developed two-dimensional wake model, *Applied Energy*, *174*, 192–200, doi:10.1016/j.apenergy.2016.04.098. 21

Glauert, H. (1935), *Airplane Propellers*, pp. 169–360, Springer Berlin Heidelberg, doi:10.1007/978-3-642-91487-4_3. 28

Global WInd Energy Council (2023), Global Offshore Wind Report, *Tech. rep.*, GWEC, Brussels, Belgium. 1

Göçmen, T., P. V. D. Laan, P. E. Réthoré, A. P. Diaz, G. C. Larsen, and S. Ott (2016), Wind turbine wake models developed at the technical university of Denmark: A review, *Renewable and Sustainable Energy Reviews*, *60*, 752–769, doi:10.1016/j.rser.2016.01.113. 19

Gronemeier, T., A. Inagaki, M. Gryschka, and M. Kanda (2015), Large-eddy simulation of an urban canopy using a synthetic turbulence inflow generation method, *Journal of Japan Society of Civil Engineers, Ser. B1 (Hydraulic Engineering)*, *71*, 43–48, doi:10.2208/jscejhe.71.I_43. 28

Hancock, P. E., and F. Pascheke (2014), Wind-tunnel simulation of the wake of a large wind turbine in a stable boundary layer: Part 2, the wake flow, *Boundary-Layer Meteorology*, *151*(1), 23–37, doi:10.1007/s10546-013-9887-x. 12

Hansen, K. S., R. J. Barthelmie, L. E. Jensen, and A. Sommer (2011), The impact of turbulence intensity and atmospheric stability on power deficits due to wind turbine wakes at Horns Rev wind farm, *Wind Energy*, *15*(1), 183–196, doi:10.1002/we.512. 12

Hasager, C., P. Vincent, J. Badger, M. Badger, A. D. Bella, A. Peña, R. Husson, and P. Volker (2015), Using satellite SAR to characterize the wind flow around offshore wind farms, *Energies*, *8*, 5413–5439, doi:10.3390/en8065413. 1

Hasager, C. B., A. Peña, M. B. Christiansen, P. Astrup, M. Nielsen, F. Monaldo, D. Thompson, and P. Nielsen (2008), Remote sensing observation used in offshore wind energy, *IEEE Journal of Selected Topics in Applied Earth Observations and Remote Sensing*, *1*, 67–79, doi:10.1109/JSTARS.2008.2002218. 2, 3

Hellsten, A., K. Ketelsen, M. Sühring, M. Auvinen, B. Maronga, C. Knigge, F. Barmpas, G. Tsegas, N. Moussiopoulos, and S. Raasch (2021), A nested multi-scale system implemented in the large-eddy simulation model PALM model system 6.0, *Geoscientific Model Development*, *14*, 3185–3214, doi:10.5194/gmd-14-3185-2021. 28

Hersbach, H., B. Bell, P. Berrisford, S. Hirahara, A. Horányi, J. Muñoz-Sabater, J. Nicolas, C. Peubey, R. Radu, D. Schepers, A. Simmons, C. Soci, S. Abdalla, X. Abellan, G. Balsamo, P. Bechtold, G. Biavati, J. Bidlot, M. Bonavita, G. D. Chiara, P. Dahlgren, D. Dee, M. Diamantakis, R. Dragani, J. Flemming, R. Forbes, M. Fuentes, A. Geer, L. Haimberger, S. Healy, R. J. Hogan, E. Hólm, M. Janisková, S. Keeley, P. Laloyaux, P. Lopez, C. Lupu, G. Radnoti, P. de Rosnay, I. Rozum,

F. Vamborg, S. Villaume, and J. N. Thépaut (2020), The ERA5 global reanalysis, *Quarterly Journal of the Royal Meteorological Society*, *146*, 1999–2049, doi: 10.1002/QJ.3803. 23

Högström, U., D. Asimakopoulos, H. Kambezidis, C. Helmis, and A. Smedman (1988), A field study of the wake behind a 2 MW wind turbine, *Atmospheric Environment*, *22*, 803–820, doi:10.1016/0004-6981(88)90020-0. 20

International Electrotechnical Commission (2005), IEC 61400-1-Ed. 3.0: Wind turbines – Part 1: Design requirements, *Tech. rep.*, International Electrotechnical Commission (IEC), Geneva, Switzerland. 19

International Energy Agency (2021), Renewables 2021 – Analysis and forecast to 2026, *Tech. rep.*, IEA, Paris, France. xiii, 1

Ishihara, T., and G.-W. W. Qian (2018), A new Gaussian-based analytical wake model for wind turbines considering ambient turbulence intensities and thrust coefficient effects, *Journal of Wind Engineering and Industrial Aerodynamics*, *177*, 275–292, doi: 10.1016/j.jweia.2018.04.010. 21, 35

Ishihara, T., A. Yamaguchi, and Y. Fujino (2004), Development of a new wake model based on a wind tunnel experiment, accesed: 22-Nov-2023. 21

Iungo, G. V., and F. Porté-Agel (2013), Measurement procedures for characterization of wind turbine wakes with scanning Doppler wind lidars, *Advances in Science and Research*, *10*, 71–75, doi:10.5194/asr-10-71-2013. 13

Ivanell, S., R. Mikkelsen, J. N. Sørensen, and D. Henningson (2010), Stability analysis of the tip vortices of a wind turbine, *Wind Energy*, *13*, 705–715, doi:10.1002/we.391. 7

Jamieson, P. (2018), *Innovation in Wind Turbine Design*, John Wiley & Sons, Ltd. 2

Janisková, M., and M. D. Fielding (2020), Direct 4D-Var assimilation of space-borne cloud radar and lidar observations. Part II: Impact on analysis and subsequent forecast, *Quarterly Journal of the Royal Meteorological Society*, *146*, 3900–3916, doi:10.1002/qj.3879. 14

Jensen, N. O. (1983), A note on wind generator interaction, *Risø-M-2411 Risø National Laboratory Roskilde*, pp. 1–16, doi:Riso-M-2411. 19

Jiménez, P. A., J. Navarro, A. M. Palomares, and J. Dudhia (2015), Mesoscale modeling of offshore wind turbine wakes at the wind farm resolving scale: a composite-based analysis with the Weather Research and Forecasting model over Horns Rev, *Wind Energy*, *18*(3), 559–566, doi:10.1002/we.1708. 24

Johlas, H. M., D. P. Schmidt, and M. A. Lackner (2022), Large eddy simulations of curled wakes from tilted wind turbines, *Renewable Energy*, *188*, 349–360, doi:10.1016/j.renene.2022.02.018. 9

Johnson, H. K., J. Højstrup, H. J. Vested, and S. E. Larsen (1998), On the dependence of sea surface roughness on wind waves, *Journal of Physical Oceanography*, *28*, 1702–1716, doi:10.1175/1520-0485(1998)028<1702:OTDOSS>2.0.CO;2. 1

Jonkman, J., S. Butterfield, W. Musial, and G. Scott (2009), Definition of a 5-MW reference wind turbine for offshore system development, doi:10.2172/947422. 30, 33

Keane, A. (2021), Advancement of an analytical double-gaussian full wind turbine wake model, *Renewable Energy*, *171*, 687–708, doi:10.1016/j.renene.2021.02.078. 22

Keane, A., P. E. O. Aguirre, H. Ferchland, P. Clive, and D. Gallacher (2016), An analytical model for a full wind turbine wake, *Journal of Physics: Conference Series*, *753*(3), 032,039, doi:10.1088/1742-6596/753/3/032039. 21, 22

Kettle, A. J. (2014), Unexpected vertical wind speed profiles in the boundary layer over the southern North Sea, *Journal of Wind Engineering and Industrial Aerodynamics*, *134*, 149–162, doi:10.1016/j.jweia.2014.07.012. 1, 11

Khan, M., Y. Odemark, and J. H. M. Fransson (2017), Effects of inflow conditions on wind turbine performance and near wake structure, *Open Journal of Fluid Dynamics*, *07*, 105–129, doi:10.4236/ojfd.2017.71008. 7

Krishnamurthy, R., J. Reuder, B. Svardal, H. J. Fernando, and J. B. Jakobsen (2017), Offshore wind turbine wake characteristics using scanning Doppler lidar, *Energy Procedia*, *137*, 428–442, doi:10.1016/j.egypro.2017.10.367. 13, 15

Kumer, V.-M., J. Reuder, B. Svardal, C. Sætre, and P. Eecen (2015), Characterisation of single wind turbine wakes with static and scanning wintwex-w lidar data, *Energy Procedia*, *80*, 245–254, doi:10.1016/j.egypro.2015.11.428. 13, 15

Larsen, G. (1988), A simple wake calculation procedure, *Risø-M*, *No. 2760*, 58. 20

Larsen, G. C. (2009), A simple stationary semi-analytical wake model, *Tech. rep.*, Risø National Laboratory for Sustainable Energy, Technical University of Denmark. Denmark. 20

Larsen, G. C., H. A. Madsen, F. Bingöl, J. Mann, S. Ott, J. N. Sørensen, V. Okulov, N. Troldborg, M. Nielsen, K. Thomsen, T. J. Larsen, and R. Mikkelsen (2007), *Dynamic Wake Meandering Modeling*, June, 84 pp., Risø National Laboratory. 9

Larsen, G. C., H. A. Madsen, K. Thomsen, and T. J. Larsen (2008), Wake meandering: a pragmatic approach, *Wind Energy*, *11*, 377–395, doi:10.1002/we.267. 2, 9

Lignarolo, L., D. Ragni, C. Krishnaswami, Q. Chen, C. S. Ferreira, and G. van Bussel (2014), Experimental analysis of the wake of a horizontal-axis wind-turbine model, *Renewable Energy*, *70*, 31–46, doi:10.1016/j.renene.2014.01.020. 7

Lilly, D. K. (1962), On the numerical simulation of buoyant convection, *Tellus*, *14*, 148–172, doi:10.1111/j.2153-3490.1962.tb00128.x. 23

Lilly, D. K. (1966), On the application of the eddy viscosity concept in the inertial sub-range of turbulence, doi:10.5065/D67H1GGQ. 23

Lin, D., B. Khan, M. Katurji, L. Bird, R. Faria, and L. E. Revell (2021), WRF4PALM v1.0: a mesoscale dynamical driver for the microscale PALM model system 6.0, *Geoscientific Model Development*, *14*, 2503–2524, doi:10.5194/gmd-14-2503-2021. 28

Lundquist, J. K., J. D. Mirocha, and B. Kosović (2008), Nesting large-eddy simulations within mesoscale simulations in WRF for wind energy applications, *AGU Fall Meeting Abstracts*, p. 6. 13, 23

Ma, Y., C. L. Archer, and A. Vasel-Be-Hagh (2022), The jensen wind farm parameterization, *Wind Energy Science*, *7*, 2407–2431, doi:10.5194/wes-7-2407-2022. 24

Mao, X., and J. N. Sørensen (2018), Far-wake meandering induced by atmospheric eddies in flow past a wind turbine, *Journal of Fluid Mechanics*, *846*, 190–209, doi:10.1017/jfm.2018.275. 9

Maronga, B., M. Gryschka, R. Heinze, F. Hoffmann, F. Kanani-Sühring, M. Keck, K. Ketelsen, M. O. Letzel, M. Sühring, and S. Raasch (2015), The Parallelized Large-Eddy Simulation Model (PALM) version 4.0 for atmospheric and oceanic flows: Model formulation, recent developments, and future perspectives, *Geoscientific Model Development*, *8*(8), 2515–2551, doi:10.5194/gmd-8-2515-2015. 24

Maronga, B., S. Banzhaf, C. Burmeister, T. Esch, R. Forkel, D. Fröhlich, V. Fuka, K. F. Gehrke, J. Geletič, S. Giersch, T. Gronemeier, G. Groß, W. Heldens, A. Hellsten, F. Hoffmann, A. Inagaki, E. Kadasch, F. Kanani-Sühring, K. Ketelsen, B. A. Khan, C. Knigge, H. Knoop, P. Krč, M. Kurppa, H. Maamari, A. Matzarakis, M. Mauder, M. Pallasch, D. Pavlik, J. Pfafferott, J. Resler, S. Rissmann, E. Russo, M. Salim, M. Schrempf, J. Schwenkel, G. Seckmeyer, S. Schubert, M. Sühring, R. von Tils, L. Vollmer, S. Ward, B. Witha, H. Wurps, J. Zeidler, and S. Raasch (2020), Overview of the PALM model system 6.0, *Geoscientific Model Development*, *13*, 1335–1372, doi:10.5194/gmd-13-1335-2020. 24, 33

Martinez, L. A., C. Meneveau, and R. Stevens (2016), Wind farm large-eddy simulations on very coarse grid resolutions using an actuator line model, in *34th Wind Energy Symposium*, American Institute of Aeronautics and Astronautics, Reston, Virginia, doi:10.2514/6.2016-1261. 28, 30

Martinez-Tossas, L., S. Leonardi, M. Churchfield, and P. Moriarty (2012), A Comparison of Actuator Disk and Actuator Line Wind Turbine Models and Best Practices for Their Use, in *50th AIAA Aerospace Sciences Meeting including the New Horizons Forum and Aerospace Exposition*, American Institute of Aeronautics and Astronautics, Reston, Virigina, doi:10.2514/6.2012-900. 29

Martínez-Tossas, L. A., M. J. Churchfield, and C. Meneveau (2015), Large eddy simulation of wind turbine wakes: detailed comparisons of two codes focusing on effects of numerics and subgrid modeling, *Journal of Physics: Conference Series*, *625*, 012,024, doi:10.1088/1742-6596/625/1/012024. 23

Martínez-Tossas, L. A., J. Annoni, P. A. Fleming, and M. J. Churchfield (2019), The aerodynamics of the curled wake: a simplified model in view of flow control, *Wind Energy Science*, *4*, 127–138, doi:10.5194/wes-4-127-2019. 42

Martínez-Tossas, L. A., J. King, E. Quon, C. J. Bay, R. Mudafort, N. Hamilton, M. F. Howland, and P. A. Fleming (2021), The curled wake model: a three-dimensional and extremely fast steady-state wake solver for wind plant flows, *Wind Energy Science*, *6*, 555–570, doi:10.5194/wes-6-555-2021. 42

Medici, D., S. Ivanell, J. Dahlberg, and P. H. Alfredsson (2011), The upstream flow of a wind turbine: blockage effect, *Wind Energy*, *14*, 691–697, doi:10.1002/we.451. 7

Michalakes, J., J. Dudhia, D. Gill, T. Henderson, J. Klemp, W. Skamarock, and W. Wang (2005), The weather research and forecast model: Software architecture and performance, *Use of High Performance Computing in Meteorology*, pp. 156–168, doi:10.1142/9789812701831_0012. 24

Mirocha, J. D., D. A. Rajewski, N. Marjanovic, J. K. Lundquist, B. Kosović, C. Draxl, and M. J. Churchfield (2015), Investigating wind turbine impacts on near-wake flow using profiling lidar data and large-eddy simulations with an actuator disk model, *Journal of Renewable and Sustainable Energy*, *7*, 43,143, doi:10.1063/1.4928873. 13, 24

Moeng, C.-H., and J. C. Wyngaard (1988), Spectral analysis of large-eddy simulations of the convective boundary layer, *Journal of the Atmospheric Sciences*, *45*, 3573–3587, doi:10.1175/1520-0469(1988)045<3573:SAOLES>2.0.CO;2. 25

Moens, M., N. Coudou, and C. Philippe (2019), A numerical study of correlations between wake meandering and loads within a wind farm, *Journal of Physics: Conference Series*, *1256*, 012,012, doi:10.1088/1742-6596/1256/1/012012. 9

Møller, M., P. Domagalski, and L. R. Sætran (2020), Comparing abnormalities in onshore and offshore vertical wind profiles, *Wind Energy Science*, *5*, 391–411, doi:10.5194/wes-5-391-2020. 4

Moriarty, P. J., and A. C. Hansen (2005), AeroDyn theory manual, *Tech. rep.*, National Renewable Energy Lab. 29

Motta, M., R. J. Barthelmie, and P. Vølund (2005), The influence of non-logarithmic wind speed profiles on potential power output at danish offshore sites, *Wind Energy*, *8*, 219–236, doi:10.1002/we.146. 11, 12

Newman, J. F., P. M. Klein, S. Wharton, A. Sathe, T. A. Bonin, P. B. Chilson, and A. Muschinski (2016), Evaluation of three lidar scanning strategies for turbulence measurements, *Atmospheric Measurement Techniques*, *9*(5), 1993–2013, doi:10.5194/amt-9-1993-2016. 13

Niayifar, A., and F. Porté-Agel (2015), A new analytical model for wind farm power prediction, *Journal of Physics: Conference Series*, *625*, 012,039, doi:10.1088/1742-6596/625/1/012039. 38

Niayifar, A., and F. Porté-Agel (2016), Analytical modeling of wind farms: A new approach for power prediction, *Energies*, *9*(9), 1–13, doi:10.3390/en9090741. 20

Nielsen, M., H. Ejsing Jørgensen, and S. Frandsen (2009), Wind and wake models for IEC 61400-1 site assessment, in *EWEC 2009 Proceedings online*, EWEC, european Wind Energy Conference and Exhibition, EWEC 2009 ; Conference date: 16-03-2009 Through 19-03-2009. 19

Nijhuis, A. O., O. Krasnov, C. Unal, H. Russchenberg, and A. Yarovoy (2014), Outlook for a new wind field retrieval technique: The 4D-Var wind retrieval, *2014 International Radar Conference*, pp. 1–6, doi:10.1109/RADAR.2014.7060421. 14

Nunalee, C. G., and S. Basu (2014), Mesoscale modeling of coastal low-level jets: implications for offshore wind resource estimation, *Wind Energy*, *17*, 1199–1216, doi:10.1002/we.1628. 4

Nybø, A., F. G. Nielsen, and J. Reuder (2019), Processing of sonic anemometer measurements for offshore wind turbine applications, *Journal of Physics: Conference Series*, *1356*, 012,006, doi:10.1088/1742-6596/1356/1/012006. 32

Nybø, A., F. G. Nielsen, J. Reuder, M. J. Churchfield, and M. Godvik (2020), Evaluation of different wind fields for the investigation of the dynamic response of offshore wind turbines, *Wind Energy*, *23*(9), 1810–1830, doi:10.1002/we.2518. 12, 32

Nygaard, N. G., L. Poulsen, E. Svensson, and J. G. Pedersen (2022), Large-scale benchmarking of wake models for offshore wind farms, *Journal of Physics: Conference Series*, *2265*, 022,008, doi:10.1088/1742-6596/2265/2/022008. 18

Peña, A., S.-E. Gryning, and J. Mann (2010), On the length-scale of the wind profile, *Quarterly Journal of the Royal Meteorological Society*, *136*(653), 2119–2131, doi:10.1002/qj.714. xiii, 11

Peña, A., P. Réthoré, and M. P. Laan (2016), On the application of the Jensen wake model using a turbulence-dependent wake decay coefficient: the Sexbierum case, *Wind Energy*, *19*, 763–776, doi:10.1002/we.1863. 19

Pitt, D., and D. Peters (1981), Theoretical prediction of dynamic-in ow derivatives, *Vertica*, *5*. 29

Platis, A., S. K. Siedersleben, J. Bange, A. Lampert, K. Bärfuss, R. Hankers, B. Cañadillas, R. Foreman, J. Schulz-Stellenfleth, B. Djath, T. Neumann, and S. Emeis (2018), First in situ evidence of wakes in the far field behind offshore wind farms, *Scientific Reports*, *8*(1), 1–10, doi:10.1038/s41598-018-20389-y. 3, 12

Porté-Agel, F., Y.-T. Wu, H. Lu, and R. J. Conzemius (2011), Large-eddy simulation of atmospheric boundary layer flow through wind turbines and wind farms, *Journal of Wind Engineering and Industrial Aerodynamics*, *99*(4), 154–168, doi:10.1016/J.JWEIA.2011.01.011. 30

Quon, E. W., P. Doubrawa, and M. Debnath (2020), Comparison of rotor wake identification and characterization methods for the analysis of wake dynamics and evolution, *Journal of Physics: Conference Series*, *1452*, 012,070, doi:10.1088/1742-6596/1452/1/012070. 14

Rahlves, C., F. Beyrich, and S. Raasch (2022), Scan strategies for wind profiling with Doppler lidar – a large-eddy simulation (LES)-based evaluation, *Atmospheric Measurement Techniques*, *15*, 2839–2856, doi:10.5194/amt-15-2839-2022. 4

Rankine, W. J. M. (1865), On the mechanical principles of the action of propellers, *Transactions of the Institution of Naval Architects*, *6*, 13–39. 29

Réthoré, P. E., P. Van Der Laan, N. Troldborg, F. Zahle, and N. N. Sørensen (2014), Verification and validation of an actuator disc model, *Wind Energy*, *17*(6), 919–937, doi:10.1002/we.1607. 29

Rodrigo, J. S., E. Cantero, B. García, F. Borbón, U. Irigoyen, S. Lozano, P. M. Fernande, and R. A. Chávez (2015), Atmospheric stability assessment for the characterization of offshore wind conditions, *Journal of Physics: Conference Series*, *625*, 012,044, doi:10.1088/1742-6596/625/1/012044. 11

Saiki, E. M., C.-H. Moeng, and P. P. Sullivan (2000), Large-eddy simulation of the stably stratified planetary boundary layer, *Boundary-Layer Meteorology*, *95*, 1–30, doi:10.1023/A:1002428223156. 25

Sathe, A., S.-E. Gryning, and A. Peña (2011), Comparison of the atmospheric stability and wind profiles at two wind farm sites over a long marine fetch in the North Sea, *Wind Energy*, *14*(6), 767–780, doi:10.1002/we.456. 11

Sathe, A., J. Mann, T. Barlas, W. Bierbooms, and G. van Bussel (2013), Influence of atmospheric stability on wind turbine loads, *Wind Energy*, *16*, 1013–1032, doi:10.1002/we.1528. 12

Schmidt, H., and U. Schumann (1989), Coherent structure of the convective boundary layer derived from large-eddy simulations, *Journal of Fluid Mechanics*, *200*, 511–562, doi:10.1017/S0022112089000753. 11

Schreiber, J., A. Balbaa, and C. L. Bottasso (2019), Brief communication: A double Gaussian wake model, *Wind Energy Science Discussions*, pp. 1–13, doi:10.5194/wes-2019-52. 21, 22

Shen, W., J. Sørensen, and J. Zhang (2007), Actuator surface model for wind turbine flow computations, in *Proceedings of European Wind Energy Conference 2007*. 30

Shen, W. Z., R. Mikkelsen, J. N. Sørensen, and C. Bak (2005a), Tip loss corrections for wind turbine computations, *Wind Energy*, *8*, 457–475, doi:10.1002/we.153. 29

Shen, W. Z., J. N. Sørensen, and R. Mikkelsen (2005b), Tip loss correction for actuator/Navier–Stokes computations, *Journal of Solar Energy Engineering*, *127*, 209–213, doi:10.1115/1.1850488. 29

Sherry, M., J. Sheridan, and D. L. Jacono (2013), Characterisation of a horizontal axis wind turbine's tip and root vortices, *Experiments in Fluids*, *54*, 1417, doi:10.1007/s00348-012-1417-y. 7

Simley, E., N. Angelou, T. Mikkelsen, M. Sjöholm, J. Mann, and L. Y. Pao (2016), Characterization of wind velocities in the upstream induction zone of a wind turbine using scanning continuous-wave lidars, *Journal of Renewable and Sustainable Energy*, *8*, 13,301, doi:10.1063/1.4940025. 7

Smagorinsky, J. (1963), General circulation experiments with the primitive equations, *Monthly Weather Review*, *91*, 99–164, doi:10.1175/1520-0493(1963)091<0099:GCEWTP>2.3.CO;2. 23

Smedman, A.-S., H. Bergström, and U. Högström (1995), Spectra, variances and length scales in a marine stable boundary layer dominated by a low level jet, *Boundary-Layer Meteorology*, *76*, 211–232, doi:10.1007/BF00709352. 12

Snel, H., and J. G. Schepers (1995), Joint investigation of dynamic inflow effects and implementation of an engineering method, *Tech. rep.*, Netherlands Energy Research Foundation (ECN). 28

Sørensen, N. N., J. A. Michelsen, and S. Schreck (2002), Navier–Stokes predictions of the NREL phase VI rotor in the NASA Ames 80 ft x 120 ft wind tunnel, *Wind Energy*, *5*, 151–169, doi:10.1002/we.64. 22

Spalart, P. R. (2009), Detached-eddy simulation, *Annual Review of Fluid Mechanics*, *41*, 181–202, doi:10.1146/annurev.fluid.010908.165130. 24

Späth, F., A. Behrendt, W. A. Brewer, D. Lange, C. Senff, D. D. Turner, T. J. Wagner, and V. Wulfmeyer (2022), Simultaneous observations of surface layer profiles of humidity, temperature, and wind using scanning lidar instruments, *Journal of Geophysical Research: Atmospheres*, *127*, e2021JD035,697, doi:10.1029/2021JD035697. 13

Stevens, R. J., D. F. Gayme, and C. Meneveau (2016), Effects of turbine spacing on the power output of extended wind-farms, *Wind Energy*, *19*, 359–370, doi:10.1002/we.1835. 3

Stull, R. (1988), *An Introduction to Boundary Layer Meteorology*, Atmospheric and Oceanographic Sciences Library, Springer Netherlands, doi:10.1007/978-94-009-3027-8. 10, 11

Tao, S., Q. Xu, A. Feijóo, G. Zheng, and J. Zhou (2020), Nonuniform wind farm layout optimization: A state-of-the-art review, *Energy*, *209*, 118,339, doi:10.1016/j.energy.2020.118339. 3, 18

The Offshore Boundary-Layer Observatory (OBLO) (2015), The Offshoe Boundary-Layer Experiment at Fino1 (OBLEX-F1), https://oblo.w.uib.no/activities/the-oblex-f1-measurment-campaign/, accessed: 24-11-2023. 31

Troldborg, N., F. Zahle, P.-E. Réthoré, and N. N. Sørensen (2015), Comparison of wind turbine wake properties in non-sheared inflow predicted by different computational fluid dynamics rotor models, *Wind Energy*, *18*(7), 1239–1250, doi:10.1002/we.1757. 29

Trujillo, J. J., F. Bingöl, G. C. Larsen, J. Mann, and M. Kühn (2011), Light detection and ranging measurements of wake dynamics. Part II: Two-dimensional scanning, *Wind Energy*, *14*(1), 61–75, doi:10.1002/we.402. 13

Türk, M., and S. Emeis (2010), The dependence of offshore turbulence intensity on wind speed, *Journal of Wind Engineering and Industrial Aerodynamics*, *98*, 466–471, doi:10.1016/j.jweia.2010.02.005. 12

van der Laan, M. P., and N. N. Sørensen (2017), Why the Coriolis force turns a wind farm wake clockwise in the Northern Hemisphere, *Wind Energy Science*, *2*, 285–294, doi:10.5194/wes-2-285-2017. 8

Vermeer, L., J. Sørensen, and A. Crespo (2003), Wind turbine wake aerodynamics, *Progress in Aerospace Sciences*, *39*, 467–510, doi:10.1016/S0376-0421(03)00078-2. 8

Volker, P. J. H., J. Badger, A. N. Hahmann, and S. Ott (2015), The Explicit Wake Parametrisation V1.0: a wind farm parametrisation in the mesoscale model WRF, *Geoscientific Model Development*, *8*(11), 3715–3731, doi:10.5194/gmd-8-3715-2015. 24

Vollmer, L., G. Steinfeld, D. Heinemann, and M. Kühn (2016), Estimating the wake deflection downstream of a wind turbine in different atmospheric stabilities: An LES study, *Wind Energy Science Discussions*, pp. 1–23, doi:10.5194/wes-2016-4. 15

Vollmer, L., G. Steinfeld, and M. Kühn (2017), Transient LES of an offshore wind turbine, *Wind Energy Science Discussions*, *2*, 603–614, doi:10.5194/wes-2017-16. 28

Wagner, D., G. Steinfeld, B. Witha, H. Wurps, and J. Reuder (2019), Low level jets over the southern North Sea, *Meteorologische Zeitschrift*, *28*, 389–415, doi:10.1127/metz/2019/0948. 4, 12, 28

Wang, H., and R. J. Barthelmie (2015), Wind turbine wake detection with a single doppler wind lidar, *Journal of Physics: Conference Series*, *625*, 012,017, doi:10.1088/1742-6596/625/1/012017. 13

Werner, C. (2005), *Doppler Wind Lidar*, pp. 325–354, Springer New York, New York, NY, doi:10.1007/0-387-25101-4_12. 13

Wharton, S., and J. K. Lundquist (2012), Assessing atmospheric stability and its impacts on rotor-disk wind characteristics at an onshore wind farm, *Wind Energy*, *15*(4), 525–546, doi:10.1002/we.483. 12

Wijk, A. V., A. Beljaars, A. Holtslag, and W. Turkenburg (1990), Evaluation of stability corrections in wind speed profiles over the North Sea, *Journal of Wind Engineering and Industrial Aerodynamics*, *33*, 551–566, doi:10.1016/0167-6105(90)90007-Y. 11

Witha, B., G. Steinfeld, and D. Heinemann (2014), *High-Resolution Offshore Wake Simulations with the LES Model PALM*, pp. 175–181, Springer, Berlin, Heidelberg, doi:10.1007/978-3-642-54696-9_26. 27, 28

Wu, Y.-T., and F. Porté-Agel (2011), Large-eddy simulation of wind-turbine wakes: Evaluation of turbine parametrisations, *Boundary-Layer Meteorology*, *138*(3), 345–366, doi:10.1007/s10546-010-9569-x. 30

Yan, C., and C. L. Archer (2018), Assessing compressibility effects on the performance of large horizontal-axis wind turbines, *Applied Energy*, *212*, 33–45, doi:10.1016/j.apenergy.2017.12.020. 17

Yang, X., and F. Sotiropoulos (2018), A new class of actuator surface models for wind turbines, *Wind Energy*, *21*(5), 285–302, doi:10.1002/we.2162. 28

Yang, X. I. A., and K. P. Griffin (2020), Grid-point and time-step requirements for direct numerical simulation and large-eddy simulation, *Physics of Fluids*, *33*, 15,108, doi:10.1063/5.0036515. 22

Zhang, W., C. D. Markfort, and F. Porté-Agel (2012), Near-wake flow structure downwind of a wind turbine in a turbulent boundary layer, *Experiments in Fluids*, *52*, 1219–1235, doi:10.1007/s00348-011-1250-8. 7

Zhang, W., C. D. Markfort, and F. Porté-Agel (2013), Wind-turbine wakes in a convective boundary layer: A wind-tunnel study, *Boundary-Layer Meteorology*, *146*(2), 161–179, doi:10.1007/s10546-012-9751-4. 7, 12

Graphic design: Communication Division, UiB / Print: Skipnes Kommunikasjon AS

uib.no

ISBN: 9788230848937 (print)
9788230845813 (PDF)